Elaboration and characterization of Nickel and/or Ruthenium based catalysts for CO valorization through the methanationor the dry reforming of methane reactions

Rita Mahfouz

▶ **To cite this version:**

Rita Mahfouz. Elaboration and characterization of Nickel and/or Ruthenium based catalysts for CO valorization through the methanationor the dry reforming of methane reactions. Analytical chemistry. Université du Littoral Côte d'Opale; Université de Balamand (Tripoli, Liban), 2021. English. NNT : 2021DUNK0581 . tel-03261791

HAL Id: tel-03261791

https://theses.hal.science/tel-03261791

Submitted on 16 Jun 2021

HAL is a multi-disciplinary open access archive for the deposit and dissemination of scientific research documents, whether they are published or not. The documents may come from teaching and research institutions in France or abroad, or from public or private research centers.

L'archive ouverte pluridisciplinaire **HAL**, est destinée au dépôt et à la diffusion de documents scientifiques de niveau recherche, publiés ou non, émanant des établissements d'enseignement et de recherche français ou étrangers, des laboratoires publics ou privés.

Thèse de Doctorat

Spécialité: Chimie théorique, physique, analytique

présentée à *l'Ecole Doctorale en Sciences Technologie et Santé (ED 585)* **de l'Université du Littoral Côte d'Opale**

Rita Mahfouz

pour obtenir le grade de Docteur de l'Université du Littoral Côte d'Opale

Synthèses et Caractérisations de Catalyseurs à Base de Nickel et/ou de Ruthénium pour la Valorisation du CO_2 via la Méthanation ou le Reformage à Sec du Méthane

Soutenue le 12 février 2021 après avis des rapporteurs, devant le jury d'examen:

M^{me} Cassia Boyadjian, Assistant Professor, American University of Beirut	**Président**
M^{me} Maya Boutros, Professeur, Université Libanaise	**Rapporteur**
M. Béchara Taouk, Professeur, Université de Rouen Normandie	**Rapporteur**
M^{me} Tamara El Zein, Directrice du Programme de Bourses Doctorales du CNRS-L	**Examinateur**
M^{me} Jane Estephane, Associate Professor, University of Balamand	**Co-encadrant**
M. Cédric Gennequin, Maître de Conférences, Université du Littoral Côte D'Opale	**Co-encadrant**
M. Samer Aouad, Professeur, University of Balamand	**Directeur de thèse**
M. Edmond Abi Aad, Professeur, Université du Littoral Côte D'Opale	**Directeur de thèse**

ACKNOWLEDGEMENTS

The opportunity to accomplish this thesis in cotutelle agreement between the Université du Littoral Côte d'Opale (ULCO, France) and the University of Balamand (UOB, Lebanon) would not been possible without the "ARCUS E2D2" Project. Three partners were responsible for the financial support of my scholarship: the Agence Universitaire de la Francophonie (AUF), the ULCO, and the National Council for Scientific Research in Lebanon (CNRS-L), and for that I am very thankful. I also want to thank the doctoral school "l'École Doctorale : Sciences, Technologie, Santé" that this thesis was attached to.

I would like to thank several key people that have participated in a way or another in my thesis experience during these past three years.

First and foremost, I would like to express my sincere gratitude to Pr. Edmond ABI-AAD and Pr. Samer AOUAD, my thesis directors in France and Lebanon, and to Dr. Cédric GENNEQUIN and Dr. Jane ESTEPHANE, my thesis supervisors in France and Lebanon for their commitment and dedication to my work, scientific guidance and encouragement.

I would also genuinely like to thank Pr. Maya BOUTROS, Pr. Béchara TAOUK, Dr. Tamara EL ZEIN, and Dr. Cassia BOYADJIAN, the jury members, for the time and effort they have devoted in the evaluation of this work.

I would like to thank Pr. Stéphane SIFFERT, director of the Unité de Chimie Environnementale et Interactions sur le Vivant (UCEIV) and all the members of the UCEIV including Pr. Dominique COURCOT, Pr. Renaud COUSIN and Miss Veronique VANVINCQ. A special thank you goes for Dr. Lucette TIDAHY and Dr. Christophe POUPIN for their help in the characterization experiments.

At the University of Balamand, I express my sincere appreciation to Pr. George BAHR, Dean of the Faculty of Arts and Sciences, Pr. Paolo YAMMINE and Pr. Rima MANNEH, chairpersons of the Chemistry and Chemical Engineering department. I would like to thank Pr. Hanna EL-NAKAT and Pr. Jihad ATTIEH for their support that goes back to my Master thesis years. I would also like to thank Miss Waed ATTIEH.

A big heartfelt thank you for the staff at the Chemistry Lab: Miss Amal AOUN, Miss Cherine SALIBA and Mr. Bilal EL-KOURY. I am really glad I got the chance to meet such wonderful people who definitely made my 5 years at UOB more pleasant and memorable. A warm thank you also goes to Miss Vanessa EL-KHOURY and Miss Lena MOUSSA for their kindness and help at the Chemical Engineering Lab.

To my friends and colleagues at Balamand: Eliane, Nathalie, Aida, Yasmine, and at ULCO: Muriel, Rebecca, Sara, Hadi, Cynthia, Guillaume, Thamy and Madan. I couldn't have made it without your help and words of encouragement. Thank you for all the laughs, tears, and craziness that we shared together inside the lab or elsewhere and for all the memories that will forever hold a special place in my heart. I am fortunate that I got to experience this journey with each and every one of you.

I thank all my family and friends without whom I would not come this far. I wish I could name every single one of them who stood by me. A special thank you to my uncle and his lovely family for their help and hospitality during my stay in France. Dad, thank you for believing in me and being my backbone since day one. I only hope that I will keep on making you proud. Patrick, thank you for your unconditional love, support and understanding. Thank you for always being there for me.

Last but not least, the biggest thank you goes to my guardian angel. Jano, I wish we got to share this chapter of my life together because it would have been much more beautiful with you in it. I am blessed to have you helping me from where you are in ways that I could not imagine. I am here today because of you.

ABSTRACT

The aim of this work is to investigate the valorization of carbon dioxide through the CO_2 methanation and the CO_2 reforming of methane reactions. Alumina, ceria, and mesoporous silica were chosen as the catalytic support materials. The wet impregnation technique was used in order to add an active phase of 15 wt% nickel (Ni), 1 wt% ruthenium (Ru) or a combination of the two metals (Ni-Ru) on each of the stabilized supports. The obtained catalysts were calcined at 550 ^oC, and then characterized using X-Ray Diffraction (XRD), Nitrogen adsorption/desorption, H_2-Temperature Programmed Reduction (H_2-TPR), and CO_2-Temperature Programmed Desorption (CO_2-TPD).

Characterization results of Ni and/or Ru catalysts supported on CeO_2, Al_2O_3, and KIT-6 showed that all supports and catalysts present a type IVa isotherms typical to mesoporous materials and that the formed RuO_2 species were well-dispersed when CeO_2 is used as a support and in the bi-metallic catalysts. The reduction of NiO was enhanced in the presence of CeO_2 support given its redox properties. The presence of RuO_2 also led to a facilitated NiO reduction in the bi-metallic catalysts.

In the CO_2 methanation reaction, a first part compared the catalytic activity of the different active phases on the same support. In each case, the bi-metallic Ni-Ru catalyst exhibited the highest conversions at 350 ^oC which was linked to a possible good RuO_2 dispersion and NiO reducibility observed in these catalysts. Moreover, regardless of the active phase used, the catalytic activity of the catalysts depended on the type of the support. The order of reactivity obtained was: CeO_2 supported catalysts > KIT-6 supported catalysts > Al_2O_3 supported catalysts. In the second part, KIT-6 was promoted with different CeO_2 percentages and impregnated with the same studied active phases in an attempt to create more economical and stable catalysts. A good dispersion of RuO_2 species, an ameliorated active phase reducibility at lower temperatures, and an enhancement in the basic properties were observed following the promotion with Ce and as the percentage of Ce in the catalyst increased. This ultimately led to higher catalytic performances especially for the bi-metallic 15Ni1Ru/Ce_xKIT-6 catalysts. The stability study showed that the 15Ni1Ru/CeO_2 catalyst exhibited good catalytic activity in terms of CO_2 conversion (70 %) and CH_4 selectivity (99 %) and showed no deactivation for 24 h on stream.

In the CO_2 reforming of methane, CeO_2 supported catalysts showed lower catalytic activity when compared to Al_2O_3 supported catalysts. However, they showed more resistance to carbon formation as proven by the thermal analyses and the XRD performed on the spent

catalysts. The effect of adding Ce to Al_2O_3 on the physico-chemical properties and the catalytic performances was then investigated. The addition of Ce was found to cause a partial destruction of the porous structure, strengthen the weak basic sites of the catalysts and enhance the catalytic activity. The 15Ni/Ce-Al_2O_3 catalyst showed higher activity and stability during a 12 hour stability test compared to the non-promoted counter-part.

The three different mesoporous silicas (15Ni/KIT-6, 15Ni/SBA-15 and 15Ni/SBA-16) were then synthesized using the wet impregnation technique, characterized and compared for their activity and stability in the CO_2 reforming reaction. In the dynamic tests, 15Ni/SBA-16 was the best performing catalyst due to its strong metal-support interactions and high contribution from strong basic sites. However, the 15Ni/KIT-6 catalyst was able to maintain a good activity and stability even at higher gas hourly space velocities GHSVs.

Finally, among the 15Ni/Ce-KIT-6, 1Ru/Ce-KIT-6, and 15Ni1Ru/Ce-KIT-6 catalysts, the latter was the most active in the DRM reaction and maintained a stable high CO_2 conversion (97 % for 12 hours). Despite the deposition of graphitic carbon during the stability test, the catalyst was not deactivated.

Keywords: CO_2 methanation, CO_2 reforming of methane, alumina, ceria, mesoporous silica, nickel, ruthenium, promotion with Ce

RÉSUMÉ

L'objectif de ce travail est d'étudier la valorisation du CO_2 par méthanation et reformage à sec du méthane. L'alumine, la cérine et la silice mésoporeuse ont été choisies comme support catalytique. La technique d'imprégnation humide est utilisée pour ajouter une phase active de 15 % de nickel (Ni), 1 % de ruthénium (Ru) ou une combinaison des deux métaux (Ni-Ru) sur chacun des supports stabilisés. Les catalyseurs obtenus ont été calcinés à 550 ^oC, puis caractérisés par la Diffraction des Rayons X (DRX), l'adsorption/désorption d'azote, la Réduction en Température Programmée sous hydrogène (RTP-H_2) et la Désorption en Température Programmée (DTP-CO_2).

Les résultats de la caractérisation des catalyseurs supportés sur CeO_2, Al_2O_3 et KIT-6 montrent que tous les supports et catalyseurs présentent des isothermes de type IVa typique des matériaux mésoporeux. Les espèces RuO_2 formées sont bien dispersées lorsque CeO_2 est utilisé comme support et dans les catalyseurs bimétalliques. La réduction de NiO est renforcée en présence de CeO_2 à cause de ses propriétés redox. La présence de RuO_2 a conduit à une plus grande réductibilité de NiO dans les catalyseurs bimétalliques.

Une première partie a comparé l'activité catalytique des différentes phases actives (le Ni, Ru ou le Ni-Ru) sur le même support (CeO_2, l'Al_2O_3 ou le KIT-6) pour la réaction de méthanation. Dans chaque cas, le catalyseur bimétallique (Ni-Ru) présentait les conversions les plus élevées à 350 ^oC. Ceci peut être lié à une bonne dispersion de RuO_2 et bonne réduction de NiO. De plus, quelle que soit la phase active utilisée, l'ordre de réactivité obtenu était: catalyseurs supportés sur CeO_2> catalyseurs supportés sur KIT-6> catalyseurs supportés sur Al_2O_3. Dans la seconde partie, le support KIT-6 est promu avec différents pourcentages de CeO_2 et imprégné avec les mêmes phases actives étudiées. Une bonne dispersion des espèces RuO_2, une réduction à des températures plus basses et une amélioration des propriétés basiques sont observées en présence de Ce et en fonction de sa teneur dans le matériau. Ceci a conduit à des performances catalytiques plus élevées, en particulier pour les catalyseurs bimétalliques 15Ni1Ru/Ce_xKIT-6. L'étude de stabilité a montré que le catalyseur 15Ni1Ru/CeO_2 présente une bonne activité en termes de conversion de CO_2 (70 %) et de sélectivité CH_4 (99 %) et ne présente pas de désactivation sur une durée de 24 h.

Lors de l'étude de la réaction de reformage à sec du méthane, les catalyseurs supportés sur CeO_2 ont montré une activité catalytique inférieure par rapport aux catalyseurs supportés sur Al_2O_3. Néanmoins, ces catalyseurs ont montré une plus grande résistance à la formation de carbone. L'effet de l'ajout de cérium sur le support Al_2O_3 a ensuite été étudié. L'addition de

cérium a causé une destruction partielle de la structure poreuse, tout en renforcant les sites basiques faibles et augmentant l'activité catalytique des catalyseurs. Le catalyseur 15Ni/Ce-Al_2O_3 a montré une activité et une stabilité élevées pendant un test de stabilité de 12 h.

Trois solides supportés à base de nickel sur silices mésoporeuses (15Ni/KIT-6, 15Ni/SBA-15 et 15Ni/SBA-16) ont été synthétisées en utilisant la technique d'imprégnation humide et ensuite caractérisées. La stabilité et l'activité de ces matériaux a été étudié dans la réaction de reformage à sec du méthane. Dans les tests dynamiques, le 15Ni/SBA-16 s'est montré le plus performant en raison de ses fortes interactions métal-support et de sa forte basicité.

Enfin, parmi les catalyseurs 15Ni/Ce-KIT-6, 1Ru/Ce-KIT-6 et 15Ni1Ru/Ce-KIT-6, le solide 15Ni1Ru/Ce-KIT-6 était le plus actif dans la réaction de reformage à sec du méthane et maintenait une conversion de CO_2 élevée et stable (97 % pendant 12 h). Le catalyseur n'a pas été désactivé malgré le dépôt de carbone graphitique lors du test de stabilité.

Mots-clés: méthanation du CO_2, reformage à sec du méthane, alumine, cérine, silice mésoporeuse, nickel, ruthénium, promotion avec Ce

Introduction Générale

Au cours de la dernière décennie, l'augmentation de la consommation d'énergie est un des problèmes majeurs actuels, principalement causé par la croissance rapide de la population humaine. Cela induit l'augmentation de la dépendance aux combustibles fossiles pour répondre à la demande énergétique. Cependant, la combustion de combustibles fossiles entraîne des émissions de gaz à effet de serre (GES) qui, une fois rejetées dans l'atmosphère, peuvent causer de graves problèmes environnementaux et sanitaires. En conséquence, des recherches approfondies visant la production de sources d'énergie propres sont encouragées. Le dioxyde de carbone (CO_2) est le gaz à effet de serre le plus abondant. L'utilisation chimique du CO_2 comme matière première pour les applications industrielles est largement appliquée comme solution au problème du changement climatique. Dans ce travail, deux réactions adaptées pour la valorisation du dioxyde de carbone ont été évaluées: la réaction de méthanation du CO_2 et le reformage à sec du méthane.

La réaction de méthanation du CO_2 consiste à combiner du dioxyde de carbone (CO_2) avec de l'hydrogène (H_2) pour produire du méthane synthétique (CH_4) également appelé gaz naturel synthétique (SNG). La deuxième solution envisageable implique le reformage du méthane en présence du dioxyde de carbone (appelé reformage à sec du méthane) qui convertit les deux principaux gaz à effet de serre (CO_2 et CH_4) en gaz de synthèse (H_2 et CO), qui est une ressource pour la fabrication de produits chimiques à fortes valeurs ajoutées.

L'activation et la transformation du CO_2 sont très difficiles à réaliser car la molécule de CO_2 ont une forte inertie chimique et est donc très stable. Pour les deux réactions étudiées, le développement de catalyseurs efficaces pour améliorer la cinétique de réaction est donc nécessaire.

Un catalyseur supporté est typiquement composé d'une phase active dispersée sur un support. Ce travail vise à comparer une série de catalyseurs avec différentes familles de supports et de phases actives pour trouver des compositions catalytiques performantes pour chacune des deux réactions étudiées. D'après la littérature, l'utilisation de promoteurs catalytiques modifie les propriétés du catalyseur et augmente son activité. Par conséquent, l'effet de la promotion sur l'activité et la stabilité des catalyseurs sera également étudié dans ce travail.

Ce manuscrit est divisé en quatre chapitres:

- Le premier chapitre consiste en une étude bibliographique sur les processus d'utilisation du CO_2. Une description détaillée des deux réactions étudiées suivra ensuite. Les phénomènes de désactivation des catalyseurs seront aussi expliqués.

Les paramètres catalytiques qui influencent les performances des catalyseurs dans les deux réactions seront également discutés. La fin du chapitre sera consacrée à la justification du choix des catalyseurs étudiés dans cette thèse.

- Dans le deuxième chapitre, les résultats de la préparation et de la caractérisation des catalyseurs à base de nickel et/ou de ruthénium seront détaillés. Tout d'abord, les catalyseurs supportés sur CeO_2 seront évalués, suivis des catalyseurs supportés sur l'Al_2O_3 et sur KIT-6. Pour chaque famille de support, les propriétés texturales, structurales, redox et basiques seront étudiées.
- Le troisième chapitre évaluera d'abord les performances catalytiques de CeO_2, Al_2O_3 et KIT-6 imprégnés avec 1 % Ru, 15 % Ni et 15 % Ni - 1 % Ru. L'effet de la promotion du support KIT-6 avec différents pourcentages de CeO_2 (15 %, 30 % et 60 %) sur les caractérisations physico-chimiques et l'activité catalytique sera développé. Une étude de vieillissement sera également réalisée pour évaluer la stabilité des catalyseurs les plus performants.
- Le $4^{ème}$ chapitre sera divisé en différentes parties. Dans la première partie, l'activité catalytique de CeO_2 et Al_2O_3 imprégnés avec de Ru (1 %), de Ni (15 %) et de Ni-Ru (15 % - 1 %) sera évaluée dans le reformage à sec du méthane. Dans la seconde partie, un compte rendu complet de la préparation et de la caractérisation des catalyseurs Ni et/ou Ru supportés sur Al_2O_3 promu avec Ce sera donné. L'effet de la promotion du support avec Ce sur l'activité catalytique et la stabilité des catalyseurs supportés sur Al_2O_3 sera ensuite présenté. La troisième partie compare les propriétés physico-chimiques, l'activité catalytique et la stabilité de catalyseurs à base de Ni supportés sur différentes silices mésoporeuses. Une dernière partie compare l'activité catalytique des catalyseurs supportés sur KIT-6 avant et après la promotion avec Ce.

Chapitre 1: Étude Bibliographique

De nos jours, les combustibles fossiles sont la principale source de production d'énergie. Les activités anthropiques ainsi que l'épuisement des réserves naturelles de la planète ces dernières années ont déclenché des recherches approfondies pour d'autres sources d'énergie.

La technologie Power to Gas (PtG) (figure 1.1) est considérée comme une alternative prometteuse pour réduire les émissions de dioxyde de carbone et fournir simultanément de l'énergie renouvelable. Dans PtG, l'électrolyse du surplus d'énergie renouvelable est utilisée pour fournir de l'hydrogène gazeux. Cet hydrogène gazeux réagit avec le dioxyde de carbone

de diverses sources (centrales électriques, industrielles ou biogaz) qui est ensuite transformé chimiquement en méthane [1,2]. Par conséquent, l'hydrogène renouvelable en excès peut être converti en méthane facilement transporté, stocké et utilisé.

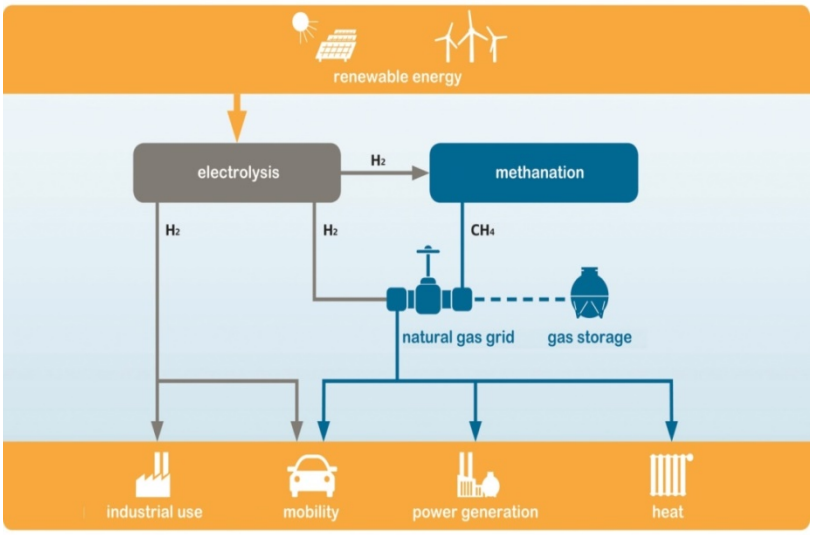

Figure 1.1: La technologie Power to Gas et ses applications possibles [3]

Le reformage est le moyen le plus utilisé dans les industries pour produire du gaz de synthèse, via l'un des trois processus de reformage: reformage à la vapeur du méthane (équation 1.1), oxydation partielle du méthane (équation 1.2) et reformage à sec du méthane (équation 1.3) [4–6]. Parmi ces procédés, le reformage à sec du méthane est le plus prometteur car il utilise les deux gaz à effet de serre les plus abondants (CO_2 et CH_4) pour produire du gaz de synthèse. Cette technique produit également un rapport H_2/CO égal à 1 qui peut être utilisé pour la synthèse de produits chimiques oxygénés.

$$CH_4 + H_2O \rightleftharpoons CO + 3H_2 \qquad \text{(équation 1.1)}$$

$$CH_4 + \frac{1}{2}O_2 \rightleftharpoons CO + 2H_2 \qquad \text{(équation 1.2)}$$

$$CH_4 + CO_2 \rightleftharpoons 2CO + 2H_2 \qquad \text{(équation 1.3)}$$

Méthanation du CO_2

La réaction de méthanation du CO_2 (équation 1.4) qui consiste à faire réagir le CO_2 et le H_2 pour produire du CH_4 a été rapportée pour la première fois en 1902 par les chimistes Sabatier et Senderens [7].

$$CO_2 + 4H_2 \rightarrow CH_4 + 2H_2O \qquad \text{(équation 1.4)}$$

La méthanation du CO_2 est une réaction hautement exothermique qui est thermodynamiquement limitée. L'équilibre de la réaction est influencé par la pression et la température. En équilibre thermodynamique, des températures de réaction basses et des

pressions élevées sont nécessaires pour maximiser la conversion et éviter la formation de CO en tant que produit [2,8]. Le rapport molaire H_2/CO_2 idéal pour la méthanation du CO_2 est de 4:1. L'équilibre réactionnel favorise de plus en plus plusieurs réactions secondaires quand la température de fonctionnement dépasse 300 °C [9].

Les catalyseurs de méthanation du CO_2 sont typiquement composés de particules métalliques actives (Ni, Fe, Co, Ru, Rh, Pt, Pd, W ou Mo) dispersées sur un support d'oxyde métallique (Al_2O_3, SiO_2, TiO_2, SiC, ZrO_2, CeO_2, $Ce_xZr_{1-x}O_2$) [10].

Reformage à sec du méthane

Le reformage à sec du méthane (équation 1.3) est une réaction réversible extrêmement endothermique qui nécessite des températures élevées pour atteindre les niveaux de conversion souhaitables [11]. Le reformage à sec du méthane s'accompagne de nombreuses réactions secondaires telles que le Reverse Water Gas Shift (RWGS) (équation 1.5) et le reformage à la vapeur du méthane (SRM) (équation 1.1) [4,11]. La présence du RWGS est responsable d'augmenter la quantité de CO par rapport à H_2 et donc d'abaisser le rapport H_2/CO à une valeur inférieure à l'unité [4,11,12].

Selon la littérature, les catalyseurs Ni se sont avérés être les catalyseurs les plus appropriés et les plus largement appliqués dans le reformage à sec du méthane. Ceux-ci sont moins chers mais plus vulnérables à la désactivation due à la formation de carbone par rapport aux métaux nobles tels que les catalyseurs Ru, Rh et Pt [13–15]. Les catalyseurs au nickel sont connus pour leur tendance à la formation de carbone principalement due à la décomposition du méthane à haute température (équation 1.5) et à la réaction de Boudouard à des températures inférieures à 700 ^oC (équation 1.6) [16].

$CH_4 \leftrightarrow C + 2H_2$ (équation 1.5)

$2CO \leftrightarrow CO_2 + C$ (équation 1.6)

Selon la figure 1.2, le reformage à sec du méthane, le RWGS et la décomposition du méthane sont favorisées à des températures élevées car leur constante d'équilibre augmente avec l’augmentation de la température. En revanche, la réaction de Boudouard est thermodynamiquement défavorable à haute température.

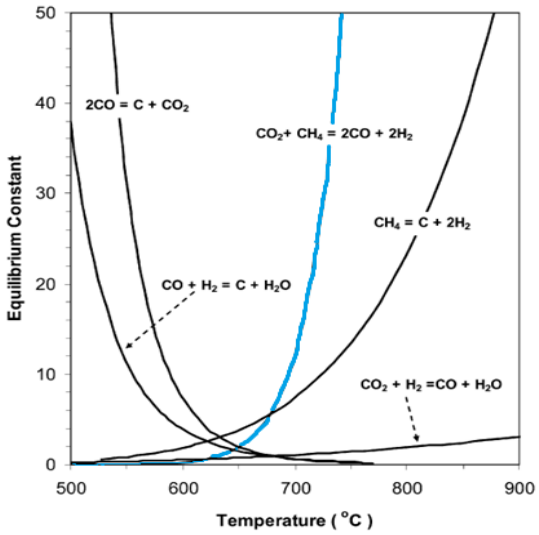

Figure 1.2: La variation des constantes d'équilibre en fonction de la température [17]

Choix des catalyseurs

Les supports ci-dessous ont été choisis pour comparaison dans cette étude:

- L'alumine: le support le moins cher et le plus utilisé dans les deux réactions.
- KIT-6, SBA-15 et SBA-16: nouveaux matériaux catalytiques qui ont récemment retenu l'attention dans diverses applications catalytiques en raison de leur structure mésoporeuse, leur grande surface spécifique et leur volume poreux important.
- CeO_2: matériaux intéressant pour sa basicité et ses propriétés redox.

Le nickel a été choisi comme phase active car il est le plus actif et sélectif parmi les métaux de transition. Il est peu onéreux, hautement disponible et largement utilisé pour la mise en œuvre commerciale des procédés de méthanation et de reformage. Dans cette étude, une phase active de 15 % de Ni a été adoptée. Parmi les métaux nobles étudiés pour les deux réactions, le ruthénium semble révéler des performances catalytiques élevées. De plus, le Ru est particulièrement connu pour sa haute sélectivité du méthane dans la réaction de méthanation du CO_2. Il est aussi le tout premier métal à montrer une activité et une stabilité pour le reformage à sec du méthane avec un comportement cinétique comparable à celui du Ni. Un pourcentage de 1 % a été choisi parce que de petites quantités se sont avérées suffisantes pour des activités élevées et en raison du coût élevé du Ru. Les catalyseurs Ni sont connus pour leur désactivation par formation de carbone, donc un troisième système bimétallique (Ni-Ru) a été étudié afin d'améliorer l'activité et la stabilité des catalyseurs à base de Ni.

Outre la phase active et le support, des promoteurs appropriés sont parfois ajoutés au catalyseur. L'oxyde de cérium est couramment étudié comme promoteur capable d'améliorer

la dispersion, la réductibilité et les propriétés basiques des matériaux permettant ainsi d'améliorer les performances des catalyseurs.

Chapitre 2: Synthèses et Caractérisations

Préparation des catalyseurs

Le support CeO_2 a été synthétisé selon une procédure standard décrite par Aouad et al. [18] où l'hydroxyde de cérium a été précipité à partir d'un hexahydrate de nitrate de cérium et d'une solution d'hydroxyde de sodium.

L'alumine a été préparée en mélangeant un bécher contenant de l'isopropoxyde d'aluminium dissous dans un mélange d'éthanol et d'isopropanol et un bécher contenant le surfactant non ionique F127 dissous dans une autre solution d'éthanol et d'isopropanol. La suspension résultante a été agitée et ensuite mis à l'étuve [19].

Pour la synthèse de KIT-6, P123 a été utilisé comme agent directeur de structure et a été mélangé avec de l'acide hydrochlorique concentré et de l'eau distillée à 35 °C jusqu'à sa dissolution complète. Ensuite, du butanol a été ajouté au mélange. Après 1 h, la source de silice a été ajoutée lentement et le mélange a ensuite été vieilli suivi d'un traitement hydrothermal à 100 °C [20].

Pour les trois synthèses, les matériaux résultants ont été lavés et séchés, puis calcinés à 550 ^oC.

La technique d'imprégnation humide a été utilisée pour synthétiser les catalyseurs où 0,5 g des supports (CeO_2, l'Al_2O_3 et le KIT-6) ont été imprégnés avec des solutions de 25 mL des précurseurs métalliques ($Ni(NO_3)_2.6H_2O$ (P> 97 %)) et/ou ($Ru(NO)(NO_3)_3$) (1,5 % Ru). Les catalyseurs ont été stabilisés thermiquement par calcination à 550 °C.

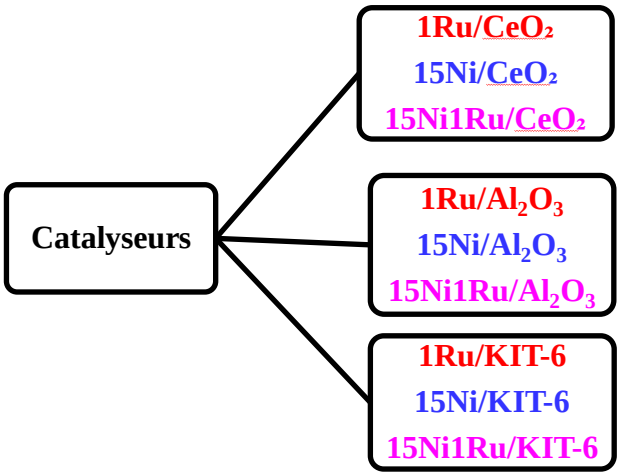

Tableau 2.1: Résumé des catalyseurs préparés

Caractérisations des catalyseurs

- D'après les résultats de diffraction de rayons X (DRX), de gros cristaux de RuO_2 se sont formés dans les catalyseurs 1Ru/KIT-6 et 1Ru/Al_2O_3. Une dispersion de RuO_2 améliorée a été observée dans le 1Ru/CeO_2 et pour tous les catalyseurs bimétalliques. Cette bonne interaction entre Ru et CeO_2 s'explique par la présence des liaisons oxygénées facilement réductibles (Ru-O-Ce) qui se créent entre le ruthénium et le cérium de surface lors de la calcination [18].
- La présence de Ru a augmenté la taille des cristallites de NiO dans le catalyseur bimétallique supporté sur CeO_2 et Al_2O_3 uniquement.
- Tous les supports et catalyseurs ont révélé des isothermes d'adsorption de type IVa suggérant leur structure mésoporeuse. Une diminution de surface spécifique suite à l'imprégnation a été observée pour tous les catalyseurs. Cependant, les volumes de pores ont diminué uniquement dans le cas des catalyseurs supportés sur l'Al_2O_3 et le KIT-6 indiquant que la condensation capillaire pour ces catalyseurs s'est produite dans la cavité des pores.
- La réductibilité de la phase active s'est produite à des températures plus basses pour les catalyseurs supportés sur CeO_2 et la réductibilité de NiO a été améliorée dans tous les catalyseurs bimétalliques en raison de la présence bénéfique de Ru.

Chapitre 3: Méthanation du CO_2

La réaction de méthanation du CO_2 étudiée ($CO_2 + 4H_2 \rightarrow CH_4 + 2H_2O$) est réalisée à pression atmosphérique, dans une plage de température comprise entre 150 °C et 350 °C, avec un rapport H_2/CO_2 égal à 4 et une vitesse volumique horaire (VVH) de 40 000 h^{-1}.

Méthanation du CO_2 sur les catalyseurs supportés sur le CeO_2, l'Al_2O_3 et le KIT-6

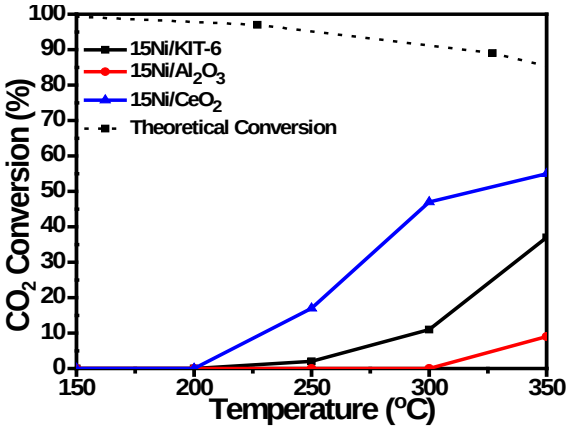

Figure 3.1: Conversion de CO_2 en fonction de la température en présence des différents catalyseurs Ni/supports

Le catalyseur supporté sur CeO_2 se montre le plus actif en raison des meilleures propriétés redox du CeO_2 qui peuvent favoriser l'activation du CO_2, et donc améliorer la réaction de méthanation du CO_2.

Méthanation du CO_2 sur les catalyseurs supportés sur le Ce_xKIT-6 (x= 15, 30, ou 60 %)

Dans cette partie du chapitre, le KIT-6 a été promu avec différents pourcentages de CeO_2 et imprégné avec les mêmes phases actives. Les propriétés physicochimiques des catalyseurs supportés sur Ce_xKIT-6 ont montré une bonne dispersion des espèces RuO_2 en présence de CeO_2 et une augmentation des tailles de cristallite lorsque la teneur en Ce augmentait. Il était également clair, d'après les profils RTP-H_2 des catalyseurs, que la réductibilité de la phase active se produisait à des températures plus basses. Les profils DTP-CO_2 ont montré que la basicité des catalyseurs augmentait après la promotion de KIT-6 avec Ce et lorsque la teneur en Ce augmentait.

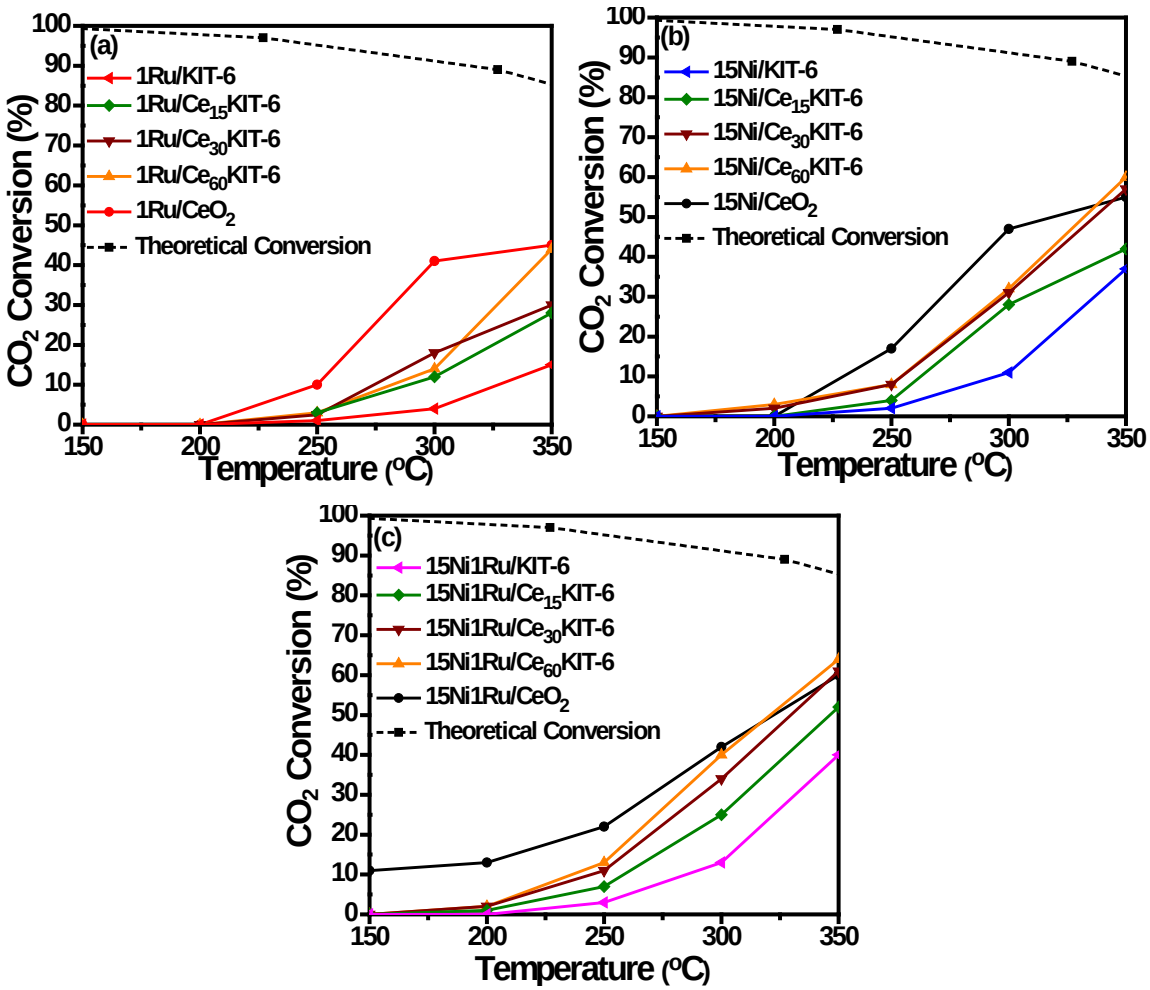

Figure 3.2: Conversion de CO_2 en fonction de la température en présence des différents catalyseurs (a) 1Ru/Ce_xKIT-6, (b) 15Ni/Ce_xKIT-6, et (c) 15Ni1Ru/Ce_xKIT-6

Pour toutes les phases actives (le Ru, Ni et le Ni-Ru), la plus grande activité suite à la promotion avec Ce est corrélée à la réductibilité améliorée et à la présence de sites plus basiques qui améliorent l'adsorption et l'activation du CO_2. L'activité la plus élevée a été observée dans le cas des catalyseurs 15Ni1Ru/Ce_xKIT-6 en raison de la présence de Ru qui a amélioré la réductibilité du NiO.

Chapitre 4: Reformage à Sec du Méthane

La réaction de reformage à sec du méthane étudiée ($CO_2 + CH_4 \rightarrow 2H_2 + 2CO$) est réalisée à pression atmosphérique, dans une plage de température comprise entre 500 ^oC et 800 °C, avec un rapport CH_4/CO_2 égal à 1 et un VVH de 60 000 h^{-1}.

Reformage à sec du méthane sur des catalyseurs supportés sur CeO_2 et Al_2O_3

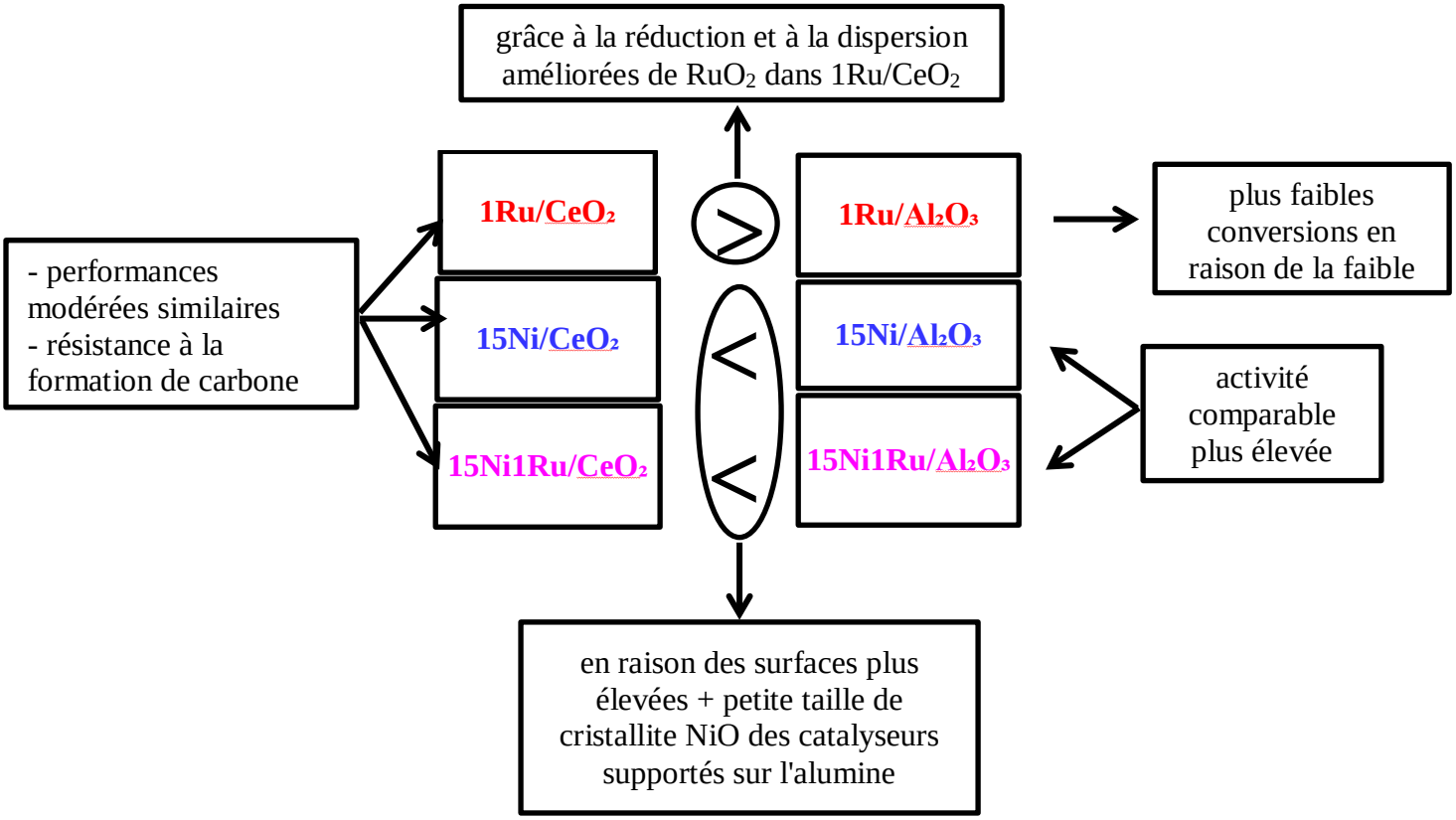

Tableau 4.1: Schéma montrant le lien entre les propriétés physico-chimiques et les performances catalytiques des catalyseurs supportés sur le CeO_2 et l'Al_2O_3

Les catalyseurs supportés sur CeO_2 (1Ru/CeO_2, 15Ni/CeO_2, and 15Ni1Ru/CeO_2) montrent une activité modérée similaire et résistent à la formation de carbone. Pour les catalyseurs supportés sur Al_2O_3, l'activité catalytique a été déterminée par la composition et la quantité de la phase active. 1Ru/Al_2O_3 avec le plus faible teneur de phase active démontre l'activité catalytique la plus faible tandis que 15Ni/Al_2O_3 et 15Ni1Ru/Al_2O_3 montrent des

performances catalytiques comparables plus élevées. L'activité catalytique de $1Ru/CeO_2$ est supérieure à celle de $1Ru/Al_2O_3$. Ceci est lié à une bonne réductibilité et dispersion des espèces de RuO_2 lorsque CeO_2 est utilisé comme support. Enfin, l'activité élevée des catalyseurs Ni et Ni-Ru supportés sur Al_2O_3 par rapport au Ni et Ni-Ru supportés sur CeO_2 est attribuée aux surfaces plus élevées et aux tailles de cristallite inférieures des catalyseurs $15Ni/Al_2O_3$ et $15Ni1Ru/Al_2O_3$ qui améliorent l'accessibilité du site actif.

Effet de la promotion de l'alumine avec du Ce sur la stabilité catalytique

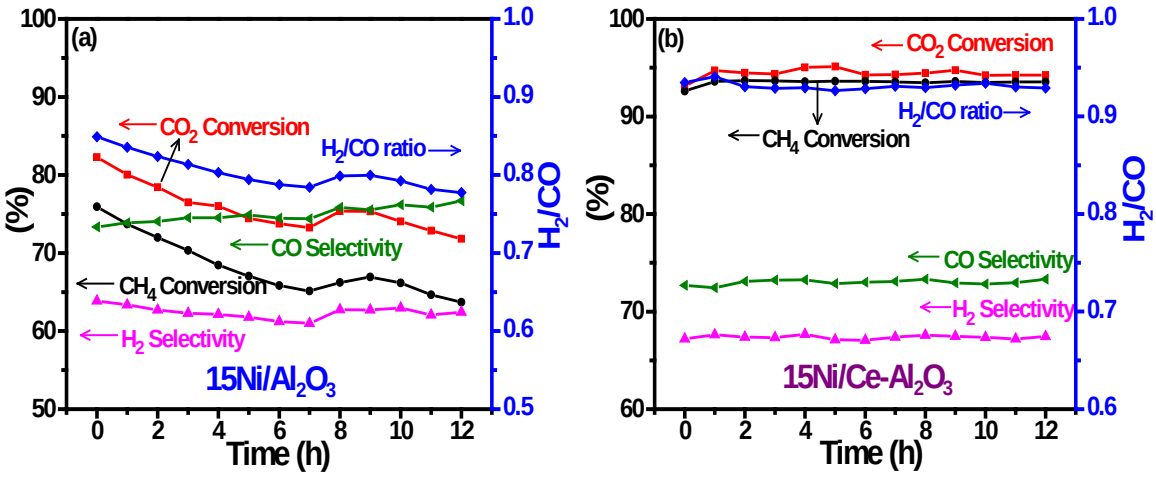

Figure 4.1: Test de stabilité à 800 °C pendant 12 h en présence de (a) $15Ni/Al_2O_3$ et (b) $15Ni/Ce\text{-}Al_2O_3$

Les tests de stabilité (figure 4.1) ont montré que les taux de désactivation du CH_4 et du CO_2 sur le catalyseur $15Ni/Al_2O_3$ se sont égaux à 11,8 % et 13,8 % respectivement. Le catalyseur $15Ni/Ce\text{-}Al_2O_3$ ne s'est pas désactivé pendant une période de 12 h. Ceci suggère que la présence de Ce conduit à l'oxydation du carbone déposé et favorise la régénération du catalyseur.

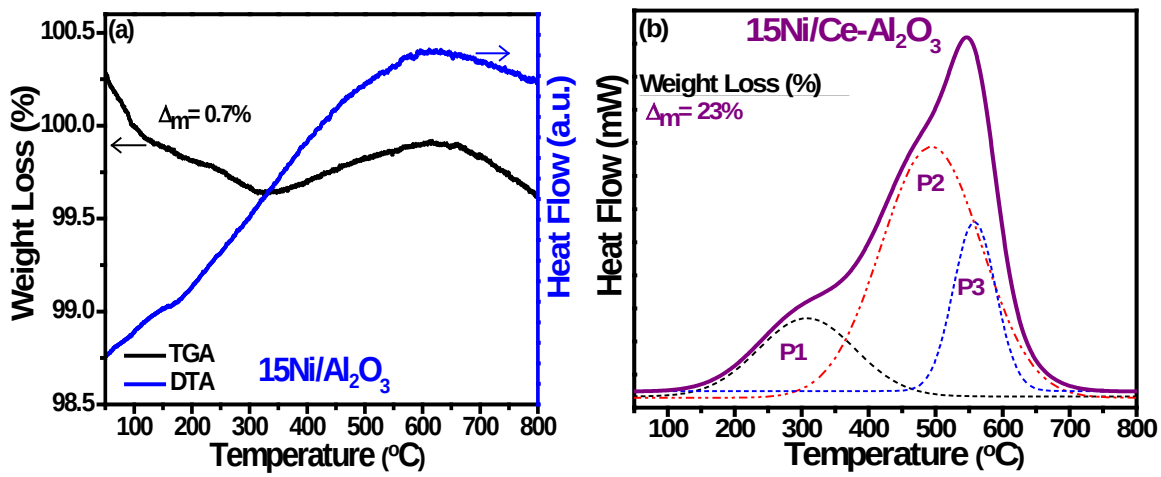

Figure 4.2: Courbes ATD/ATG de 15Ni/Al_2O_3 et (b) courbe ATD de 15Ni/Ce-Al_2O_3 après le test de stabilité

Les pertes de poids enregistrées pour les catalyseurs 15Ni/Al_2O_3 et 15Ni/Ce-Al_2O_3 sont égaux à 0,7 % et 23 % respectivement. Pour le catalyseur 15Ni/Ce-Al_2O_3 (figure 4.2 (b)), trois pics exothermiques différents sont présents (P1, P2 et P3) indiquant la présence de différentes espèces carbonées à la surface de ce catalyseur. Le pic 1 (P1) avec une intensité relativement faible et un maximum à 305 ^oC est attribué à l'oxydation des particules métalliques présentes sur la surface du catalyseur. Le deuxième pic (P2) centré autour de 490 ^oC est attribué à l'oxydation du carbone déposé (carbone amorphe ou filaments de carbone) [21,22]. Le troisième pic exothermique (P3) à des températures T> 500 ^oC est attribué à l'oxydation du carbone graphitique [21].

Conclusion Générale

L'objectif de ce travail était de comparer différents matériaux catalytiques et d'évaluer le rôle du support et de la phase active dans deux réactions communément adoptées pour l'utilisation et la valorisation du CO_2. Le travail détaille la synthèse et la caractérisation de catalyseurs à base de Ni et/ou de Ru supportés sur différents oxydes mésoporeux et met en évidence l'effet de promotion des supports avec de l'oxyde de cérium.

Les structures cristallines et poreuses ainsi que la réductibilité et la basicité de tous les supports et catalyseurs ont été étudiées avant les essais catalytiques. Tous les supports et catalyseurs évalués dans ce travail ont révélé des isothermes d'adsorption typiques de type IVa suggérant la méso-structure et l'apparition d'une condensation capillaire. Pour la plupart des catalyseurs, la structure mésoporeuse du support a été partiellement détruite suite à une promotion avec du Ce et/ou une imprégnation de métal actif comme en témoigne le

changement de forme des isothermes et la diminution des surfaces et des volumes de pores. Les résultats DRX et RTP-H_2 ont montré que dans les catalyseurs monométalliques à base de Ru (1Ru/CeO_2, 1Ru/Al_2O_3, 1Ru/KIT-6, 1Ru/Ce_xKIT-6, et 1Ru/Ce-Al_2O_3), la dispersion et la réductibilité de la phase active sont améliorées lorsque CeO_2 est utilisé comme support et lorsque KIT-6 et Al_2O_3 sont promus avec Ce. La combinaison de Ni et Ru a amélioré la dispersion de RuO_2 et la réductibilité de NiO à des températures plus basses quel que soit le support utilisé.

Dans la réaction de méthanation du CO_2, la disponibilité des sites actifs a été déterminée par le traitement de réduction et a affecté l'activité des catalyseurs à base de Ni. Pour les catalyseurs 15Ni/Al_2O_3 et 15Ni/KIT-6, les espèces NiO n'ont pas été complètement réduites à 350 ^oC en l'absence de Ce, ce qui a entraîné une activité catalytique inférieure par rapport au catalyseur 15Ni/CeO_2. Le catalyseur 15Ni1Ru/Ce_{60}KIT-6 a été choisi pour étudier l'effet de la variation de la VVH sur l'activité catalytique. La VVH optimale s'est avérée égale à 40 000 h^{-1}. Le catalyseur 15Ni1Ru/CeO_2 a montré l'activité et la stabilité les plus élevées. La désactivation des catalyseurs contenant moins de Ce a été attribuée au frittage des particules de métal Ni.

Dans la réaction de reformage à sec du méthane, le support et la phase active ont déterminé le degré de formation de carbone dans la réaction. Les catalyseurs supportés sur CeO_2 (1Ru/CeO_2, 15Ni/CeO_2, 15Ni1Ru/CeO_2) et les catalyseurs à base de Ru (1Ru/Al_2O_3, 1Ru/Ce-Al_2O_3, 1Ru/KIT-6, 1Ru/Ce-KIT-6) étaient résistants à la formation de carbone. La quantité de carbone déposé était inférieure dans les catalyseurs bimétalliques 15Ni1Ru/Al_2O_3, 15Ni1Ru/KIT-6 et 15Ni1Ru/Ce-KIT-6 par rapport aux catalyseurs monométalliques. Malgré la plus grande teneur en carbone, aucune désactivation n'a été observée pour les catalyseurs contenant du Ce indiquant que les sites actifs restaient accessibles aux réactifs. Une explication possible est la régénération des sites catalytiques actifs due à l'élimination continue du carbone par gazéification au CO_2. Parmi tous les catalyseurs testés dans le reformage à sec, les catalyseurs supportés sur la silice mésoporeuse 15Ni/KIT-6, 15Ni/SBA-15 et 15Ni/SBA-16 ont montré une activité élevée et aucune désactivation dans nos conditions catalytiques adoptées.

Plusieurs études supplémentaires pour valider les hypothèses émises pour l'explication des résultats obtenus doivent être réalisées pour compléter le travail effectué dans cette thèse. Tout d'abord, il est important de réaliser une analyse en microscopie électronique (MEB) afin de vérifier la dispersion des phases actives sur les supports mésoporeux (en surface ou à l'intérieur des pores) et d'évaluer clairement l'incorporation de Ce. Les analyses MEB peuvent

également permettre d'évaluer les phénomènes de dépôt de carbone et de confirmer le frittage et l'agglomération du Ni. La mesure des pourcentages en phase active par des techniques quantitatives sont également cruciales pour caractériser les catalyseurs. Pour mieux comprendre le rôle joué par les différentes phases actives et le promoteur dans le mécanisme des deux réactions étudiées, il serait intéressant de réaliser une étude par FTIR in situ.

Dans la méthanation du CO_2, il est important de réaliser des études supplémentaires qui peuvent aider à mettre à l'échelle les processus pour une application industrielle. Un catalyseur n'est considéré comme efficace que s'il peut être réutilisé pour plusieurs cycles de réaction. Tester le catalyseur optimal 15Ni1Ru/CeO_2 dans une étude de réutilisabilité rendra l'utilisation de ce catalyseur plus attirante pour une utilisation commerciale.

Dans le reformage à sec du méthane, des tests de stabilité plus longs doivent être effectués sur les catalyseurs promus et les catalyseurs à base de Ni supportés sur de la silice mésoporeuse pour vérifier si la régénération de ces catalyseurs sera efficace après plusieurs cycles de dépôt-élimination de carbone.

Références

[1] A. Ricca, L. Truda, and V. Palma, "Study of the role of chemical support and structured carrier on the CO2 methanation reaction," *Chemical Engineering Journal*, vol. 377, p. 120461, Dec. 2019.

[2] M. Mihet, O. Grad, G. Blanita, T. Radu, and M. D. Lazar, "Effective encapsulation of Ni nanoparticles in metal-organic frameworks and their application for CO2 methanation," *International Journal of Hydrogen Energy*, vol. 44, no. 26, pp. 13383–13396, May 2019.

[3] "How to store renewable energy in a smart way."[Online]. Available: https://engineered.thyssenkrupp.com/en/smart-storage-wie-funktionieren-eigentlich-energiespeicher/ (accessed Mar. 30, 2021).

[4] B. Abdullah, N. A. Abd Ghani, and D.-V. N. Vo, "Recent advances in dry reforming of methane over Ni-based catalysts," *Journal of Cleaner Production*, vol. 162, pp. 170–185, Sep. 2017.

[5] Q. Wei *et al.*, "Facile one-step synthesis of mesoporous Ni-Mg-Al catalyst for syngas production using coupled methane reforming process," *Fuel*, vol. 211, pp. 1–10, Jan. 2018.

[6] S. S. Itkulova, Y. Y. Nurmakanov, S. K. Kussanova, and Y. A. Boleubayev, "Production of a hydrogen-enriched syngas by combined CO2-steam reforming of methane over Co-based catalysts supported on alumina modified with zirconia," *Catalysis Today*, vol. 299, pp. 272–279, Jan. 2018.

[7] L. Xu *et al.*, "CO2 methanation over CoNi bimetal-doped ordered mesoporous Al2O3 catalysts with enhanced low-temperature activities," *International Journal of Hydrogen Energy*, vol. 43, no. 36, pp. 17172–17184, Sep. 2018.

[8] T. Sakpal and L. Lefferts, "Structure-dependent activity of CeO2 supported Ru catalysts for CO2 methanation," *Journal of Catalysis*, vol. 367, pp. 171–180, Nov. 2018.

[9] L. Pastor-Pérez, V. Patel, E. Le Saché, and T. R. Reina, “CO2 methanation in the presence of methane: Catalysts design and effect of methane concentration in the reaction mixture,” *Journal of the Energy Institute*, vol. 93, pp. 415-424, Feb. 2019.
[10] W. Jin Lee *et al.*, “Recent trend in thermal catalytic low temperature CO2 methanation: a Critical Review,” *Catalysis Today*, Feb. 2020. In press.
[11] N. A. K. Aramouni, J. G. Touma, B. A. Tarboush, J. Zeaiter, and M. N. Ahmad, “Catalyst design for dry reforming of methane: Analysis review,” *Renewable and Sustainable Energy Reviews*, vol. 82, pp. 2570–2585, Feb. 2018.
[12] R. K. Singha, A. Yadav, A. Shukla, M. Kumar, and R. Bal, “Low temperature dry reforming of methane over Pd-CeO2 nanocatalyst,” *Catalysis Communications*, vol. 92, pp. 19–22, Mar. 2017.
[13] A A. S. Al-Fatesh, Y. Arafat, H. Atia, A. A. Ibrahim, Q. L. Manh Ha, M. Schneider et al. CO2-reforming of methane to produce syngas over Co-Ni/SBA-15 catalyst: Effect of support modifiers (Mg, La and Sc) on catalytic stability. *J. CO2 Util.*, vol. 21, pp. 395-404, Sept. 2017.
[14] H. Arbag, S. Yasyerli, N. Yasyerli, G. Dogu, and T. Dogu, “Enhancement of catalytic performance of Ni based mesoporous alumina by Co incorporation in conversion of biogas to synthesis gas,” *Applied Catalysis B: Environmental*, vol. 198, pp. 254–265, Dec. 2016.
[15] K. Rouibah *et al.*, “Dry reforming of methane on nickel-chrome, nickel-cobalt and nickel-manganese catalysts,” *International Journal of Hydrogen Energy*, vol. 42, no. 50, pp. 29725–29734, Dec. 2017.
[16] G. Moradi, F. Khezeli, and H. Hemmati, “Syngas production with dry reforming of methane over Ni/ZSM-5 catalysts,” *Journal of Natural Gas Science and Engineering*, vol. 33, pp. 657–665, Jul. 2016.
[17] J. Zhang, H. Wang, and A. K. Dalai, “Development of stable bimetallic catalysts for carbon dioxide reforming of methane,” *Journal of Catalysis*, vol. 249, no. 2, pp. 300–310, Jul. 2007.
[18] S. Aouad, E. Abi-Aad, and A. Aboukaïs, “Simultaneous oxidation of carbon black and volatile organic compounds over Ru/CeO2 catalysts,” *Applied Catalysis B: Environmental*, vol. 88, no. 3, pp. 249–256, May 2009.
[19] V. Vosoughi, S. Badoga, A. K. Dalai, and N. Abatzoglou, “Modification of mesoporous alumina as a support for cobalt-based catalyst in Fischer-Tropsch synthesis,” *Fuel Processing Technology*, vol. 162, pp. 55–65, Jul. 2017.
[20] S. Liu *et al.*, “Studies on toluene adsorption performance and hydrophobic property in phenyl functionalized KIT-6,” *Chemical Engineering Journal*, vol. 334, pp. 191–197, Feb. 2018.
[21] J. Estephane *et al.*, “CO2 reforming of methane over Ni–Co/ZSM5 catalysts. Aging and carbon deposition study,” *International Journal of Hydrogen Energy*, vol. 40, no. 30, pp. 9201–9208, Aug. 2015.
[22] C. Gennequin *et al.*, “Influence of the presence of ruthenium on the activity and stability of Co-Mg-Al-based catalysts in CO2 reforming of methane for syngas production,” *Environ Sci Pollut Res Int*, vol. 23, no. 22, pp. 22744–22760, Nov. 2016.

LIST OF FIGURES

LIST OF TABLES

TABLE OF CONTENTS

GENERAL INTRODUCTION

"If we continue at the rate we are now, by the year 2030 we will set off an irreversible chain reaction which will trigger events beyond human control, then there's no going back…"

Greta Thunberg, 17 years old climate activist

Because the whole world is under threat from climate change, on 22 April 2016, 195 countries signed the Paris Agreement. World leaders have set a target of limiting average warming to a value of 1.5 ^{o}C above preindustrial temperatures. This goal may be achieved by the implementation of different technologies aiming either at capture and storage (CCS) or capture and utilization (CCU) of the most dangerous and ubiquitous atmospheric pollutant "CO_2". CCS technologies include the capture of CO_2 from power plants or industrial processes, its transport, and its underground injection and geologic sequestration into deep oceanic rock formations. The necessity of a site for CO_2 sequestration and the costly transportation of captured CO_2 to the storage site render CCS economically unfavorable and reduce the efficiency of the process. Chemical utilization of CO_2, on the other hand, allows CO_2 recycling through means that permit the application of CO_2 as a chemical feedstock that is further converted into added-value products. This mitigation of CO_2 emissions that offers a low-carbon economy has increasingly attracted researchers and policymakers in their quest to alleviate the buildup of greenhouse gases in the Earth's atmosphere.

In the scope of this thesis, two practical solutions that have been adopted for decades as prospective processes for the valorization of carbon dioxide were evaluated: the ***CO_2 METHANATION REACTION*** and the ***CO_2 REFORMING OF METHANE.***

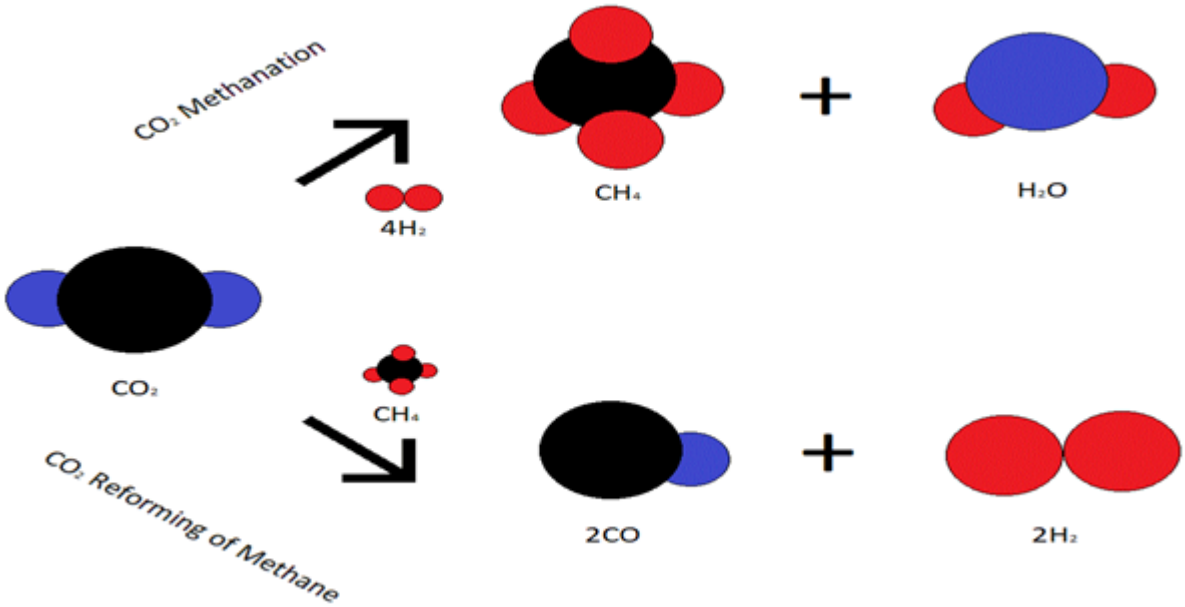

Power to Gas technology is considered a promising alternative to diminish carbon dioxide emissions and simultaneously provide renewable energy. In this concept, the CO_2 methanation reaction emerged as an additional step which consists of combining carbon dioxide (CO_2) with hydrogen (H_2) to produce synthetic methane (CH_4) also called Synthetic Natural Gas (SNG). Therefore, excess renewable hydrogen can be converted to methane which can be easily transported, stored, and used.

The second feasible solution involves the reforming of methane with carbon dioxide (called dry reforming of methane, DRM) that converts the two main greenhouse gases GHGs (CO_2 and CH_4) into synthesis gas or syngas (H_2 and CO), which is a resource for the manufacture of useful chemical products.

CO_2 activation and transformation is very difficult to achieve because the CO_2 molecules have high chemical inertia and are hence very stable. For both studied reactions, the development of efficient catalysts to enhance the reaction kinetics is a must. An ideal catalyst is typically composed of an active phase dispersed on a support. This work aims to compare a series of catalysts with different support families and active phases in an attempt to find industrially viable efficient catalytic compositions for each of the two studied reactions. According to the literature, the use of catalytic promoters modifies the catalyst's properties and enhances the activities. Therefore, the effect of promotion on the activity and stability of the catalysts will be also investigated in this work.

This manuscript is divided into four chapters:

Chapter 1: Literature Review

This chapter begins with a summary of established CO_2 utilization processes that are related to the scope of this study. A detailed description of the two studied reactions: CO_2 METHANATION and CO_2 REFORMING OF METHANE will then follow. The history, thermodynamics, mechanism, current applications as well as the catalysts commonly used for both reactions will be highlighted. A spotlight will be shed on the inevitable phenomena of catalyst deactivation. Catalytic parameters that influence the performance of the catalysts in both reactions will be also discussed. The end of the chapter is dedicated to the justification of the choice of the catalysts that are investigated in this thesis.

Chapter 2: Synthesis and Characterization

In this chapter, a full account of the synthesis and physico-chemical characterization of the prepared supports and catalysts that were evaluated in the two studied reactions is presented. Several physico-chemical techniques such as X-Ray Diffraction, N_2 adsorption/desorption,

H_2-TPR, and CO_2-TPD were applied. The investigated catalysts were Ni and/or Ru supported on the mesoporous oxides CeO_2 and Al_2O_3 and on mesoporous silica KIT-6.

Chapter 3: CO_2 Methanation Results

The catalytic performances of CeO_2, Al_2O_3 and KIT-6 impregnated with (1 wt%) Ru, (15 wt%) Ni, and (15 wt%) Ni – (1 wt%) Ru will be first evaluated. The effect of promoting the KIT-6 support with different percentages of CeO_2 (15 %, 30 %, and 60 %) on the physico-chemical characterizations and catalytic activity is then evaluated. An aging study is carried out to assess the stability of the most performing catalysts.

Chapter 4: CO_2 Reforming of Methane Results

In the first part of the chapter, the catalytic activity of CeO_2 and Al_2O_3 supported catalysts is evaluated. The effect of promoting Al_2O_3 with Ce on the physico-chemical characterizations, activity, and stability of Al_2O_3 supported catalysts will then be studied. A third part compares the catalytic activity and stability of three mesoporous silica supports impregnated with 15 wt% Ni. From these catalysts, 15Ni/KIT-6 was chosen for comparison with 1Ru/KIT-6 and 15Ni1Ru/KIT-6 with and without promoting the support with Ce. For all the spent catalysts, characterizations after test are performed in order to evaluate the carbon deposition phenomena. The best performing catalysts are put on stream for a period of 12 h to study their stability.

*Appendix A: details the used physico-chemical characterization techniques (XRD, N_2 adsorption/desorption, H_2-TPR, CO_2-TPD, and DTA/TGA) as well as the laboratory set-up of both catalytic tests.

* Appendix B: includes the thermodynamic calculations for both reactions and the synthesis calculations.

CHAPTER 1
LITERATURE REVIEW

Since CO_2 is the common reactant in the two studied reactions, the first part of this chapter will discuss the situation of CO_2 emissions in the last years, the Power-to-Gas technology (PtG), and the utilization of CO_2 as a feedstock for the production of synthesis gas. The second and third parts provide information about the two studied reactions including their thermodynamics, mechanisms, and most investigated catalysts. The deactivation of the catalyst and the influence of some catalytic properties on the catalytic activity in both reactions will be then explained. Finally, the choice of the catalysts will be clarified.

1.1. Utilization of Carbon Dioxide

Nowadays, fossil fuels are the primary source of energy production; however, the rise of anthropogenic activities as well as the depletion of the worlds' natural reserves in recent years triggered extensive research for other energy sources. Knowing that the amount of carbon emitted from fossil fuels combustion is 100 times higher than that used for synthesis of chemicals [1], it seems more appropriate to convert CO_2 into different energy vectors such as methane through the CO_2 methanation reaction and synthesis gas through the CO_2 reforming reaction.

1.1.1. CO_2 Emissions In Recent Years

From 2000 to 2018, the total GHG emissions increased by 43 % [2]. This increase has been primarily attributed to the increase in energy consumption resulting from a robust global economy. Between 2014 and 2016 (figure 1.1), global emissions remained relatively constant despite the ongoing economy expansion as a result of the development of low-carbon technologies leading to a decline in the demand for coal [3,4]. For the first time in Earth's history, atmospheric CO_2 concentrations rose above 400 ppm in 2018 [5]. In fact, global fossil CO_2 emissions in 2018 increased by 1.9 % to a total of 37.9 Gt, continuing the increasing trend observed between 2016 and 2017 (+1.2 %) [3].This change in trend between 2017 and 2018 is explained by the failure of the energy production to meet with the higher economic growth. In 2019, global energy related CO_2 emissions declined to reach a value of 33 Gt as a consequence of the expanding role of renewable sources, the reduced emissions from electric generators and the shift towards the use of natural gases. Global CO_2 emissions from coal use declined by 1.3 % from 2018 levels and those from the power sector decreased by 6 % in comparison with 2012 [6]. Global CO_2 emissions from fossil fuels are set to drop

by up to seven percent in 2020 because of the coronavirus pandemic. This dramatic decline is believed to be the sharpest since WWII, yet would not be really able to dent long term global warming.

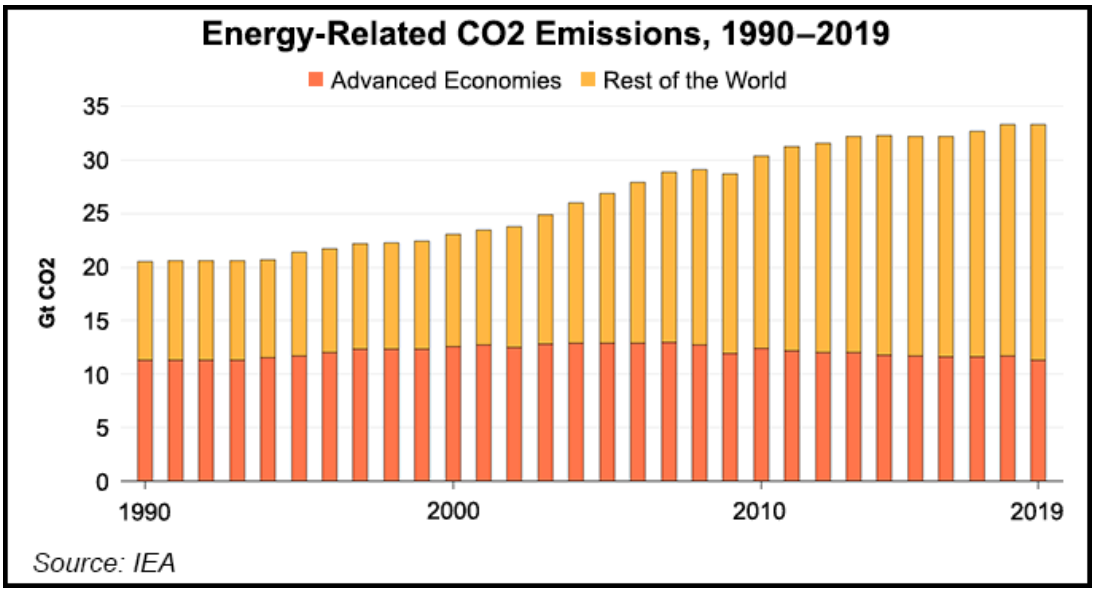

Figure 1.1: Energy Related CO_2 emissions 1990-2019 [6]

Five countries constitute more than half of the global emissions (figure 1.2). China is by far, Asia's and the world's largest CO_2 emitter: it emits nearly 10 billion tons each year, more than one-quarter of global emissions. USA is the second largest regional emitter and accounts for 16 % of global emissions. It is followed by the 27 European countries that form the European Union (the United Kingdom withdrew from the European Union). Furthermore, other small emitters such as India, Russia, Africa, and South America also contribute to an extent in global emissions.

Taking in account the population in each country, the CO_2 emission rankings per capita favor the Middle Eastern oil producing companies. For instance, in 2016, Saudi Arabia ranked first with a total of 16.3 tons of CO_2 emissions [7] while in 2017, Qatar had the highest emissions at 49 tons [5].

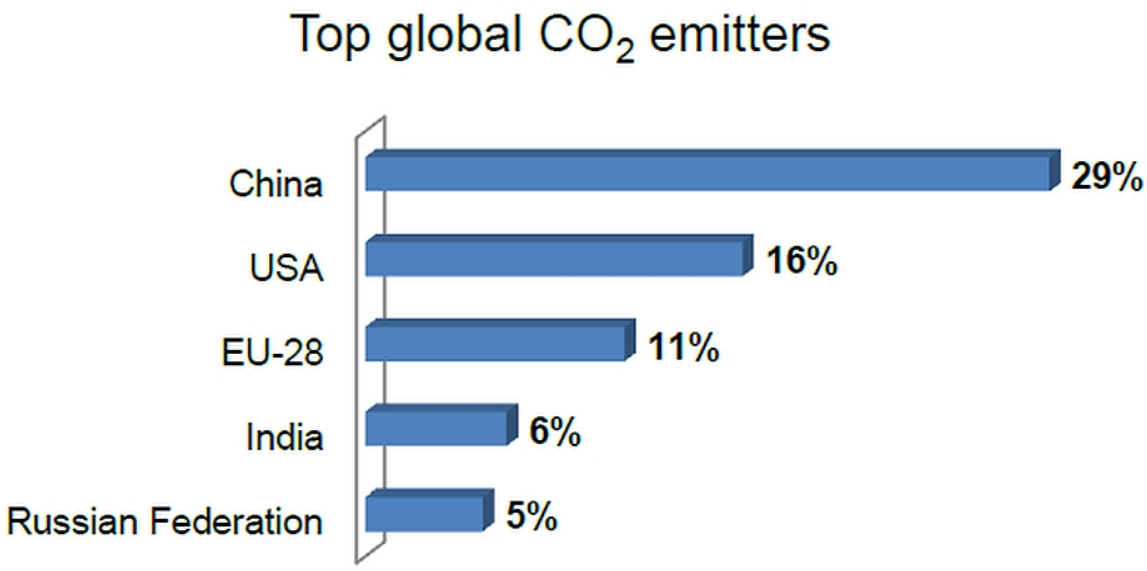

Figure 1.2: Emissions of top CO_2 emitters, as percentage of total global emissions [8]

1.1.2. Utilization of CO_2 for the Application of Power-to-Gas Technology:

Power to gas (PtG) technologies, especially Power to Methane, are considered one of the promising pathways for the conversion of CO_2 into valuable gaseous fuel. In 1978, George Long was the first to introduce the notion of producing Synthetic Natural Gas (SNG) to store electricity [9]. In the concept of the transition from a carbon-based energy system to a low-carbon energy system, the PtG technology converts the extra energy of variable renewable energy resources to SNG by a chemical process [10]. This innovative concept for storing energy represents a suitable solution for the long-term storage of electricity. Water electrolysis is one of the processes that supply excess electrical power in the form of hydrogen gas. Using electric power, an electrolyzer splits water into its two components: oxygen on one hand and hydrogen as combustible gas on the other. CO_2 and H_2 are used as educts in the CO_2 methanation process. If electrolysis hydrogen is supplied as an educt instead of traditional methanation processes where hydrogen is supplied by a gasifier, then the chemical storage of electricity is allowed.

In PtG, CO_2 from various sources (power plants, industrial or biogas) reacts with hydrogen (from renewable energy surplus), which is then chemically transformed to methane [11,12].

Nowadays, the major focus of research and application of PtG coupled with methanation technology lies in Europe especially in north-west of Germany, Hauts-de-France, Normandie, and in the North Sea [13].

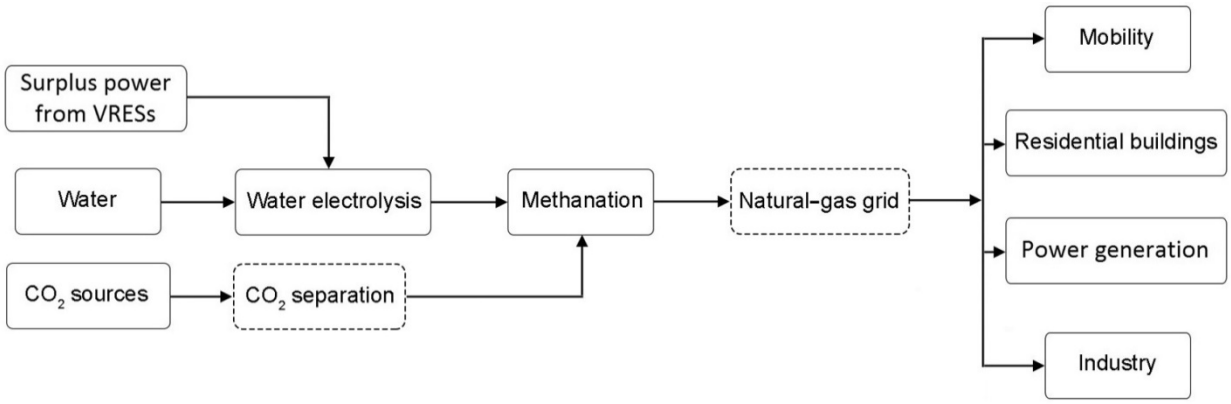

Figure 1.3: Principle of power to methane (PtM) technology and its applications [14]

1.1.3. Utilization of CO_2 for the Production of Synthesis Gas

In the last decade, the capture and utilization of CO_2 as a valuable feedstock for industrial products has attracted the attention of the scientific community. CO_2 is naturally abundant, nontoxic, cheap, FDA approved for food related use and renewable [15]. Despite the fact that large-scale utilization of CO_2 is still limited, industrial production of several organic chemicals such as methanol, salicylic acid, carbonates and urea are widely implemented. Among these processes, the production of urea is currently the largest use of CO_2 in organic synthesis [16].

Synthesis gas, or syngas, is a mixture of hydrogen and carbon monoxide, an industrial gas used for the production of many chemicals. The production of synthesis gas was proposed by Fischer and Tropsch in 1928. Since then, synthesis gas has become an important feedstock for methanol and ammonia synthesis. Chemical industry is the largest application of syngas (figure 1.4).

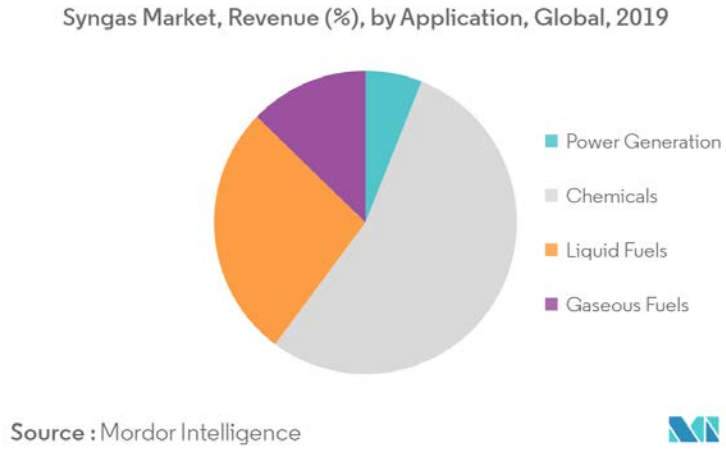

Figure 1.4: Global applications of synthesis gas, 2019 [17]

Reforming is the most prominent way used in industries to produce syngas, via one of the three reforming processes: steam reforming of methane (SRM) (equation 1.1), partial oxidation of methane (POM) (equation 1.2) and dry reforming methane (DRM) (equation 1.3) [18–20]. In the process of reforming, methane is combined with various oxidants to produce synthesis gas. In the case where water is used as an oxidant, it is called steam reforming of methane (SRM). Although the latter requires an extravagant ratio of heat in the form of steam, it is still one of the most important and conventional chemical processes for the production of syngas due to its high hydrogen yield. In fact, around 75 % of hydrogen produced is derived from SRM processes [18]. Moreover, the exothermic nature of the partial oxidation of methane reaction causes the induction of hot spots arising from poor heat removal rate which makes the operation difficult to control and require an additional post treatment cost to separate oxygen from the air. Dry reforming of methane, on the other hand, works with CO_2 as an oxidant and therefore offers the advantage of eliminating not one but two powerful greenhouse gases from the atmosphere**.**

Although both SRM and DRM processes share the common economic disadvantage of being highly endothermic requiring temperatures between 800 ^{o}C and 1000 ^{o}C, the DRM technology remains the most promising for the production of synthesis gas as it eliminates the complicated gas separation of end products rendering the process more economically favorable.

A fourth alternative, bi-reforming (equation 1.4) combines both SRM and DRM and is more interesting on several levels. From an industrial point of view, the supply of water and carbon dioxide produces an intermediate synthesis gas with a high proportion of H_2 to CO which allows direct transformation of synthesis gas into higher value hydrocarbons and reduces the need to add H_2 from external sources [21]. Not only does bi-reforming or the combination of steam and dry reforming (Combined Steam and Dry Reforming of methane (CSDR)) eliminate the potential fire hazards resulting from the flammable property of methane, but also reduces the need to separate CH_4 and CO_2, thereby reducing post-processing costs [22].

$$CH_4 + H_2O \rightleftharpoons CO + 3H_2 \qquad \text{(equation 1.1)}$$

$$CH_4 + \frac{1}{2}O_2 \rightleftharpoons CO + 2H_2 \qquad \text{(equation 1.2)}$$

$$CH_4 + CO_2 \rightleftharpoons 2CO + 2H_2 \qquad \text{(equation 1.3)}$$

$$3CH_4 + CO_2 + 2H_2O \rightleftharpoons 4CO + 8H_2 \qquad \text{(equation 1.4)}$$

1.2. CO_2 Methanation

1.2.1. History

The production of methane from syngas goes back to more than 100 years of research and development. The CO_2 methanation reaction (equation 1.5) which consists of reacting CO_2 and H_2 in order to produce CH_4 was first reported in 1902 by the chemists Sabatier and Senderens [23,24]. Methanation was first used for the removal of the residual CO_x from H_2 in ammonia synthesis process. During the oil crisis in the late 70s, methanation gained important interest as a means for the production of SNG by using syngas obtained from coal gasification as feedstock [25]. Preliminary studies regarding CO_2 methanation processes were established in the 1980s and focused on the use of coke oven gas or blast furnace gas. However, the significant effort required to purify these gases hindered most of these processes from reaching the commercial scale [26]. In the 1980-1990s, a combination of sea water electrolysis and CO_2 methanation was proposed by Hashimoto et al. [27]. CO_2 methanation concepts gained new attention at the beginning of the 21st century due to the increasing demand for electricity storage.

$CO_2 + 4H_2 \rightarrow CH_4 + 2H_2O$ $\Delta H_{298} = -164$ kJ/mol (equation 1.5)

1.2.2. Thermodynamic Studies

From a chemical point of view, CO_2 methanation is a linear combination of an exothermic CO methanation (equation 1.6) and an endothermic reverse water-gas shift reaction (equation 1.7).

$CO + 3H_2 \rightarrow CH_4 + H_2O$ $\Delta H_{298} = -206$ kJ/mol (equation 1.6)

$CO_2 + H_2 \rightarrow CO + H_2O$ $\Delta H_{298} = 41$ kJ/mol (equation 1.7)

The efficiency of the conversion of H_2 to CH_4 amounts to 83 % according to the Standard Conditions, whereby the remaining 17 % is released as heat [14]. CO_2 methanation is a highly exothermic reaction that is thermodynamically limited. The reaction equilibrium is influenced by pressure and temperature. In thermodynamic equilibrium, low reaction temperatures and high pressures are needed to maximize conversion and avoid the formation of CO as a product [12,28,29]. Moreover, higher pressures often lead to higher CO_2 conversion and higher CH_4 selectivity. CH_4 yield increases with decreasing temperature and increasing pressure (figure 1.5) [14]. At low temperatures (< 300 °C), conversion and selectivity are not affected with an increase in pressure especially above 10 bar. This

validates the possibility for a low temperature with reduced pressure methanation pathway that contradicts the conventional high temperature and high pressure processes [30].

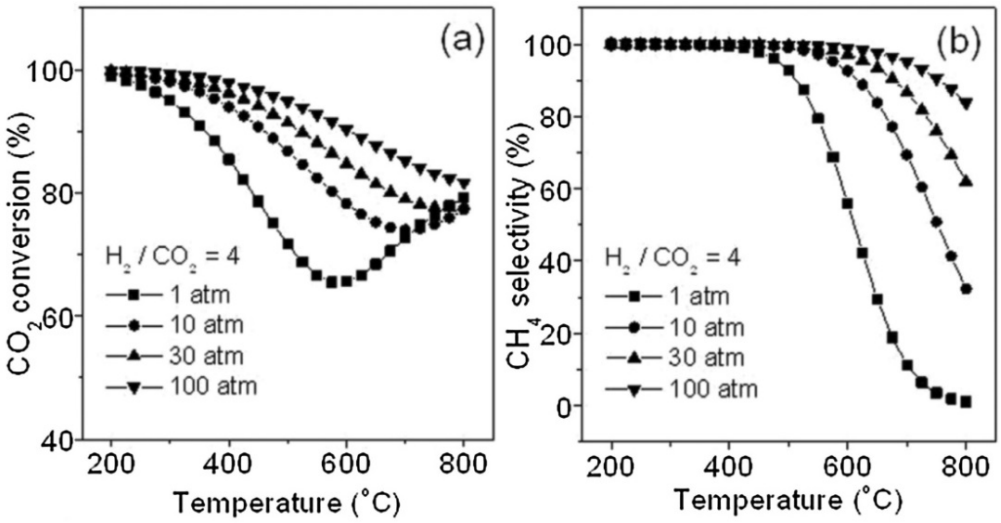

Figure 1.5: The effect of temperature and pressure on (a) CO_2 Conversion and (b) CH_4 selectivity at thermodynamic equilibrium [30]

The ideal H_2/CO_2 mole ratio for CO_2 methanation is 4:1. The reaction equilibrium increasingly favors several competing reactions as the operating temperature exceeds 300 °C [31]. The presence of these reactions reduces the selectivity of methane in comparison with CO. CO_2 methanation is not investigated above 500 ^oC because increasing the temperature favors the RWGS reaction [32]. Theoretically, carbon deposition is negligible if the H_2/CO_2 ratio is equal to or higher than the stoichiometric ratio due to the formation of excess steam which can inhibit the deposition of carbon [33,34]. Table 1.1 lists the possible side reactions involved in CO_2 methanation reported by Massa et al. [34].

Table 1.1: Possible reactions involved in the CO_2 methanation reaction [34]

Reaction #	Formula	$\Delta H_{298\ K}$ (kJ/mol)	Description
1	$CO_2 + 4H_2 \leftrightarrow CH_4 + 2H_2O$	−165.0	CO_2 methanation
2	$CO + 3H_2 \leftrightarrow CH_4 + H_2O$	−206.2	CO methanation
3	$CO_2 + H_2 \leftrightarrow CO + H_2O$	41.2	Reverse water-gas shift
4	$2CO + 2H_2 \leftrightarrow CH_4 + CO_2$	−247.3	Reverse dry reforming of CH_4
5	$2CO \leftrightarrow C + CO_2$	−172.4	Boudouard reaction
6	$CH_4 \leftrightarrow 2H_2 + C$	74.8	CH_4 cracking
7	$CO_2 + 2H_2 \leftrightarrow C + 2H_2O$	−90.1	CO_2 reduction
8	$CO + H_2 \leftrightarrow C + H_2O$	−131.3	CO reduction

1.2.3. Reaction Mechanism

Although several papers have been published on the subject, no general agreement exists on the reaction's operating mechanism due to the uncertainty in determining the intermediate compound and on the methane formation scheme [35,36]. Two different routes are proposed for CO_2 methanation. The first route involves the dissociation of CO_2 to CO followed by the subsequent conversion of CO to CH_4 by reacting with H_2. The second route includes a single step hydrogenation of CO_2 into CH_4 and excludes the formation of CO as an intermediate step [37].

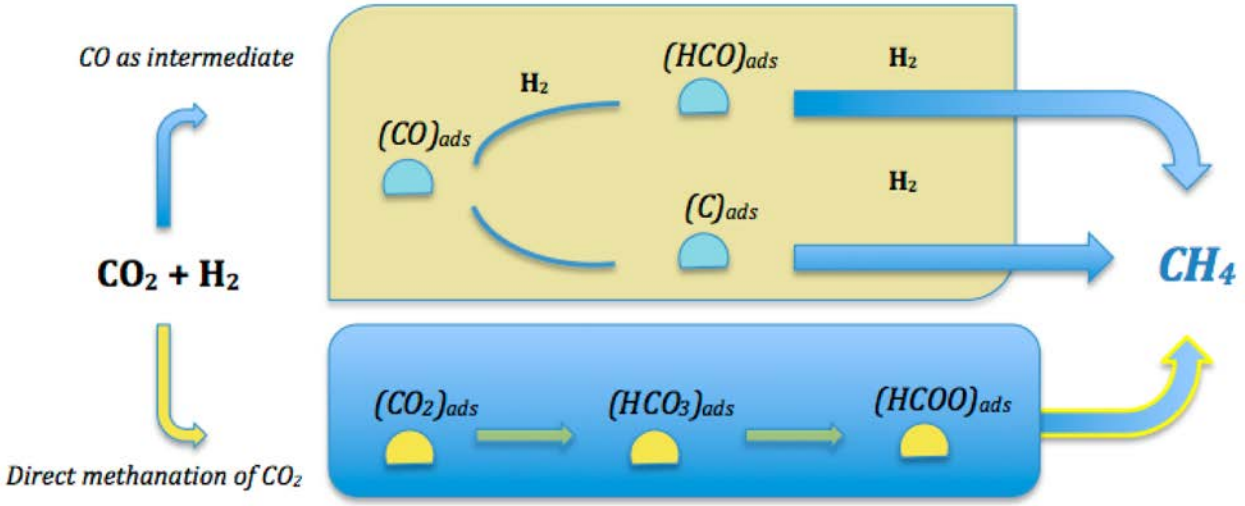

Figure 1.6: Simplified reaction mechanisms of CO_2 methanation [35]

In the case of the first route, the steps leading to methane formation could be: (i) chemisorption of carbon dioxide; (ii) dissociation of CO_2 into CO and O adsorbed on the surface; and (iii) reaction of dissociated species with hydrogen [35]. This dissociative adsorption of H_2 and CO_2 on the surface of the active metal nanoparticle results in the formation of adsorbed hydrogen atoms (H_{ad}), carbonyl groups (CO_{ad}) and oxygen atoms (O_{ad}) on the metal surface. Carbonyl groups may successively dissociate into the surface oxygen (O_{ad}) and carbon (C_{ad}) atoms that could be hydrogenated to CH_x species [28]. Hence, CO_2 adsorption takes place preferably on the metal-support interface while CO_2 dissociation takes place on the active metal surface. The dissociation of CO_{ads}, considered as the rate-determining step of the CO_2 methanation process has been proposed to proceed by two main pathways [36]: direct CO_{ads} dissociation and H-assisted CO_{ads} dissociation.

$CO_{ads} + * \rightarrow C_{ads} + O_{ads}$

CO_{ads}+ H_{ads} → COH_{ads} + * → C_{ads} + OH_{ads}

The second route involves the formation of carbonate, formate or methanol species (not CO) as the main intermediate during the reaction.

1.2.4. Current Applications

There exist two possible main paths for CO_2 methanation: biological and thermochemical [38]. Another emerging path that is not as common as the above paths includes the electrochemical methanation of CO_2.

Biological methanation

This reaction has been established since 1906. It involves the use of a microorganism as a biocatalyst that converts hydrogen and carbon dioxide into methane. Biological methanation proceeds at low temperatures (40 °C to 70 °C) in stirred tank reactors or trickle-bed reactors. Moreover, the microorganisms are said to possess high tolerance against the impurities (sulfur, ammonia, oxygen...) found in the feed gases used for methanation.

Thermochemical or catalytic methanation

The conversion of H_2 and CO_2 takes place in the presence of a catalyst. Typical operating conditions are temperatures in the range of 250 °C to 550 °C and pressures from 1 to 100 bars. The three main established process concepts for thermochemical methanation are: fixed bed methanation, fluidized bed methanation, and three phase methanation.

Electrochemical methanation

Recently, numerous studies have been carried out on the electrochemical reduction of CO_2 [39–41]. This type of CO_2 methanation requires mild reaction conditions which makes it more environmentally friendly than thermochemical processes. There are many advantages for electrochemical reduction of CO_2 to CH_4 such as versatility, energy efficiency, and cost effectiveness [37].

1.2.5. Catalysts Used in CO_2 Methanation

The development of efficient catalysts to enhance the reaction kinetics is a must in order to realize the conversion of CO_2 into CH_4 [31,42,43]. CO_2 methanation catalysts must provide high thermal stability as well as good resistance to carbon formation. Methanation catalysts are typically composed of active metal particles (Ni, Fe, Co, Ru, Rh, Pt, Pd, W or Mo) dispersed on a metal oxide support (Al_2O_3, SiO_2, TiO_2, SiC, ZrO_2, CeO_2, $Ce_xZr_{1-x}O_2$) [30].

Supports

The morphology, active phase dispersion, degree of the metal oxide reducibility, and catalyst stability in the CO_2 methanation reaction are influenced by the nature of the support used [11,44, 45].

A typical commercial support for methanation processes is Al_2O_3 because of its ability to finely disperse metal species and its relatively low price [11,14]. In fact, Ni/Al_2O_3 catalysts demonstrate high catalytic activities yet are more prone to severe carbon deposition as a result of the high reaction temperature used. Therefore, researchers are constantly attempting to develop alumina supported catalysts that have both high activity and stability in the CO_2 methanation reaction [35]. Mesoporous alumina having large surface areas and good thermal stability are used to optimize the Ni based catalyst performances [46]. For instance, in a study reported by Aljishi et al. [47], the authors concluded that varying synthesis parameters such as the type of acid, nickel loading, calcination temperature as well as synthesis method in a series of ordered mesoporous nickel alumina catalysts influenced the catalyst morphology and its activity towards CO_2 methanation. The chemistry of Al_2O_3 is a bit complicated due to its various crystallographic modifications (γ, κ, δ, θ, α phase). Among those, the γ-Al_2O_3 phase has been widely investigated due to its high surface area, porous properties, as well as its surface acid–base properties [30].

The use of mesoporous silicas (MCM-41, SBA-15, SBA-16...) based materials as supports for metal catalysts has recently gained interest in the CO_2 methanation reaction. For example, Wang et al. [48] reported the synthesis of a series of Ni-xCeO_2/MCM-41 (x= 0, 5, 10, 20 and 30 %) catalysts with a nickel content of 20 wt% via the deposition precipitation method. The catalyst modified with 20 wt% CeO_2 showed the best catalytic performance at 380 °C (85.6 % CO_2 conversion and 99.8 % CH_4 selectivity) and was stable even after 30 h under stream.

Cerium oxide is widely investigated as a support in the catalysts used for the CO_2 methanation reaction due to its redox properties. For Ni catalysts, it was found that the use of the partially reduced support CeO_2 can promote the activation of CO_2 by allowing the surface to be effectively covered by CO_2 derivatives which in turn improves the CO_2 methanation performances [42].

Active phase

Sabatier and Senderens first discovered the ability of nickel in catalyzing methanation reactions. Now, after more than 100 years on their discovery, basically all metals located in

groups 8–10 of the periodic table (figure 1.7) have been reported to be efficient materials for CO_2 methanation [26,49].

CO_2 methanation has mainly been investigated using Ni and noble metals such as Ru, Rh and Pd as active species on various metal oxides [44,50,51]. Despite their considerable activity in methanation reactions, the use of noble metal based catalysts is industrially limited due to their high price and low availability [51,52]**.** Among the transition metals investigated, Ru shows the highest CO_2 methanation activity and CH_4 selectivity because of its ability to activate CO_2 molecules and dissociate H_2 [25,53]. From an industrial point of view, Ni-based catalysts are preferred because of their relatively fair activity, low cost, and high availability [23,54]

6	7	8	9	10	11
24 **Cr** Chromium	25 **Mn** Manganese	26 **Fe** Iron	27 **Co** Cobalt	28 **Ni** Nickel	29 **Cu** Copper
42 **Mo** Molybdenum	43 **Tc** Technetium	44 **Ru** Ruthenium	45 **Rh** Rhodium	46 **Pd** Palladium	47 **Ag** Silver
74 **W** Tungsten	75 **Re** Rhenium	76 **Os** Osmium	77 **Ir** Iridium	78 **Pt** Platinum	79 **Au** Gold

Figure 1.7: Active metals for methanation processes (marked in grey) [26]

Promoters

In addition to supports, promoters help to enhance the performance of methanation catalysts by improving the adsorption and dissociation of H_2 and CO_2 [31]. Not only do promoters improve metal-support interactions, but also minimize carbon deposition and sintering of metallic particles [55]. The addition of promoters aims to ameliorate catalytic performances via substantial modifications of surface basicity [14].

Noble metal promoters are said to increase the conversion to methane and maintain greater activity than non-promoted catalysts even in the presence of sulfur poisoning [56]. In fact, the stability of nickel catalysts can be improved by addition of promoters: doped Ni systems (Ni-Mg, Ni-Fe, Ni–Ru, Ni-Pd) were reported to enhance the activity and stability of methanation catalysts [57]. Wang et al. [58] showed that the incorporation of 0.05 % Fe into $NiAl_2O_3$-HT increased the activity of the catalyst as a result of an ameliorated NiO dispersion and reducibility. Moreover, Vrijburg et al. [59] studied the promotional effect of MnO on Ni catalysts supported on silica-modified γ-Al_2O_3 in CO_2 and CO methanation. They concluded that a higher activity was remarkably obtained for Mn-promoted compositions. Mn addition

weakened the interaction between the Ni-oxide precursor and the support which hence improved the active phase dispersion and reducibility. Zhao et al. [60] also reported that promoting Ni/Al_2O_3 catalysts with manganese can enhance the catalyst's textural and crystal properties by increasing surface areas and pore volumes and decreasing NiO crystallite sizes.

Alkaline earth metals such as Ca and Mg are used as promoters due to their strong basicity. Actually, MgO can enhance the capacity of CO_2 adsorption, alter the acid–base property of catalysts and improve the dispersion of the active phase [61].

Alkali metals are also used to improve CO dissociation and increase the selectivity towards hydrocarbons. Among the three alkali metals Li, K and Na, Cimino et al. [62] concluded that doping a 1 wt% Ru/Al_2O_3 catalyst with Li synthesized with nitrate precursors increases both CO_2 capture capacity and methanation activity as a result of the formation of a mixed spinel phase.

Moreover, the addition of promoters to Ni-based catalysts is considered an alternative to prevent physico-chemical deactivation. CeO_2 has often been employed as a promoter to enhance the activity of Ni/Al_2O_3 catalysts because of its ability to [35]:

(i) improve thermal stability of Al_2O_3

(ii) promote the dispersion of the metal onto the support

(iii) change the properties of the metal due to strong metal–support interaction

1.2.6. Challenges Facing CO_2 Methanation

Considerable efforts have been devoted to investigate various aspects of CO_2 methanation reaction. From the catalytic aspects, and despite the fact that methanation catalysts have already been investigated for a long time, the biggest challenge researchers still face is the ability to develop catalysts with high activity at low temperatures [32]. Because of the kinetic limitations facing the CO_2 methanation reaction such as its exothermic nature, the conversion at low temperatures is practically difficult to achieve. Moreover, Ni-based catalysts suffer oxidation during the adsorption phase and are hence not efficiently reduced in the methanation/regeneration step which makes it hard to withstand real process conditions [62]. In addition to this, nickel carbonyl, which is very toxic to humans, can be formed during the process. The industrialization of CO_2 methanation remains a great challenge due to the lack of the efficient and stable catalysts. Furthermore, reaction conditions such as temperature, pressure, gas hourly space velocity (GHSV), as well as initial CH_4 concentration are critical parameters that are constantly tackled as research materials. Over the past few years, great

efforts have been made both in methanation catalysts development and reaction mechanism investigation [55].

From the process design and implementation standpoint, it is said that the process parameters may affect the product yield. The key parameters that influence designing methanation reactors are heat dissipation and temperature control. An obstacle facing the reactor design is to remove heat produced by the exothermic reaction without generating hot spots or quenching the reaction [11].

1.3. CO_2 Reforming of Methane

1.3.1. History

As the Industrial Revolution and the exploration of fossil fuels began, the emission of anthropogenic GHGs has progressively increased. Historically, the over-emissions of CO_2 were not given any account. However, in the 1880s, Svante Arrhenius was the first person who predicted the relation between human activities and global warming [63]. With this idea coming to light, the CO_2 or dry reforming of methane reaction (equation 1.3) with a standard enthalpy (ΔH_{298}) of 247 kJ/mol started to be tackled as early as 1888. Later on, Fischer and Tropsch thoroughly investigated the DRM reaction over Ni and Co catalysts in 1928 [64]. In the 1970s, DRM received renewed interest as a response to repeated oil crises. Since then, there is extensive research on the CO_2 reforming of methane and a variety of catalysts for DRM have been widely tested.

1.3.2. Thermodynamic Studies

CH_4 and CO_2 are very stable molecules with high dissociation energy. The co-activation of both bonds faces challenging difficulties. Therefore, a very high temperature is needed to drive the reaction in the forward direction and achieve the equilibrium conversion to synthesis gas. CO_2 reforming of methane is hence an extremely endothermic reversible reaction that requires high operating temperatures in the range of 900 K – 1273 K to achieve the desirable conversion levels [65]. Consequently, the use of catalytic systems to induce sufficient conversions may lead to a reduction of the energy invested in the process. Even though the DRM reaction is mainly governed by the interaction between CH_4 and CO_2, it is inevitably accompanied by many side reactions such as the Reverse Water Gas Shift (RWGS) (equation 1.7) and the steam reforming of methane (SRM) (equation 1.1) [18,65,66].

The DRM reaction produces an H_2/CO ratio of unity. However, the presence of the endothermic reverse water gas shift which can compete with the DRM reaction is responsible for increasing the amount of CO compared to H_2 and thus lowering the H_2/CO ratio to a value lower than unity [18,65,67]. This is in fact advantageous for many industrial applications such as the synthesis of oxygenated chemicals (acetic acid and di-methyl ether) [64,68]. The RWGS reaction also contributes to the slightly higher CO_2 than CH_4 conversions.

Carbon formation is the most important reason for fatal catalyst deactivation during DRM. The carbon formed during DRM is primarily due to two reactions: methane decomposition

(equation 1.8) at high temperatures and CO disproportionation or Boudouard reaction (equation 1.9) at temperatures lower than 750 ^{o}C [69–71].

$CH_{4\,(g)} \leftrightarrow C_{(s)} + 2H_{2\,(g)}$ ΔH_{298}= 74.9 kJ/mol (equation 1.8)

$2CO_{\,(g)} \leftrightarrow CO_{2\,(g)} + C_{(s)}$ ΔH_{298}= -172.4 kJ/mol (equation 1.9)

According to figure 1.8, the DRM, RWGS, and methane decomposition are favored at high temperatures as their equilibrium constant increases with rising temperatures. On the other hand, the Boudouard reaction and the hydrogenation of CO are exothermic and thermodynamically unfavorable at high temperatures. This suggests that the DRM reaction becomes more favorable at temperatures greater than 700 ^{o}C. When the DRM reaction temperature is above 800 °C, carbon formation mainly originates from CH_4 decomposition which also generates CO_2 which facilitates the oxidation of the carbon formed [72].

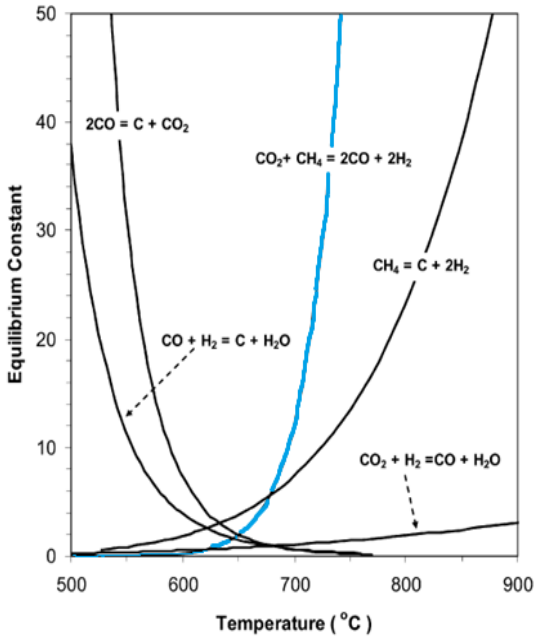

Figure 1.8: The variation of equilibrium constants as a function of temperature [73]

1.3.3. Reaction Mechanism

Various mechanisms have been proposed in the literature in an attempt to explain the interactions between CO_2 and CH_4 and the active sites of the catalysts using experiments and kinetic computations. The elementary mechanism of the dry reforming of methane can be summarized into four steps: firstly, the dissociation and adsorption of CH_4 is the most kinetically significant phase in DRM. This is the first step of the reaction sequence and it involves the decomposition of CH_4 into CH_x* species and hydrogen. Each partially dissociated CH_x* species adsorbs differently on a site. This preferential dissociation of the CH_x-H bonds is said to depend on the surface properties [65]. This rate determining step is followed by the dissociative adsorption of CO_2 on the metal and metal-support interface which is triggered by the adsorbed hydrogen on the surface of the catalyst. Niu et al. [74] investigated the dry reforming of methane over Pt catalysts and proposed three possible pathways to CO_2 activation:

1- $CO_2* + * \rightarrow CO* + O*$

2- $CO_2* + H* \rightarrow COOH* + * \rightarrow CO* + OH*$

3- $CO_2* + H* \rightarrow HCOO* + * \rightarrow CHO* + O*$

In paths 2 and 3, CH_4 initially dissociates into atomic H, which in turn activates the CO_2, whereas path 1 describes the direct CO_2 dissociation into adsorbed CO and adsorbed O. In a third step, the formation of hydroxyl groups on the surface will take place. Actually, the presence of surface hydrogen atoms (from CH_4 dissociation) and adsorbed oxygen species, resulting from the dissociative adsorption of CO_2 leads to the formation of adsorbed hydroxyl groups. This step also leads to the formation of H_2O via the reverse water gas shift reaction where an adsorbed oxygen species combines with H_2 gas to give a molecule of H_2O. A final fourth step involves the reaction of adsorbed oxygen atoms on the metal particles with surface CH_x groups to form CO. The latter forms along with the H_2 what is referred to as the synthesis gas.

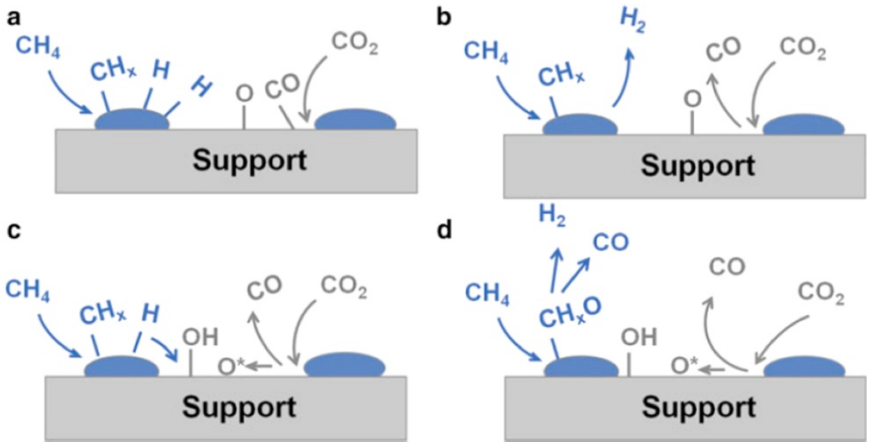

Figure 1.9: CO_2 reforming of methane mechanism: (a+b) Dissociative adsorption of CH_4 and CO_2 activation (c) Formation of surface hydroxyls and oxygen spillover and (d) Surface hydroxyls and oxygen species oxidize CH_x and induce the formation of CO and H_2 [65]

1.3.4. Current Applications

Fischer-Tropsch

The synthesis gas obtained in DRM is a key in the chemical industry since it is used as a sustainable alternative to fossil fuel and also a precursor for important chemicals such as methanol, ammonia and synthetic hydrocarbon for fuel production.

By definition, Fischer-Tropsch Synthesis (FTS) is the catalytic conversion of syngas into higher hydrocarbons that are further upgraded into cleaner fuels, lubricants and chemicals. Compared to hydrocarbons derived from fossil fuel (gasoline and diesel), FTS hydrocarbon fuels generally have very low sulfur and aromatic compounds content and are thus considered cleaner [75].

The catalysts most often used in FTS are iron, cobalt, ruthenium, and nickel [76]. From a thermodynamic point of view, the FT process is preferentially conducted in the 200 ^{o}C – 300 ^{o}C temperature range with water being the most undesirable byproduct [77].

Biogas

Generally, raw biogas is mainly composed of 35 % – 75 % CH_4 and 25 % – 55 % CO_2. Traces of N_2, O_2, H_2, H_2S, H_2O, CO, NH_3, siloxanes, aromatics, as well as some dust particles may also be found [78]. The CO_2 reforming of methane is one of the emerging technologies that tackle the recovery of biogas produced by converting its two major components CH_4 and CO_2 together into syngas. To understand the origin of biogas, it is important to emphasize on the basis of its formation: biogas is produced by anaerobic methanization or anaerobic digestion which is a natural biological process that converts

organic matter (carbohydrates, lipids, proteins) into simple elements that constitute the biogas by means of specific microbial flora. Not only does the anaerobic digestion produce energy rich biogas from biomass resources, but also releases nutrient rich digested residues which can be used as soil fertilizers in the agriculture field [79]. One major drawback regarding the direct use of biogas as a source of renewable energy is the presence of inorganic and organic sulfur contained in the feedstock. Under anaerobic conditions, the latter can be reduced or fermented resulting in the formation of hydrogen sulphide (H_2S). H_2S is notorious for its bad smell and toxic properties. The poisoning of biogas by H_2S is handled either during the anaerobic process itself or by treating the biogas and controlling the feedstocks [80].

1.3.5. Catalysts Used in CO_2 Reforming of Methane

Supports

The high reaction temperature of the DRM reaction necessitates the use of a thermally resistant high melting point support. Besides thermal stability, the support used in the DRM reaction must provide certain textural and physico-chemical properties such as high surface area for the dispersion of the active metals, basicity, oxygen storage capacity, and reducibility [64]. Generally, the support has no catalytic performance, but its properties play an essential role in the capability of the catalysts [81]. Furthermore, a suitable support suppresses carbon deposition by favoring the activation of CO_2 and enhancing the dispersion of active sites due to the existence of metal-support interactions [82].

Different supports having different properties have been tested in the dry reforming of methane. Alkaline metal oxides such as MgO and CaO are known for their high thermal stability and basicity; TiO_2 and ZrO_2, on the other hand, are used because their reducibility allows the creation of strong metal support interactions [66]. Nevertheless, the two supports most used in methane reforming are Al_2O_3 and SiO_2.

Mesoporous silicas have been widely studied by researchers not only because they possess large surface areas and pore volumes, but also because they provide a remarkable thermal stability and high metal dispersion. In addition, mesoporous alumina is the most extensively used support for industrial and lab-scale catalytic reactions due to its low cost and excellent physico-chemical properties. Incorporating Ni particles inside the pores of the mesoporous support improves the performance of the catalysts by avoiding the sintering of metal particles and strengthening the metal-support interaction [18,83]. Table 1.2 lists the physico-chemical properties of the most common mesoporous supports used in the CO_2 reforming of methane.

Table 1.2: Summary of the crystal and porous properties of the most common mesoporous supports used in CO_2 reforming of methane

Mesoporous Support	Full name	Crystal Structure	Specific Surface Area (m^2/g)	Pore Volume (cm^3/g)	Pore size distribution (nm)	Reference
SBA-15	Santa Barbara Amorphous type material	2-D hexagonal	682	0.9	5 – 15 nm	**[84]**
KIT-6	Korea Institute of Science and Technology	3-D cubic *Ia*3*d*	745	0.8	5 – 15 nm	**[84]**
MCM-41	Mobil Composition of Matter No.41	2-D hexagonal *P6mm*	858	0.8	2 – 6 nm	**[84]**
SBA-16	Santa Barbara Amorphous-16	3-D body-centered cubic *Im3m*	837	0.137	2 – 10 nm	**[85]**
MSC	Mesoporous Silica Carbon	2-D hexagonal	389	0.4	2 – 7 nm	**[86]**
meso-Al_2O_3	Alumina	γ-Al_2O_3	207	0.25	2 – 6 nm	**[87]**
meso-ZrO_2	Zirconia	tetragonal and cubic	192	0.16	1 – 10 nm	**[88]**
TUD-1	Technische Universiteit Delft	3-D amorphous	632	0.97	2 – 8 nm	**[89,90]**
HMS	Hexagonal Mesoporous silica	hexagonal	896	1.12	2 – 6 nm	**[91]**
ZSM-5	Zeolite Socony Mobil–5	MFI zeolite topology	292	0.425	3 – 10 nm	**[92]**

Active phase

According to the literature, Ni and other non-noble metal catalysts exhibit remarkable catalytic performances and are cheaper yet more susceptible to deactivation due to carbon formation when compared with noble metals such as Ru, Rh and Pt catalysts [68,93–95]. The ability to disperse on the support and retain a small particle size as well as reduce the carbon formed is what differentiates the catalytic performance of noble metals from their non-noble counter-parts [65].

From these noble metals, Ru seems to be the most active noble metal explored for DRM. In their work, Anil et al. [96] synthesized materials with ionic substitutions of 2 wt% Ru, Pt, and Pd in a $LaAlO_3$ perovskite structure and tested their catalytic activity in DRM. Among the three noble metals partially substituted perovskite $LaAlO_3$ catalysts, $LaAl_{0.98}Ru_{0.02}O_{3-\delta}$ was found to be the best performing catalyst as a result of a synergetic effect between Ru and Al that promoted a high sintering stability. Moreover, Whang et al. [97] showed that a very small amount of Ru (0.13 wt%) deposited on ZrO_2-SiO_2 support is very active and stable for the DRM reaction performed at 800 °C even at high space velocities.

Many studies were devoted to the development of Ni based catalysts which are the most appropriate and widely applied catalysts in DRM due to their low cost and availability compared to noble metal catalysts. Research on nickel based catalysts mainly focuses on increasing the catalysts stability. According to Dębek et al. [98], several approaches to enhance the catalyst stability have been adopted and they include the use of the following:

i) suitable preparation methods
ii) basic supports or promoters
iii) bi-metallic catalysts
iv) sulphur passivation of Ni catalysts
v) oxidizing agents such as water or oxygen

The third approach includes the creation of an alloy catalyst (usually bi-metallic), where a noble or non-noble metal is added to another metal. The ability of a bi-metallic catalyst is not only limited to overcoming the drawbacks imposed by excessive carbon formation as well as the operational and economical limitations of the process, but also to improving catalytic activity by enhancing metal dispersion and interaction. Recently, Turap et al. [99] compared a monometallic Ni/CeO_2 catalyst to a series of bi-metallic $Co–Ni/CeO_2$ catalysts with Co/Ni ratios between 0 and 1.0 and found that the catalyst with a Co/Ni ratio of 0.8 demonstrated the highest catalytic activity and stability. This remarkable performance was ascribed to the formation of a Co–Ni alloy that restricted the occurrence of the reverse water gas shift reaction. In a second recent study reported by Zhang et al. [100], the contribution of a Ni-Fe alloy catalyst was assessed in DRM. After test characterizations revealed that lower amounts of carbon were found on spent Ni-Fe alloy catalysts when compared to Ni catalyst. Fe was also able to modify the type of surface carbon.

Noble metals, on the other hand, are normally added to Ni based catalysts in small quantities. This introduction can potentially overcome the deactivation of this non-noble catalyst while simultaneously reducing total cost and promoting active phase dispersion.

Promoters

Alkaline earth metals (AEM) are used as promoters in the DRM reaction because they are able to ameliorate the active phase-support interactions by forming solid solutions with the active phase and because their basicity aids in the suppression of carbon formation by oxidizing the carbon deposits.

Rare earth metals (REM) such as cerium and lanthanum and transition metals (TM) such as zirconia are used because they exhibit redox properties that also aid in the oxidation of carbon deposits. For instance, the redox properties of CeO_2 ($Ce^{4+} \leftrightarrow Ce^{3+}$) trigger the formation of oxygen vacancies which can prevent carbon deposition by enhancing the mobility of surface oxygen and adsorbing the mild acidic CO_2 species on the catalyst surface.

Nevertheless, the amount of promoter affects the catalytic activity; excessive amounts of promoters normally decrease catalytic activity as a consequence of the coverage of active sites [101]. Table 1.3 below summarizes a few reports about the effect of different promoters on the activity of Ni based catalysts in the CO_2 reforming of methane reaction.

Promoter	Group	Loading (wt. %)	Support	Preparation Method	Effect of promoter on the Ni based catalyst	Reference
Yttrium	REM	4, 8, 12 %	KIT-6	incipient wet impregnation	Higher NiO reducibility and dispersion; formation of Ni agglomerates on the surface of the support resulting in higher extent of carbon formation	**[102]**
Samarium	REM	0.5, 1.5, 3 %	SBA-15	two-solvent impregnation	decreased surface areas; enhanced NiO-support interactions; increased amount of deposited coke	**[103]**
MgO	AEM	3 %	Al_2O_3	wet impregnation	high Ni dispersion and reducibility; reduced surface areas and pore volumes; MgO had the most promotional effect on activity and carbon formation	**[104]**
CaO						
BaO						
Zirconia	TM	5 %	SiO_2	co-impregnation method	Synergetic effect of Ni and Zr led to enhancement of CO_2 activation even at low temperatures (400 ^oC)	**[105]**
Cerium	REM	6 %	SBA-15	ultrasonic assisted impregnation	smaller Ni particles and homogeneous metal dispersion; superior catalytic performance at 800 ^oC ; lowest carbon formation	**[106]**
Potassium	AEM	0.2 – 5 %	Al_2O_3	excess solution impregnation	no modification of the structure of Ni particles; neutralization of some active sites by the migration of K from the support to the Ni surface; K catalyzes the gasification of coke	**[107]**
Zirconia	TM	25, 56, 72 %	CeO_2	co-precipitation	higher activity and stronger resistance to carbonaceous deposits; improved reducibility as well as textural and structural features; Zr stabilizes ceria under thermal reductive conditions	**[108]**

Table 1.3: Effect of different promoters on the activity of Ni based catalysts in the CO_2 reforming of methane reaction

1.3.6. Challenges Facing CO_2 Reforming of Methane

Despite its substantial environmental potentials, DRM is still an unpractical process that is not industrially mature. The main barriers behind progress for profit oriented commercialization are the extremely high endothermic nature coupled with catalyst deactivation by the inevitable carbon formation [65,109]. Moreover, according to Aouad et al. [66], the increase in the costs of the dry reforming process is also linked to the scarcity of clean and steady CO_2 sources. While choosing an appropriate catalyst, researchers find themselves in a constant dilemma between the catalysts' cost and performance: transition metals are inexpensive and abundant but their accelerated deactivation at reforming conditions constitutes a major challenge. On the other hand, noble metals are more resistant to carbon formation but economically unfavorable because of their high cost [110]. In addition, the inevitable formation of water as a byproduct reduces the syngas selectivity and lowers the H_2/CO ratio [111].

1.4. Catalysts Deactivation

It is well-known that Ni based catalysts are subject to severe deactivation during the CO_2 methanation and the CO_2 reforming of methane reactions. Several deactivation phenomena are classified in the literature. These can be divided into two main categories: chemical and physical deactivation. Poisoning and vapor-solid reactions are classified as chemical deactivation whereas fouling, sintering (thermal degradation), and attrition are classified as physical types of catalysts deactivation [37]. The causes behind these types of deactivation are discussed below:

Poisoning

Catalysts react sensitively to a multitude of gas impurities such as ammonia, chlorine and sulfur compounds, tars, particles… Deactivation by sulfur poisoning is one of the main drawbacks that face methanation and reforming catalysts. Moreover, when the catalyst is poisoned, the substance becomes irreversibly chemisorbed to the active site. A chemical retreatment of the surface or the replacement of the poisoned catalyst is thus necessary [112].

Fouling

The physical deposition of species from the gas phase onto the catalyst active surface that results in the blockage of sites and pores and hence activity is referred to as fouling [37]. The latter occurs as carbon deposition where CO_2 decomposes into CO and further to solid carbon by the Boudouard reaction (equation 1.9). This type of deactivation is partially reversible, and the carbonaceous deposits can be removed by gasification or burning with O_2, H_2O, CO_2, and H_2.

Nickel Sintering

Thermal degradation, in other words sintering, is a physical type of deactivation caused by the agglomeration of metal particles of either the support material or the active phase because of the severe opperating conditions. Sintering leads to the reduction of the number of active sites and causes the formation of crystals of larger sizes thus leading to a loss of catalytic activity. This type of deactivation depends on the time that the catalyst spends in the high temperature environment.

Attrition

The catalyst deactivation through mechanical straining occurs via the process of attrition. By definition, attrition is the loss of catalytic material due to abrasion or loss of internal surface area due to mechanical crushing of the catalyst [113]. Temperature fluctuations such as

reactor startup or shutdown induce thermal stress. Attrition is evident by a reduction in the particle size and/or destruction of catalyst granules or pellets.

Vapor−solid reactions

This type of deactivation occurs as a result of the reaction of vapor, support, or promoter with the catalytic phase, which produces an inactive phase and causes a form of chemical deactivation. The interactions of the catalysts with the reactants and/or products greatly influence the structure of the catalyst's surface. This deactivation is also referred to as chemical assisted sintering because it also restructures the surface but at temperatures which are below the melting point of the material [113].

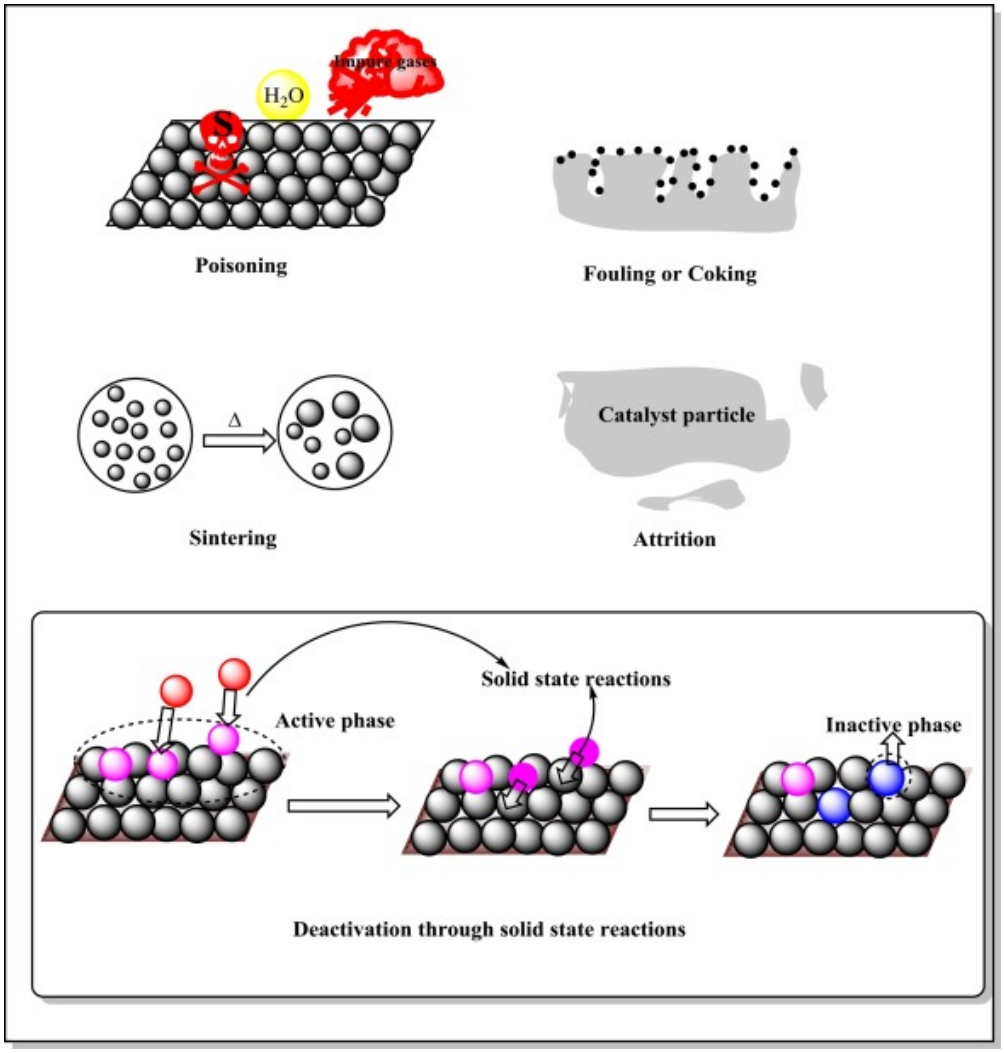

Figure 1.10: Types of catalysts deactivation [114]

Generally, catalysts' deactivation in DRM is attributed to carbon formation, sintering and/or oxidation of active metal particles [66,110]. High operating temperatures raise the molecular

energy to high levels that cause the cleavage of the C-H bonds in methane and induce coke deposition on the reforming catalyst which eventually leads to the clogging of the reactor and deactivation.

Carbon deposits are classified according to their ability to be hydrogenated [66,115]. Cα is surface carbide that can be hydrogenated below 50 ^{o}C, Cß can be hydrogenated between 100 ^{o}C and 300 ^{o}C and is referred to as amorphous carbon, and Cγ can be hydrogenated at above 500 ^{o}C and is referred to as graphitic carbon [65]. The order of reactivity of these carbonaceous species is as follows: $C\alpha > C_{ß} > C\gamma$.

Cα species are easily eliminated by gasification and are believed to originate from the decomposition of methane. However, at high reaction temperatures where both the Boudouard reaction and the decomposition of methane occur, the formation of carbon is most likely to occur when the Boudouard reaction predominates [116].

1.5. Catalytic Parameters

While choosing a suitable catalyst for both reactions, certain catalytic parameters must be taken into consideration. Such parameters include the significant effect of the interaction between components, particle size and dispersion, basicity, oxygen storage capacity, the reducibility as well as the porosity and surface area. Process parameters like reactor type and the gas hourly space velocity (GHSV) employed also determine the catalytic performance. Some of these parameters will be highlighted in the section below.

Effect of metal-support interactions

An important aspect underlined by a number of researchers is the type of interaction between the metal and the support. For the CO_2 methanation reaction, it is commonly discussed that the improvement of the stability towards CO poisoning requires a strong metal-support interaction to provide more anchoring sites for the active sites [117]. Metal-support interaction (MSI) in catalysts can be tuned by altering the active component loading, which also achieves the purpose of controlling the products distribution in the CO_2 methanation reaction [118]. Ideally, the MSI should be strong enough to offer highly dispersed active sites, but not too strong to prevent the active species from being maintained in the active metallic form. In their study, Italiano et al. [45] reported that Ni-support interactions clearly depend on the type of oxide support used. From the H_2-TPR profiles, they deduced the following order of MSI: $Ni/CeO_2 < Ni/Y_2O_3 < Ni/Al_2O_3$. The relatively weak MSI of the $15Ni/CeO_2$ catalyst resulted in catalytic performance degradation as a consequence of the presence of Ni sites that are vulnerable to CO-poisoning. Moreover, a strong MSI is said to avoid the sintering of the active phase of the catalysts employed in CO_2 methanation. For instance, the severe thermal sintering of a series of Co-Ni doped ordered mesoporous Al_2O_3 was successfully inhibited because of the formation of a strong interaction between the metal and the mesoporous framework accounting for no serious deactivation after 50 h stability tests [23].

In the CO_2 reforming of methane, metal-support interactions influence the carbon deposition phenomena. Strong interactions between the metal and the support prevent carbon deposition and deactivation [106]. A strong MSI offers better active phase dispersion by maintaining a small size of the active species and preventing agglomeration that increase the particle sizes and hence better resistance to carbon deposition [64,66]. For instance, Guo et al. [119] attributed the excellent catalytic performance of $Ni/MgAl_2O_4$ to the application of magnesium aluminate spinel ($MgAl_2O_4$) which is characterized by high sintering-resistance

ability and low acidity. The strong interaction between NiO and co-precipitated $MgAl_2O_4$ produced highly dispersed active Ni species and increased the catalyst's resistance to heat and coking. Moreover, while comparing the two catalysts Ni/SiO_2 and Ni/Al_2O_3, Xu et al. [120] concluded that the weak metal-support interaction in Ni/SiO_2 promoted the formation of large Ni particles which lead to the fast carbonaceous deposition and ultimately deactivation.

Effect of reducibility

Prior to any CO_2 methanation or CO_2 reforming of methane reaction, the catalyst is first activated by means of a reduction of its metal oxides. The reduced oxides are considered the active phases of the catalyst. The design of a catalyst with high reducibility is a must in order to obtain the highest amount of available active sites.

While comparing the activity of a 10 wt% Ni supported on ceria and ceria-zirconia to a sample supported on alumina in the CO_2 methanation reaction, an excellent activity was observed over the ceria-zirconia based samples. This was attributed to an improved reducibility both in terms of NiO reduction temperature and of hydrogen uptake [11]. Mg, Ca, Sr and Ba were investigated as promoters to a Ni/SiO_2 catalyst in the CO_2 methanation reaction under a gas hourly space velocity of 15,000 mL/g.h, an H_2/CO_2 ratio of 4 and a pressure of 1 atm. Promoting with Sr and Ba ameliorated CO_2 conversions at 350 °C by 5.8 % and 2.9 % respectively. The addition of Ca had a negligible effect on both the CO_2 conversion and CH_4 selectivity. Meanwhile, promoting with Mg decreased CO_2 conversion by 29.8 % as a result of the declined reducibility of Ni species in the presence of Mg as a promoter [121].

In the CO_2 reforming of methane reaction**,** the incorporation of Co to a Ni/mesoporous alumina catalyst significantly enhanced the activity and stability of the monometallic catalysts as a result of the improvements in the reducibility of Co in the presence of Ni. Co was completely reduced in the bi-metallic catalyst whereas the formation of cobalt aluminate that could not be reduced up to 750 °C in the catalyst containing only 5 wt% Co hindered the catalyst's activity [122]. Moreover, a support with suitable reducibility favors high activity and low deactivation. Among the following catalysts evaluated in the DRM reaction: Pt/Al_2O_3, $Pt/CePr/Al_2O_3$, $Pt/CeNb/Al_2O_3$, and $Pt/CeZr/Al_2O_3$, the Pt/Al_2O_3 catalyst demonstrated the strongest deactivation and the highest Pt sintering which was attributed to the absence of support reducibility. However, the sample doped with Pr exhibited the highest reducibility of ceria (23 %) and thus the highest activity and stability [123].

Effect of basicity

There is no controversy whatsoever regarding the vital role the basicity of a catalyst plays in CO_2 methanation [124]. An improved basicity ameliorates the catalysts surface property by increasing the adsorption and chemisorption capacity of the acidic CO_2 molecule which results in superior catalytic performance in methanation of CO_2 [44,125]. CO_2 methanation mechanism was compared over a 7 wt% $Ni/Ce_{0.5}Zr_{0.5}O_2$ and 7 wt% $Ni/\gamma\text{-}Al_2O_3$ catalysts [126]. The authors concluded that the only difference of mechanism relied in the reactive basic sites: alumina showed the presence of medium and strong basic sites; meanwhile, $Ni/Ce_{0.5}Zr_{0.5}O_2$ exhibited the presence of intermediate strength basic sites which promoted the formation of monodentate formate species that are easily hydrogenated and thus lead to a superior catalytic activity.

It has been also reported that basic catalysts enhance the adsorption of CO_2 in the CO_2 reforming of methane reaction by providing more surface oxygen species on the catalyst's surface and enabling the gasification of intermediate carbonaceous species [127,128]. In addition, the ability of the catalyst to chemisorb oxidants such as H_2O and CO_2 which facilitates the inhibition of coking is improved by the addition of basic oxides to the support [129]. Dahdah et al [68] reported that the addition of La to a series of hydrotalcite $Ni_xMg_{6\_x}Al_2$ (x= 2, 4 or 6) catalysts improved the catalytic activity by creating more basic sites that favor CO_2 adsorption and participate in the removal of carbonaceous deposits. Similar conclusions were given by Liu et al. [130] and Yu et al.[131].

Effect of GHSV

Extensive investigations have been made to evaluate the effects of changing the process parameters on the catalyst performance for both studied reactions. A gas hourly space velocity (GHSV) is defined by the ratio of gas flow rate to the volume of the catalytic bed:

$$\text{GHSV } (h^{-1}) = \frac{exhaust\ flow\ (mL/h)}{catalyst\ volume\ (mL)}$$

Generally, a low GHSV and high catalyst amount can maximize the amount of external and internal mass transfer limitations, and oppositely a high GHSV and low catalyst amount is expected to lead to lower mass transfer limitations [18,72]. It is evidenced that neither too low nor too high GHSV values are beneficial to the catalytic activity: a value higher than the optimal GHSV yields shorter contact time for the gaseous reactants and the catalyst, and thus a decline in activity is observed [132]. Researchers are constantly attempting to design a catalyst that not only resists carbon formation but can reveal high catalytic activity even

under severe conditions of activation and reaction, i.e. high GHSVs (low masses and high flow rates).

Recently, Kosaka et al. [133] reported a high-performance Ni-based structured CO_2 methanation catalyst with different Ni contents that can be used without causing a pressure drop in the reactor. The effect of varying the GHSV was evaluated at the level of the obtained CH_4 yields which decreased slightly with increasing GHSV. A high CH_4 yield of 92.6 % and 91.8 % was observed at 300 °C with a GHSV of 13,100 h^{-1} and 17,500 h^{-1} respectively. Similarly, Ye et al. [134] succeeded in synthesizing a Ni/CeO_2 catalyst that is highly stable for the CO_2 methanation under low temperature and high GHSV. The latter can convert 80.5 % of CO_2 and achieve 95.8 % CH_4 selectivity at 250 °C under a GHSV of 40,000 h^{-1} for 106 h. A slight decrease in CO_2 conversion and CH_4 selectivity to 79.3 % and 93.3 % were observed in the stability test at 290 ^oC for 100 h upon doubling the GHSV to 80,000 mL/g.h.

While comparing the short and long term stability in the CO_2 reforming of methane of a Ni catalyst supported on $LaAlO_3$ perovskite and a commercial α-Al_2O_3 support, Figueredo et al. [135] proved that their synthesized Ni/$LaAlO_3$ catalyst showed 7.8 % and 11.5 % higher CH_4 and CO_2 conversions respectively than Ni/α-Al_2O_3 under a GHSV of 18 L/g.h for 10 h on stream. Increasing the GHSV to 72 L/g.h and time on stream to 20 h decreased the CH_4 conversion and H_2 yield for both catalysts.

1.6. Choice of the Catalysts

In an attempt to create an ideal catalyst, one must highlight the crucial importance of the main components of a catalyst: the support and the active phase. In this section, the choice of the catalysts for both reactions is explained. Selection of a suitable active phase is very important not only from the catalytic point of view but also from the economic standpoint.

The supports below were chosen for comparison in this study:

Alumina: the cheapest, most widely used support in the CO_2 methanation reaction and the CO_2 reforming of methane

KIT-6, **SBA-15** and **SBA-16**: novel catalytic materials that are recently receiving attention in various catalytic applications because of their mesoporous structure and high surface area and large pore volumes

CeO_2: appears particularly interesting for its basicity and redox properties

Among the noble metals investigated for both reactions, **Ru** seems to reveal high catalytic performances, is widely applied as an active site in various chemical reactions, and is cheaper than other noble metals. In addition, Ru is particularly known for its high selectivity towards methane in the CO_2 methanation reaction. Ru is also the very first metal to show activity and durability for the CO_2 reforming of methane with kinetic behavior comparable to that of Ni. Hence, Ru was chosen as the first active phase in this study. A small weight percentage of 1 % was chosen as the metal loading because of the high cost of Ru.

On the other hand, **Ni** was also chosen as an active phase because it seems to be the most active and selective among the non-noble metals, and is cheap, highly available and widely used for commercial implementation of methanation and reforming processes. A high loading is required to achieve high activity. In this study, an active phase of 15 wt% Ni was adopted.

However, a specific drawback that hinders Ni-based catalysts is their high rate of deactivation, which is due to the tendency of carbon deposition as well as Ni sintering at higher metal loadings. Bi-metallic systems have been studied in order to improve the activity and stability of Ni-based catalysts. Hence, Ni was promoted with Ru to form a third bi-metallic active phase Ni (15 wt%) – Ru (1 wt%). Tables 1.4 and 1.5 present a summary of the conditions and performances of some previously reported Ru, Ni, and Ni-Ru based catalysts used for the CO_2 methanation reaction and CO_2 reforming of methane respectively.

Catalysts	Metal Loading	Reduction Temperature	Operating Conditions	CO_2 Conversion (at 350 ^oC)	Reference
Ni/Al_2O_3	25 % Ni	600 ^oC	m= 200 mg P= 1 atm H_2/CO_2= 3.5 GHSV= 9,000 mL/gh	70 %	**[44]**
Ru/TiO_2	2.5 % Ru	500 ^oC	m= 200 mg P= 1 atm H_2/CO_2= 4 Total flow= 20 mL/min	90 %	**[136]**
Ni/SiO_2	8.47 % Ni	600 ^oC	m= 200 mg P= 2 bar H_2/CO_2= 4 Total flow= 100 mL/min WHSV= 4.6 L/gh	70 %	**[28]**
Ru/CeO_2 **Ru/SiO_2-CeO_2** **Ru/TiO_2-CeO_2**	3 % Ru	120 ^oC	m= 100 mg P= 1 atm H_2/CO_2= 4 Total flow= 20 mL/min	80 %	**[137]**
Ni/CeO_2-ZrO_2 (sol-gel)	5 % Ni	400 ^oC	m= 150 mg P= 1 atm H_2/CO_2= 4 Total flow= 55 mL/min Space Velocity= 43000 h^{-1}	80 %	**[138]**
Ni-Ru/Al_2O_3	20 % Ni 0.5 % Ru	600 ^oC	m= 150 mg P= 1 atm H_2/CO_2 = 4 Total flow= 140 mL/min GHSV= 56,000 mL/gh	82 %	**[43]**
Ni/CeO_2	20 % Ni	500 ^oC	m= 300 mg P= 1 atm H_2/CO_2= 4 GHSV= 10,000 mL/gh	88 %	**[134]**
Ni/MSN	5 % Ni	500 ^oC	m= 200 mg P= 1 atm H_2/CO_2= 4 GHSV= 50,000 mL/gh	85.4 %	**[139]**
Ni/Y_2O_3	10 % Ni	350 ^oC	m= 500 mg P= 1 atm H_2/CO_2= 4 Space Velocity= 14,400 h^{-1}	75 %	**[140]**
Ni-Ru/γ-Al_2O_3	10 % Ni 1 % Ru	450 ^oC	m= 100 mg P= 1 atm H_2/CO_2= 4 Total flow= 90 mL/min GHSV= 9,000 h^{-1}	70 %	**[141]**

Table 1.4: Conditions and performances of some previously reported Ni, Ru, and Ni-Ru based catalysts used for the CO_2 methanation reaction

Catalysts	Metal Loading	Reduction Temperature	Operating Conditions	CO_2 Conversion (at 800 ^oC)	Reference
Ni/γ-Al_2O_3	15 % Ni	400 ^oC	m= 200 mg CH_4/CO_2= 0.6 GHSV= 30 L/gh	81.5 %	**[95]**
Ru/ZrO_2-SiO_2	0.13 % Ru	600 ^oC	CH_4/CO_2= 1 GHSV= 20,000 mL/gh Total flow= 45 mL/min	98.8 %	**[97]**
Ni/ZSM5	7 % Ni	650 ^oC	m= 100mg CH_4/CO_2= 1 GHSV= 60,000 mL/gh Total flow= 100 mL/min	72 %	**[142]**
Ru/$LaAlO_3$	2 % Ru	400 ^oC	m= 100 mg CH_4/CO_2 = 1 GHSV= 48,000 h^{-1} Total flow= 100 mL/min	100 %	**[96]**
Ni-Ru/Al_2O_3 (sonication assisted wet impregnation)	10 % Ni 0.5 % Ru	800 ^oC	m= 50 mg CH_4/CO_2 = 1 GHSV= 180,000 mL/hg Total flow= 150 mL/min	48 %	**[143]**
Ni/Al_2O_3	6 % Ni	700 ^oC	m= 100 mg CH_4/CO_2= 1 WHSV= 30 L/gh	98.3 %	**[144]**
Ni/CeO_2	5 % Ni	800 ^oC	m= 50 mg CH_4/CO_2 = 1 GHSV= 60,000 cm^3/gh Total flow= 50 mL/min	74 %	**[145]**
Ru/$MgAlO_x$	2 % Ru	800 ^oC	m= 100 mg CH_4/CO_2 = 1 GHSV= 92,727 cm^3/gh Total flow= 85 mL/min	98 %	**[146]**
Ru-Ni-MgO	10 % Ru 6 % Ni	800 ^oC	m= 35 mg CH_4/CO_2 = 1 GHSV= 86,000 mL/gh Total flow= 50 mL/min	95 %	**[147]**

Table 1.5: Conditions and performances of some previously reported Ni, Ru, and Ni-Ru based catalysts used for the CO_2 reforming of methane

1.7. Conclusion

Over the past decade, there has been an increase in energy consumption, mainly due to a rapid growth in the human population. This causes the increase in the dependence on fossil fuels to meet the energy demands. However, fossil fuel combustion results in GHGs emissions which once released into the atmosphere may cause atmospheric air pollution. As a result, extensive researches aiming at the production of clean, renewable, and sustainable energy sources are encouraged. This may be achieved by the valorization of the most important greenhouse gas CO_2 into synthetic natural gas and synthesis gas through the CO_2 methanation and the CO_2 reforming of methane reactions. Both reactions necessitate appropriate catalysts that induce sufficient conversions and resist deactivation through carbon formation and sintering. The key to develop a more resistant catalyst is using suitable metals, adding basic compounds, ameliorating active phase reducibility, as well as the combination of several metals and supports. All these factors were taken into consideration while choosing the catalysts to be evaluated in our studied reactions.

CHAPTER 2

SYNTHESIS AND CHARACTERIZATION

In this chapter, the preparation and characterization results of Ni and/or Ru based catalysts will be detailed. First, CeO_2 supported catalysts will be evaluated followed by Al_2O_3 supported catalysts and KIT-6 supported catalysts. For every support family, the crystal structure will be studied using X-Ray diffraction analysis (XRD), the porous structure using N_2 adsorption/desorption, and the redox and basic properties using H_2- temperature programmed reduction (H_2-TPR) and CO_2-temperature programmed desorption (CO_2-TPD) respectively.

2.1. CeO_2 Supported Catalysts

2.1.1. Catalysts Preparation

Synthesis of the CeO_2 support

The CeO_2 support was synthesized according to a standard procedure described by Aouad et al. [148] where cerium hydroxide $Ce(OH)_4$ was precipitated from a 0.25 M cerium (III) nitrate hexahydrated solution $Ce(NO_3)_3 \cdot 6H_2O$ and a 1 M sodium hydroxide alkali solution NaOH. The resulting hydroxide $Ce(OH)_4$ was filtered, washed and dried overnight in a drying oven at 100 °C. The dried support was then calcined in flowing air at 550 ^oC for 4 h at a heating rate of 1 ^oC/min.

Synthesis of the CeO_2 supported catalysts

The wet impregnation technique was used to synthesize the catalysts. 0.5 g of the CeO_2 support was impregnated with 25 mL solutions of the metal precursors ($Ni(NO_3)_2.6H_2O$ (P> 97 %)) and/or ($Ru(NO)(NO_3)_3$ (1.5 wt% Ru). The mixture was stirred for 2 h at room temperature. Water was removed using a rotary evaporator and the slurry was then dried at 100 ^oC overnight before thermal stabilization by calcination for 4 h at 550 ^oC with a heating rate of 1 ^oC/min. The nominal percentages of nickel and ruthenium in the catalysts were 15 wt% and/or 1 wt% respectively. The obtained catalysts are 1Ru/CeO_2, 15Ni/CeO_2 and 15Ni1Ru/CeO_2.

2.1.2. Catalysts Characterization

2.1.2.1. X-ray diffraction analyses (XRD)

Figure 2.1 shows the wide angle XRD patterns of the calcined CeO_2 supported catalysts.

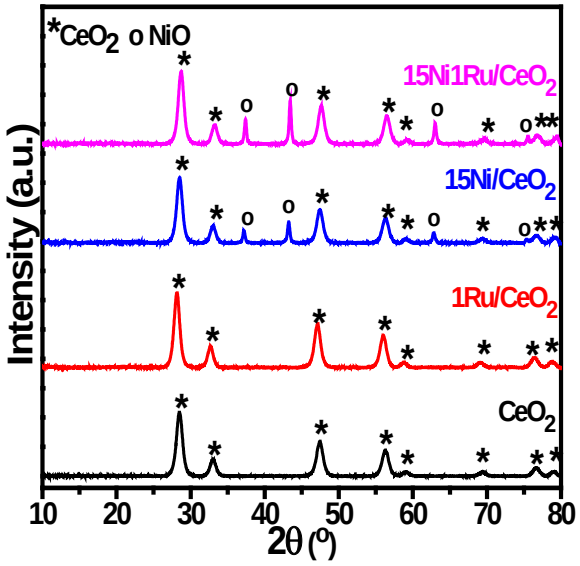

Figure 2.1: XRD patterns of CeO_2 supported catalysts after calcination at 550 °C

The XRD patterns of all calcined CeO_2 supported catalysts present diffraction lines at 2θ= 28°, 33°, 47°, 56°, 59°, 69°, 76° and 79° typical to a ceria fluorite structure (JCPDS 34-0394) [149]**.** The calcined $1Ru/CeO_2$ and $15Ni1Ru/CeO_2$ diffraction patterns didn't present any RuO_2 diffraction peak. This is explained by the good dispersion of ruthenium when CeO_2 is used as a support and to the low percentage of Ru. The diffraction patterns of calcined $15Ni/CeO_2$ and $15Ni1Ru/CeO_2$ catalysts present peaks at 2θ= 37°, 43.2°, 62.8°, and 75.3°. These latter are characteristic of NiO phase (JCPDS 44-1159). The calculated NiO crystallite sizes for $15Ni/CeO_2$ and $15Ni1Ru/CeO_2$ catalysts are 22.9 nm and 25.7 nm respectively. This indicates that relatively large NiO crystallites were formed over the CeO_2 supported catalysts.

2.1.2.2. N_2 adsorption/desorption analyses

The nitrogen adsorption/desorption isotherms and the pore size distributions of the calcined CeO_2 supported catalysts are shown on figures 2.2 (a) and (b) respectively. The corresponding textural parameters are reported in table 2.1.

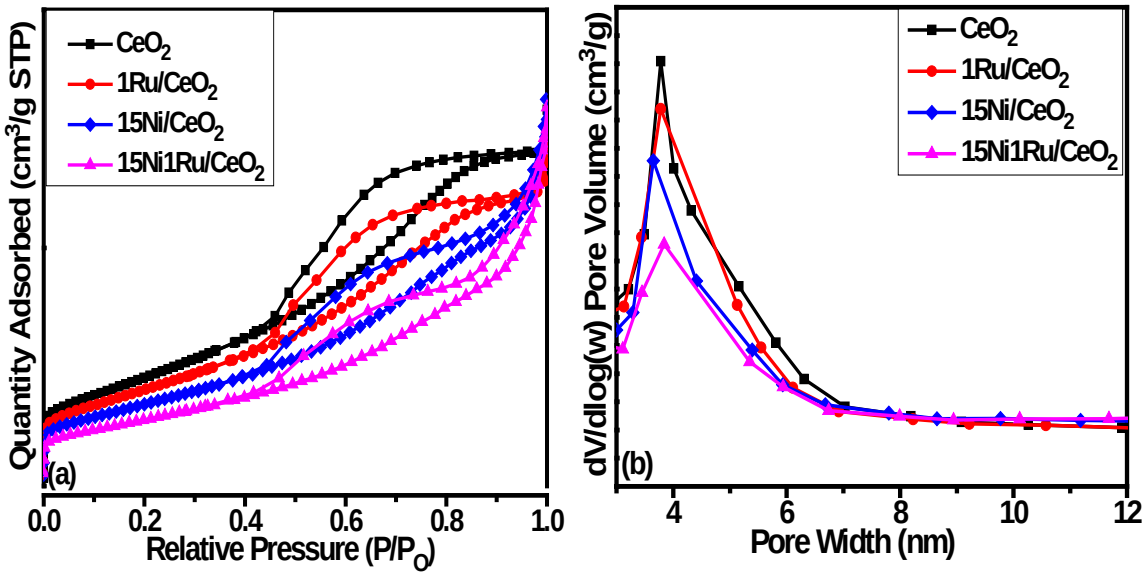

Figure 2.2: (a) N_2 adsorption/desorption isotherms and (b) Pore size distributions of CeO_2 supported catalysts

According to the IUPAC classification of adsorption isotherms, the N_2 adsorption/desorption isotherms of all CeO_2 supported catalysts show a type IVa isotherm indicating the presence of a porous structure. For the CeO_2 support, an H2 hysteresis loop is obtained emphasizing the presence of a complex pore network consisting of pores with ill-defined shape and wide pore size distribution. For $1Ru/CeO_2$ and $15Ni/CeO_2$ catalysts, the obtained hysteresis loops are a mixture of H2 and H4. However, for $15Ni1Ru/CeO_2$, a dominant H4 hysteresis is observed. The pore size distribution shows one type of pores for all CeO_2 supported catalysts. These pores are narrow and range in size between 3 nm and 8 nm. Table 2.1 shows that the support alone has a surface area of 84 m^2/g. All the catalysts exhibited a decrease in surface area after metal impregnation.

Table 2.1: Textural properties of CeO_2 supported catalysts

Catalysts	Specific Surface area (m^2/g)	Pore Volume (cm^3/g)	Pore Diameter (nm)
CeO_2	84	0.13	3.8
1Ru/CeO_2	74	0.12	3.8
15Ni/CeO_2	62	0.13	3.7
15Ni1Ru/CeO_2	50	0.13	3.8

2.1.2.3. H_2-Temperature programmed reduction analyses (H_2-TPR)

Figure 2.3 illustrates the deconvoluted H_2-TPR profiles of the calcined CeO_2 supported catalysts. Table 2.2 lists the corresponding experimental and theoretical hydrogen consumptions.

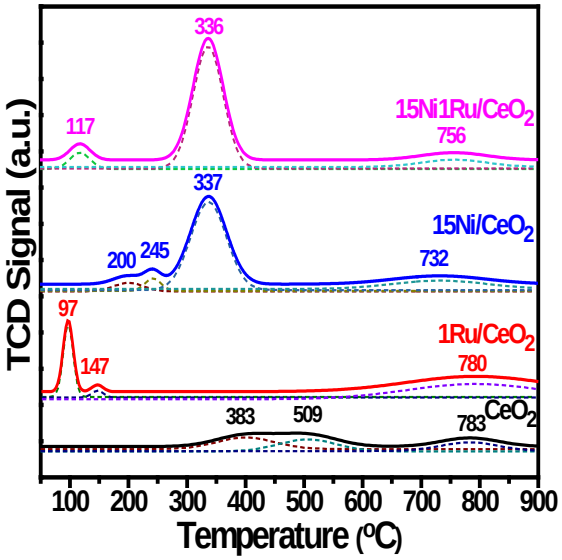

Figure 2.3: H_2-TPR profiles of CeO_2 supported catalysts

The TPR profile of CeO_2 support exhibits three reduction peaks: the first two peaks which are in the range of 300 ^oC – 600 ^oC and correspond to a hydrogen consumption of 1268 µmol/g (table 2.2) are mainly attributed to easily reducible surface ceria species. The third higher temperature peak (T> 700 ^oC) assigned to the reduction of ceria species in the bulk corresponds to a consumption of 466 µmol/g (table 2.2) [150,151].

The TPR profile of 1Ru/CeO_2 catalyst shows two low temperature reduction peaks at 97 ^oC and 147 ^oC. The total H_2 consumption obtained for these peaks (438 µmol/g) is greater than the theoretical H_2 consumption corresponding to the total reduction of RuO_2 to Ru (200 µmol/g) (table 2.2). It has been demonstrated that during calcination, easily reducible

oxygenated bonds (Ru-O-Ce) are created between ruthenium and surface cerium [148]. Thus, the reduction of surface ceria is facilitated by the presence of ruthenium metal; this phenomenon is known as a hydrogen "spillover" effect whereby a part of H_2 molecules dissociated on the already reduced Ru migrates to nearby metal oxides under H_2-rich condition [152]. Therefore, these two peaks correspond to the reduction of RuO_2 and a part of surface ceria. The $1Ru/CeO_2$ catalyst also exhibits a shoulder-like wide reduction peak at 780 ^oC similar to that of CeO_2 which is ascribed to the reduction of Ce^{4+} located in the bulk into Ce^{3+}.

The TPR profile of the $15Ni/CeO_2$ catalyst shows three reduction peaks in the 100 °C – 450 °C temperature range and one large peak at 732 ^oC. This indicates the formation of different metal-support interactions and different types of Ni oxide species upon calcination. According to table 2.2, the total experimental NiO hydrogen consumption for the $15Ni/CeO_2$ catalyst (summation of peaks I, II, and III) is 3659 μmol/g which is greater than the theoretical hydrogen consumption corresponding to the reduction of NiO into Ni (2871 μmol/g)**.** This indicates the simultaneous reduction of some CeO_2 along with NiO species at lower temperatures. According to the literature, large agglomerated NiO particles are reduced at high temperatures [153–155]. The reduction of the "outer shell" of these particles hinders H_2 diffusion to core nickel oxide species which will become more difficult to reduce. The first two peaks observed around 200 °C and 242 °C can be hence attributed to the reduction of easily reducible small NiO particles [154,155]. The third peak centered at 337 °C is attributed to the reduction of larger NiO particles or NiO particles that are in strong interaction with the CeO_2 support [134,156]. The peak at 732 ^oC is attributed to the reduction of bulk ceria.

The $15Ni1Ru/CeO_2$ catalyst shows a first reduction peak at 117 ^oC. The H_2 consumption of this peak (342 μmol/g) is greater than the theoretical H_2 consumption corresponding to RuO_2 alone. Several authors [157–160] report that ruthenium facilitates the reduction of nickel oxides. Thus, this peak is assigned to the reduction of small size RuO_2 and NiO species. The second peak at 336 ^oC is attributed to the reduction of nickel oxide and surface ceria. The third peak centered at 756 ^oC is assigned to the reduction of bulk ceria.

Table 2.2: Experimental and theoretical H_2 consumptions of CeO_2 supported catalysts

Catalyst	H_2 consumption [µmol H_2/g catalyst]								
	Experimental Consumption					Theoretical Consumption			
	I	II	III	IV	Total	NiO/Ni	RuO_2/Ru	Ce^{4+}/Ce^{3+}	Total
CeO_2	627	641	-	466	**1734**	-	-	2905	**2905**
1Ru/CeO_2	396	42	-	946	**1384**	-	200	2866	**3066**
15Ni/CeO_2	256	203	3200	779	**4438**	2871	-	2372	**5243**
15Ni1Ru/CeO_2	342	3856	-	495	**4693**	2871	200	2353	**5424**

2.1.2.4. CO_2-Temperature programmed desorption analyses (CO_2-TPD)

Figure 2.4 shows the CO_2-TPD profiles of the calcined CeO_2 supported catalysts. Table 2.3 lists the total CO_2 desorbed quantities for each catalyst.

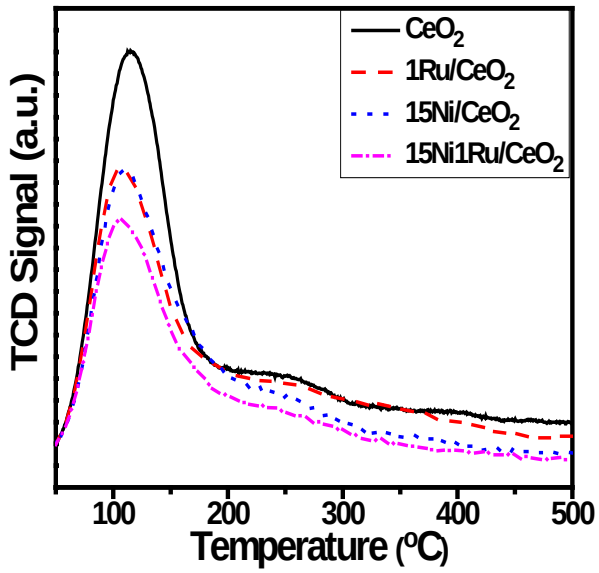

Figure 2.4: CO_2-TPD profiles of CeO_2 supported catalysts

Bian et al. [161] reported that CO_2 desorption peaks that evolve at less than 200 °C are attributed to the interaction of CO_2 with weak basic sites, peaks between 200 °C and 500 °C correspond to medium basic sites, and peaks above 500 °C are attributed to strong basic sites. Accordingly, it is deduced from the graph that weak basic sites are prevalent in all CeO_2 supported catalysts. The total basicity (table 2.3) decreases as follows: CeO_2 > 15Ni/CeO_2 > 1Ru/CeO_2 > 15Ni1Ru/CeO_2.

Table 2.3: CO_2 desorbed quantities of CeO_2 supported catalysts

Catalyst	CO_2 quantity [µmol CO_2/g catalyst]
CeO_2	293
1Ru/CeO_2	224
15Ni/CeO_2	235
15Ni1Ru/CeO_2	192

2.2. Al_2O_3 Supported Catalysts

2.2.1. Catalysts Preparation

Synthesis of the Al_2O_3 support

To prepare mesoporous Al_2O_3, aluminum isopropoxide ($Al(O\text{-}i\text{-}Pr)_3$, 98 %) was dissolved in a mixture of ethanol and isopropanol solution by heating at 50 °C for 1 h. In another beaker, non-ionic F127 copolymer $(EO)_{106}(PO)_{70}(EO)_{106}$) was dissolved in another ethanol and isopropanol solution at 50 °C for half an hour. Then, water was added dropwise to the beaker containing the F127 mixture in order to hydrolyze the aluminum alkoxide followed by the gradual addition of the dissolved aluminum isopropoxide solution. The resultant white suspension was stirred at 50 °C for 4 h and subsequently aged at room temperature for 24 h. The gel type solution was then kept for hydrothermal treatment at 80 °C for 24 h followed by 150 °C for 24 h. The resulting material was washed with anhydrous ethanol. Finally, the powder was filtered, dried, and calcined in flowing air at 550 ^oC for 4 h at a heating rate of 1 ^oC/min to remove the organic template [162].

Synthesis of the Al_2O_3 supported catalysts

The wet impregnation technique previously described (part 2.1.1.) was used to synthesize the following catalysts: $1Ru/Al_2O_3$, $15Ni/Al_2O_3$, and $15Ni1Ru/Al_2O_3$

2.2.2. Catalysts Characterization

2.2.2.1. X-ray diffraction analyses (XRD)

Figure 2.5 shows the wide angle XRD patterns of the calcined Al_2O_3 supported catalysts. Table 2.4 lists the corresponding crystallite sizes.

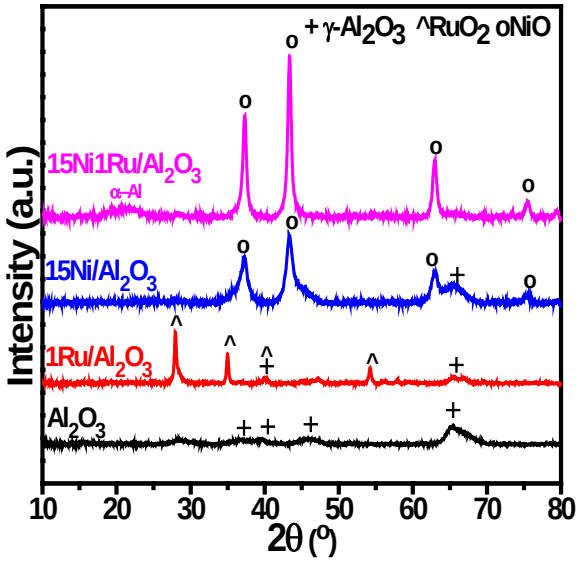

Figure 2.5: XRD patterns of Al_2O_3 supported catalysts after calcination at 550 °C

For Al_2O_3 support, the peaks at 2θ= 37°, 39°, 46°, and 66° represent the cubic structures of γ-Al_2O_3 phase (JCPDS 50-0741). The relatively broad peaks reveal that our synthesized Al_2O_3 is amorphous and that the platelets forming the pores are highly disordered [1,162]. RuO_2 diffraction peaks at 28°, 35°, 40° and 54° (JCPDS 40-1290) are observed in the calcined 1Ru/Al_2O_3 catalyst pattern. This indicates the presence of large RuO_2 crystallites formed by the agglomeration of several RuO_2 nanocrystals. RuO_2 peaks are absent in the XRD pattern of the bi-metallic catalyst which indicates a better dispersion of RuO_2 in this solid. For calcined 15Ni/Al_2O_3 and 15Ni1Ru/Al_2O_3 catalysts, the diffraction lines at 2θ= 37°, 43.2°, 62.8°, and 75.3° are attributed to the NiO phase. An additional α-Al_2O_3 broad peak (JCPDS 50-1496) is present at 2θ= 21.5° for 15Ni1Ru/Al_2O_3 catalyst. Table 2.4 shows that the crystallite size of RuO_2 in the 1Ru/Al_2O_3 catalyst (25.2 nm) is remarkably higher than NiO crystallite sizes in the 15Ni/Al_2O_3 (8 nm) and 15Ni1Ru/Al_2O_3 (15.4 nm) catalysts. This trend also means that larger NiO crystallite sizes were formed in the bi-metallic catalyst compared to the mono-metallic catalyst. Therefore, it seems that the combination of Ni and Ru led to the formation of a better crystallized NiO phase.

Table 2.4: Crystallite sizes of Al_2O_3 supported catalysts

Catalysts	Crystallite Sizes (nm)	
	RuO_2	NiO
Al_2O_3	-	-
$1Ru/Al_2O_3$	25.2	-
$15Ni/Al_2O_3$	-	8
$15Ni1Ru/Al_2O_3$	-	15.4

2.2.2.2. N_2 adsorption/desorption analyses

The nitrogen adsorption/desorption isotherms and the pore size distributions of the calcined Al_2O_3 supported catalysts are shown on figures 2.6 (a) and (b) respectively. The corresponding textural parameters are reported in table 2.5.

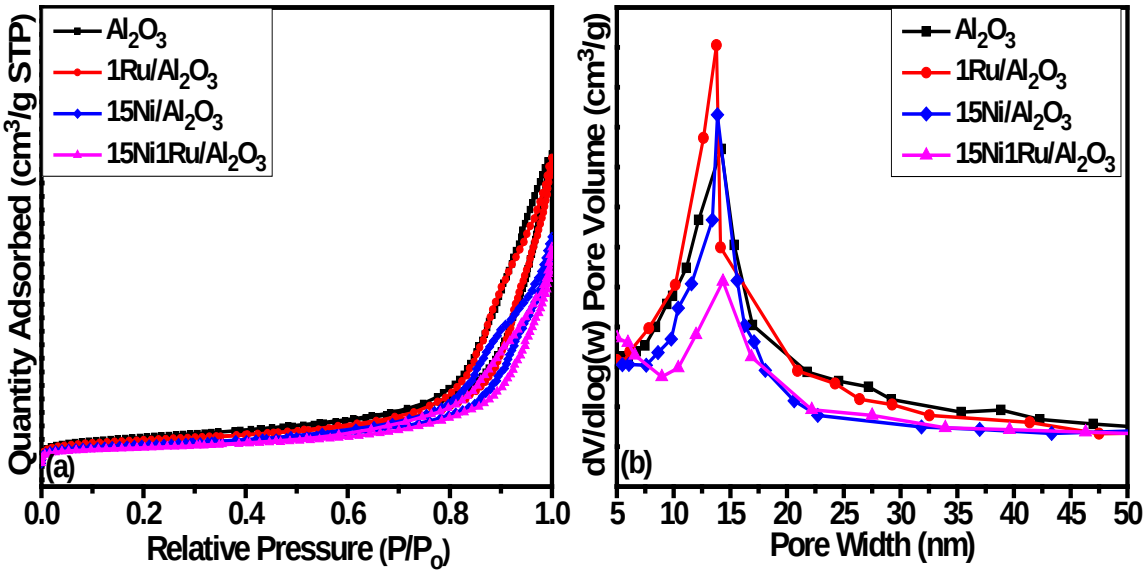

Figure 2.6: (a) N_2 adsorption/desorption isotherms and (b) Pore size distributions of Al_2O_3 supported catalysts

The N_2 adsorption/desorption isotherms of all Al_2O_3 supported catalysts reveal a type IVa isotherm with H1 & H3 composites implying the slit-shape pores or plate-like particles [163]. The shape of the isotherms slightly changes upon metal impregnation which implies that the synthesized mesoporous alumina material is resistant to structural alteration. The synthesized mesoporous alumina and corresponding catalysts exhibited a mono-modal pore size distribution ranging between ~7.5 nm and ~25 nm. The broad range of pore distribution is a result of the disordered structure of mesoporous alumina [162] in agreement with the XRD results. The surface area obtained for Al_2O_3 is 380 m^2/g (table 2.5). After impregnation with 1

wt% Ru, the specific surface area of the support decreased by 13 %. Impregnating with 15 wt% Ni and 15 wt% Ni – 1 wt% Ru deceased surface areas by 28 % and 38 % respectively. Moreover, during impregnation, the pore volume of mesoporous alumina drops from 1.86 cm^3/g to 1.83 cm^3/g for $1Ru/Al_2O_3$, to 1.35 cm^3/g for $15Ni/Al_2O_3$ catalyst and to 1.3 cm^3/g for $15Ni1Ru/Al_2O_3$ catalyst. This suggests that the pore structures of the supports were partially filled by the addition of ruthenium and/or nickel.

Table 2.5: Textural properties of Al_2O_3 supported catalysts

Catalysts	Specific Surface area (m^2/g)	Pore Volume (cm^3/g)	Pore Diameter (nm)
Al_2O_3	380	1.86	14.2
$1Ru/Al_2O_3$	331	1.83	13.8
$15Ni/Al_2O_3$	273	1.35	13.9
$15Ni1Ru/Al_2O_3$	235	1.3	14.4

2.2.2.3. H_2- Temperature programmed reduction analyses (H_2-TPR)

Figure 2.7 illustrates the deconvoluted H_2-TPR profiles of the calcined Al_2O_3 supported catalysts and table 2.6 lists the corresponding total experimental and theoretical hydrogen consumptions.

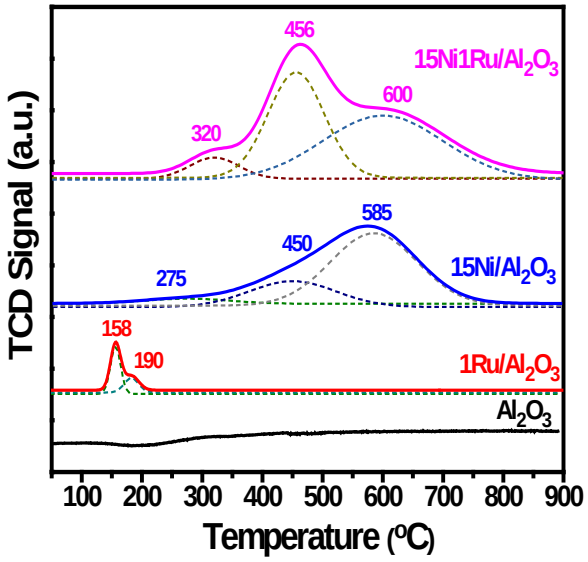

Figure 2.7: H_2-TPR profiles of Al_2O_3 supported catalysts

The TPR profile of the support alone showed no reduction peaks which means that Al_2O_3 is not reducible in the considered temperature range.

The TPR profile of the $1Ru/Al_2O_3$ catalyst shows two reduction peaks at 158 ^oC and 190 ^oC. The first peak is attributed to the reduction of surface Ru^{4+} species and the second peak is the result of the reduction of Ru^{4+} species from the bulk of RuO_2 clusters in correlation with the reported literature for Ru/Al_2O_3 systems [53,164].

The TPR profile of the $15Ni/Al_2O_3$ catalyst exhibits three reduction peaks at 275 ^oC, 450 ^oC, and 585 ^oC respectively. All three peaks correspond to the reduction of α-type NiO that are weakly bound to the alumina support and in weak chemical interaction with it [1,120,165].

The TPR profile of $15Ni1Ru/Al_2O_3$ catalyst also exhibits three reduction peaks. Moreover, from table 2.6, the hydrogen consumptions of peaks I (320 ^oC, 210 μmol/g) and II (456 ^oC, 1202 μmol/g) are higher than those of $15Ni/Al_2O_3$ (275 ^oC, 128 μmol/g and 450 ^oC, 642 μmol/g respectively). In addition, the hydrogen consumption of peak III centered at 585 ^oC for $15Ni/Al_2O_3$ and at 600 ^oC for $15Ni1Ru/Al_2O_3$ is lower in the $15Ni1Ru/Al_2O_3$ catalyst (table 2.6). This means that more NiO oxide species have been reduced at lower temperature ranges probably due to the enhanced dispersion observed in the bi-metallic catalyst.

Table 2.6: Experimental and theoretical H_2 consumptions of Al_2O_3 supported catalysts

Catalyst	H_2 consumption [μmol H_2/g catalyst]						
	Experimental Consumption				Theoretical Consumption		
	I	II	III	Total	NiO/Ni	RuO_2/Ru	Total
Al_2O_3	-	-	-	-	-	-	-
$1Ru/Al_2O_3$	163	35	-	**198**	-	200	**200**
$15Ni/Al_2O_3$	128	642	1798	**2568**	2871	-	**2871**
$15Ni1Ru/Al_2O_3$	210	1202	1553	**2965**	2871	200	**3071**

2.2.2.4. CO_2- Temperature programmed desorption analyses (CO_2-TPD)

Figure 2.8 shows the CO_2-TPD profiles of calcined Al_2O_3 supported catalysts. Table 2.7 lists the amount of desorbed CO_2 for the different catalysts.

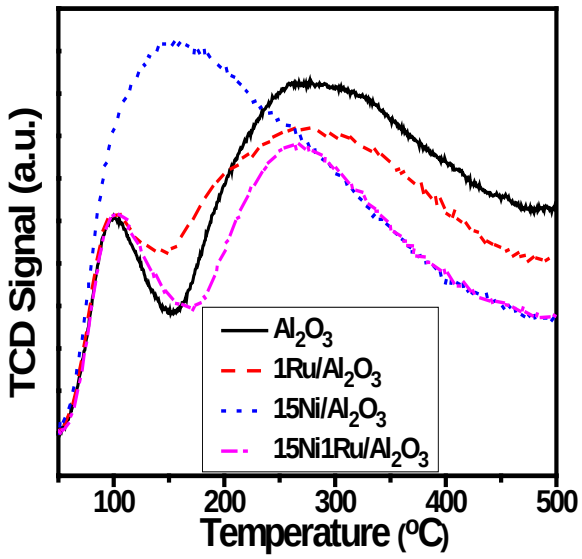

Figure 2.8: CO_2-TPD profiles of Al_2O_3 supported catalysts

The TPD profile of Al_2O_3 support shows two peaks with different temperature regions. This indicates two types of active sites for CO_2 adsorption on the catalyst surface. The low temperature CO_2 desorption peak centered around 100 °C is attributed to weak basic sites and the second broader higher temperature peak with a maximum at about 270 °C is attributed to the presence of medium basic sites [166]. The profiles of $1Ru/Al_2O_3$ and $15Ni1Ru/Al_2O_3$ are more or less similar to that of the support. Meanwhile the profile of the $15Ni/Al_2O_3$ catalyst shows one large peak centered at 156 ^oC assigned to the presence of weak and moderate basic sites. Table 2.7 shows that the latter has the highest basicity (419 µmol/g) amongst all catalysts.

Table 2.7: CO_2 desorbed quantities of Al_2O_3 supported catalysts

Catalyst	CO_2 quantity [µmol CO_2/g catalyst]
Al_2O_3	360
$1Ru/Al_2O_3$	371
$15Ni/Al_2O_3$	419
$15Ni1Ru/Al_2O_3$	286

2.3. KIT-6 Supported Catalysts

2.3.1. Catalysts Preparation

Synthesis of the KIT-6 support

The synthesis of the KIT-6 support was done according to the method reported by Liu et al. [167]. Appropriate amounts of Pluronic P123 ($EO_{20}PO_{70}EO_{20}$, average M_n = 5800, Aldrich), concentrated HCl (37 wt%) and deionized water were stirred for 3 h at 35 °C. Then, n-butyl alcohol (BuOH, 99.5 %) was added to the mixture. After mixing for 1 h, tetraethoxysilane (TEOS, 98 %) was added dropwise. The mixture was kept stirring for 20 h at 35 °C. Subsequently, the mixture was transmitted to Teflon bottles and was left for 24 h at 100 °C (hydrothermal treatment). The P123 template was removed by filtering the hydrothermal products without washing and later on drying at 160 °C for 5 h. The obtained powders were then washed with ethanol and concentrated HCl (37 wt%) at 40 °C for 1 h. Finally, the products were dried at 100 °C for 10 h and were later on calcined in flowing air at 550 ^{o}C for 4 h at a heating rate of 1 ^{o}C/min.

Synthesis of the KIT-6 supported catalysts

The wet impregnation technique previously described (part 2.1.1.) was used to synthesize the following catalysts: 1Ru/KIT-6, 15Ni/KIT-6, and 15Ni1Ru/KIT-6

2.3.2. Catalysts Characterization

2.3.2.1. X-Ray diffraction analyses (XRD)

Figure 2.9 shows the wide angle XRD patterns of calcined KIT-6 supported catalysts. Table 2.8 lists the crystallite sizes of the catalysts.

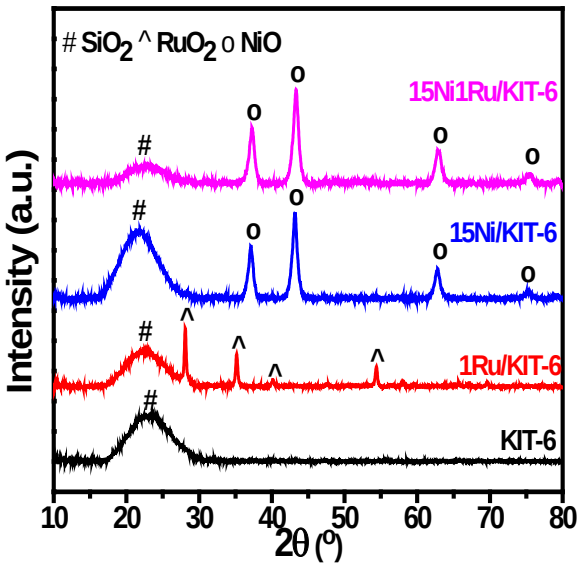

Figure 2.9: XRD patterns of KIT-6 supported catalysts after calcination at 550 ^{o}C

All KIT-6 supported catalysts show a broad scattering peak at 2θ= 23^{o} attributed to amorphous SiO_2 phase [102]. RuO_2 diffraction peaks are observed in the calcined 1Ru/KIT-6 catalyst which indicates the presence of agglomerated RuO_2 species with large crystallite sizes (table 2.8). The absence of any RuO_2 peak in the XRD pattern of the bi-metallic catalyst suggests an ameliorated RuO_2 dispersion in the 15Ni1Ru/KIT-6 catalyst. The characteristic NiO phase is present in the calcined 15Ni/KIT-6 and 15Ni1Ru/KIT-6 catalysts. From table 2.8, the 15Ni1Ru/KIT-6 catalyst possesses smaller NiO crystallite sizes (10.8 nm) compared to the 15Ni/KIT-6 catalyst.

Table 2.8: Crystallite sizes of KIT-6 supported catalysts

Catalysts	Crystallite Sizes (nm)	
	RuO_2	NiO
KIT-6	-	-
1Ru/KIT-6	31.3	-
15Ni/KIT-6	-	12.6
15Ni1Ru/KIT-6	-	10.8

2.3.2.2. N_2 adsorption/desorption analyses

The nitrogen adsorption/desorption isotherms and pore size distributions of the calcined KIT-6 supported catalysts are shown on figures 2.10 (a) and (b). The corresponding textural parameters are reported in table 2.9.

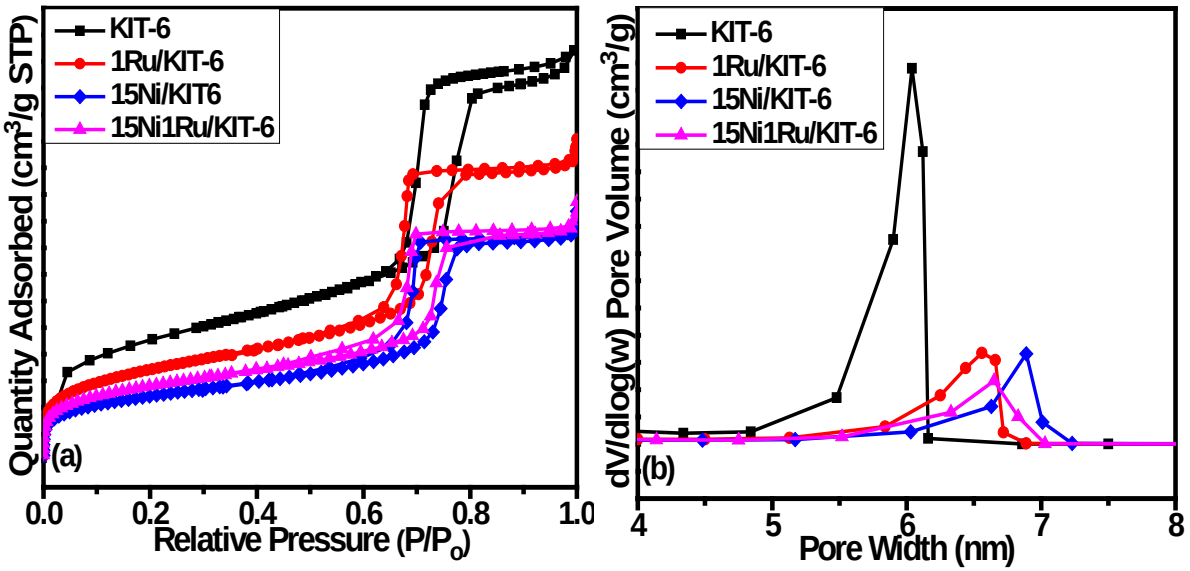

Figure 2.10: (a) N_2 adsorption/desorption isotherms and (b) Pore size distributions of KIT-6 supported catalysts

The N_2 sorption isotherm of all KIT-6 supported catalysts is a type IVa isotherm with H1 hysteresis loop that is characteristic of a homogeneous three-dimensionally ordered mesoporous structure [167,168]**.** Following the impregnation, the hysteresis loop becomes smaller. All catalysts show a mono-modal narrow pore size distribution ranging between 4.5 nm and 6.5 nm for KIT-6, and between 5.5 nm and 7.5 nm for the impregnated catalysts. From table 2.9, the largest surface area (S_{BET} = 630 m^2/g) and pore volume (V_p = 1 cm^3/g) were recorded for the KIT-6 support. The specific surface areas and pore volumes decreased

respectively to 601 m^2/g and 0.89 cm^3/g for 1Ru/KIT-6, 422 m^2/g and 0.72 cm^3/g for 15Ni/KIT-6, and 488 m^2/g and 0.71 cm^3/g for 15Ni1Ru/KIT-6. This is an anticipated consequence of pore filling during the impregnation process. The shift in the pore size distribution to wider diameters (figure 2.10 (b), table 2.9) suggests that the mesopore range became larger following active phase addition. This is probably linked to the evaporation and drying processes that occur during impregnation: as the solvent in the precursor solution evaporates during drying, the active phase solution becomes more concentrated and gets drawn into the smaller pores due to capillary action. When the solution containing the active phase solution and stabilized support is saturated, the precursor starts to crystallize in these smaller pores, effectively blocking them off which causes the average pore sizes of the catalysts to increase after impregnation [169].

Table 2.9: Textural properties of KIT-6 supported catalysts

Catalysts	Specific Surface area (m^2/g)	Pore Volume (cm^3/g)	Pore Diameter (nm)
KIT-6	630	1	6
1Ru/KIT-6	601	0.89	6.5
15Ni/KIT-6	422	0.72	6.9
15Ni1Ru/KIT-6	488	0.71	6.7

2.3.2.3. H_2-Temperature programmed reduction analyses (H_2-TPR)

Figure 2.11 illustrates the deconvoluted H_2-TPR profiles of the calcined KIT-6 supported catalysts. Table 2.10 lists the total experimental and theoretical hydrogen consumptions.

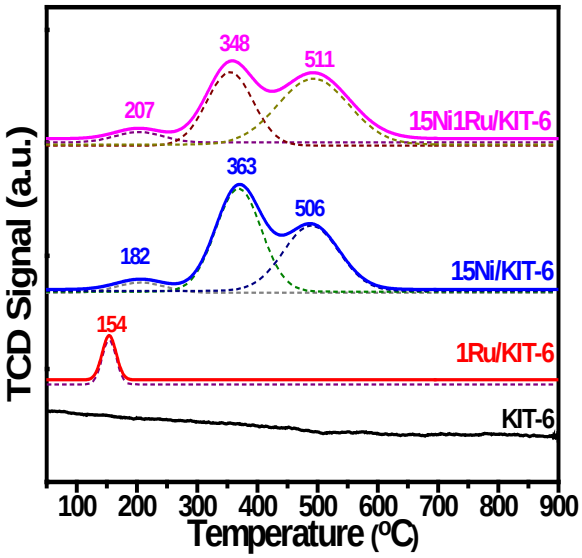

Figure 2.11: H_2-TPR profiles of KIT-6 supported catalysts

KIT-6 support showed no hydrogen consumption in the considered temperature range. The TPR profile of the 1Ru/KIT-6 catalyst exhibits one H_2 consumption peak at 154 °C. This latter is attributed to the reduction of relatively large RuO_2 particles [170].

The TPR profile of the 15Ni/KIT-6 catalyst exhibits three reduction peaks centered at 182 °C, 363 °C, and 506 °C. The first two peaks are derived from the reduction of easily reducible NiO and NiO in weak interaction with the support and the third higher temperature peak corresponds to the reduction of NiO with moderate interaction with the support in agreement with reported literature for Ni/KIT-6 catalysts [102,171].

For 15Ni1Ru/KIT-6 catalyst, the TPR profile also exhibits three reduction peaks. The first peak centered at 207 °C is attributed to the reduction of NiO and RuO_2 species since the H_2 consumption of this peak (435 µmol/g) is higher than that of RuO_2 alone (200 µmol/g) (table 2.10). The reduction peaks at 334 °C and 511 °C are similar to the ones observed on the TPR profile of 15Ni/KIT-6 catalyst.

Table 2.10: Experimental and theoretical H_2 consumptions of KIT-6 supported catalysts

Catalyst	H_2 consumption [µmol H_2/g catalyst]						
	Experimental Consumption				Theoretical Consumption		
	I	II	III	Total	NiO/Ni	RuO_2/Ru	Total
KIT-6	-	-	-	-	-	-	-
1Ru/KIT-6	181	-	-	**181**	-	200	**200**
15Ni/KIT-6	268	1309	1052	**2629**	2871	-	**2871**
15Ni1Ru/KIT-6	435	849	1373	**2657**	2871	200	**3071**

2.3.2.4. CO_2-Temperature programmed desorption analyses (CO_2-TPD)

Figure 2.12 shows the CO_2-TPD profiles of calcined KIT-6 supported catalysts. Table 2.11 lists the total desorbed CO_2 quantities of the catalysts.

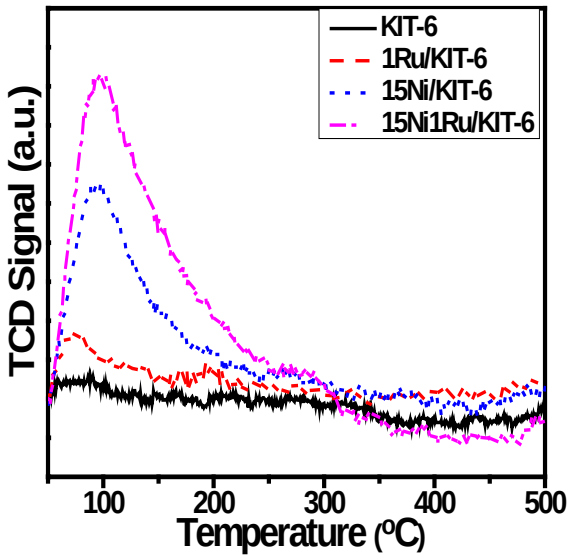

Figure 2.12 CO_2-TPD profiles of KIT-6 supported catalysts

The CO_2-TPD profile of the support KIT-6 presents a low intensity peak at ~74 °C which is attributed to the desorption of weak CO_2 adsorption on the surface of KIT-6 [118]. This latter corresponds to 4 µmol/g of CO_2 (table 2.11). The impregnated catalysts showed a similar type of weak basic sites but with increasing concentration according to the following order: 15Ni1Ru/KIT-6 > 15Ni/KIT-6 > 1Ru/KIT-6 > KIT-6. Furthermore, it is noticed that the basicity of the bi-metallic catalyst is more than additive when compared to the basicity of both monometallic catalysts which emphasizes a synergy between nickel and ruthenium in the 15Ni1Ru/KIT-6 catalyst.

Table 2.11: CO_2 desorbed quantities of KIT-6 supported catalysts

Catalyst	CO_2 quantity [µmol CO_2/g catalyst]
KIT-6	4
1Ru/KIT-6	16
15Ni/KIT-6	64
15Ni1Ru/KIT-6	118

2.4. Main Conclusions

- It is inferred from XRD and TPR results that large RuO_2 crystals are formed in the 1Ru/KIT-6 and 1Ru/Al_2O_3 catalysts. An enhanced dispersion is observed in the 1Ru/CeO_2 and the bi-metallic catalysts.The smaller NiO crystals obtained on Al_2O_3 and KIT-6 compared to the ones obtained on CeO_2 can be attributed to the better dispersion due to higher surface area of the supports [172].
- The presence of Ru increased NiO crystallite sizes in the bi-metallic catalysts supported on CeO_2 and Al_2O_3 only.
- All supports and catalysts revealed typical type IVa adsorption isotherms suggesting their mesoporous structure. A decrease in surface area following impregnation was observed for all the catalysts. However, the pore volumes decreased only in the case of Al_2O_3 and KIT-6 supported catalysts indicating that capillary condensation for these catalysts occurred in the cavity of the pores.
- The reduction of the active phases (RuO_2 and/or NiO) is enhanced when CeO_2 is used as a support.
- NiO reducibility is enhanced in the bi-metallic catalysts due to the beneficial presence of Ru.

CHAPTER 3

CO_2 METHANATION RESULTS

In this chapter, the catalytic activity of CeO_2, Al_2O_3, and KIT-6 supports impregnated with Ru (1 wt%), Ni (15 wt%), and Ni-Ru (15 wt% – 1 wt%) in the CO_2 methanation was first evaluated. The aim of this part was to compare the activity of the active phases and the contribution of the different supports. In the second part of the chapter, KIT-6 was promoted with different CeO_2 percentages. The preparation and characterization of the Ce_XKIT-6 supports and catalysts will be first described followed by an elaboration of the catalytic performances obtained over the promoted catalysts. The best performing catalysts were later on tested for their stability over long periods on stream.

3.1. CO_2 Methanation over CeO_2, Al_2O_3, and KIT-6 Supported Catalysts

The studied CO_2 methanation reaction ($CO_2 + 4H_2 \rightarrow CH_4 + 2H_2O$) is carried out at atmospheric pressure, in a temperature range between 150 ^oC and 350 °C, with an H_2/CO_2 ratio equal to 4 and a GHSV of 40,000 h^{-1}. The thermodynamic curve shows the optimal composition that would be obtained when the thermodynamic equilibrium is reached. Theoretical calculations for the obtained thermodynamic curve are shown in Appendix B. Because of the exothermic nature of the methanation reaction, the activation of the stable CO_2 molecule requires a significant energy input due to its chemical inertness. This energy is provided in thermal form which is why CO_2 conversion increases with temperature. The catalytic activities of the supports alone are not presented because there was no noticeable reactant conversion in the absence of the active phases.

3.1.1. CeO_2 Supported Catalysts

Figure 3.1 shows the CO_2 conversion as a function of temperature in the presence of the $1Ru/CeO_2$, $15Ni/CeO_2$ and $15Ni1Ru/CeO_2$ catalysts.

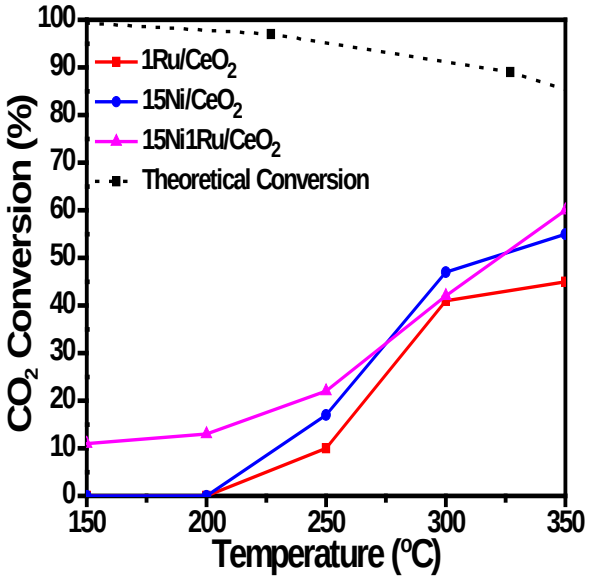

Figure 3.1: Conversion of CO_2 as a function of temperature in the presence of the different CeO_2 supported catalysts

At 350 °C, the CO_2 conversion varies according to the following order: $1Ru/CeO_2$ < $15Ni/CeO_2$ < $15Ni1Ru/CeO_2$ and the selectivity towards methane formation is very high (99 %) and equal for all the catalysts. Despite the low Ru content, the $1Ru/CeO_2$ catalyst was able to catalyze the reaction (45 % at 350 °C). This is explained by the good dispersion and reducibility of RuO_2 in the presence of ceria: the formation of well-dispersed and easily reducible RuO_2 species in this catalyst was validated by XRD (chapter 2, part 2.1.2.1.) and TPR results (chapter 2, part 2.1.2.3.). The $15Ni/CeO_2$ catalyst shows a higher performance (55 % at 350 °C) which is probably attributed to the higher loading and better reducibility of this catalyst. From chapter 2, the TPR profile of $15Ni/CeO_2$ (figure 2.3) shows that almost all NiO species are fully reduced before 350 °C as a result of the promotional effect of Ce on the reduction of Ni. This means that a high amount of active sites was present for reaction. The $15Ni1Ru/CeO_2$ catalyst shows the highest performance (60 % at 350 °C). Unlike the monometallic $15Ni/CeO_2$ and $1Ru/CeO_2$ catalysts, the bi-metallic catalyst showed a conversion value even at 150 °C. This suggests that small amounts of Ru addition can improve the performances of the catalysts. This is in accordance with the findings of Shang et

al. [173] who demonstrated that Ru can be combined with Ni to form a bi-metallic methanation catalyst, which showed much enhanced low-temperature catalytic performances.

3.1.2. Al_2O_3 Supported Catalysts

Figures 3.2 (a) and (b) show the CO_2 conversion as a function of temperature and the CH_4 and CO selectivity at 350 °C in the presence of the $1Ru/Al_2O_3$, $15Ni/Al_2O_3$ and $15Ni1Ru/Al_2O_3$ catalysts.

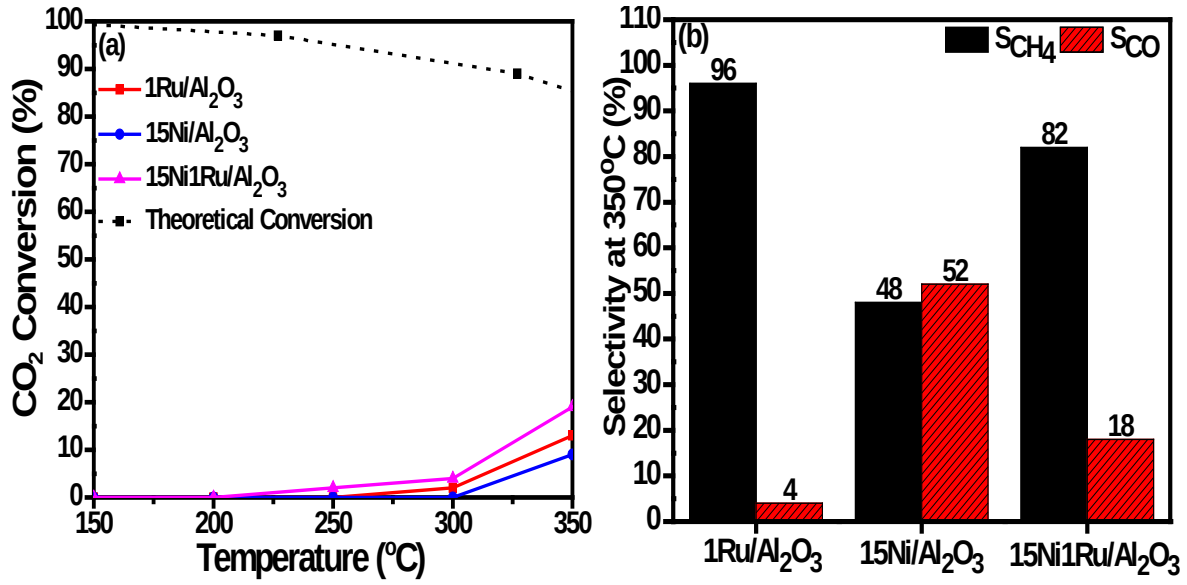

Figure 3.2: (a) Conversion of CO_2 as a function of temperature and (b) CH_4 and CO selectivities at 350 °C in the presence of the different Al_2O_3 supported catalysts

The conversion of CO_2 at 350 °C varies according to the following order: $15Ni/Al_2O_3$ < $1Ru/Al_2O_3$ < $15Ni1Ru/Al_2O_3$. The $15Ni/Al_2O_3$ catalyst shows the lowest methane selectivity at 350 °C (48 %) while the $1Ru/Al_2O_3$ catalyst shows the highest (96 %). Although all catalysts show low conversion values at all temperature ranges, the worst catalytic performance is obtained in the presence of the $15Ni/Al_2O_3$ catalyst (9 % at 350 °C). TPR profiles of alumina based catalysts (chapter 2, figure 2.7) demonstrated that only few NiO species have been reduced before 350 °C whereas the reduction of RuO_2 is complete at lower temperatures (T < 250 °C). This suggests that the $15Ni/Al_2O_3$ catalyst has fewer active sites on its surface. Our results are in accordance with a report given by Quindimil et al. [1] where, regardless of the studied temperature, Ru/Al_2O_3 catalysts with different Ru contents (1 wt% – 5 wt%) produce more methane than Ni/Al_2O_3 catalysts having a Ni nominal content

between 4 and 20 wt%. The authors indicated that all Ru but not all Ni were available to dissociate hydrogen which was also attributed to the reducibility of the active phase and the strength of the metal-support interaction.

3.1.3. KIT-6 Supported Catalysts

Figures 3.3 (a) and (b) show the CO_2 conversion as a function of temperature as well as the CH_4 and CO selectivity at 350 ^oC in the presence of the 1Ru/KIT-6, 15Ni/KIT-6 and 15Ni1Ru/KIT-6 catalysts.

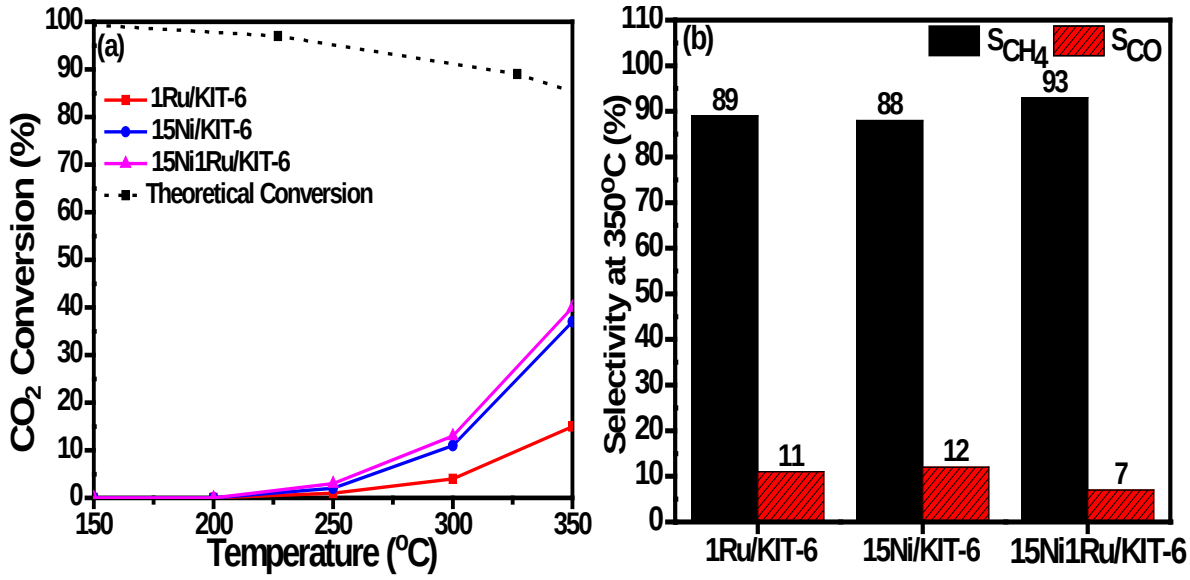

Figure 3.3: (a) Conversion of CO_2 as a function of temperature and (b) CH_4 and CO selectivities at 350 ^oC in the presence of the different KIT-6 supported catalysts

No noticeable conversions were observed in the 150 ^oC – 250 ^oC temperature range. At T > 250 ^oC, 15Ni/KIT-6 and 15Ni1Ru/KIT-6 catalysts showed comparable catalytic activity that was slightly higher for the bi-metallic catalyst whereas the 1Ru/KIT-6 catalyst produced the lowest CO_2 conversions. This low activity obtained for 1Ru/KIT-6 compared to the other catalysts is probably due to the low Ru content. The selectivity of methane at 350 ^oC is highest for the bi-metallic catalyst (93 %). This is probably linked to several reasons: the 15Ni1Ru/KIT-6 catalyst presented enhanced redox properties (chapter 2, part 2.3.2.3), smaller NiO crystallite sizes (chapter 2, table 2.8), as well as the highest basicity among the KIT-6 supported catalysts (chapter 2, table 2.11).

3.1.4. Discussion

- Regardless of the active phase used, the order of activity was: CeO_2 supported catalysts > KIT-6 supported catalysts > Al_2O_3 supported catalysts. CeO_2 supported catalysts were the most active and selective due to the better redox properties of CeO_2 which can promote the activation of CO_2, and therefore improves the CO_2 methanation reaction. This order of activity is in compliance with several studies reported in the literature. For instance, in an attempt to give a thorough understanding on the CO_2 methanation mechanism catalyzed by Ru/CeO_2 and Ru/Al_2O_3, Wang et al. [174] observed that CO_2 methanation follows formate route in the presence of oxygen vacancies (Ru/CeO_2), and CO route over Ru surface in the absence of oxygen vacancies (Ru/Al_2O_3). It was noticed that Ru/CeO_2 catalyzes the formate dissociation at a much lower activation temperature. Our results also prove that at 250 ^oC, under our catalytic conditions, $1Ru/CeO_2$ was able to catalyze the reaction while $1Ru/Al_2O_3$ was not. Moreover, Cárdenas-Arenas et al. [172] attributed one of the mechanistic aspects that were behind the higher methanation activity and 100 % CH_4 selectivity of the Ni/CeO_2 catalyst when comparing it with Ni/Al_2O_3 (8.5 wt% Ni) to the presence of more types of active sites efficient for CO_2 and H_2 dissociation on Ni particles at the NiO-Ceria interface. Another explanation to such difference in activity between Ni/Al_2O_3 and Ni/CeO_2 (10 wt% Ni) catalysts was given by Tada et al. [156] whereby the study acknowledged that the high CO_2 conversion of Ni/CeO_2 is due to the surface coverage by CO_2-derived species on CeO_2 surface and the partial reduction of CeO_2 surface. Few scientific papers [118,175–177] have been published on the performance of KIT-6 supported catalysts in the CO_2 methanation reaction. However, none of the existing literature evaluated the catalytic activity of KIT-6 impregnated with ruthenium and nickel. Zhou et al. [177] compared a 20 wt% Co/KIT-6 with a 20 wt% Co/meso-SiO_2 and found that the high dispersion of the Co species and the large specific surface area (368.9 m^2/g) of the Co/KIT-6 catalyst is the reason behind the latter's excellent CO_2 catalytic hydrogenation activity and methane product selectivity.
- The extent to which NiO species were reduced played an important role in the evaluation of the catalytic performance. Comparing the TPR profiles of the Ni based catalysts $15Ni/CeO_2$, $15Ni/Al_2O_3$, and 15Ni/KIT-6 (chapter 2, figures 2.3, 2.7, and 2.11), it is noticed that NiO species were completely reduced in $15Ni/CeO_2$ before

350 ^oC but not entirely reduced in 15Ni/Al_2O_3 and 15Ni/KIT-6 before 350 ^oC. It is also observed that, at this temperature, more NiO species were reduced in the 15Ni/KIT-6 catalyst compared to 15Ni/Al_2O_3. This explains the availability of active sites for reaction and ultimately the obtained order of activity (15Ni/CeO_2 >15Ni/KIT-6 >15Ni/Al_2O_3). The TPR profiles also showed that the temperature at which NiO species are fully reduced was 750 ^oC for 15Ni/Al_2O_3 and 600 ^oC for 15Ni/KIT-6. Hence, in order to fully understand if the activity is only attributed to the availability of Ni sites, the 15Ni/Al_2O_3 and 15Ni/KIT-6 catalysts were reduced at 750 ^oC and 600 ^oC respectively and used in the methanation test. Figure 3.4 below compares the catalytic activity of 15Ni/Al_2O_3 reduced at T_R = 750 ^oC, 15Ni/KIT-6 reduced at T_R = 600 ^oC, and 15Ni/CeO_2 reduced at T_R = 350 ^oC.

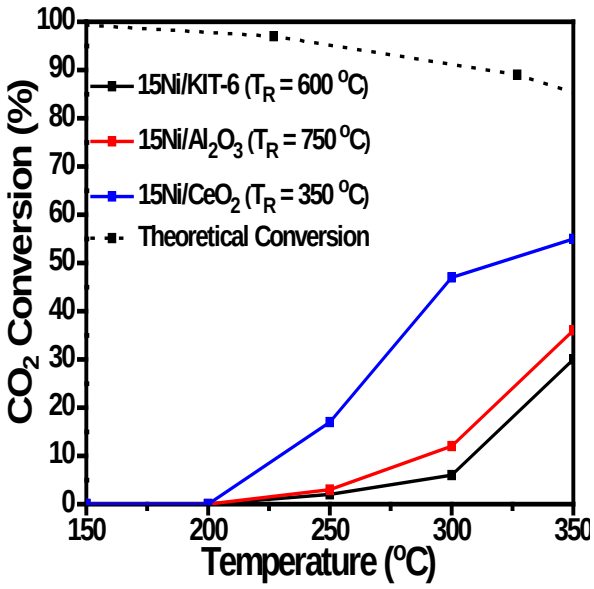

Figure 3.4: Conversion of CO_2 as function of temperature for 15Ni/Al_2O_3 reduced at T_R = 750 ^oC, 15Ni/KIT-6 reduced at T_R = 600 ^oC, and 15Ni/CeO_2 reduced at T_R = 350 ^oC

When a reduction temperature of 750 ^oC was used, the CO_2 conversion at 350 ^oC over the 15Ni/Al_2O_3 catalyst increased from 9 % to 36 %. This clearly validates that more Ni species became accessible after increasing the pre-treatment temperature. Surprisingly, the CO_2 conversion at 350 ^oC over the 15Ni/KIT-6 reduced at 600 ^oC decreased from 37 % to 30 %. While evaluating the effect of the reduction temperature on the catalytic activity of a Co/KIT-6 catalyst, Liu et al. [175] proved that a very low pre-treatment temperature cannot successfully reduce Co^{2+} species and

a very high pre-treatment temperature stimulates the formation of Co^{2+} species (Co_2SiO_4 and Co-O-Si species) that are difficult to reduce. The poor reducibility can eventually lead to poor CO_2 adsorption, activation and catalytic hydrogenation. Similarly, Bacariza et al. [178] observed that although increasing the reduction temperature of Ni-based zeolite catalysts resulted in a greater amount of reduced Ni species, the negative impact of metal particles sintering on the CO_2 methanation catalytic activity was also evident. It is reported in the literature [168,179] that Ni particles on SiO_2 support with weak interaction can be reduced easily and the reduced metal Ni would easily migrate and aggregate during the reduction and reaction process. Hence, this low activity of the 15Ni/KIT-6 catalyst obtained after increasing the reduction temperature is probably due to the aggregation and sintering of the Ni particles and to the instability of the KIT-6 support at high reducing temperatures. Even though the reduction temperature of both 15Ni/KIT-6 and 15Ni/Al_2O_3 catalysts was increased, the activity of 15Ni/CeO_2 reduced at 350 ^oC remained higher. According to the above results, it is clear that besides the availability and concentration of the active sites, the support plays an important role in the CO_2 methanation activity.

- The presence of ruthenium enhanced the catalytic performances at 350 ^oC by 10 % for 15Ni/Al_2O_3, 3 % for 15Ni/KIT-6 and 5 % for 15Ni/CeO_2.The improvement of the catalytic activity in the case of the bi-metallic catalysts can be related to the improvement of the dispersion of the ruthenium and nickel particles. Indeed, from chapter 2, and for all the catalysts, TPR and XRD analyses showed that the reduction of NiO is facilitated in the presence of ruthenium and that dispersion of RuO_2 is enhanced in the bi-metallic catalysts.

3.2. CO_2 Methanation over Ce_xKIT-6 (x= 15, 30, and 60 wt%) Supported Catalysts

From the results obtained in the first part of the chapter, it was noticed that when using the same pre-treatment temperature, CeO_2 catalysts demonstrated the highest catalytic activities while KIT-6 supported catalysts showed activities that were intermediate between Al_2O_3 and CeO_2. Ceria catalysts possess small surface areas, are expensive and subject to destabilization under high temperatures and reducing conditions. It is economically interesting to find a more suitable combination that complies with cost-effectiveness and efficiency. Several researchers [180–183] report the use of SiO_2 promoted with Ceria (mixed oxide) in several catalytic applications. In addition, and according to Prabhu et al. [182], the facile incorporation of cerium ions into the walls of mesoporous materials like SBA-15 and KIT-6 can affect the catalytic properties. Therefore, in this part of the chapter, KIT-6 was promoted with different CeO_2 percentages and impregnated with the same active phases and evaluated in the CO_2 methanation reaction. From a kinetic point of view, CO_2 is said to be adsorbed on the basic ceria and the abundant oxygen vacancies in ceria are expected to adsorb and activate the C-O bond hence greatly increasing the reaction rate [184].

3.2.1. Catalysts Preparation

Synthesis of the Ce_xKIT-6 supports

For the synthesis of the mesoporous Ce_xKIT-6 with different CeO_2 weight percentages (x = 15, 30 or 60 wt%), siliceous KIT-6 has been used as a template. The procedure was adopted from a work done by Piumetti et al. [185], where the nanocasting technique was used to synthesize mesoporous ceria using SBA-15 as the hard template**.** Therefore, an appropriate amount of $Ce(NO_3)_3{\cdot}6H_2O$ (Sigma–Aldrich) was dissolved in 20 mL of absolute ethanol. 0.5 g of KIT-6 was added to this solution and heated at 60 °C under vigorous stirring. After the ethanol had evaporated, the obtained powder was dried at 110 °C overnight and calcined at 550 °C (1 ^oC/min) in synthetic air for 4 h. To obtain 60 wt% Ce, an additional step after the evaporation of ethanol process is required: the powder obtained was first calcined at 450 °C for 4 h to remove the nitrate species and another $Ce(NO_3)_3{\cdot}6H_2O$ dissolved in ethanol solution was added to the powder [150]**.** The powder was then dried and calcined at 550 °C (1 ^oC/min). The calculations done to obtain the mass of the precursor required are found in Appendix B.

Synthesis of the Ce_xKIT-6 supported catalysts

The wet impregnation technique previously described (chapter 2, part 2.1.1.) was used for the preparation. The active phase loading remained also the same. The catalysts described in this part were referred to as 1Ru/Ce_xKIT-6, 15Ni/Ce_xKIT-6, and 15Ni1Ru/Ce_xKIT-6 with x = 15, 30, or 60 wt%.

3.2.2. Catalysts Characterization

3.2.2.1. X-ray diffraction analyses (XRD)

Figures 3.5 (a), (b), (c), and (d) show the wide angle XRD patterns of the calcined Ce_xKIT-6 supports as well as the 1Ru/Ce_xKIT-6, 15Ni/Ce_xKIT-6, and 15Ni1Ru/Ce_xKIT-6 catalysts respectively. Table 3.1 lists the crystallite sizes of the identified oxide species in the catalysts.

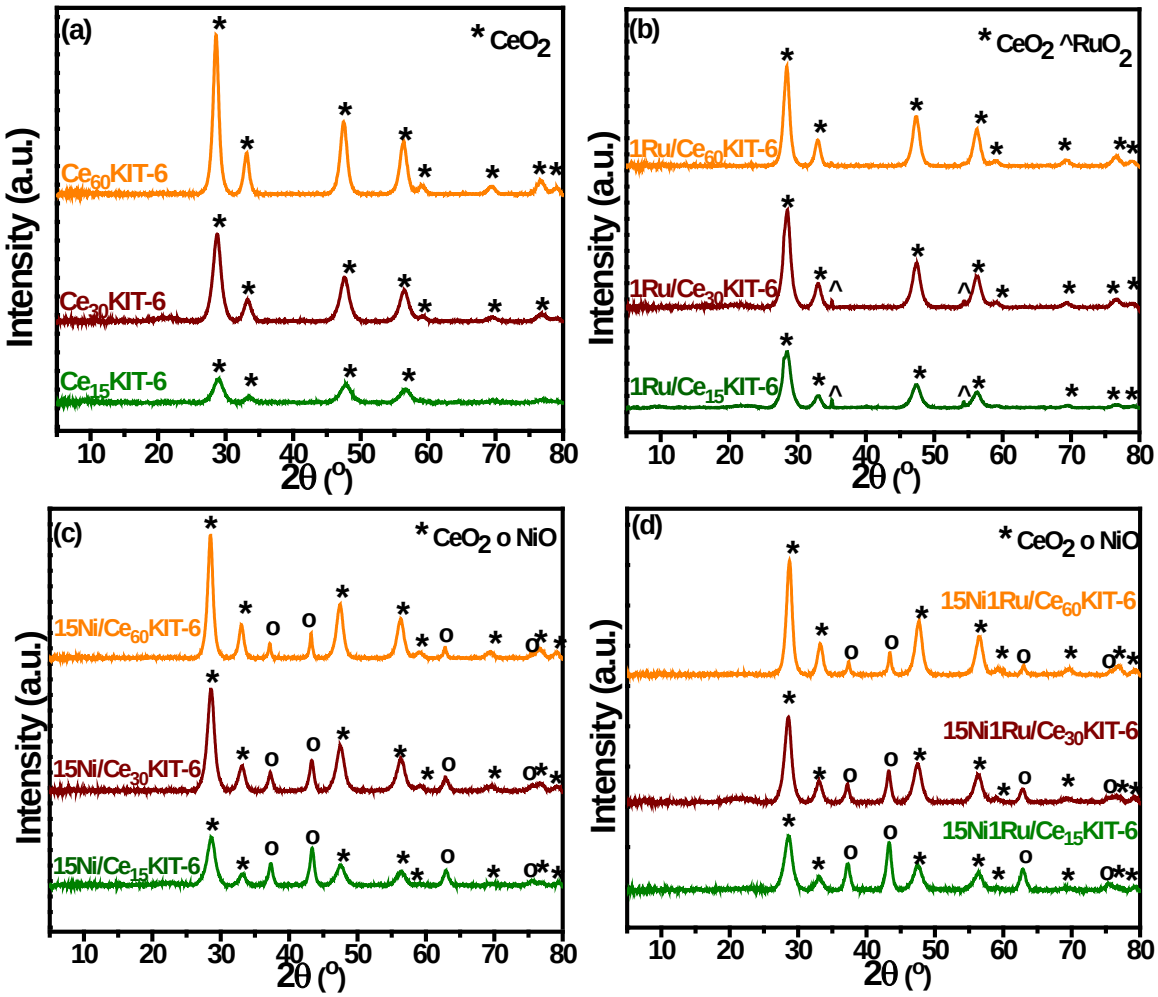

Figure 3.5: XRD patterns of (a) Ce_xKIT-6 supports, (b) 1Ru/Ce_xKIT-6 catalysts, (c) 15Ni/Ce_xKIT-6, and (d) 15Ni1Ru/Ce_xKIT-6 after calcination at 550 °C

The diffraction patterns of KIT-6 promoted with 15, 30 and 60 wt% Ce after their calcination at 550 ^oC are shown on figure 3.5 (a). The SiO_2 phase that was present prior to Ce promotion (chapter 2, figure 2.9) is very weak on the diffractogram and practically absent for the Ce_xKIT-6 supports. This is due to the higher amount of CeO_2 compared to SiO_2. The XRD patterns of the cerium containing catalysts contain diffraction lines typical to the ceria fluorite structure. According to the diffractograms, as Ce content increases the intensity of the peaks increases as well. The CeO_2 fluorite phase is consistent in all catalysts after impregnation. From figures 3.5 (b) and (d), it is noticed that small intensity RuO_2 peaks are present in the mono-metallic 1Ru/Ce_{15}KIT-6 and 1Ru/Ce_{30}KIT-6 catalysts but absent in the 1Ru/Ce_{60}KIT-6 and all the bi-metallic 15Ni1Ru/Ce_xKIT-6 catalysts. In all patterns of 15Ni/Ce_xKIT-6 and 15Ni1Ru/Ce_xKIT-6 catalysts (figure 3.5 (c) and (d)), the characteristic XRD reflections of NiO are observed. It is also noticed that the intensity of these NiO peaks decreases with increasing Ce content. Table 3.1 shows that the CeO_2 crystallite sizes increase with the Ce content for all Ce_xKIT-6 supports and catalysts. Similarly, RuO_2 and NiO crystallite sizes are higher at high Ce loadings. NiO crystallite sizes vary between 12.6 nm and 22.9 nm in the 15Ni/Ce_xKIT-6 catalysts and between 10.8 nm and 25.7 nm in the 15Ni1Ru/Ce_xK series.

Table 3.1: Crystallite sizes of Ce_xKIT-6 supported catalysts

Catalyst	Crystallite Size (nm)		
	CeO_2	RuO_2	NiO
KIT-6	-	-	-
Ce_{15}KIT-6	3.9	-	-
Ce_{30}KIT-6	4.8	-	-
Ce_{60}KIT-6	8.4	-	-
CeO_2	8.7	-	-
1Ru/KIT-6	-	31.3	-
1Ru/Ce_{15}KIT-6	6.2	36.3	-
1Ru/Ce_{30}KIT-6	7	41.5	-
1Ru/Ce_{60}KIT-6	8	-	-
1Ru/CeO_2	9	-	-
15Ni/KIT-6	-	-	12.6
15Ni/Ce_{15}KIT-6	6.1	-	12.9
15Ni/Ce_{30}KIT-6	6.9	-	13.4
15Ni/Ce_{60}KIT-6	8.8	-	22.1
15Ni/CeO_2	9	-	22.9
15Ni1Ru/KIT-6	-	-	10.8
15Ni1Ru/Ce_{15}KIT-6	6.2	-	11.2
15Ni1Ru/Ce_{30}KIT-6	7	-	11.8
15Ni1Ru/Ce_{60}KIT-6	8.2	-	18.2
15Ni1Ru/CeO_2	9.1	-	25.7

3.2.2.2. N_2 adsorption/desorption analyses

The nitrogen adsorption/desorption isotherms of the calcined Ce_xKIT-6 supports as well as the 1Ru/Ce_xKIT-6, 15Ni/Ce_xKIT-6 and 15Ni1Ru/Ce_xKIT-6 catalysts are shown on figures 3.6 (a), 3.7 (a), 3.8 (a) and 3.9 (a) respectively. Their respective pore size distributions are also represented on figures 3.6 (b), 3.7 (b), 3.8 (b) and 3.9 (b). The corresponding textural parameters are reported in table 3.2.

N_2 adsorption/desorption of Ce_xKIT-6 supports

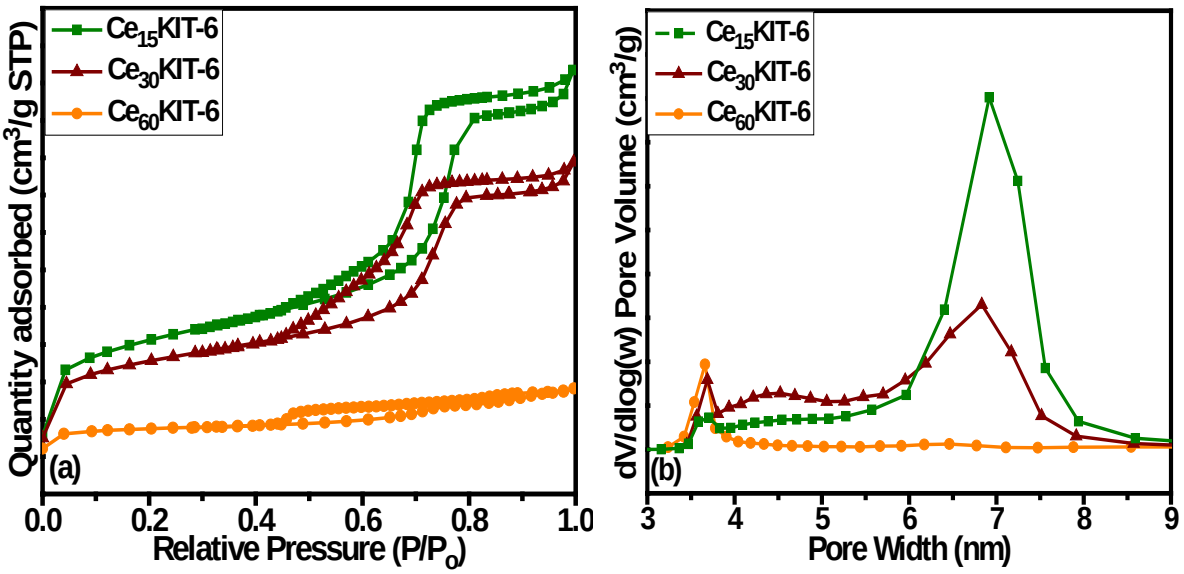

Figure 3.6: (a) N_2 adsorption/desorption isotherms and (b) Pore size distributions of Ce_xKIT-6 supports

Upon promoting with 15 wt% and 30 wt% Ce, the shape of the KIT-6 isotherm (chapter 2, figure 2.10 (a)) varies slightly. However, promoting with 60 wt% Ce remarkably modifies the shape of the isotherm which becomes irregularly flat and small. An H2 hysteresis loop is observed for the Ce_{15}KIT-6 and Ce_{30}KIT-6 supports, whereas an H4 hysteresis loop is obtained for the Ce_{60}KIT-6 support. Obtaining an H4 hysteresis in the isotherm of Ce_{60}KIT-6 support indicates an irregular mesopore structure explained by the larger density of CeO_2 compared to that of SiO_2 and the possibility of pore blockage [168]. Figure 3.6 (b) and table 3.2 show a bimodal pore size distribution around 3.7 nm and 6.9 nm for the Ce_{15}KIT-6 support, and around 3.6 nm and 6.8 nm for the Ce_{30}KIT-6 support. This bimodal distribution suggests that not all the pores of the support were partially filled by the addition of 15 wt% and 30 wt% Ce. However, a mono-modal pore size distribution centered at 3.6 nm is present for the Ce_{60}KIT-6 support. This shift in the pore diameter to a narrower range implies that all the pores of KIT-6 support were partially filled when the Ce loading was 60 wt%. From table 3.2, the surface area and the pore volume of KIT-6 decreased from 630 m^2/g to 555 m^2/g and from 1 cm^3/g to 0.74 cm^3/g respectively following the addition of 15 wt% Ce. As the amount of Ce in the support increased, a more prominent decrease was observed. This decrease in the

surface area and pore volume as the Ce loading increases is probably due to the decreased regularity of mesopores in the presence of Ce [182].

N_2 adsorption/desorption of Ce_xKIT-6 supported catalysts

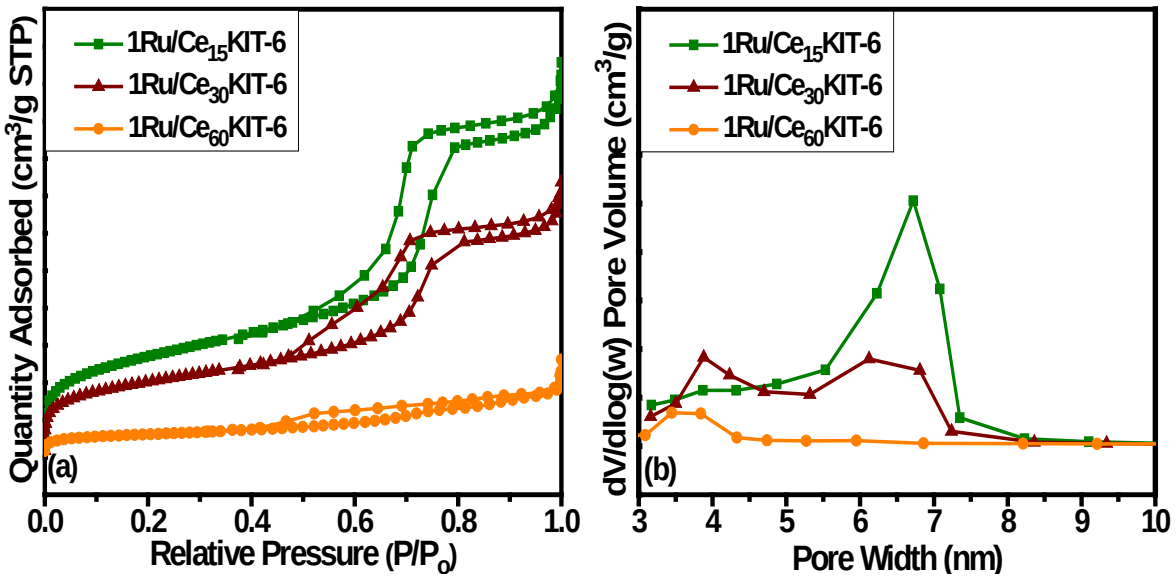

Figure 3.7: (a) N_2 adsorption/desorption isotherms and (b) Pore size distributions of 1Ru/Ce_xKIT-6 supports

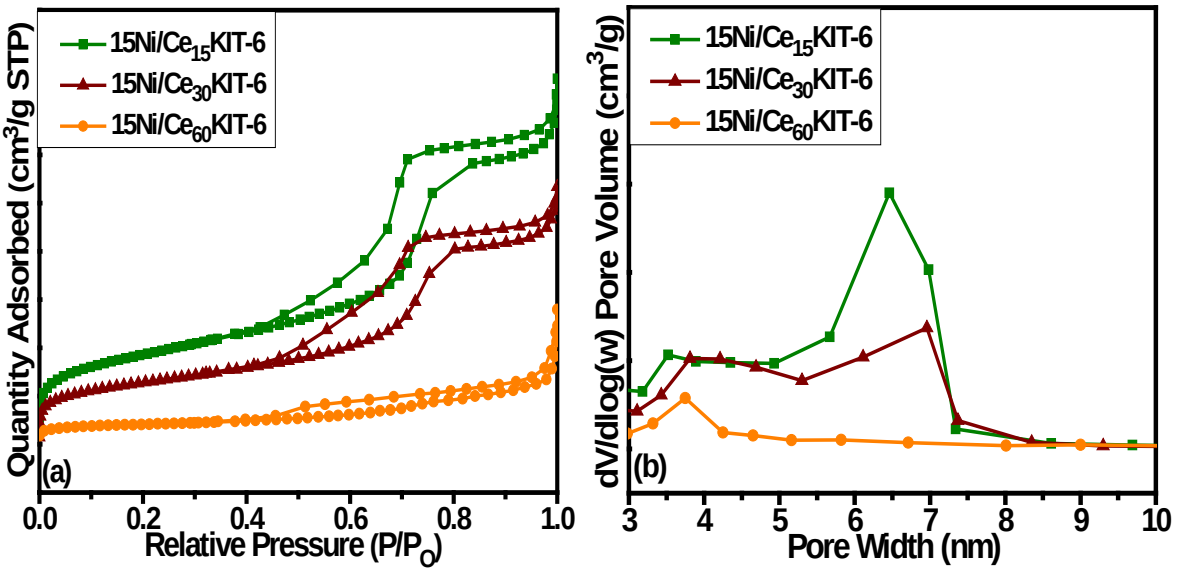

Figure 3.8: (a) N_2 adsorption/desorption isotherms and (b) Pore size distributions of 15Ni/Ce_xKIT-6 supports

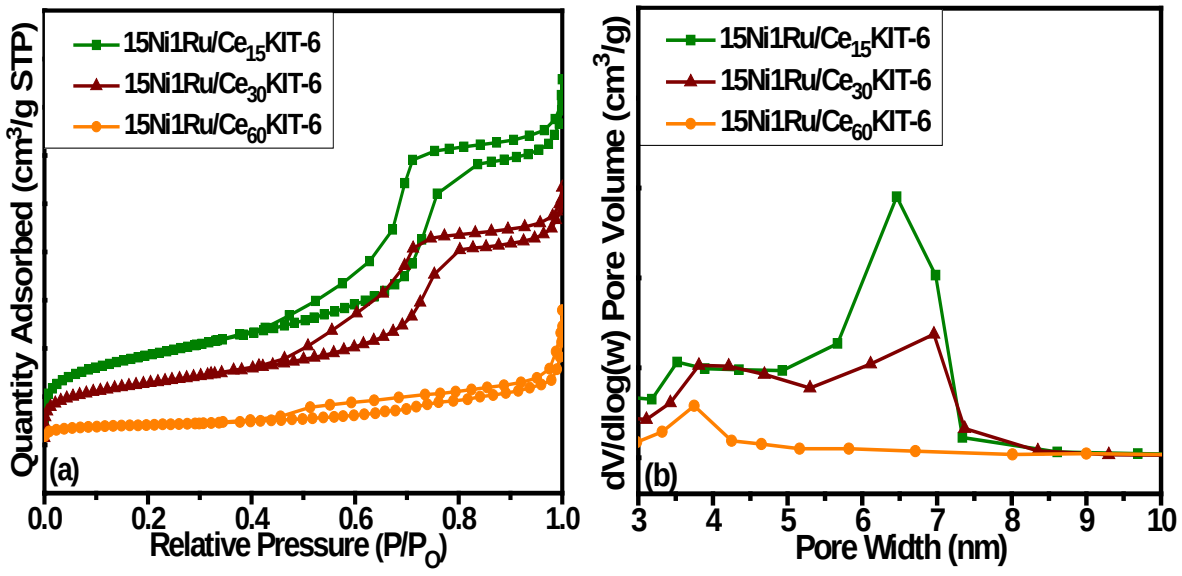

Figure 3.9: (a) N_2 adsorption/desorption isotherms and (b) Pore size distributions of 15Ni1Ru/Ce_xKIT-6 supports

The addition of 1 wt% Ru, 15 wt% Ni, and 15 wt% Ni – 1 wt% Ru to Ce_xKIT-6 supports did not significantly modify the porous structure of the promoted supports. Actually, the shapes of the isotherms and hysteresis loops were very similar to the ones obtained for the supports (figure 3.6 (a)). This indicates that impregnation following promotion with Ce did slightly alter the porous structure of the catalyst. Table 3.2 shows that for all active phases, the surface areas and pore volumes decrease as the amount of Ce loading in the catalyst increases. All the Ce_xKIT-6 supports and catalysts with $x \leq 30$ % show a bi-modal pore size distribution ranging between 3 nm and 5 nm and 6 nm and 7 nm. However, the Ce_{60}KIT-6 support as well as the 1Ru/Ce_{60}KIT-6, 15Ni/Ce_{60}KIT-6, and 15Ni1Ru/Ce_{60}KIT-6 catalysts show one type of pores centered at ~3.6 nm.

Table 3.2: Textural properties of Ce_xKIT-6 supported catalysts

Catalyst	Specific Surface Area(m^2/g)	Pore Volume (cm^3/g)	Pore Diameter (nm)	
KIT-6	630	1	6	
Ce_{15}KIT-6	555	0.74	3.7	6.9
Ce_{30}KIT-6	451	0.57	3.6	6.8
Ce_{60}KIT-6	174	0.17	3.6	
CeO_2	84	0.13	3.8	
1Ru/KIT-6	601	0.89	6.5	
1Ru/Ce_{15}KIT-6	475	0.8	3.8	6.7
1Ru/Ce_{30}KIT-6	350	0.56	3.8	6.1
1Ru/Ce_{60}KIT-6	104	0.19	3.4	
1Ru/CeO_2	74	0.12	3.8	
15Ni/KIT-6	422	0.72	6.9	
15Ni/Ce_{15}KIT-6	326	0.58	3.52	6.5
15Ni/Ce_{30}KIT-6	222	0.42	3.8	6.9
15Ni/Ce_{60}KIT-6	88	0.15	3.8	
15Ni/CeO_2	62	0.13	3.7	
15Ni1Ru/KIT-6	488	0.71	6.7	
15Ni1Ru/Ce_{15}KIT-6	338	0.54	3.7	6.7
15Ni1Ru/Ce_{30}KIT-6	271	0.4	3.85	7
15Ni1Ru/Ce_{60}KIT-6	69	0.16	3.8	
15Ni1Ru/CeO_2	50	0.13	3.8	

3.2.2.3. H_2-Temperature programmed reduction analyses (H_2-TPR)

Figure 3.10 illustrates the deconvoluted H_2-TPR profiles of the calcined Ce_xKIT-6 supports. Table 3.3 lists the total experimental and theoretical hydrogen consumptions for the different supports.

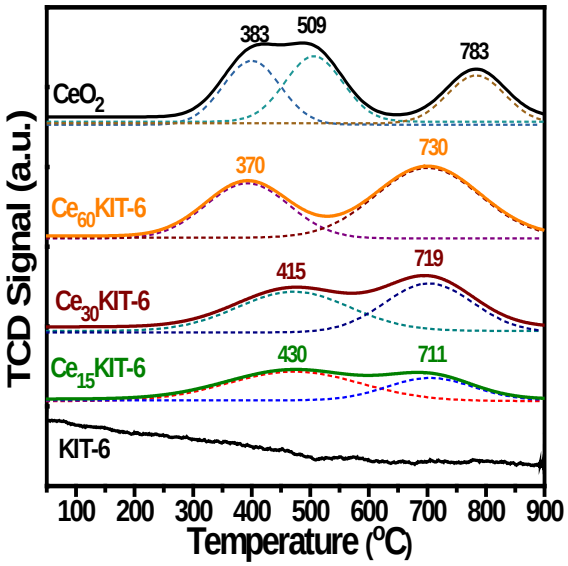

Figure 3.10: H_2-TPR profiles of Ce_xKIT-6 supports

All the TPR profiles of Ce_xKIT-6 supports present a low temperature reduction peak (Peak I) centered at 430 °C for x = 15 wt%, 415 °C for x = 30 wt% and at 370 °C for x = 60 wt% assigned to the reduction of surface ceria. This shift in the temperature of peak I towards lower ranges as Ce content increases means that the reduction of surface ceria becomes easier. A second reduction peak (Peak III) centered at 711 °C for x = 15 wt%, 719 °C for x = 30 wt% and 730 °C for x = 60 wt% is also observed and attributed to the reduction of bulk ceria species. The reduction of surface ceria and bulk ceria is facilitated in the CexKIT-6 supports compared to pure CeO_2 due to the high specific surface area of KIT-6 (table 3.2) that promotes the exposure of CeO_2 species to the gaseous phase. It is also noticed from table 3.3 that as Ce content increases in the Ce_xKIT-6 supports, the hydrogen consumptions increase because more surface and bulk CeO_2 species are present.

Table 3.3: Experimental and theoretical H_2 consumptions of Ce_xKIT-6 supports

Catalyst	H_2 consumption [µmol H_2/g catalyst]					
	Experimental Consumption				Theoretical Consumption	
	I	II	III	Total	Ce^{4+}/Ce^{3+}	Total
KIT-6	-	-	-	-	-	-
$Ce_{15}KIT$-6	267	-	132	**399**	435	**435**
$Ce_{30}KIT$-6	382	-	373	**755**	871	**871**
$Ce_{60}KIT$-6	608	-	955	**1563**	1743	**1743**
CeO_2	627	641	466	**1734**	2905	**2905**

Figure 3.11 illustrates the deconvoluted H_2-TPR profiles of the calcined 1Ru/Ce_xKIT-6 catalysts. Table 3.4 lists the corresponding experimental and theoretical H_2 consumptions.

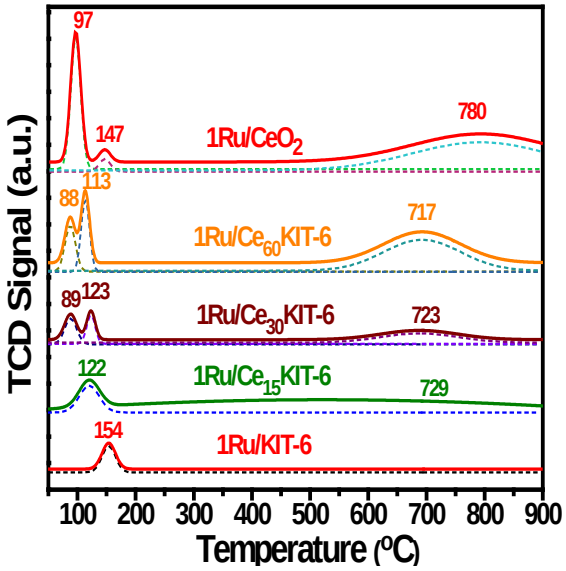

Figure 3.11: H_2-TPR profiles 1Ru/Ce_xKIT-6 catalysts

The hydrogen consumption of Peak I at 154 °C attributed to the reduction of crystallized RuO_2 shown on the TPR profile of 1Ru/KIT-6 (chapter 2, part 2.3.2.3.) is shifted towards a lower temperature (122 °C) in the TPR profile of the 1Ru/Ce_{15}KIT-6 catalyst. From table 3.4, Peak I for the latter corresponds to a hydrogen consumption (504 µmol/g) that is greater than the theoretical consumption of RuO_2. This suggests a simultaneous reduction of RuO_2 and surface CeO_2. The TPR profiles of 1Ru/Ce_{30}KIT-6 and 1Ru/Ce_{60}KIT-6 catalysts show an additional peak at lower temperatures (89 °C and 88 °C respectively) which corresponds to the reduction of RuO_2 species that are well-dispersed and weakly interacting with the surface of ceria [186]. From these results, it appears that the simultaneous reduction of RuO_2 and CeO_2 occurs at lower temperatures as the amount of Ce increases in the 1Ru/Ce_xKIT-6

catalysts. Another very low intensity reduction peak III (not clearly seen) centered at 729 ^oC for 1Ru/Ce_{15}KIT-6 catalyst corresponding to a hydrogen consumption of 81 µmol/g is assigned to the small amount of bulk ceria present in the catalyst. The hydrogen consumption of peak III further increases upon promoting KIT-6 with 30 wt% Ce (723 ^oC, 634 µmol/g) and 60 wt% Ce (717 ^oC, 705 µmol/g).

Table 3.4: Experimental and theoretical H_2 consumptions of 1Ru/Ce_xKIT-6 catalysts

Catalyst	H_2 consumption [µmol H_2/g catalyst]						
	Experimental Consumption				Theoretical Consumption		
	I	II	III	Total	RuO_2/Ru	Ce^{4+}/Ce^{3+}	Total
1Ru/KIT-6	181	-	-	**181**	20	-	**200**
1Ru/Ce_{15}KIT-6	504	-	81	**585**	200	430	**630**
1Ru/Ce_{30}KIT-6	210	167	634	**1011**	200	860	**1060**
1Ru/Ce_{60}KIT-6	216	259	705	**1180**	200	1720	**1920**
1Ru/CeO_2	396	42	946	**1384**	200	2866	**3066**

Figure 3.12 illustrates the deconvoluted H_2-TPR profiles of the calcined 15Ni/Ce_xKIT-6 catalysts. Table 3.5 lists the corresponding experimental and theoretical H_2 consumptions.

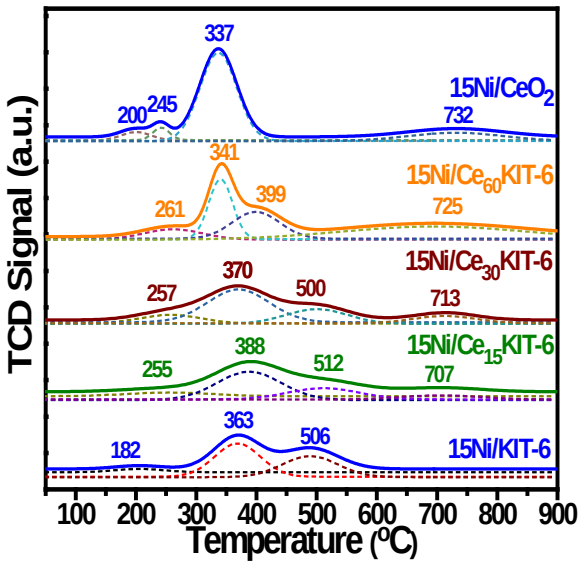

Figure 3.12: H_2-TPR profiles 15Ni/Ce_xKIT-6 catalysts

The TPR profiles of all 15Ni/Ce_xKIT-6 catalysts present four reduction peaks. The first low temperature peak in the range of 100 ^oC – 250 ^oC (255 ^oC for 15Ni/Ce_{15}KIT-6, 257 ^oC for 15Ni/Ce_{30}KIT-6, and 261 ^oC for 15Ni/Ce_{60}KIT-6) can be attributed to the reduction of very

small particles of NiO. The second reduction peak in the 250 ^oC – 600 ^oC temperature range (Peaks II and III) for all 15Ni/Ce_xKIT-6 catalysts are attributed to reduction of large NiO particles and a fraction of surface ceria [24]. The higher temperature peak (Peak IV) in the range of 600 ^oC – 800 ^oC is assigned to the reduction of bulk ceria.

It is noticed that the reduction temperature of peak III decreases with the increase of the amount of Ce in the catalysts. However, the hydrogen consumptions increase for higher Ce loadings (15Ni/CeO_2 (337 ^oC, 3200 μmol/g), 15Ni/Ce_{60}KIT-6 (409 ^oC, 1951 μmol/g), 15Ni/Ce_{30}KIT-6 (500 ^oC, 801 μmol/g), 15Ni/Ce_{15}KIT-6 (512 ^oC, 600 μmol/g)). This suggests that more surface CeO_2 species are being reduced and that NiO reduction at lower temperatures is improved in the presence of high Ce loadings. The intensity and hydrogen consumption of peak IV also increases with the increase in Ce loading as more bulk ceria species are being reduced.

Table 3.5: Experimental and theoretical H_2 consumptions of 15Ni/Ce_xKIT-6 catalysts

Catalyst	H_2 consumption [μmol H_2/g catalyst]							
	Experimental Consumption					Theoretical Consumption		
	I	II	III	IV	Total	NiO/Ni	Ce^{4+}/Ce^{3+}	Total
15Ni/KIT-6	268	1309	1052	-	**2629**	2871	-	**2871**
15Ni/Ce_{15}KIT-6	102	2302	219	270	**2893**	2871	354	**3225**
15Ni/Ce_{30}KIT-6	481	1803	801	401	**3486**	2871	712	**3583**
15Ni/Ce_{60}KIT-6	367	1951	1309	433	**4060**	2871	1423	**4294**
15Ni/CeO_2	256	203	3200	779	**4438**	2871	2372	**5243**

Figure 3.13 shows the deconvoluted H_2-TPR profiles of the 15Ni1Ru/Ce_xKIT-6 catalysts. Table 3.6 lists the corresponding experimental and theoretical H_2 consumptions.

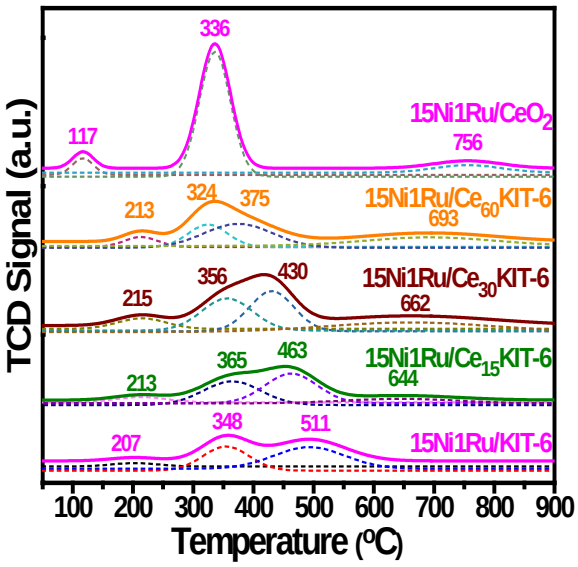

Figure 3.13: H_2-TPR profiles of 15Ni1Ru/Ce_xKIT-6 catalysts

The TPR profiles and the hydrogen consumptions of the 15Ni1Ru/Ce_xKIT-6 catalysts show that the first peak in the 150 °C – 250 °C temperature range for all the catalysts is the result of the simultaneous reduction of some NiO species along with RuO_2. For 15Ni1Ru/Ce_{15}KIT-6, 15Ni1Ru/Ce_{30}KIT-6, and 15Ni1Ru/Ce_{60}KIT-6, the second and third peaks are attributed to the reduction of large NiO particles in interaction with ceria. Similar observations as the ones made from the TPR profiles of 15Ni/Ce_xKIT-6 catalysts regarding the facilitated NiO reducibility and harder bulk ceria reduction at high Ce loadings were concluded.

Table 3.6: Experimental and theoretical H_2 consumptions of 15Ni1Ru/Ce_xKIT-6 catalysts

Catalyst	H_2 consumption [µmol H_2/g catalyst]								
	Experimental Consumption					Theoretical Consumption			
	I	II	III	IV	Total	NiO/Ni	RuO_2/Ru	Ce^{4+}/Ce^{3+}	Total
15Ni1Ru/KIT-6	435	849	1373	-	**2657**	2871	200	-	**3071**
15Ni1Ru/Ce_{15}KIT-6	238	1192	1355	449	**3234**	2871	200	352	**3423**
15Ni1Ru/Ce_{30}KIT-6	337	1180	1082	1026	**3625**	2871	200	703	**3774**
15Ni1Ru/Ce_{60}KIT-6	470	1203	1646	719	**4038**	2871	200	1409	**4480**
15Ni1Ru/CeO_2	342	3856	-	495	**4693**	2871	200	2353	**5424**

3.2.2.4. CO_2- Temperature programmed desorption analyses (CO_2-TPD)

Figures 3.14 (a), (b), (c), and (d) show the CO_2-TPD profiles recorded over Ce_xKIT-6 supports, as well as the 1Ru/Ce_xKIT-6, 15Ni/Ce_xKIT-6, and 15Ni1Ru/Ce_xKIT-6 catalysts respectively. Figure 3.15 illustrates the total desorbed CO_2 quantity for the different supports and catalysts.

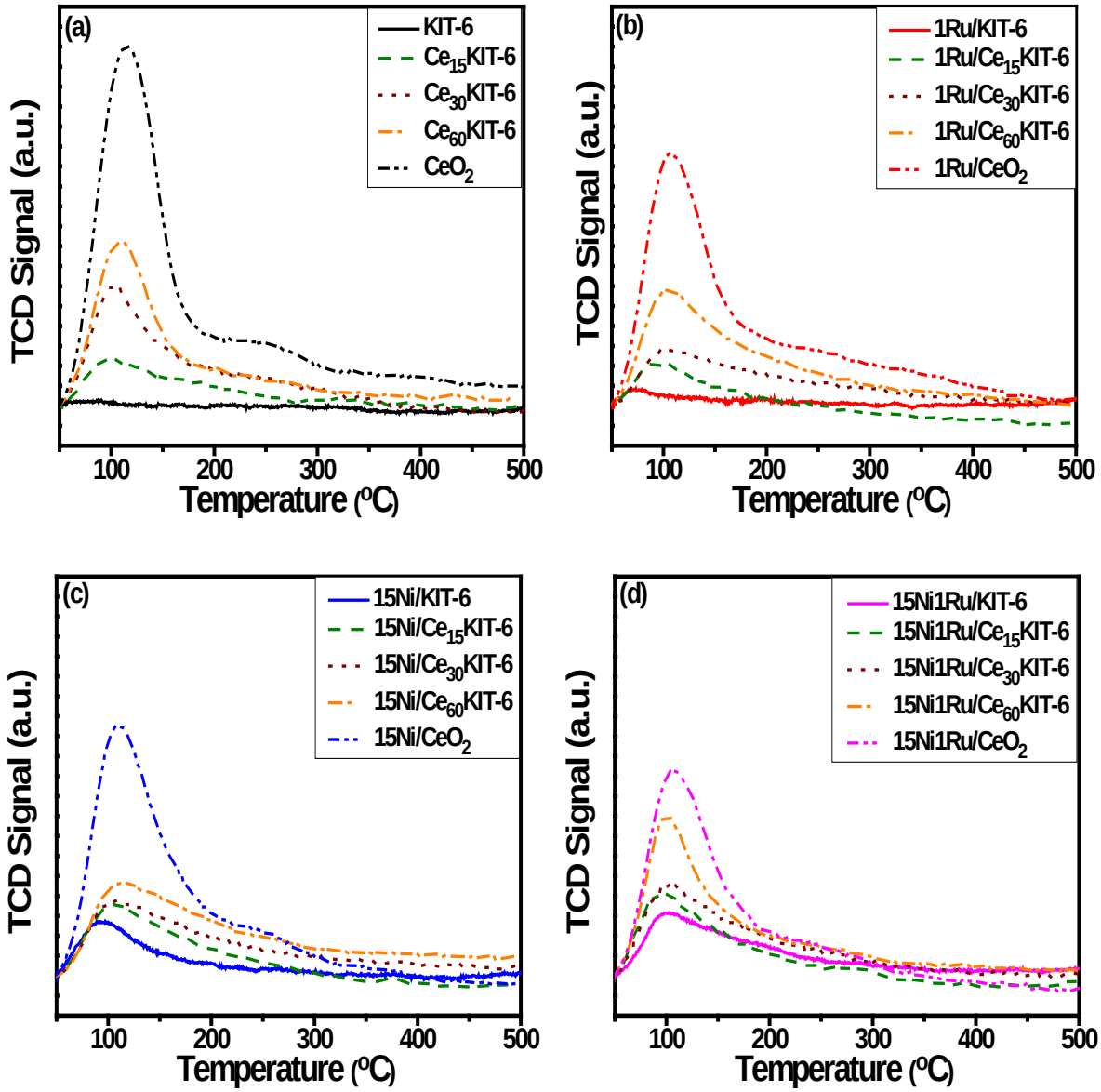

Figure 3.14: CO_2-TPD profiles of (a) Ce_xKIT-6 supports, (b) 1Ru/Ce_xKIT-6, (c) 15Ni/Ce_xKIT-6, and (d) 15Ni1Ru/Ce_xKIT-6 catalysts

The CO_2-TPD profiles of all supports and catalysts show a common peak centered at temperatures lower than 200 ^oC attributed to the presence of weak basic sites. From figure

3.14 (a), as the percentage of Ce in the support increases, the larger the CO_2 desorption peak area becomes. This indicates that there are more desorbed CO_2 species and that the catalysts have more CO_2 adsorption centers [175]. Similar trends are observed in the presence of the different active phases. From the values reported in figure 3.15, it is clear that regardless of the active phase used, the total basicity increases as the amount of Ce loading in the catalyst increases.

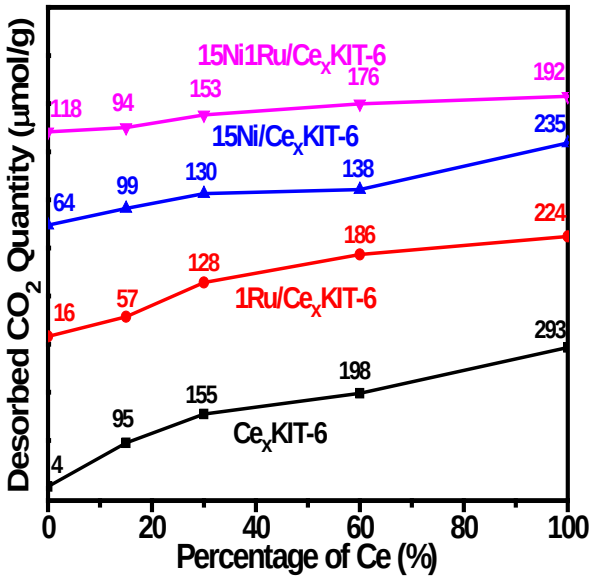

Figure 3.15: Total desorbed CO_2 quantities of Ce_xKIT-6 supported catalysts in function of Ce percentage

3.2.2.5. Discussion

- XRD results proved that RuO_2 species dispersion is ameliorated in the presence of high CeO_2 loading (60 wt%) and when nickel and ruthenium are present together.
- For all the catalysts, a significant destruction of the porous structure resulting from the addition of high Ce loadings (60 wt%) was observed. This was revealed by the change in the shape of the obtained isotherm, as well as the decreased surface areas and pore volumes.
- Active phase reducibility occurred at lower temperatures following the addition of Ce and as the percentage of Ce in the catalyst increases.
- The catalysts basicity increased after promotion with Ce and when Ce content increased in the catalyst.

3.2.3. Catalytic Activity

The purpose of this part is to assess the effect of Ce promotion on the methanation activity of the catalysts. The TPR profiles of 15Ni/Ce_xKIT-6 (x = 15, 30, and 60 wt%) showed that a pre-treatment at 350 °C under H_2/Ar (50 mL/min) for 2 hours was sufficient to completely reduce all NiO species. Therefore, in this part, a reduction temperature of 350 °C was chosen for all the studied catalysts. It is important to note that the same CO_2 methanation catalytic test conditions used in the first part of the chapter (P= 1 atm, H_2/CO_2 = 4, temperature range: 150 °C – 350 °C, GHSV= 40,000 h^{-1}, and total flow = 100 ml/min) were applied.

3.2.3.1. 1Ru/Ce_xKIT-6 catalysts

Figures 3.16 (a) and (b) show the CO_2 conversion as a function of temperature and the CH_4 and CO selectivity at 350 °C in the presence of Ru (1 wt%) supported on Ce_xKIT-6 catalysts.

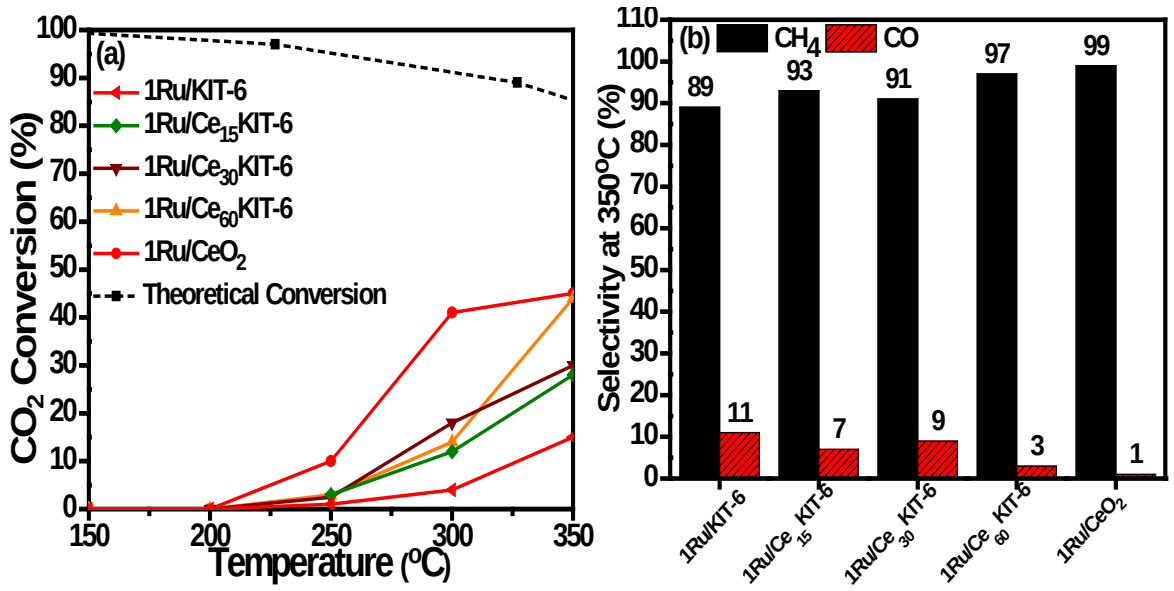

Figure 3.16: (a) Conversion of CO_2 as a function of temperature and (b) CH_4 and CO selectivities at 350 °C in the presence of the different 1Ru/Ce_xKIT-6 catalysts

At 250 °C, all the catalysts except 1Ru/CeO_2 show negligible conversions. At 350 °C, the order of reactivity is: 1Ru/CeO_2 ≈ 1Ru/Ce_{60}KIT-6 > 1Ru/Ce_{30}KIT-6 ≈ 1Ru/Ce_{15}KIT-6 > 1Ru/KIT-6. Hence, it is clear from the obtained trend that adding Ce to the KIT-6 support leads to more efficient catalysts. Among the promoted catalysts, 1Ru/Ce_{60}KIT-6 shows the highest CH_4 selectivity at 350 °C (97 %). TPR results (figure 3.11) show that as Ce content increases, the reduction of RuO_2 and CeO_2 species is facilitated as a result of the Ru-Ce

interaction. The improved reducibility resulting from Ce addition was translated into an enhanced catalytic activity. In addition, TPD results (figure 3.14 (b) + figure 3.15) prove that the basicity of the catalysts increased with Ce loadings. The obtained CO_2 conversions at 350 ^oC of the 1Ru/Ce_xKIT-6 catalysts were related to the desorbed CO_2 quantity of the catalysts: as the latter increased, the CO_2 conversions increased as well. Hence, the more basic the catalyst the higher its activity in the CO_2 methanation reaction was.

3.2.3.2. 15Ni/Ce_xKIT-6 catalysts

Figures 3.17 (a) and (b) show the CO_2 conversion as a function of temperature and the CH_4 and CO selectivity at 350 ^oC in the presence of Ni (15 wt%) supported on Ce_xKIT-6 catalysts.

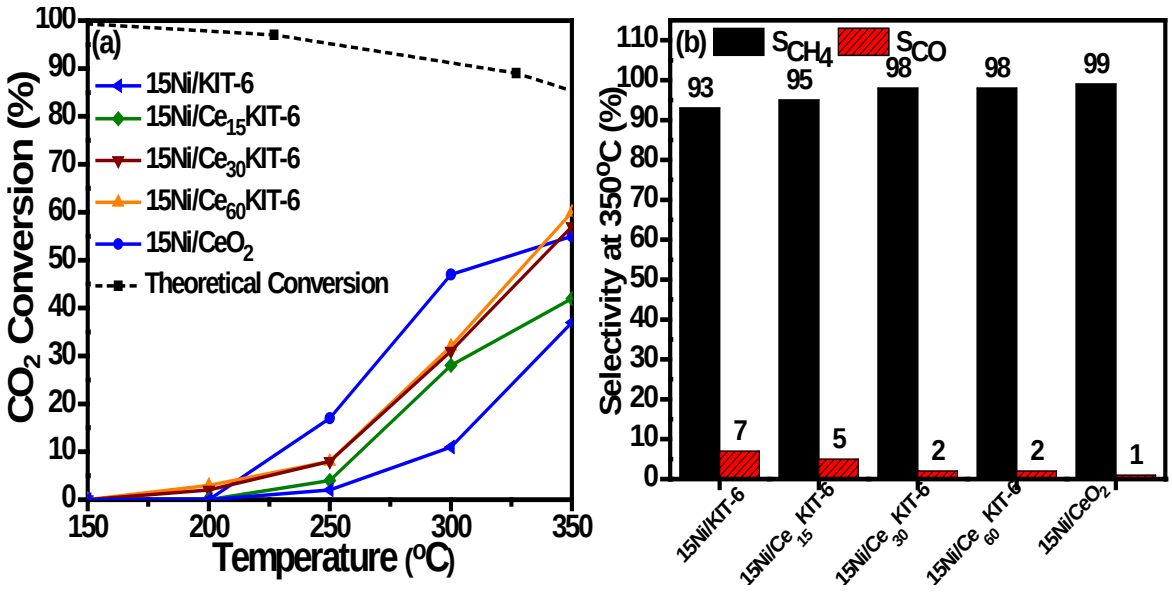

Figure 3.17: (a) Conversion of CO_2 as a function of temperature and (b) CH_4 and CO selectivities at 350 ^oC in the presence of the different 15Ni/Ce_xKIT-6 catalysts

All Ni based catalysts exhibit negligible activity at temperatures lower than 200 ^oC. The CO_2 conversions at 350 ^oC were as follows: 37 % for 15Ni/KIT-6, 42 % for 15Ni/Ce_{15}KIT-6, 57 % for 15Ni/Ce_{30}KIT-6, 60 % for 15Ni/Ce_{60}KIT-6, and 55 % for 15Ni/CeO_2. It is also noticed that the CO_2 conversions of the 15Ni/Ce_{60}KIT-6 and 15Ni/Ce_{30}KIT-6 catalysts over all the temperature ranges were very close. Hence, it can be concluded that doubling the amount of Ce from 30 wt% to 60 wt% in the presence of 15 wt% Ni did not seem to affect the activity. 15Ni/CeO_2, 15Ni/Ce_{60}KIT-6 and 15Ni/Ce_{30}KIT-6 catalysts demonstrate the highest CH_4 selectivities at 350 ^oC.

3.2.3.3. 15Ni1Ru/Ce$_x$KIT-6 catalysts

Figures 3.18 (a) and (b) show the CO_2 conversion as a function of temperature and the CH_4 and CO selectivity at 350 °C in the presence of Ni (15 wt %) – Ru (1 wt%) supported on Ce$_x$KIT-6 catalysts.

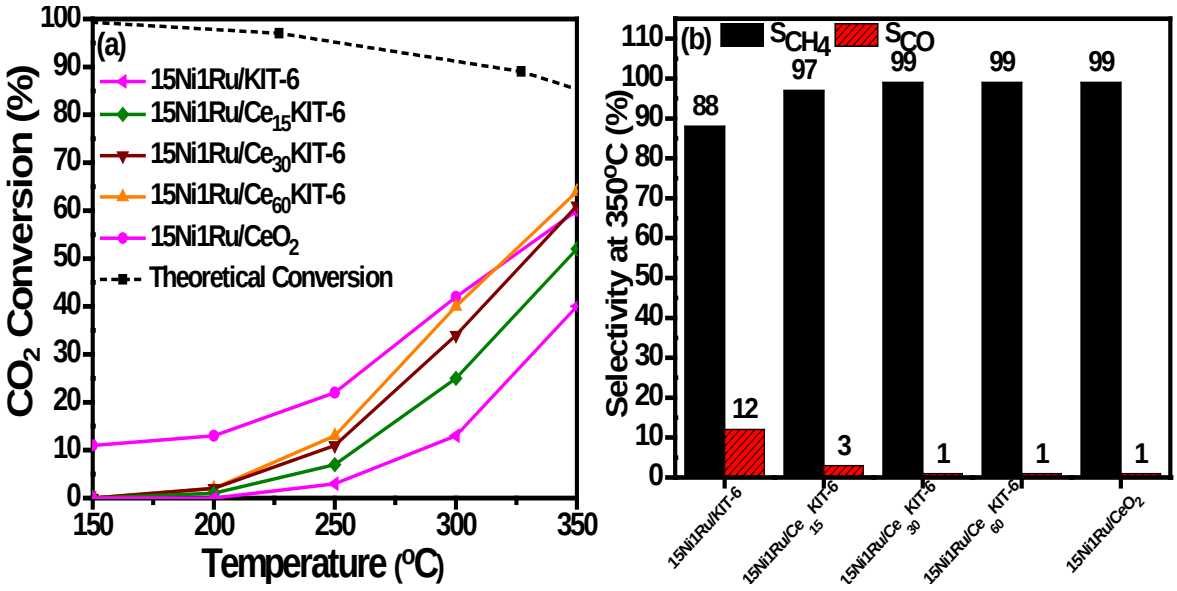

Figure 3.18: (a) Conversion of CO_2 as a function of temperature and (b) CH_4 and CO selectivities at 350 °C in the presence of the different 15Ni1Ru/Ce$_x$KIT-6 catalysts

For the 15Ni1Ru/Ce$_x$KIT-6 series, the same trend of reactivity as the one obtained for the 15Ni/Ce$_x$KIT-6 catalysts is noticed. However, in the bi-metallic catalysts, the CO_2 conversions at 350 °C were higher by 3 % for 15Ni/KIT-6, by 10 % for 15Ni/Ce$_{15}$KIT-6, by 4 % for 15Ni/Ce$_{30}$KIT-6 and 15Ni/Ce$_{60}$KIT-6, and by 5 % for 15Ni/CeO_2. The highest CO_2 conversion at 350 °C was equal to 64 % and was recorded in the presence of the 15Ni1Ru/Ce$_{60}$KIT-6. The methane selectivity recorded at 350 °C for the 15Ni1Ru/CeO_2, 15Ni1Ru/Ce$_{60}$KIT-6, and 15Ni1Ru/Ce$_{30}$KIT-6 catalysts is 99 %.

3.2.3.4. Effect of varying the GHSV on the dynamic activity of 15Ni1Ru/Ce$_{60}$KIT-6

To study the effect of varying the GHSV on the catalytic activity, two methanation tests with different GHSVs (20,000 h^{-1} and 80,000 h^{-1}) were performed on the 15Ni1Ru/Ce$_{60}$KIT-6 catalyst that showed the highest CO_2 conversion among all the studied catalysts. Considering that the flow rate remains constant (100 ml/min), a catalyst mass of 150 mg corresponds to a GHSV of 40,000 h^{-1}, whereas a catalyst mass of 75 mg and 300 mg correspond to GHSVs of

80,000 h^{-1} and 20,000 h^{-1} respectively. Figure 3.19 compares the catalytic performances of the 15Ni1Ru/Ce_{60}KIT-6 catalyst with different GHSVs.

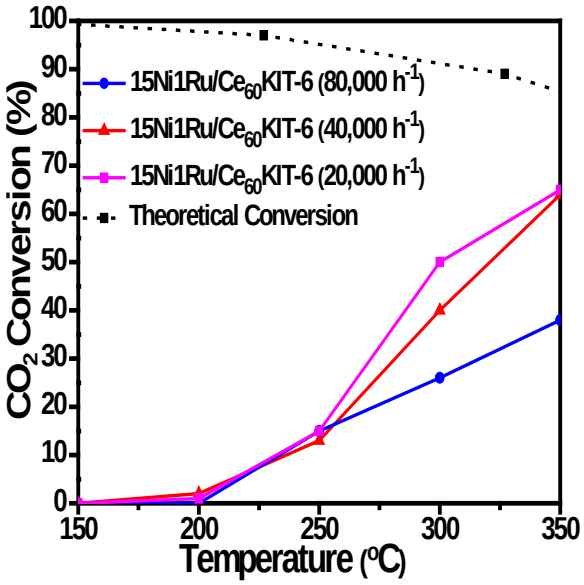

Figure 3.19: Conversion of CO_2 as function of temperature for 15Ni1Ru/Ce_{60}KIT-6 catalysts with different GHSVs

The obtained CO_2 conversions at 250 °C are the same regardless of the GHSV used. In the 250 °C – 300 °C temperature range, the catalytic activity of the 15Ni1Ru/Ce_{60}KIT-6 catalyst using a GHSV of 40,000 h^{-1} is intermediate between the activities obtained using a GHSV of 80,000 h^{-1} and 20,000 h^{-1}. However, at 350 °C, the CO_2 conversion of the 15Ni1Ru/Ce_{60}KIT-6 catalyst using a GHSV of 40,000 h^{-1} becomes equal to the conversion obtained using a GHSV of 20,000 h^{-1}.

3.2.3.5. Discussion

- For all active phases, the enhanced activity following the promotion with Ce is correlated to the improved reducibility and to the presence of more basic sites that enhance CO_2 adsorption and activation.
- The enhanced activity of the 15Ni1Ru/Ce_xKIT-6 catalysts is attributed to the presence of Ru that enhanced NiO reducibility (TPR, (figures 3.12 and 3.13).
- Normally, lower GHSV allow more contact time between the reactants and the catalysts and thus result in higher conversions. Higher GHSV, on the other hand, result in lower contact time and therefore a lower catalytic activity is obtained. From

our results, it appears that the optimal GHSV is around 40,000 h^{-1}. Any deviation from this value is not beneficial for the methanation activity.

3.2.4. Stability Tests

From the dynamic test results, it was deduced that the catalytic activity of the catalysts increased as a result of the promotion with Ce and in the presence of Ru. Hence, in this section, the stability of the three best performing catalysts 15Ni1Ru/Ce_{30}KIT-6, 15Ni1Ru/Ce_{60}KIT-6 and 15Ni1Ru/CeO_2 was evaluated at 350 °C.

3.2.4.1. Test results

Figures 3.20 (a), (b), and (c) show respectively the CO_2 conversions and CH_4 selectivities during aging tests for the 15Ni1Ru/Ce_{30}KIT-6, 15Ni1Ru/Ce_{60}KIT-6 and 15Ni1Ru/CeO_2 catalysts.

The deactivation rate is calculated according to the formula below:

$$\text{Deactivation rate} = \frac{X_{t1} - X_{t2}}{X_{t1}}\ x100$$

where t_1 and t_2 are time values under flow (with t_2=12 h and t_1=0 h for 15Ni1Ru/Ce_{30}KIT-6 and t_2=24 h and t_1=0 h for 15Ni1Ru/Ce_{60}KIT-6 and 15Ni1Ru/CeO_2) and X the CO_2 conversion in %.

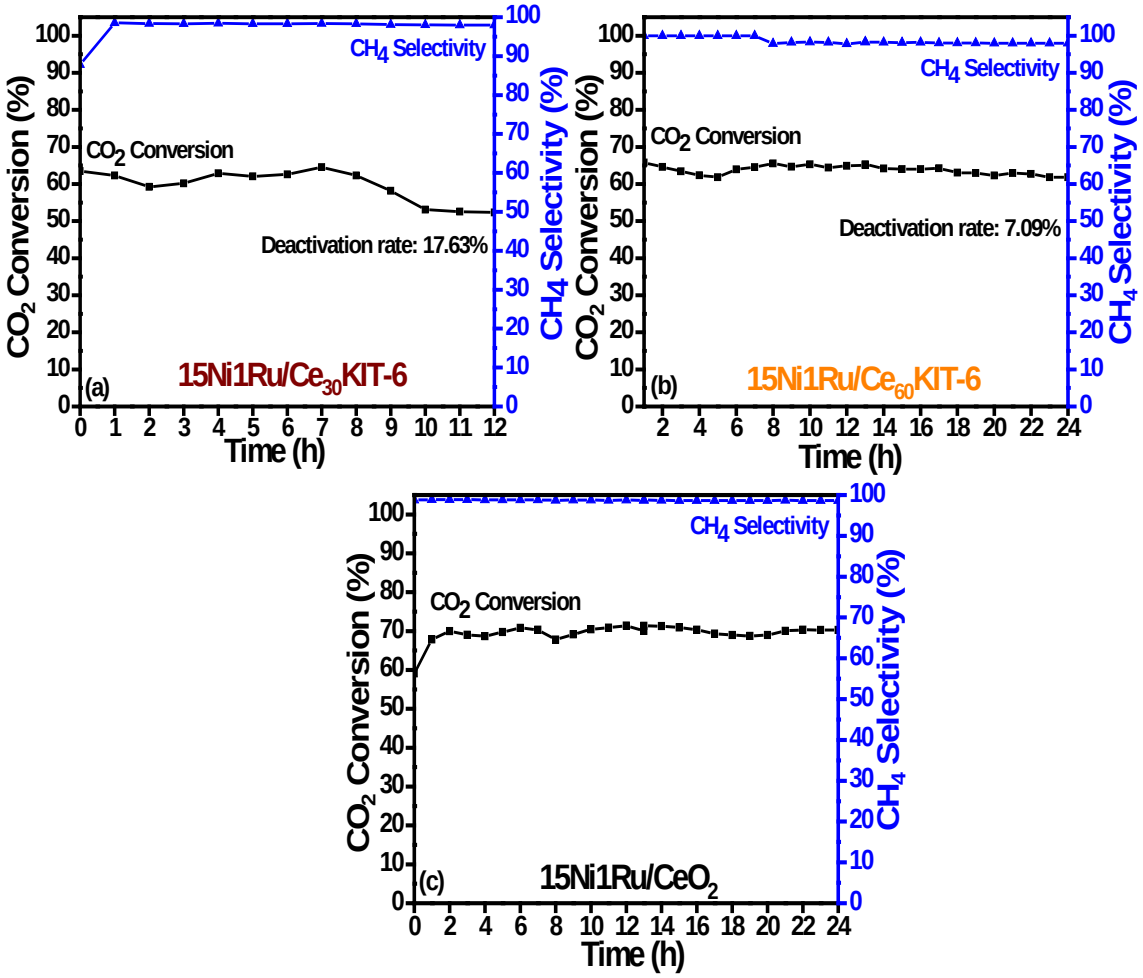

Figure 3.20: Evolution of the CO_2 conversion and CH_4 selectivity as a function of time at 350 °C for (a) 15Ni1Ru/Ce_{30}KIT-6, (b) 15Ni1Ru/Ce_{60}KIT-6 and (c) 15Ni1Ru/CeO_2 during the methanation reaction (P =1 atm, H_2/CO_2 =4, GHSV=40,000 h^{-1})

15Ni1Ru/Ce_{30}KIT-6 and 15Ni1Ru/Ce_{60}KIT-6 catalysts present an initial CO_2 conversion of 63.5 % and 66.5 % respectively. The CO_2 conversion of the 15Ni1Ru/Ce_{30}KIT-6 catalyst started to decrease after 7 h and reached a value of 52.3 % after 12 h on stream. The calculated deactivation rate over the 15Ni1Ru/Ce_{30}KIT-6 catalyst was equal to 17.63 %.

A slight loss of activity was observed at the 13th hour for the 15Ni1Ru/Ce_{60}KIT-6 catalyst. The decrease of activity continued at a low pace and at the end of the test the deactivation rate was found to be equal to 7.09 %. Furthermore, the initial CO_2 conversion obtained for the 15Ni1Ru/CeO_2 catalyst was 60 % in agreement with the dynamic test results. For the latter, it is noticed that after 1 h on stream CO_2 conversion increases from 60 % to 68 % and further increases to reach 70 % during all the time on stream and no loss of activity was observed. Hence, as the amount of Ce in the catalyst increases, the deactivation decreases.

This highlights the importance of CeO_2 support in promoting the complete oxidation of carbon by allowing the gasification of carbon deposits [11].

3.2.4.2. Characterization after stability tests

Thermal analysis

Figures 3.21 (a), (b), and (c) show the DTA/TGA curves obtained for the spent 15Ni1Ru/Ce_{30}KIT-6, 15Ni1Ru/Ce_{60}KIT-6 and 15Ni1Ru/CeO_2 catalysts respectively after the stability tests.

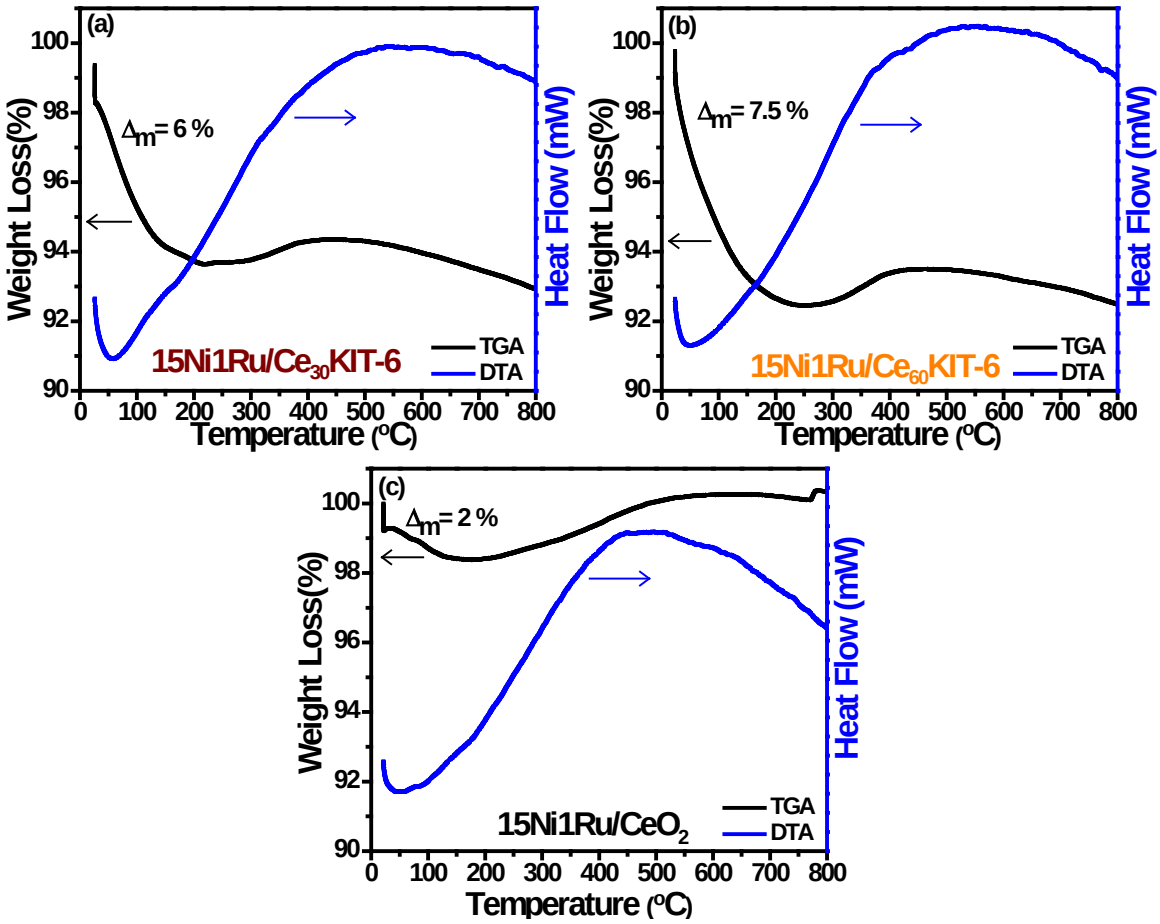

Figure 3.21: DTA/TGA curves of spent (a) 15Ni1Ru/Ce_{30}KIT-6, (b) 15Ni1Ru/Ce_{60}KIT-6 and (c) 15Ni1Ru/CeO_2 catalysts after stability tests

All the catalysts show a small weight loss (~6 % for 15Ni1Ru/Ce_{30}KIT-6, ~7.5 % for 15Ni1Ru/Ce_{60}KIT-6, and ~2 % for 15Ni1Ru/CeO_2) at temperatures lower than 200 ^oC accompanied with an endothermic peak which is associated with the removal of physisorbed/chemisorbed water. A small weight gain accompanied with a wide exothermic

peak were observed for the 15Ni1Ru/Ce_{30}KIT-6 catalyst in the 250 ^{o}C – 350 ^{o}C temperature range, for the 15Ni1Ru/Ce_{60}KIT-6 catalyst in the 250 °C – 450 °C temperature range, as well as for the 15Ni1Ru/CeO_2 catalyst in the 200 °C – 600 °C temperature range. This peak is assigned to the oxidation of metallic Ni and Ru to NiO and RuO_2 respectively ($Ni + \frac{1}{2} O_2 \rightarrow NiO$, $Ru + O_2 \rightarrow RuO_2$).

X-ray diffraction

Figure 3.22 shows the XRD patterns of the spent catalysts after stability.

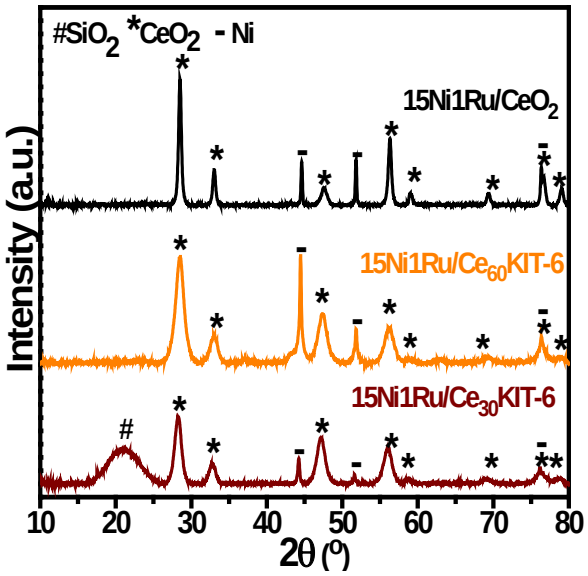

Figure 3.22: XRD patterns of spent 15Ni1Ru/Ce_{30}KIT-6, 15Ni1Ru/Ce_{60}KIT-6 and 15Ni1Ru/CeO_2 after stability tests

The XRD patterns show reflections typical of CeO_2 and peaks at 2θ= 44^{o}, 52^{o}, and 76.3^{o} attributed to metallic Ni (JCPDS 04-0850) that are present in all catalysts. An additional silica phase is present in the bi-metallic catalyst promoted with 30 wt% Ce. No peak attributed to carbon formation was detected.

3.2.4.3. Discussion

- In the CO_2 methanation reaction, the 15Ni1Ru/CeO_2 catalyst was active starting at 150 ^oC and showed no deactivation after aging for 24 h.
- The stability tests showed that Ce promotion led to better catalytic performances and contributed in minimizing the catalyst's deactivation.
- Thermal analyses along with XRD results validate the absence of carbon formation in any of the spent catalysts following their time on stream. The average nickel crystallite sizes are calculated for the catalysts that showed deactivation after stability test in order to study the phenomenon of metal particles sintering. The obtained Ni crystallite sizes were 30.6 nm and 33.9 nm for 15Ni1Ru/Ce_{30}KIT-6 and 15Ni1Ru/Ce_{60}KIT-6 catalysts respectively. Comparing to the NiO crystallite sizes of these catalysts (table 3.1), an increase in the size of nickel particles is observed thus proving the sintering of the particles. Ocampo et al [187] and Bukhari et al. [188] also reported smaller NiO crystallite sizes in their fresh catalysts and higher Ni crystallite sizes in the spent catalysts. Hence they excluded catalytic deactivation due to carbonaceous deposits, and attributed it to the nickel particles sintering during the reaction.
- Ce promotion enhanced the catalytic properties of KIT-6 supported catalysts, increased catalytic performances and contributed in minimizing the catalyst's deactivation. However, over long runs, the optimal catalyst was the non-promoted 15Ni1Ru/CeO_2. This implies that ceria alone is more efficient in the CO_2 methanation and the combination of ceria and KIT-6 did not improve the catalytic performances. Hence from our results, the CO_2 methanation activity was not influenced by the mesoporous structure or high surface areas of alumina and KIT-6 supported catalysts. It was the good redox and basic properties of CeO_2 supported catalysts that determined the optimal catalytic activity.

CHAPTER 4

CO_2 REFORMING OF METHANE RESULTS

In the first part of this chapter, the catalytic activity of CeO_2 and Al_2O_3 impregnated with Ru (1 wt%), Ni (15 wt%), and Ni-Ru (15 wt% – 1 wt%) will be evaluated in the CO_2 reforming of methane reaction. In the second part, a full account of the preparation and characterization of Ni and/or Ru catalysts supported on Al_2O_3 promoted with Ce will be given. The effect of promoting the support with Ce on the catalytic activity and stability of the Al_2O_3 supported catalysts is then presented. The third part compares the physico-chemical properties, catalytic activity and stability of Ni based catalysts supported on different mesoporous silicas. A final part compares the catalytic activity of KIT-6 supported catalysts prior to and after promotion with Ce.

4.1. CO_2 Reforming of Methane over CeO_2 and Al_2O_3 Supported Catalysts

Given its endothermic nature, the CO_2 reforming of methane is thermodynamically favored at high temperatures. As a consequence, the conversion increases with temperature. The studied CO_2 reforming reaction ($CO_2 + CH_4 \rightarrow 2H_2 + 2CO$) is carried out at atmospheric pressure, in a temperature range between 500 ^oC and 800 °C, with a CH_4/CO_2 ratio equal to 1 and a GHSV of 60,000 h^{-1}. Theoretical calculations for the obtained thermodynamic curve are found in Appendix B.

4.1.1. CeO_2 Supported Catalysts

4.1.1.1. Catalytic activity

Figures 4.1 (a), (b), (c), (d), and (e) show respectively the CH_4 conversion, CO_2 conversion, H_2/CO molar ratio, CO selectivity and the H_2 selectivity in the presence of the 1Ru/CeO_2, 15Ni/CeO_2 and 15Ni1Ru/CeO_2 catalysts.

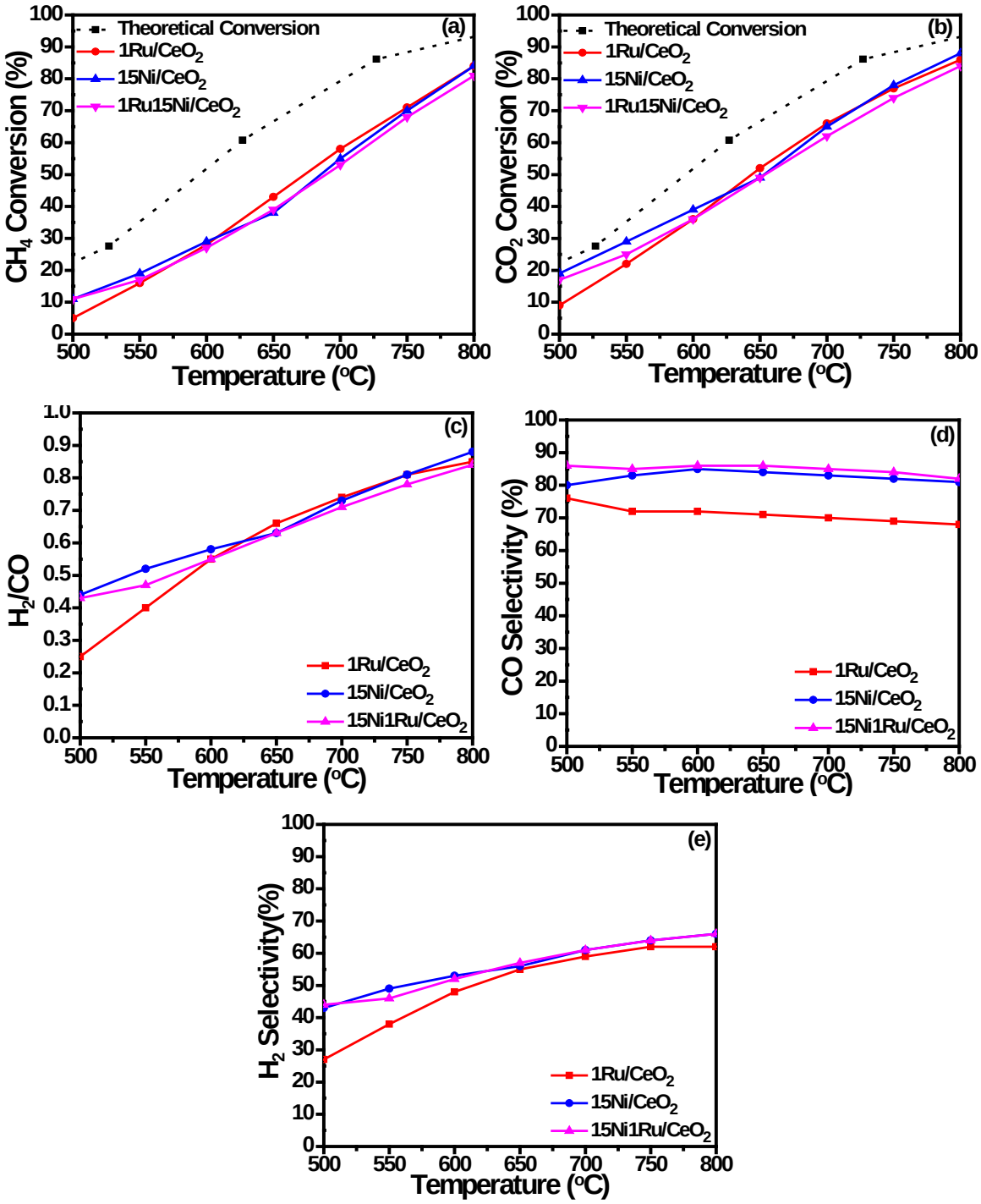

Figure 4.1: Catalytic performance of the different CeO_2 supported catalysts in the CO_2 reforming of methane

It is clear from the graph that as the temperature increases, the CO_2 and CH_4 conversion as well as the H_2/CO molar ratio and H_2 selectivity increase. At 500 ^oC, the lowest CO_2 and CH_4 conversions were obtained in the presence of the 1Ru/CeO_2 catalyst. As the temperature increases, 1Ru/CeO_2 activity increases and becomes close to the activity of 15Ni/CeO_2 and 15Ni1Ru/CeO_2 catalysts. At 800 ^oC, the CO_2 conversion reached 86 % for 1Ru/CeO_2, 88 % for 15Ni/CeO_2, and 84 % for the bi-metallic catalyst. Hence, the CH_4 and CO_2 conversions of 1 wt % Ru supported on CeO_2 were equivalent to those of 15 wt% Ni and combining the two metals did not show any improvement in the obtained conversions.

CO_2 conversions were always greater than CH_4 conversions indicating the spontaneity of the reverse water gas shift RWGS reaction that competes with DRM ($CO_2+H_2 \leftrightarrow CO+H_2O$) and consumes both CO_2 and H_2. The dominance of CO in comparison to H_2 and the H_2/CO molar ratio that were lower than unity at all temperatures are also an indication of the occurrence of the RWGS. However, the H_2/CO molar ratio and H_2 selectivity values increased with the increasing of temperature, suggesting a better selectivity towards the formation of syngas (H_2/CO) and hence the dominance of DRM at high temperatures [189]. It is noticed from figure 4.1 (d), that the 1Ru/CeO_2 catalyst has the lowest CO selectivity at all temperature ranges signifying that the RWGS is minimized in the presence of Ru which is in agreement with previously reported data [159,190].

4.1.1.2. Characterization after test

Thermal analysis

Figures 4.2 (a), (b) and (c) show the thermal analysis of the spent CeO_2 supported catalysts.

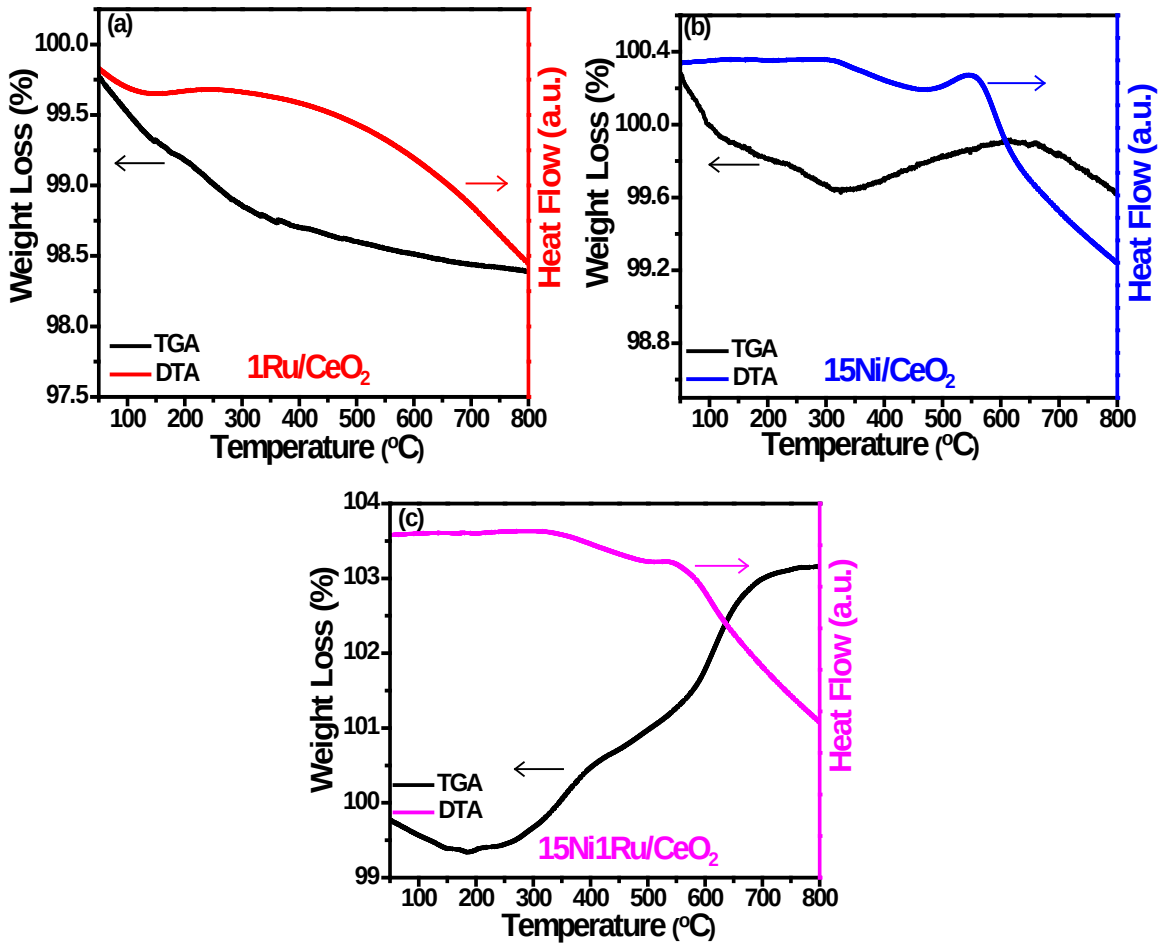

Figure 4.2: DTA/TGA curves of the spent (a) $1Ru/CeO_2$, (b) $15Ni/CeO_2$, and (c) $15Ni1Ru/CeO_2$ catalysts

The obtained DTA curve of $1Ru/CeO_2$ shows no exothermic peak in the studied temperature range. The DTA curves of $15Ni/CeO_2$ and $15Ni1Ru/CeO_2$ show a small exothermic peak in the 450 ^oC – 600 ^oC temperature range. This peak centered at 553 ^oC for $15Ni/CeO_2$ and at 537 ^oC for $15Ni1Ru/CeO_2$ is assigned to the oxidation of Ni particles and accompanied by a small mass gain in the same temperature range.

X-ray diffraction

Figures 4.3 (a) and (b) show respectively the XRD patterns of the CeO_2 supported catalysts after their reduction in a mixture of 5 % H_2/Ar at 800 ^oC for 2 h and after their usage in the DRM reaction.

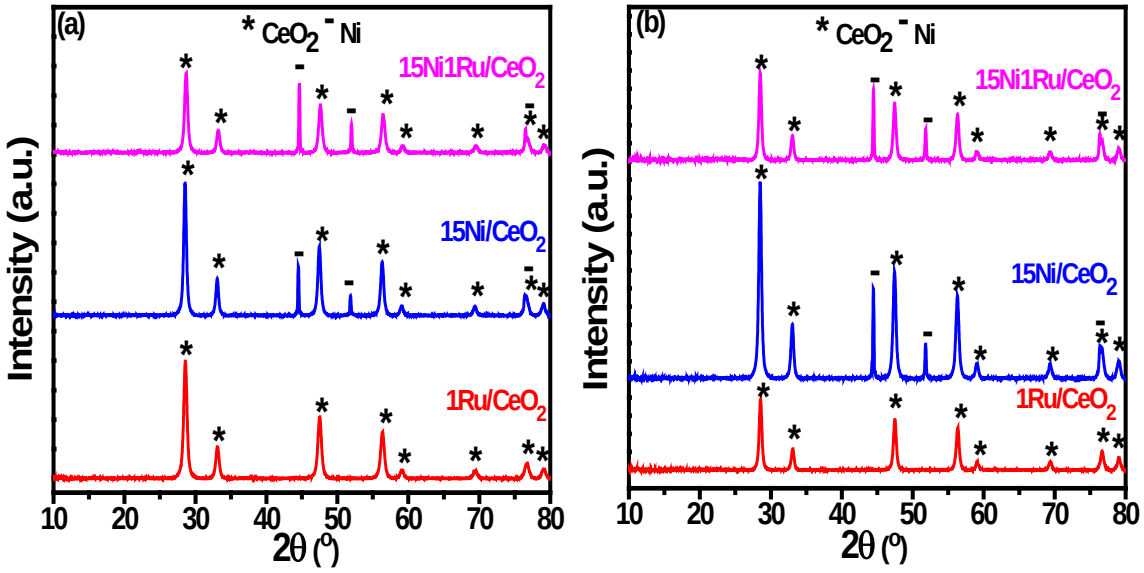

Figure 4.3: XRD patterns of the (a) reduced and (b) spent CeO_2 supported catalysts

The XRD profiles of all the reduced and spent catalysts are similar. Diffraction peaks attributed to the oxidized form of the CeO_2 support are present in all the diffractograms. This is due to the fact that Ce^{3+} can readily oxidize to Ce^{4+} in the presence of atmospheric oxygen. No Ru diffraction peaks were observed in the reduced and spent 1Ru/CeO_2 catalyst. The diffraction patterns of reduced and spent 15Ni/CeO_2 and 15Ni1Ru/CeO_2 catalysts show the presence of the metallic Ni phase. The absence of the NiO diffraction peaks that were present in the calcined catalysts suggests that NiO remained in the reduced form during the reaction and was not re-oxidized under the catalytic test conditions. Moreover, it is noticed from table 4.1, that the values obtained for Ni crystallite sizes of the spent catalysts are very close to the ones obtained after reduction meaning that the active phases constituting the catalysts remained intact despite the reforming conditions.

Table 4.1: Crystallite sizes of reduced and spent CeO_2 supported catalysts

Catalyst	Ni Crystallite Size (nm)	
	Reduced	Spent
1Ru/CeO_2	-	-
15Ni/CeO_2	42.5	43.2
15Ni1Ru/CeO_2	42.3	42.8

4.1.2. Al_2O_3 Supported Catalysts

4.1.2.1. Catalytic activity

Figures 4.4 (a), (b), (c), (d), and (e) show respectively the CH_4 conversion, CO_2 conversion, H_2/CO molar ratio, CO selectivity and the H_2 selectivity in the presence of the 1Ru/Al_2O_3, 15Ni/Al_2O_3 and 15Ni1Ru/Al_2O_3 catalysts.

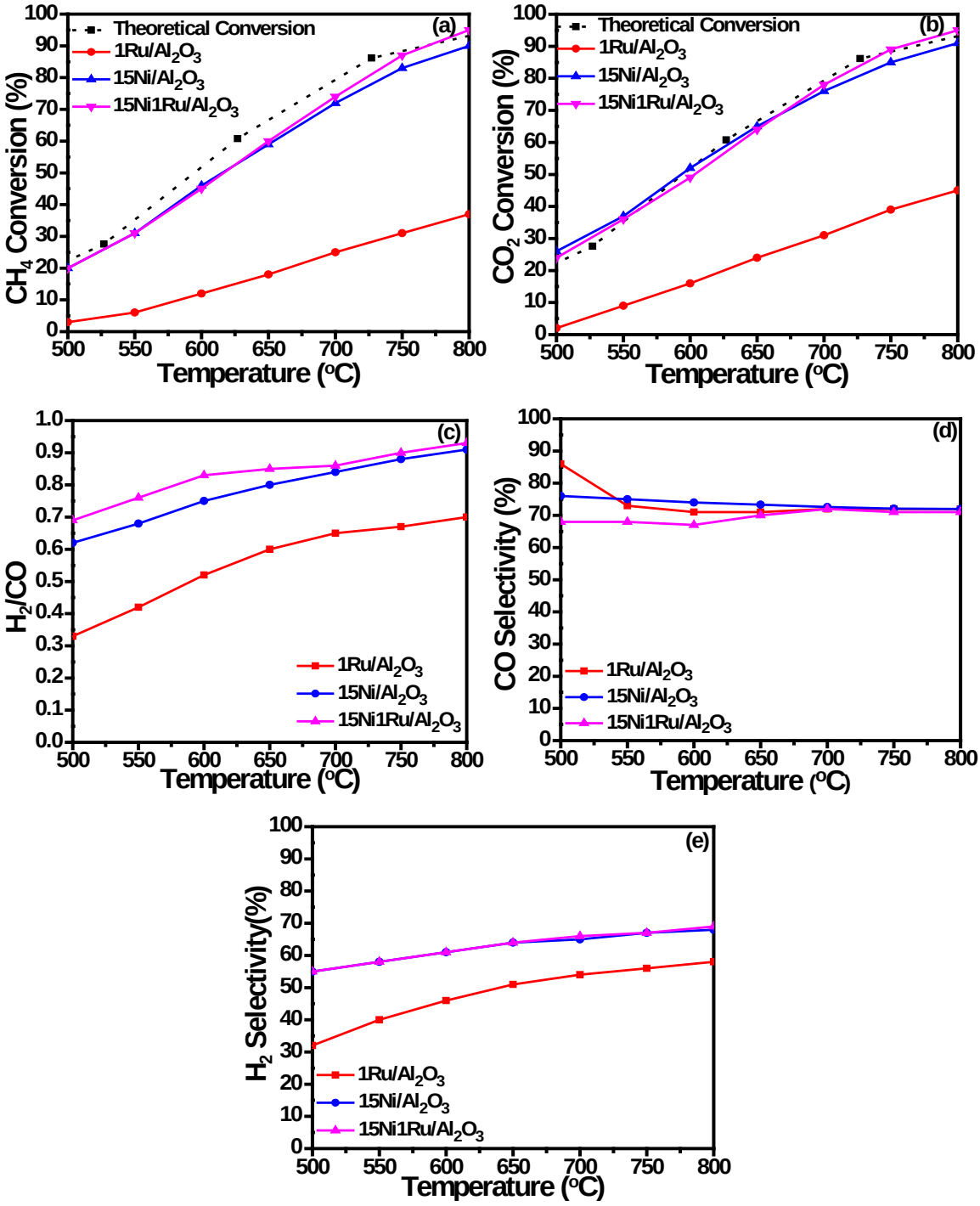

Figure 4.4: Catalytic performance of the different Al_2O_3 supported catalysts in the CO_2 reforming of methane

At all temperature ranges, the $1Ru/Al_2O_3$ catalyst records the lowest CO_2 and CH_4 conversion, H_2/CO molar ratio and H_2 selectivity. On the contrary, $15Ni/Al_2O_3$ and $15Ni1Ru/Al_2O_3$ catalysts show higher comparable conversion values and selectivity. At 800 ^oC, the bi-metallic catalyst gave the highest performance (94.6 % CH_4 conversion and 95 % CO_2 conversion). For alumina supported catalysts, the catalytic activity was determined by the active phase composition and amount. Indeed, at T≥ 700 ^oC, as the metal loading in the catalyst increases, the obtained CH_4 and CO_2 conversions and H_2/CO molar ratios increased. During the test, the CO_2 conversions were higher than the CH_4 conversions and the molar ratios H_2/CO were less than unity which suggests the contribution of the RWGS.

4.1.2.2. Characterization after test

Thermal analysis

Figures 4.5 (a), (b), and (c) show the thermal analysis of the spent Al_2O_3 supported catalysts.

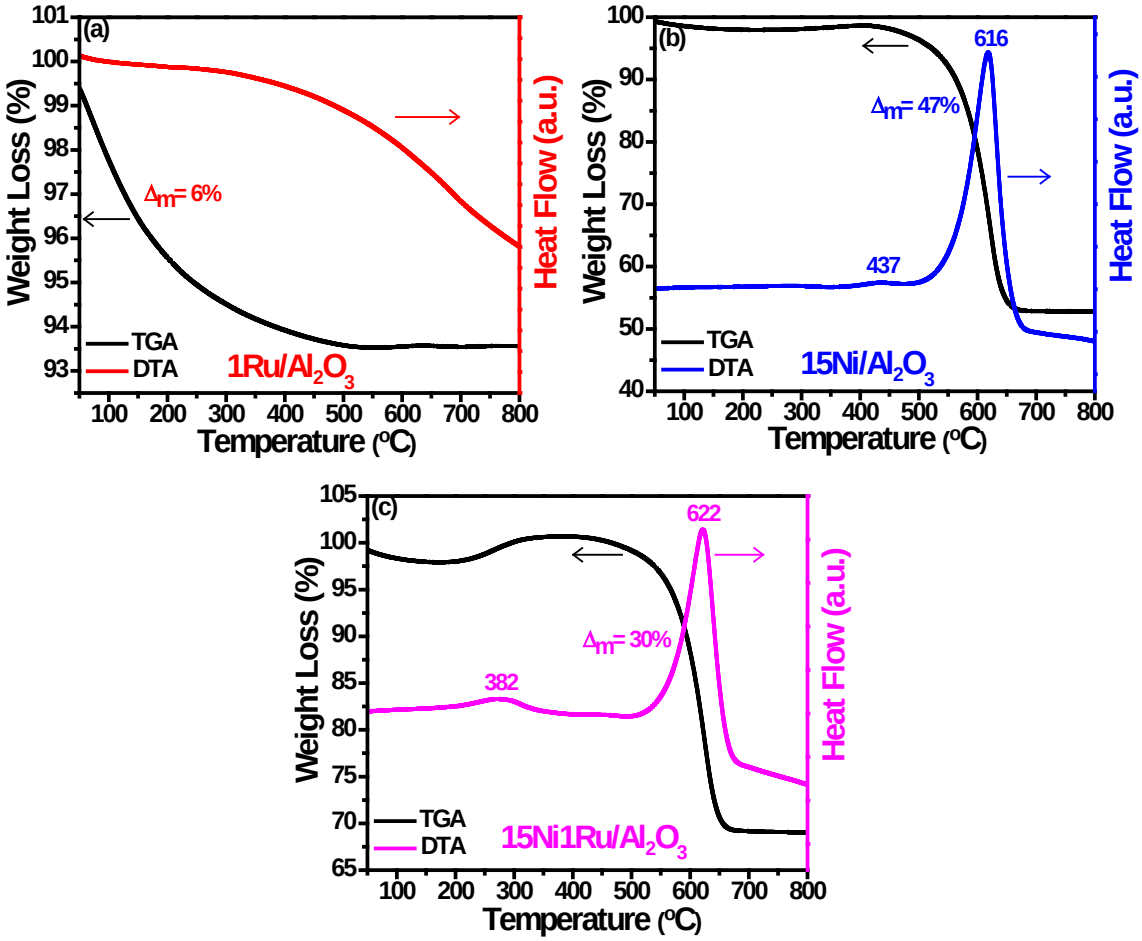

Figure 4.5: DTA/TGA curves of the spent (a) $1Ru/Al_2O_3$, (b) $15Ni/Al_2O_3$, and (c) $15Ni1Ru/Al_2O_3$ catalysts

The absence of any exothermic combustion peak on the DTA curve of the $1Ru/Al_2O_3$ catalyst indicates that no carbon was formed on its surface. This catalyst was the least active in the DRM reaction; moreover, Ru based catalysts do not favor carbon formation reactions. This is probably due to the ability of ruthenium species to provide a reactional pathway to adsorbed carbon species transforming them into gaseous compounds. The 6 % weight loss appearing on the TGA curve is caused by the departure of physisorbed water. The DTA curves of $15Ni/Al_2O_3$ and $15Ni1Ru/Al_2O_3$ show a main exothermic peak at 616 ^oC and 622 ^oC respectively attributed to the oxidation of graphitic carbon species [142,190]. These peaks are accompanied by a weight loss of 47 % and 30 % for $15Ni/Al_2O_3$ and $15Ni1Ru/Al_2O_3$ respectively. Therefore, it appears that for Ni based catalysts supported on alumina, the presence of Ru increased the resistance towards carbon deposition which is in agreement with relevant literature [143,159]. An additional peak centered at 437 ^oC for $15Ni/Al_2O_3$ and at 382 ^oC for $15Ni1Ru/Al_2O_3$ accompanied with a small weight gain in the same temperature range is present on the DTA/TGA curves of these catalysts and is assigned to the oxidation of Ni particles.

X-ray diffraction

Figures 4.6 (a) and (b) show respectively the XRD patterns of the Al_2O_3 supported catalysts after their reduction in a mixture of 5 % H_2/Ar at 800 ^oC for 2 h and after their usage in the DRM reaction.

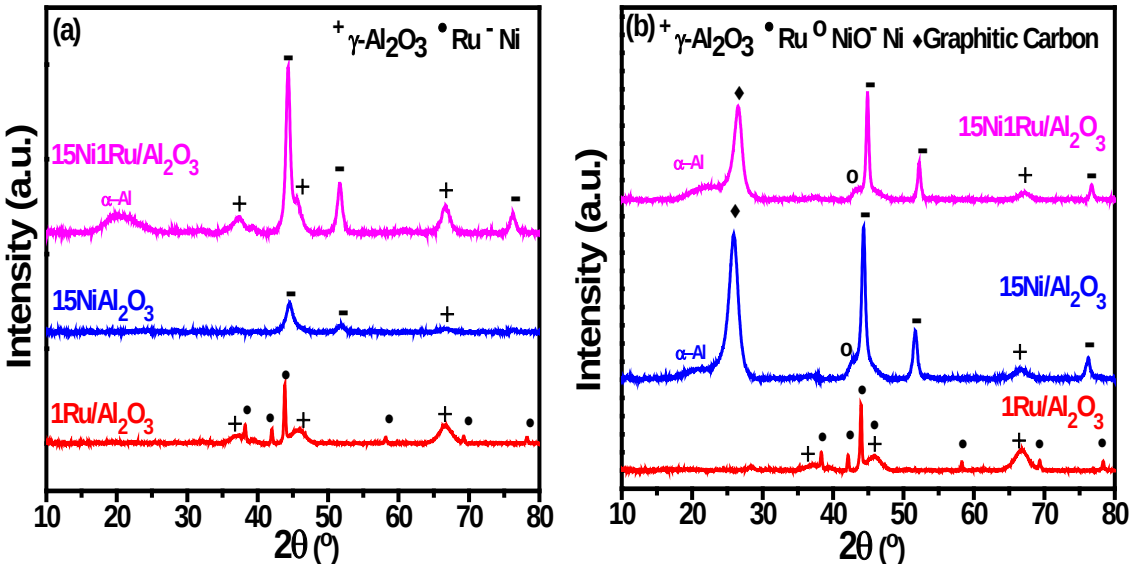

Figure 4.6: XRD patterns of the (a) reduced and (b) spent Al_2O_3 supported catalysts

The presence of the alumina characteristic peaks after reduction and after test confirms the irreducibility of this support that was already observed in the TPR analysis (chapter 2, figure 2.7). The XRD patterns of the reduced and spent $1Ru/Al_2O_3$ catalysts show reflections at $2\theta = 38^o$, 42^o, 44^o, 58^o, 69^o, and 78^o typical of metallic Ru (JCPDS 06-0663). Ni peaks were present for the reduced and spent $15Ni/Al_2O_3$ and $15Ni1Ru/Al_2O_3$ catalysts. The XRD patterns of the spent $15Ni/Al_2O_3$ and $15Ni1Ru/Al_2O_3$ catalysts also show a peak at $2\theta = 27^o$ assigned to graphitic carbon (JCPDS 75-1621) which is in agreement with the DTA/TGA results. This peak is less intense for the $15Ni1Ru/Al_2O_3$ catalyst indicating a lower amount of deposited carbon compared to $15Ni/Al_2O_3$. The presence of part of Ni in the oxidized form (NiO peak at $2\theta = 43.2^o$) on the XRD patterns of spent $15Ni/Al_2O_3$ and $15Ni1Ru/Al_2O_3$ indicates that Ni was also engaged in a redox cycle during the reaction. In addition, it is noticed from table 4.2 that the values obtained for Ni crystallite sizes after test are higher than the ones obtained after reduction as a consequence of a possible active phase agglomeration occurring during the reaction.

Table 4.2: Crystallite sizes of reduced and spent Al_2O_3 supported catalysts

Catalyst	Ru Crystallite Sizes (nm)		Ni Crystallite Sizes (nm)	
	Reduced	Spent	Reduced	Spent
$1Ru/Al_2O_3$	32	31	-	-
$15Ni/Al_2O_3$	-	-	7.5	20.4
$15Ni1Ru/Al_2O_3$	-	-	13.6	18.6

4.1.3. Discussion

- It appears from the dynamic tests that the catalytic activity of the $1Ru/Al_2O_3$ catalyst (figure 4.4) is much lower than that of $1Ru/CeO_2$ (figure 4.1). This activity trend is in accordance with a report given by Safariamin et al. [191] where the activity of a 5 wt% Ru impregnated on CeO_2 was found to be higher than the activity of a 5 wt% Ru impregnated on Al_2O_3 mainly for reducibility reasons. Indeed, from chapter 2, the TPR results (parts 2.1.2.3. and 2.2.2.3.) validated that RuO_2 species are more easily reduced in the presence of CeO_2 compared to Al_2O_3 because of the special interaction between Ru and Ce and the formation of easily reducible Ru-O-Ce bond.

- The higher activity of Ni and Ni-Ru supported on Al_2O_3 compared to Ni and Ni-Ru supported on CeO_2 might be attributed to their higher surface areas and lower crystallite sizes that greatly improve the active site accessibility [192].
- Despite the fact that they revealed lower catalytic performances, CeO_2 supported catalysts were resistant to carbon formation. In fact, CeO_2 supports are widely investigated because they seem to be the most promising in limiting deactivation due to carbon deposition through the gasification of the deposited carbon. This property is owed to the oxygen storing capacity of CeO_2 attributable to the presence of the redox couple Ce^{4+}/Ce^{3+}.
- The superior catalytic activity of $15Ni/Al_2O_3$ and $15Ni1Ru/Al_2O_3$ catalysts, the presence of weak Ni-support interactions (chapter 2, part 2.2.2.3) as well as the high Ni loading (15 wt%) contributed to a considerable deposition of carbon on the surface of these catalysts. This carbon may have been generated by the methane decomposition reaction ($CH_{4\,(g)} \leftrightarrow C_{(s)} + 2H_{2\,(g)}$) that produces additional H_2 and is favorable at T > 500 ^oC, and by the Boudouard reaction ($2CO_{(g)} \leftrightarrow CO_{2\,(g)} + C_{(s)}$) that forms CO_2 and decreases conversion and is favorable at T < 750 ^oC [71].
- Our results showed that the presence of Ru enhances the activity of the monometallic $15Ni/Al_2O_3$ catalyst in the DRM reaction and also decreases carbon formation. Different authors [143,159,193] reported that the incorporation of ruthenium in the proximity of active nickel sites stabilizes a reduced surface while promoting carbon gasification by limiting the accumulation of carbon inside the nickel particle.

4.2. CO_2 Reforming of Methane over Ce-Al_2O_3 Supported Catalysts

In this part, CeO_2 is used as a promoter for Al_2O_3 supported catalysts. This allows the combination of the large surface area of such mesoporous supports with the oxygen storage and release capability of CeO_2. Moreover, one adopted approach for alumina stabilization is doping or mixing with different metal oxides as a stabilizing agent [194]. Several researches investigate the use of ceria as a stabilizing agent for alumina and ceria/alumina is a very promising combination for the dry reforming of methane [195].

4.2.1. Catalysts Preparation

Synthesis of Al_2O_3 promoted with Ce (Ce-Al_2O_3 support)

The same procedure used to synthesize Ce_{60}KIT-6 (chapter 2, part 3.2.1.) was adopted to synthesize the Ce-Al_2O_3 support with Al_2O_3 as the template and with 60 wt% Ce loading.

Synthesis of Ce-Al_2O_3 supported catalysts

The wet impregnation technique previously described (chapter 2, part 2.1.1.) was used to synthesize the Ni and/or Ru based catalysts supported on Al_2O_3 promoted with Ce. The active phase percentages remained the same (1 wt% Ru, 15 wt% Ni, and 15 wt% Ni – 1 wt% Ru). The obtained catalysts are named: 1Ru/Ce-Al_2O_3, 15Ni/Ce-Al_2O_3, and 15Ni1Ru/Ce-Al_2O_3.

4.2.2. Catalysts Characterization

4.2.2.1. X-ray diffraction analyses (XRD)

Figure 4.7 shows the wide angle XRD patterns of the calcined Ce-Al_2O_3, 1Ru/Ce-Al_2O_3, 15Ni/Ce-Al_2O_3, and 15Ni1Ru/Ce-Al_2O_3 catalysts. Table 4.3 lists the obtained crystallite sizes of the catalysts.

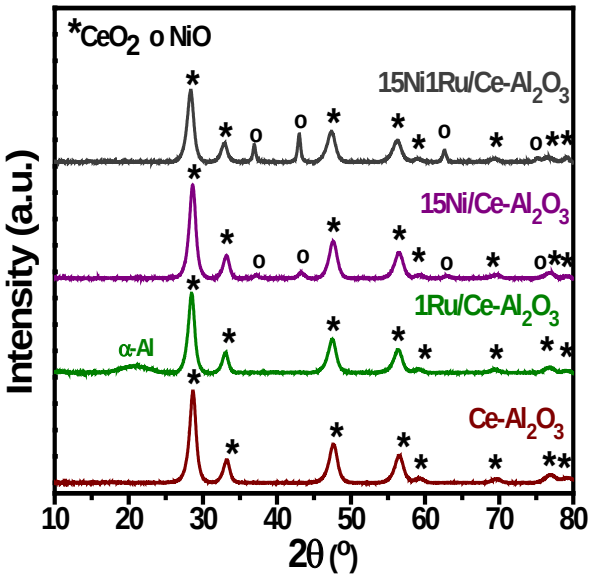

Figure 4.7: XRD patterns of Ce-Al_2O_3 supported catalysts after calcination at 550 °C

In all patterns, XRD reflections typical of ceria fluorite phase are present. Interestingly, the 1Ru/Ce-Al_2O_3 diffraction pattern didn't present any RuO_2 diffraction peaks. The addition of Ce allowed a good dispersion of RuO_2 compared to the non-promoted Al_2O_3 mesoporous support (chapter 2, figure 2.5). NiO peaks are present in 15Ni/Ce-Al_2O_3 and 15Ni1Ru/Ce-Al_2O_3 catalysts. Table 4.3 shows that CeO_2 crystallite sizes are similar in all Ce-Al_2O_3 supported catalysts and that NiO crystallite sizes of 15Ni1Ru/Ce-Al_2O_3 (18.4 nm) are larger than those of 15Ni/Ce-Al_2O_3 (9.2 nm). In addition, NiO crystallite sizes are larger in the promoted catalysts compared to the non-promoted 15Ni/Al_2O_3 (8 nm) and 15Ni1Ru/Al_2O_3 (15.4 nm) catalysts (chapter 2, table 2.4).

Table 4.3: Crystallite sizes of Ce-Al_2O_3 supported catalysts

Catalyst	Crystallite Size (nm)	
	CeO_2	NiO
Al_2O_3	-	-
Ce-Al_2O_3	8.2	-
1Ru/Ce-Al_2O_3	8.3	-
15Ni/Ce-Al_2O_3	7.8	9.2
15Ni1Ru/Ce-Al_2O_3	8	18.4

4.2.2.2. N_2 adsorption/desorption analyses

Figures 4.8 (a) and (b) present the nitrogen adsorption/desorption isotherms and pore size distributions of Ce-Al_2O_3 supported catalysts. The corresponding textural parameters are also reported in table 4.4.

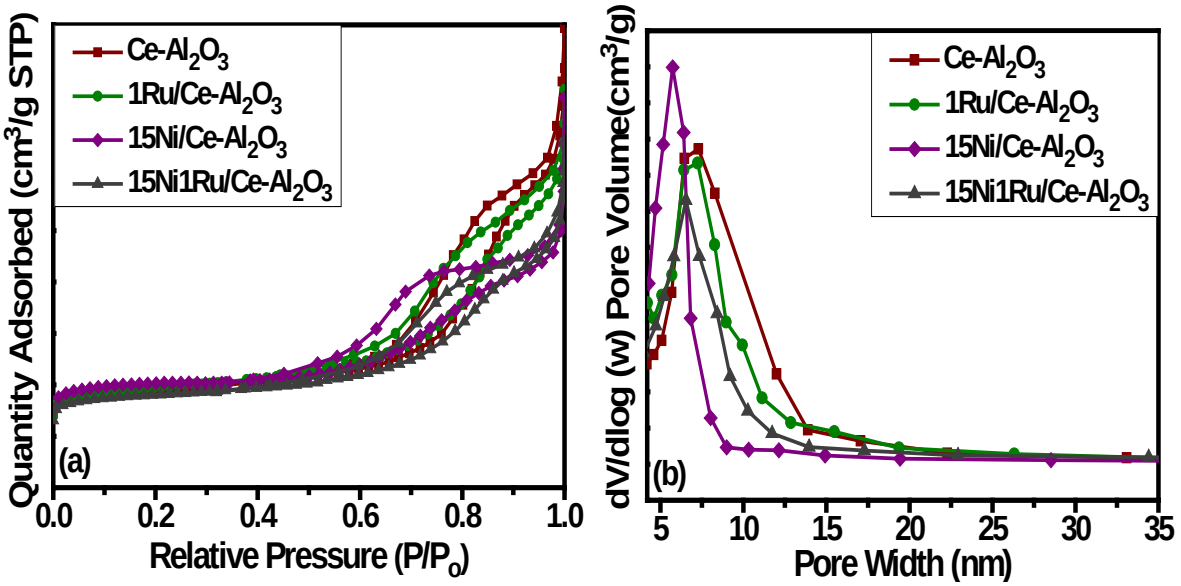

Figure 4.8: (a) N_2 adsorption/desorption isotherms and (b) Pore size distributions of Ce-Al_2O_3 supported catalysts

The Ce-Al_2O_3 supported catalysts isotherms show a type IVa isotherm with H3 hysteresis loops. The shape of these isotherms is irregular compared to those obtained for Al_2O_3 supported catalysts and presented in chapter 2 (figure 2.6 (a)). It seems that promoting the support with Ce partially modified the mesoporous structure. The presence of Ce drastically decreased the surface area and pore volume of Al_2O_3 from 380 m^2/g to 74 m^2/g and from 1.86 cm^3/g to 0.32 cm^3/g respectively (table 4.4) as a consequence of the partial filling of the pore

structures in the Al_2O_3 support. It appears that most of the area of Al_2O_3 was covered by ceria as a result of the high CeO_2 percentage (60 wt%) compared to Al_2O_3. This trend was observed for all the Ce promoted catalysts with a surface area loss ranging between ~70 % and ~76 % and a pore volume reduction of ~83 % compared to the non-promoted counter-parts (chapter 2, table 2.5). From figure 4.8 (b) and table 4.4, all catalysts present one type of mesopore with a pore size distribution ranging between 5 nm and 15 nm.

Table 4.4: Textural properties of Ce-Al_2O_3 supported catalysts

Catalysts	Specific Surface Area (m^2/g)	Pore Volume (cm^3/g)	Pore Diameter (nm)
Al_2O_3	380	1.86	14.2
Ce-Al_2O_3	74	0.32	7.3
1Ru/Ce-Al_2O_3	78	0.27	7.2
15Ni/Ce-Al_2O_3	80	0.26	5.7
15Ni1Ru/Ce-Al_2O_3	67	0.23	6.5

4.2.2.3. H_2- Temperature programmed reduction analyses (H_2-TPR)

Figure 4.9 shows the obtained deconvoluted H_2-TPR profiles of Ce-Al_2O_3 supported catalysts. Table 4.5 lists the total experimental and theoretical hydrogen consumptions obtained.

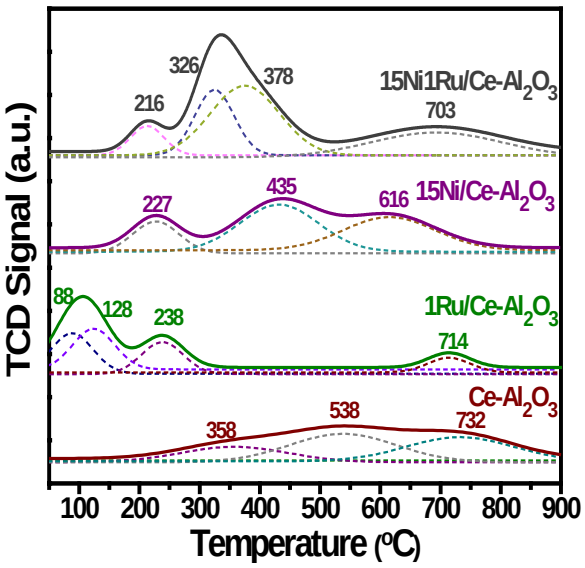

Figure 4.9: H_2-TPR profiles of Ce-Al_2O_3 supported catalysts

The TPR profile of Ce-Al_2O_3 support presents three peaks: the first two peaks are attributed to the reduction of small surface Ce^{4+} species whereas the third higher temperature peak corresponds to the reduction of large and bulk ceria particles [189,196].

The TPR profile of 1Ru/Ce-Al_2O_3 catalyst exhibits two deconvoluted reduction peaks at 88 ^oC and 128 ^oC and one reduction peak at 238 ^oC. From the H_2 consumptions (table 4.5), these peaks correspond to the simultaneous reduction of RuO_2 and easily reducible species on the CeO_2 surface. The reason behind this simultaneous reduction is the selective reduction of CeO_2 in the vicinity of Ru species facilitated by the spillover of hydrogen molecules [148,152,197].

The TPR profile of 15Ni/Ce-Al_2O_3 shows three reduction peaks. The first peak detected at 227 ^oC can be associated with NiO interacting with surface ceria (NiO–CeO_2) and the second peak at 435 ^oC to NiO species with weak interaction with the alumina support NiO–Al_2O_3 [198].

For 15Ni1Ru/Ce-Al_2O_3 catalyst, the H_2-TPR profiles and the hydrogen consumptions obtained (table 4.5) show that the first peak centered at 216 ^oC is assigned to the simultaneous reduction of RuO_2 and some NiO interacting with CeO_2. The second and third peaks at 326 ^oC and 378 ^oC are attributed to the reduction of NiO-Al_2O_3 species. NiO reduction temperatures were shifted to lower ranges in the bi-metallic catalyst (from 227 ^oC and 435 ^oC for 15Ni/Ce-Al_2O_3 to 216 ^oC, 326 ^oC, and 378 ^oC for 15Ni1Ru/Ce-Al_2O_3). This validates the beneficial role of Ru in facilitating the reduction of NiO. Finally, the higher temperature reduction peak for all Ce-Al_2O_3 supported catalysts is assigned to the reduction of bulk ceria species.

Table 4.5: Experimental and theoretical H_2 consumptions of Ce-Al_2O_3 supported catalysts

Catalyst	H_2 consumption [µmol H_2/g catalyst]								
	Experimental Consumption					Theoretical Consumption			
	I	II	III	IV	Total	NiO/Ni	RuO_2/Ru	Ce^{4+}/Ce^{3+}	Total
Ce-Al_2O_3	369	678	-	558	**1605**	-	-	1743	**1743**
Ru/Ce-Al_2O_3	367	384	302	139	**1192**	-	200	1720	**1920**
Ni/Ce-Al_2O_3	638	1589	-	1305	**3532**	2871	-	1423	**4294**
Ni-Ru/Ce-Al_2O_3	662	526	2308	428	**3924**	2871	200	1409	**4480**

Figures 4.10 (a), (b), and (c) compare the H_2-TPR profiles obtained for the Al_2O_3 supported catalysts and their Ce-Al_2O_3 counter-parts.

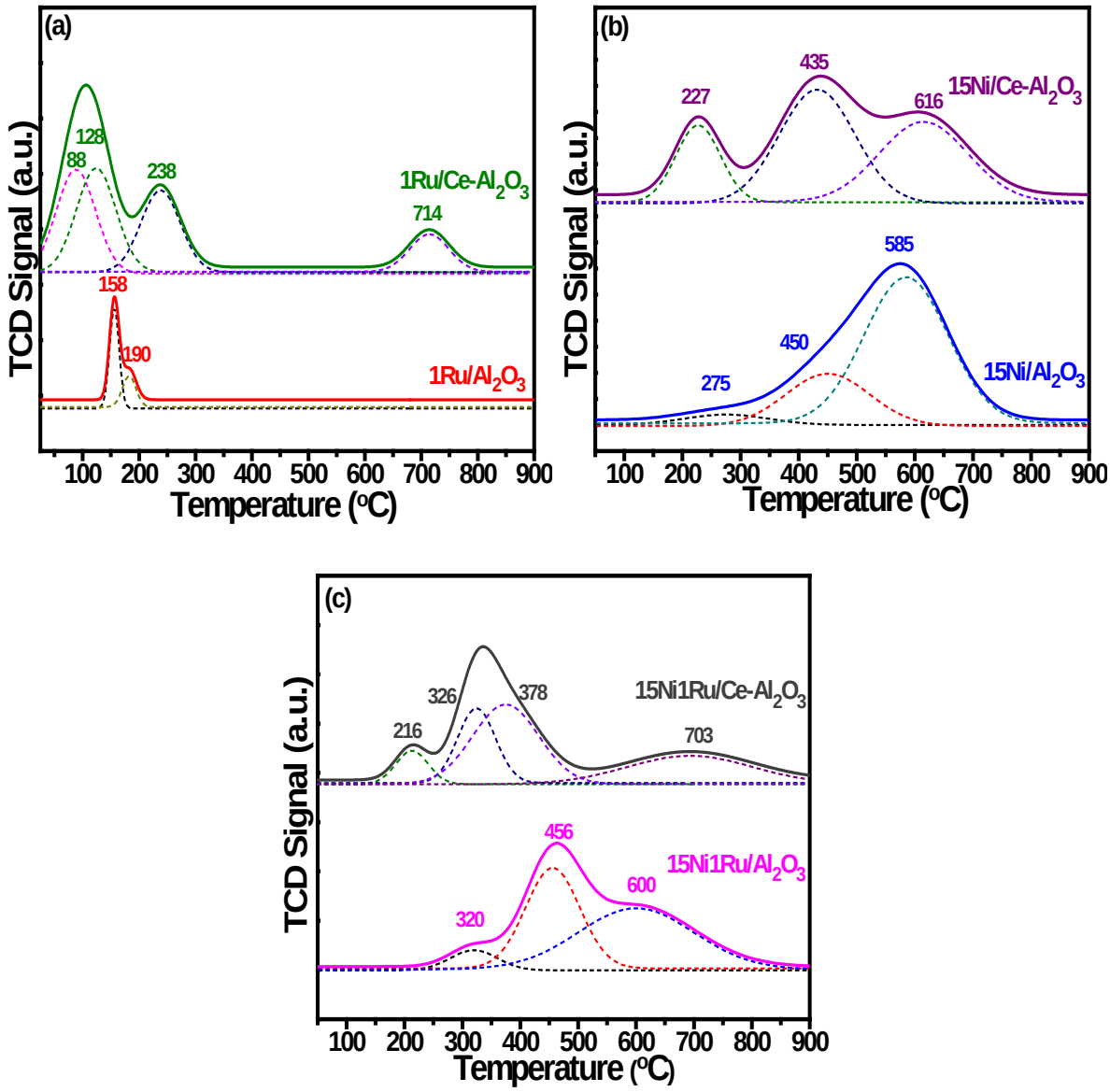

Figure 4.10: H_2-TPR profiles of (a) 1Ru, (b) 15Ni, and (c) 15Ni1Ru based catalysts supported on Al_2O_3 and Ce-Al_2O_3

Compared to the TPR profile of 1Ru/Al_2O_3 catalyst, the addition of ceria led to more readily reducible ruthenium oxide species. This is evident as the RuO_2 reduction peak shifted from 158 ^oC and 190 ^oC (1Ru/Al_2O_3) to 88 ^oC and 128 ^oC (1Ru/Ce-Al_2O_3). The special interaction established between ruthenium and cerium oxide species facilitates the formation of well dispersed, easily reducible ruthenium oxide species which is in agreement with XRD results.

In addition, in the presence of Ce, the three NiO reduction peaks at 275 ^oC, 450 ^oC, and 585 ^oC that were attributed to NiO in weak interaction with Al_2O_3 (chapter 2, part 2.2.2.3) were shifted to two lower temperature peaks: one peak at 227 ^oC attributed to small NiO particles not interacting with the support and one peak at 435 ^oC assigned to the presence of a different NiO particle size weakly interacting with the Al_2O_3 support. The peak at 616 ^oC is attributed to the large amount of bulk ceria in the promoted catalyst. Furthermore, the hydrogen consumptions (table 4.5) of the peaks at 227 ^oC (638 µmol/g) and at 435 ^oC (1589 µmol/g) for the 15Ni/Ce-Al_2O_3 catalyst are much higher than those of at 275 ^oC (128 µmol/g) and 450 ^oC (642 µmol/g) for the 15Ni/Al_2O_3 catalyst (chapter 2, table 2.6). This shift in the peak temperatures and higher hydrogen consumptions indicate that more NiO are being reduced at lower temperatures due to the presence of ceria that facilitates the formation of small easily reducible NiO particles.

Similar conclusions are observed from the comparison of the TPR profiles of 15Ni1Ru/Al_2O_3 and 15Ni1Ru/Ce-Al_2O_3.

4.2.2.4. CO_2-Temperature programmed desorption analyses (CO_2-TPD)

Figure 4.11 shows the deconvoluted CO_2-TPD profiles obtained for Ce-Al_2O_3 supported catalysts. Table 4.6 lists their total CO_2 desorbed amount.

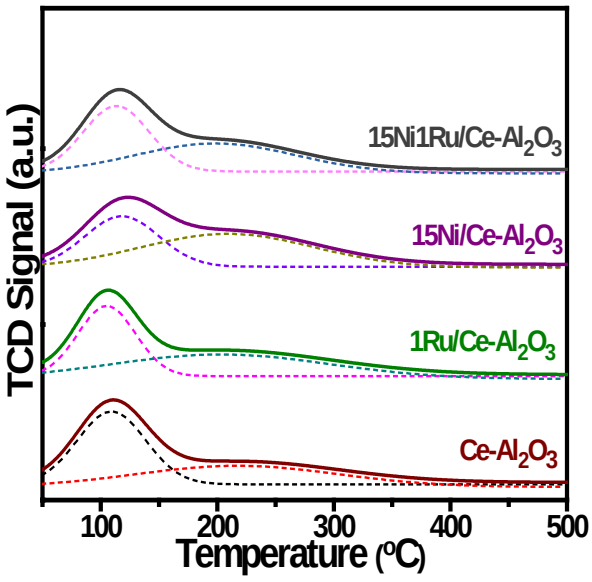

Figure 4.11: CO_2-TPD profiles of Ce-Al_2O_3 supported catalysts

The CO_2-TPD profiles of the promoted catalysts reveal that most CO_2 molecules are desorbed around 100 ^oC. This indicates that most CO_2 adsorption occurred on weak basic sites after Ce promotion. Moderate basic sites were also present in all the catalysts but in lower concentrations compared to the weak basic sites.

Table 4.6: CO_2 desorbed quantities of Ce-Al_2O_3 supported catalysts

Catalyst	CO_2 quantity [µmol CO_2/g catalyst]
Ce-Al_2O_3	391
1Ru/Ce-Al_2O_3	396
15Ni/Ce-Al_2O_3	436
15Ni1Ru/Ce-Al_2O_3	331

Figures 4.12 (a), (b), and (c) compare the CO_2-TPD profiles of the Al_2O_3 supported catalysts and their Ce-Al_2O_3 counter-parts.

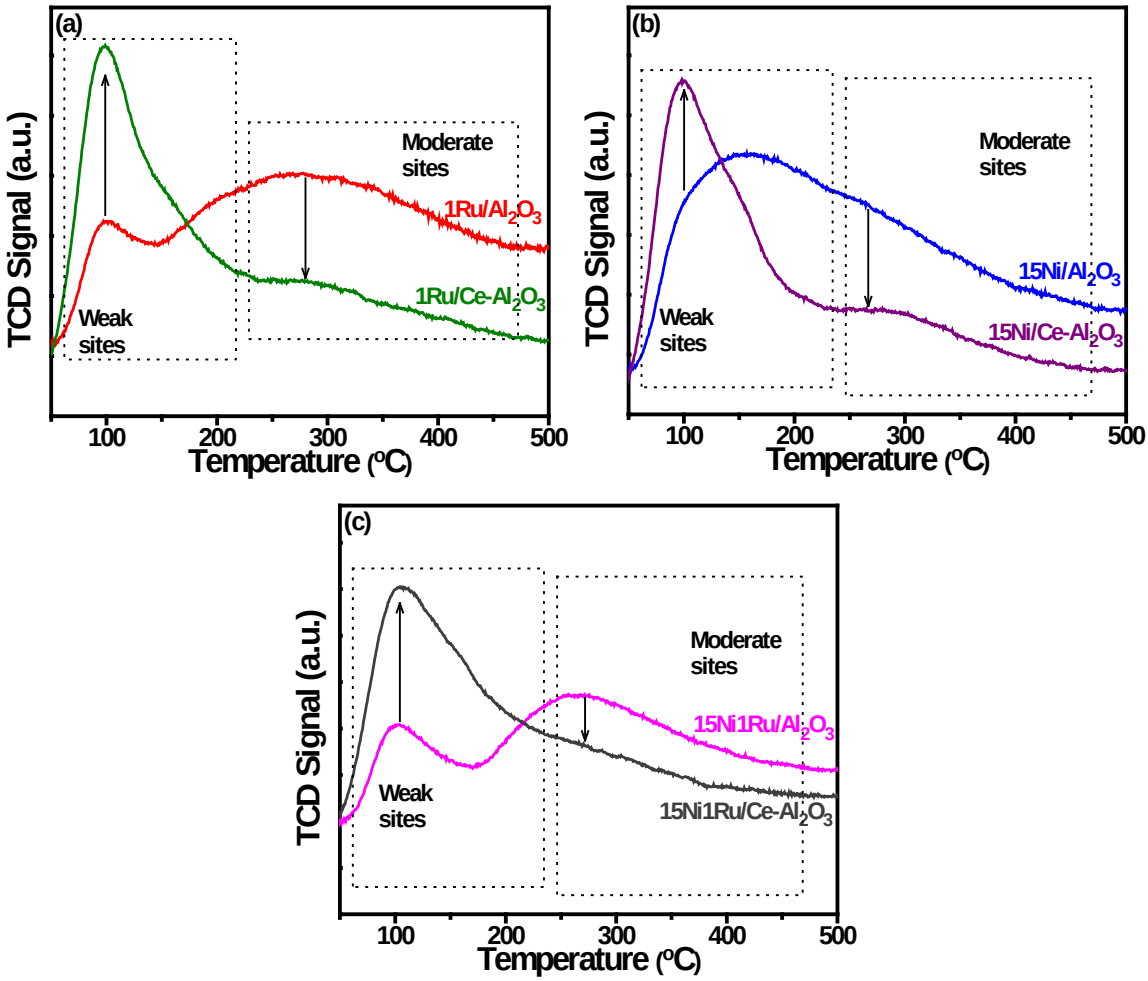

Figure 4.12: CO_2-TPD profiles of (a) 1Ru, (b) 15Ni, and (c) 15Ni1Ru based catalysts supported on Al_2O_3 and Ce-Al_2O_3

For all catalysts, promoting the Al_2O_3 support with Ce increased the amount of weak basic sites while decreasing the number of moderate basic sites that were present in the non-promoted catalysts. This is expected for a mixture containing 60 wt% Ce as the CO_2-TPD analysis of CeO_2 supported catalysts (chapter 2, part 2.1.2.4.) containing 100 wt% Ce showed the dominance of weak basic sites. After Ce addition, the total basicity increased by 31 µmol/g for Al_2O_3, by 25 µmol/g for $1Ru/Al_2O_3$, by 17 µmol/g for $15Ni/Al_2O_3$, and by 45 µmol/g for $15Ni1Ru/Al_2O_3$.

4.2.2.5. Discussion

- XRD analyses showed that the addition of Ce to the support allowed a good dispersion of RuO_2 species that were crystallized in the non-promoted catalyst.
- The porous structure was partially destroyed as a result of Ce addition.
- TPR analyses for all the catalysts showed that active phase reduction is enhanced after Ce addition.
- The addition of Ce increased the amount of weak basic sites of the catalysts.

4.2.3. Catalytic Activity

In the same CO_2 reforming of methane catalytic test conditions (P = 1 atm, CH_4/CO_2 = 1, temperature range: 500 ^oC – 800 °C, GHSV: 60,000 h^{-1}, and total flow = 100 ml/min) of the non-promoted catalysts, the catalytic activity of the Ru, Ni and Ni-Ru supported on Al_2O_3 catalysts will be compared with and without promoting Al_2O_3 with 60 wt% Ce.

4.2.3.1. Catalytic activity of $1Ru/Al_2O_3$ and $1Ru/Ce\text{-}Al_2O_3$

The effect of promoting Al_2O_3 with Ce on the catalytic activity of $1Ru/Al_2O_3$ is shown on figure 4.13.

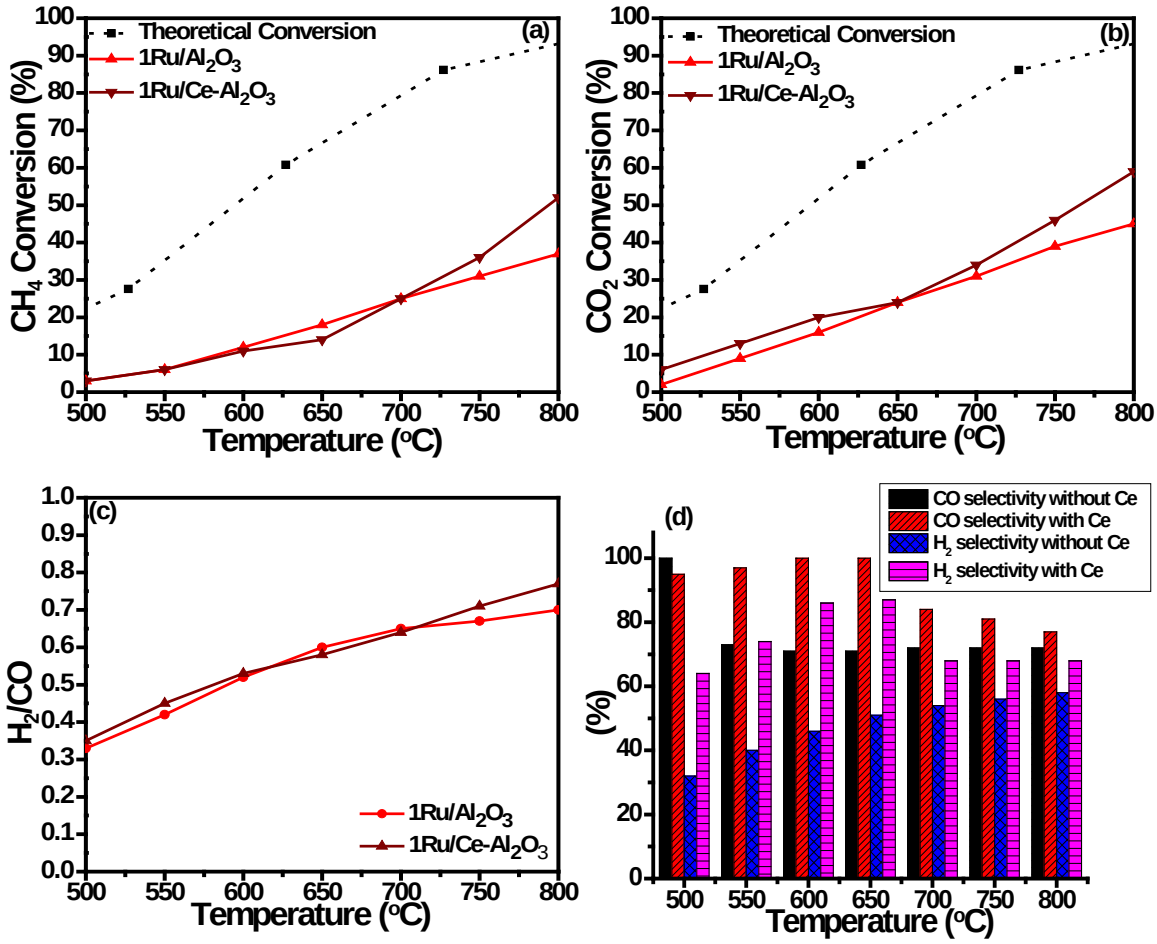

Figure 4.13: Effect of promoting Al_2O_3 with Ce on the (a) CH_4 conversion, (b) CO_2 conversion, (c) H_2/CO molar ratio, and (d) CO and H_2 selectivity of $1Ru/Al_2O_3$

At temperatures ≤ 700 °C, the presence of Ce did not enhance the catalytic activity of the $1Ru/Al_2O_3$ catalyst. At 800 °C, the CH_4 and CO_2 conversions were higher by 15 % and 14 % respectively following Ce addition. From figure 4.13 (d), it is noticed that in the 550 °C – 800 °C temperature range, CO selectivity in the presence of Ce is higher than CO selectivity without Ce. Moreover, H_2 selectivity is higher in the presence of Ce at all temperature values. This indicates that the presence of Ce yielded catalysts that are more selective towards H_2 and CO production. In addition, for $1Ru/Ce\text{-}Al_2O_3$, starting at T ≥ 650 °C, H_2 selectivity decreased with temperature and CO selectivity was higher than that of H_2 at all temperature ranges indicating that the RWGS is starting to operate.

4.2.3.2. Catalytic activity of 15Ni/Al_2O_3 and 15Ni/Ce-Al_2O_3

The effect of promoting Al_2O_3 with Ce on the catalytic activity of 15Ni/Al_2O_3 is shown on figure 4.14.

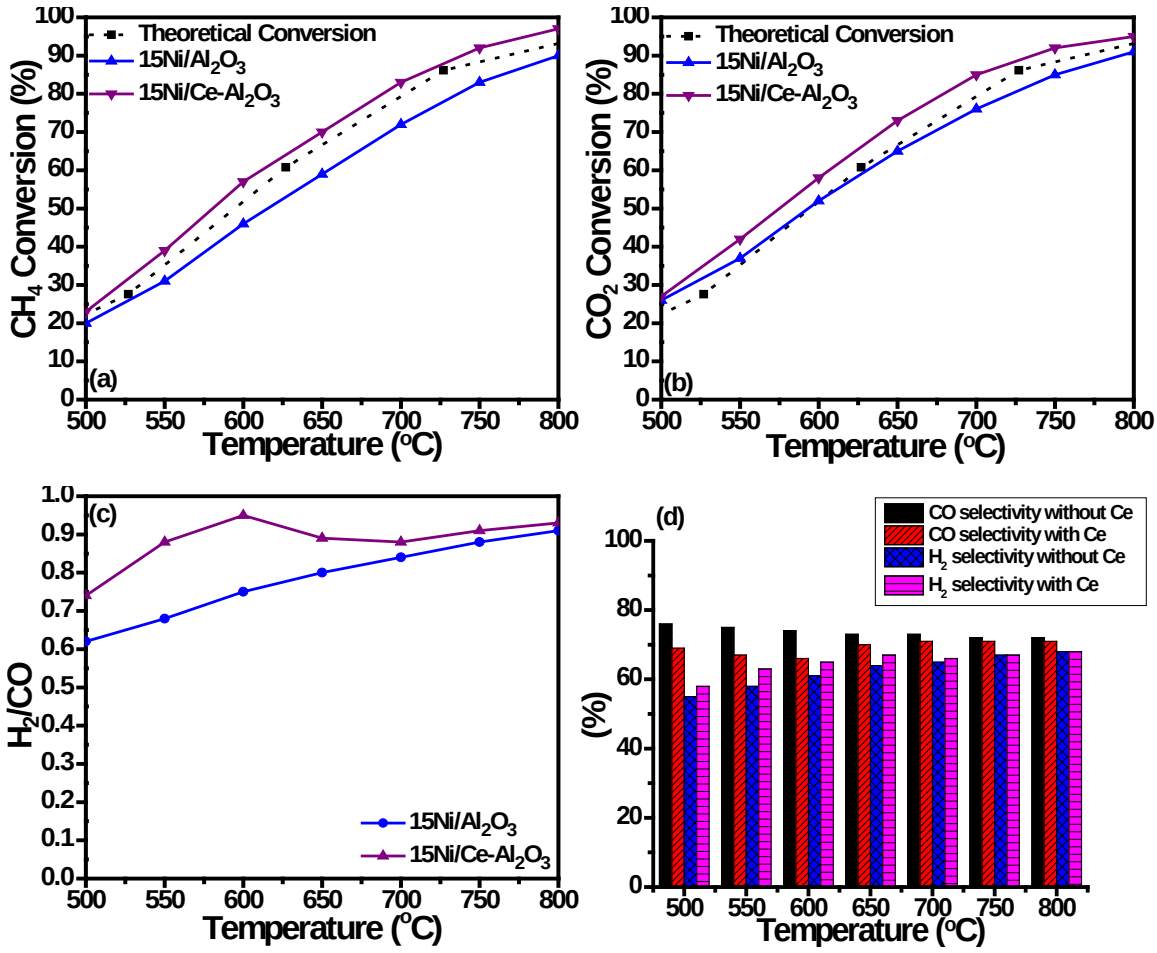

Figure 4.14: Effect of promoting Al_2O_3 with Ce on the (a) CH_4 conversion, (b) CO_2 conversion, (c) H_2/CO molar ratio, and (d) CO and H_2 selectivity on 15Ni/Al_2O_3

It is clear from the obtained results that Ce promotion led to higher CH_4 and CO_2 conversions over all the studied temperature ranges compared to those recorded for the 15Ni/Al_2O_3 catalyst. The CH_4 and CO_2 conversion curves for the 15Ni/Ce-Al_2O_3 catalyst exceed the thermodynamic DRM curve. According to Gennequin et al. [190], experimental results showing conversions above the equilibrium curves suggest the dominance of carbon formation reactions. The H_2/CO molar ratio increases in the presence of Ce, and reaches a maximum of 0.95 at 600 °C. Moreover, at this temperature, CO selectivity is the lowest (figure 4.14 (d)) for the 15Ni/Ce-Al_2O_3 catalyst indicating the dominance of the Boudouard reaction that consumes CO.

4.2.3.3. Catalytic activity of 15Ni1Ru/Al_2O_3 and 15Ni1Ru/Ce-Al_2O_3

The effect of promoting Al_2O_3 with Ce on the catalytic activity of 15Ni1Ru/Al_2O_3 is shown on figure 4.15.

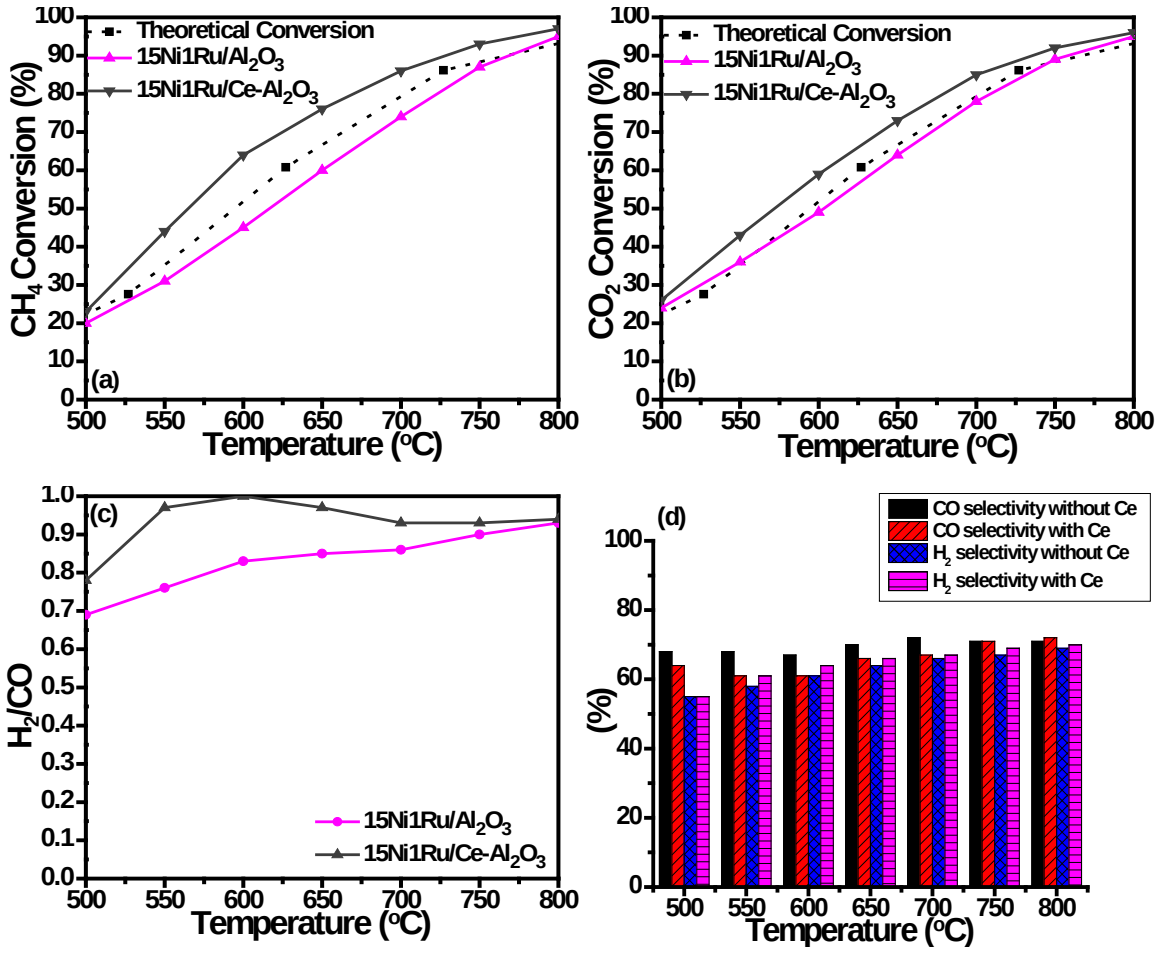

Figure 4.15: Effect of promoting Al_2O_3 with Ce on the (a) CH_4 conversion, (b) CO_2 conversion, (c) H_2/CO molar ratio, and (d) CO and H_2 selectivity of 15Ni1Ru/Al_2O_3

In the 550 °C – 700 °C temperature range, a large difference was observed between the CH_4 and CO_2 conversion curves of non-promoted and promoted 15Ni1Ru/Al_2O_3. For the latter, the conversion curves are higher than the equilibrium curves which is explained by the occurrence of secondary reactions. In addition, the CH_4 conversions were slightly greater than CO_2 conversions at all temperature ranges. Xia et al. [199] investigated the secondary reactions behind the shift towards more CH_4 and less CO_2 conversions: thermal cracking of CH_4 into H_2 and carbon black increases the conversion of methane, whereas CO disproportionation (Boudouard reaction) and water gas shift reactions replenish the CO_2 consumed causing a decrease in CO_2 conversion. Finally, for the 15Ni1Ru/Ce-Al_2O_3 catalyst,

the H_2/CO molar ratio increases in the 550 °C – 650 °C temperature range and is greater than 1 at 600 °C. Elevated H_2/CO values imply pronounced occurrence of the methane cracking reaction and/or Boudouard reaction [127].

4.2.3.4. Characterization after test

Thermal analysis

Figures 4.16 (a), (b), and (c) show the thermal analysis of the spent Ce-Al_2O_3 supported catalysts.

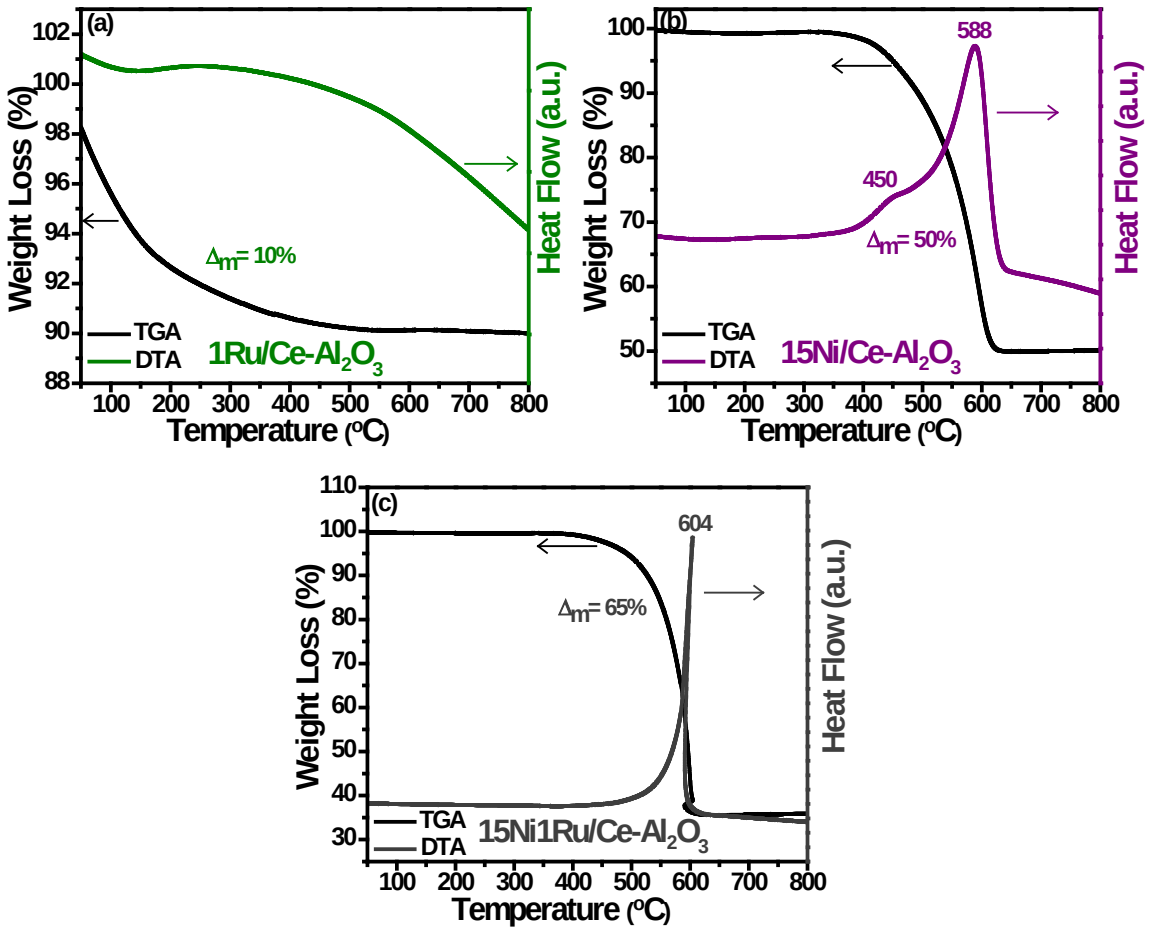

Figure 4.16: DTA/TGA curves of the spent (a) 1Ru/Ce-Al_2O_3, (b) 15Ni/Ce-Al_2O_3, and (c) 15Ni1Ru/Ce-Al_2O_3 catalysts

No exothermic phenomenon was observed for the promoted 1Ru/Ce-Al_2O_3 catalyst in the considered temperature range. This indicates the absence of deposited carbon attributed to the positive role played by ruthenium in carbon gasification. A small endothermic peak at T< 200 °C accompanied by a weight loss of 10 % are present on the DTA/TGA curves. This peak is

assigned to the departure of adsorbed water. However, for 15Ni/Ce-Al_2O_3, two exothermic peaks at 450 ^oC (P1) and 588 ^oC (P2) are observed. P1 is ascribed to the oxidation of a deposited carbon type that is in the proximity of the metal catalytic sites and is removed at low temperature under oxidative atmosphere [71]. The second higher temperature peak (P2) is assigned to the graphitic carbon which is oxidized at higher temperatures. As expected, the 15Ni1Ru/Ce-Al_2O_3 catalyst with the highest conversions had the highest amount of deposited carbon (65 %) which mainly corresponds to the graphitic carbon type.

X-ray diffraction

Figures 4.17 (a) and (b) show respectively the XRD patterns of the Ce-Al_2O_3 supported catalysts after their reduction in a mixture of 5 % H_2/Ar at 800 ^oC for 2 h and after their usage in the DRM reaction.

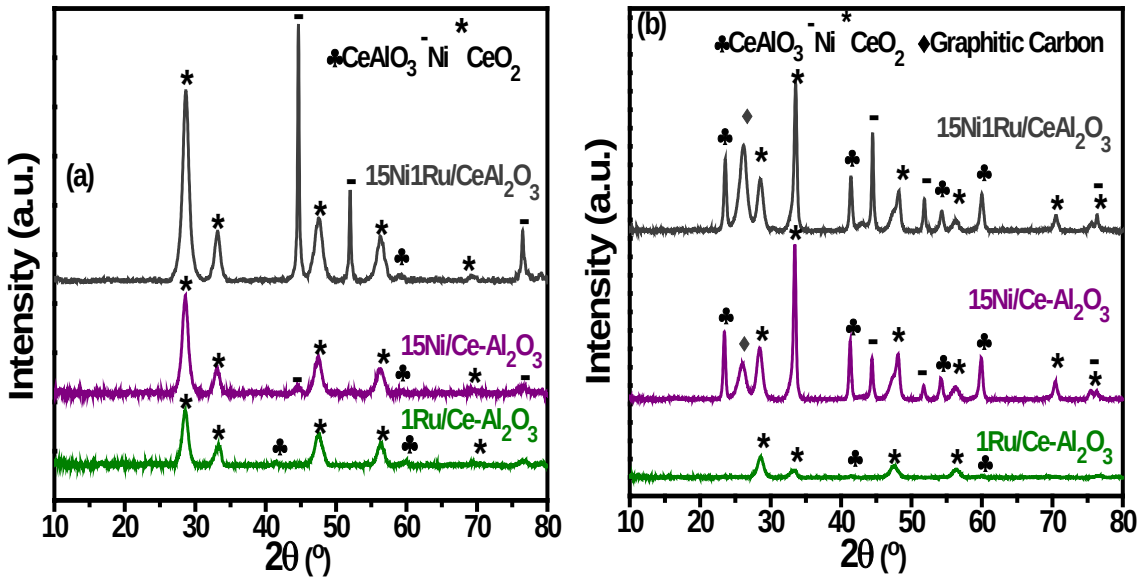

Figure 4.17: XRD patterns of the (a) reduced and (b) spent Ce-Al_2O_3 supported catalysts

The XRD patterns of spent 15Ni/Ce-Al_2O_3 and 15Ni1Ru/Ce-Al_2O_3 catalysts are identical and present a graphitic carbon peak at $2\theta = 27^o$ that is more intense for the15Ni1Ru/Ce-Al_2O_3 catalyst. From our results, diffraction peaks typical of $CeAlO_3$ phase were present on the diffractograms of the reduced and spent catalysts. In a high temperature reducing atmosphere, CeO_2 supported on γ-Al_2O_3 reacts to form $CeAlO_3$-like species [194,200]. The presence of $CeAlO_3$ peaks is due to the solid-state reaction between Ce_2O_3 and γ-Al_2O_3 ($Ce_2O_3 + Al_2O_3 \rightarrow 2CeAlO_3$). The Ce_2O_3 is formed by H_2 reduction of CeO_2 ($2CeO_2 + H_2 \rightarrow Ce_2O_3 + H_2O$)

but is not observed due to the rapid oxidation of Ce^{3+} to Ce^{4+} upon exposure to ambient atmosphere [189].

4.2.3.5. Discussion

- For Ni and Ni-Ru supported on Al_2O_3, promoting the support with Ce resulted in higher conversions and H_2/CO molar ratios. The positive role of cerium promotion has already been reported in the literature. For instance, Debek et al. [201] observed that a 3.7 wt% cerium promotion to a Ni based hydrotalcite catalyst (18 wt% Ni) led to the highest conversion among the tested catalysts. This observation was explained by the positive influence of cerium on the reducibility of Ni species and the introduction of new basic sites resulting from the Mg and Ce synergetic effect on CO_2 adsorption capacity. Characterization results of Ce-Al_2O_3 supported catalysts (part 4.2.2) validate the enhanced active phase dispersion and reducibility as well as an ameliorated catalyst's basicity produced from the promotional effect of Ce. All these factors lead to an enhanced catalytic performance.
- The positive effect of ceria on carbon removal significantly depends on the CeO_2 concentration and on the method of catalyst preparation, which can affect the metal-support interaction, as well as the dispersion of the active metal sites [195]. Thermal analyses show that the amount of carbon deposited on the Ce promoted catalysts (figure 4.16) is greater than that obtained for the non-promoted catalysts (figure 4.5). From our results, it appears that promoting with 60 wt% Ce weakened the metal-support interactions, enhanced the active phase dispersion and ultimately increased catalytic activity and carbon formation.
- Finally, comparing the temperatures at which carbon oxidation occurred without (figure 4.5) and with Ce promotion (figure 4.16), one can conclude that the mechanism of carbon deposition is highly dependent on the active phase composition of the catalysts. The oxidation of deposited carbon occurs at higher temperatures for 15Ni/Al_2O_3 (616 ^oC) and 15Ni1Ru/Al_2O_3 (622 ^oC) catalysts compared to 15Ni/Ce-Al_2O_3 (588 ^oC) and 15Ni1Ru/Ce-Al_2O_3 (604 ^oC) catalysts. This is attributed to the positive role of ceria in improving oxygen mobility and promoting coke gasification.

4.2.4. Catalytic Stability

To further investigate the effect of Ce promotion, the 15Ni/Al_2O_3 catalyst and its promoted counter-part 15Ni/Ce-Al_2O_3 were chosen for a stability study over long periods of time. The stability tests were performed at 800 ^oC using the same catalytic conditions as the dynamic tests (GHSV = 60,000 h^{-1}, CH_4/CO_2 = 1 and total flow = 100 mL/min).

4.2.4.1. Stability test results

Figures 4.18 (a) and (b) represent respectively the CH_4 and CO_2 conversions, H_2/CO molar ratio and the CO and H_2 selectivity obtained during 12 h at 800 ^oC in the presence of 15Ni/Al_2O_3 and 15Ni/Ce-Al_2O_3 catalysts.

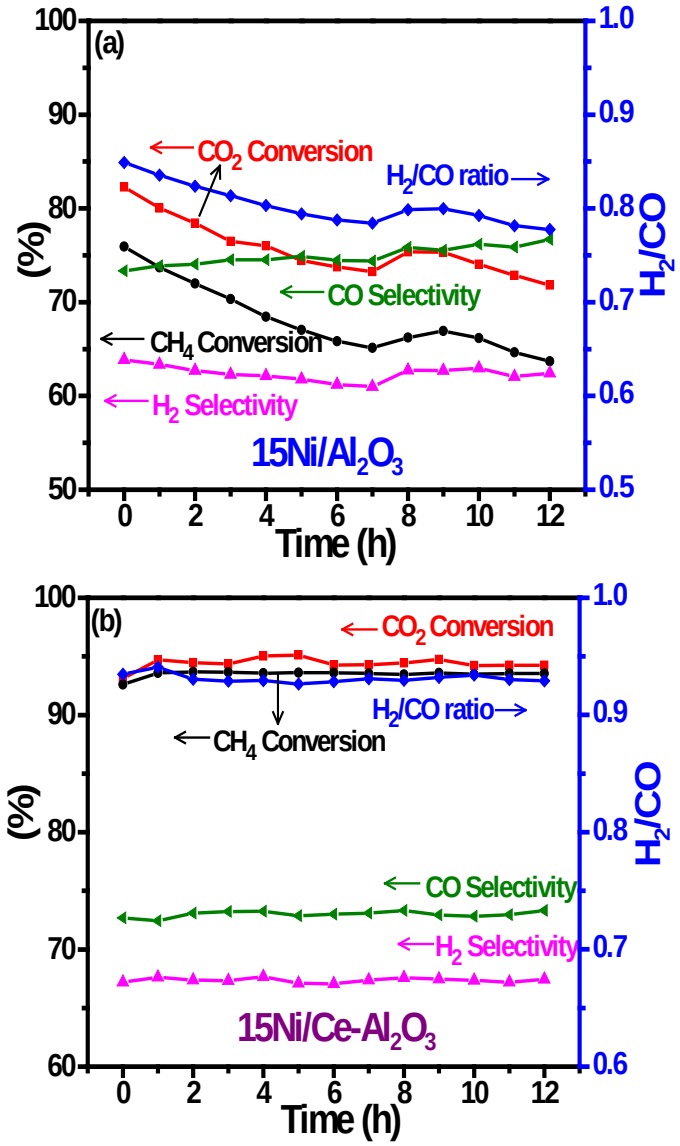

Figure 4.18: Stability test at 800 ^oC for 12 h on stream in the presence of (a) 15Ni/Al_2O_3 and (b) 15Ni/Ce-Al_2O_3

Initially, the CH_4 and CO_2 conversions were 75.9 % and 82.3 % for the 15Ni/Al_2O_3 catalyst and 92.6 % and 93.1 % for the 15Ni/Ce-Al_2O_3 catalyst respectively. After 1 hour on stream, the CH_4 and CO_2 conversions of the 15Ni/Al_2O_3 catalyst decreased to 73.7 % and 80 % respectively. With every hour, the conversions continued to decrease by ~1 % or ~2 % and after 12 h on stream, the CH_4 and CO_2 deactivation rates over the 15Ni/Al_2O_3 catalyst were found to be 11.8 % and 13.8 % respectively. On the other hand, the CH_4 and CO_2 conversion values over the 15Ni/Ce-Al_2O_3 catalyst increased after 1 hour to 93.6 % and 94.7 % respectively and remained stable after 12 h on stream. The H_2/CO molar ratio of the 15Ni/Al_2O_3 catalyst decreased from 0.85 to 0.77 after 12 h on stream. However, in the presence of Ce, the H_2/CO molar ratios were higher and remained constant at ~0.93 during the test period. H_2 selectivity values decreased from 63.9 % at t = 0 h to 62.4 % at t = 12 h for the 15Ni/Al_2O_3 catalyst while remaining constant around 67 % for the 15Ni/Ce-Al_2O_3 catalyst. A different trend was observed for the CO selectivity which was slightly higher in the absence of Ce. At the end of the run, CO selectivity increased from 73.3 % to 76.7 % for 15Ni/Al_2O_3 and from 72.7 % to 73.3 % for the 15Ni/Ce-Al_2O_3 catalyst.

4.2.4.2. Characterization after stability tests

Figures 4.19 (a) and (b) show respectively the thermal analysis of the spent 15Ni/Al_2O_3 and 15Ni/Ce-Al_2O_3 catalysts after stability.

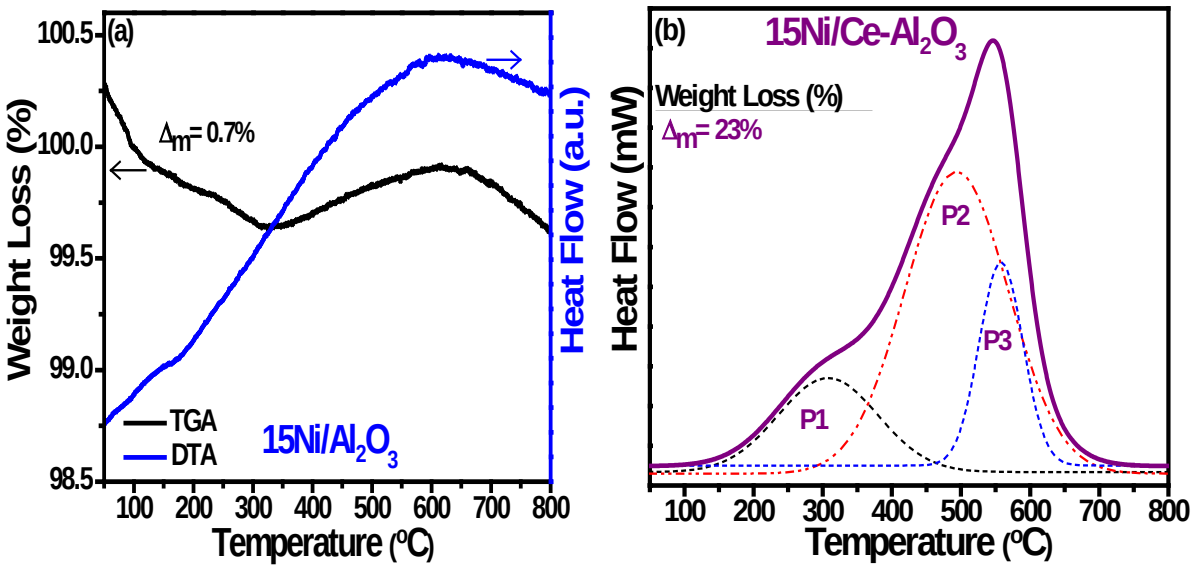

Figure 4.19: (a) DTA/TGA curves of 15Ni/Al_2O_3 and (b) DTA curve and weight loss value of 15Ni/Ce-Al_2O_3 after stability for 12 h

The weight losses recorded for the spent 15Ni/Al_2O_3 and 15Ni/Ce-Al_2O_3 catalysts were equal to 0.7 % and 23 % respectively. For the promoted catalyst, three different exothermic peaks are present (P1, P2, and P3) which indicates the presence of different carbonaceous species on the surface of this catalyst. A broad peak (P1) with a relative low intensity and a maximum at 305 ^oC is assigned to the oxidation of adsorbed carbon species forming complexes with the metallic surface species and to the oxidation of metal particles present on the catalyst surface. The second peak (P2) centered around 490 ^oC is attributed to the oxidation of deposited carbon (amorphous carbon or carbon filaments) [142,190]. The third exothermic peak (P3) at T > 500 ^oC is ascribed to the oxidation of graphitic carbon formed.
The XRD patterns (not shown) of the catalysts after stability show a graphitic carbon diffraction peak in the pattern of the 15Ni/Ce-Al_2O_3 catalyst which is in agreement with the thermal analysis of this catalyst.

4.2.4.3. Discussion

- Although the 15Ni/Al_2O_3 catalyst started to deactivate from the first hour on stream, no carbon was deposited on its surface. Therefore, to understand the cause of such deactivation, the crystallite sizes of the Ni particles were calculated after stability and were found to be equal to 27.5 nm (3.5 times the crystallite size after reduction (table 4.2)). Hence, nickel agglomerates of large crystal sizes were formed on the surface of the catalyst after stability indicating that the metal particles had sintered and eventually led to the loss of activity.
- The weight losses obtained for the 15Ni/Al_2O_3 and 15Ni/Ce-Al_2O_3 catalysts after stability tests (figure 4.19) are lower than those obtained after the dynamic tests (figures 4.5 and 4.16). In the dynamic tests, carbon formation must have been generated by the accumulation of carbon by the Boudouard reaction which is dominant in the 450 ^oC - 650 ^oC temperature range or the decomposition of methane which is more likely to occur at a higher temperature range. At 800 ^oC, DRM is more dominant than the reactions causing carbon formation. It is already reported that high temperatures favor the anti-coking performance and the catalyst is more susceptible to carbon deposition at low temperatures due to the strong thermodynamic tendency of coking [202], [203].

- The stability tests showed that the Ce promoted catalyst 15Ni/Ce-Al_2O_3 did not deactivate during a period of 12 h. This suggests that the presence of Ce led to the oxidation of the deposited carbon and promoted the regeneration of the catalyst.

4.3. CO_2 Reforming of Methane over Mesoporous Silica Supported Catalysts

Since 1990,the ordered mesoporous silicas such as SBA-15, SBA-16, KIT-6 and MCM-41 have been considered in catalysis due to their thermal stability, ordered porous channels and large surface areas which help ameliorate active site dispersion and accessibility [204,205]. In this part, three different mesoporous supports (KIT-6, SBA-15, and SBA-16,) will be compared in the CO_2 reforming of methane.

4.3.1. Catalysts Preparation

Synthesis of the mesoporous silica supports

KIT-6: previously described (chapter 2, part 2.3.1.)

SBA-15: According to Zucchetto et al. [206], the reference article used, SBA-15 was synthesized by dissolving an amount of P123 in a hydrochloric acid solution of 1.55 M. Once a clear solution is obtained, TEOS was slowly added. The mixture remained stirring for 20 h at 35 °C. After mixing, the latter was transferred to a Teflon bottle and heated in an oven at 100 °C for 24 h. After the hydrothermal treatment, the product was recovered by filtration and washing and dried overnight at room temperature. The dried product is then calcined in air at 550 °C for 12 h at a heating rate of 2 °C/min.

SBA-16: SBA-16 synthesis was also done according to the report given by Zuchetto et al. [206]. Non-ionic F127 copolymer ($(EO)_{106}(PO)_{70}(EO)_{106}$, Aldrich) and Hexadecyltrimethylammonium bromide (CTAB, 96 %) were dissolved in 0.4 M hydrochloric acid solution. Once a clear solution was obtained, a suitable amount of TEOS was added under strong stirring. After 30 minutes, the mixture was transferred to a Teflon bottle and placed in a preheated oven at 95 °C for 120 h. The Teflon bottle was then removed from the oven, cooled to room temperature and subsequently filtered. Washing, drying, and calcination processes were done similarly to the processes described for SBA-15.

Synthesis of the different mesoporous silica supported catalysts

The wet impregnation technique previously described (chapter 2, part 2.1.1.) was used in order to synthesize the catalysts. The nominal percentage of nickel in all the catalysts was 15 wt%. The catalysts obtained are: 15Ni/KIT-6, 15Ni/SBA-15, and 15Ni/SBA-16.

4.3.2. Catalysts Characterization

4.3.2.1. X-Ray Diffraction analyses (XRD)

Figures 4.20 (a) and (b) show respectively the wide angle XRD patterns of the calcined supports (KIT-6, SBA-15, and SBA-16) before and after Ni impregnation.

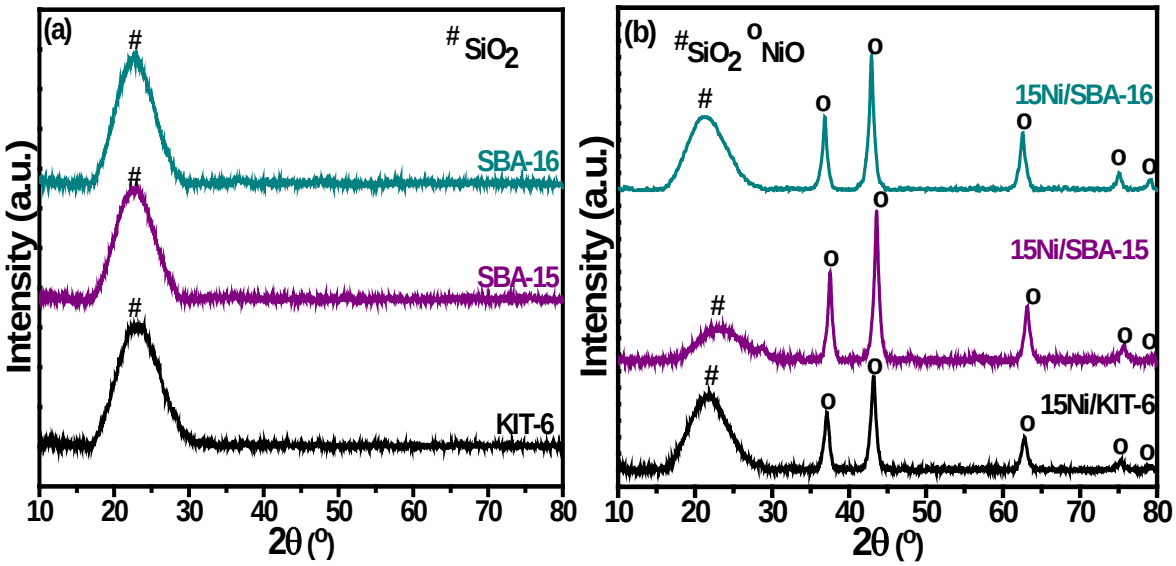

Figure 4.20: XRD patterns of the different (a) supports and (b) Ni/supports after calcination at 550 °C

In agreement with literature [102, 207, 208], the XRD patterns of KIT-6, SBA-15 and SBA-16 supports show one broad scattering peak of identical intensity attributed to the amorphous SiO_2 phase. It is noticed that the diffraction patterns of the 15Ni/KIT-6, 15Ni/SBA-15, and 15Ni/SBA-16 catalysts reveal the presence of the rhombohedral NiO phase. The distinct SiO_2 diffraction peak is observed for all the catalysts following the impregnation of Ni but with lower intensities compared to the peak recorded for the lone supports. The obtained NiO crystallite sizes are similar for all the catalysts (12.6 nm for 15Ni/KIT-6, 12.7 nm for 15Ni/SBA-15, and 13.1 nm for 15Ni/SBA-16)

4.3.2.2. N_2 adsorption/desorption analyses

Figures 4.21 (a), (b), and (c) show the N_2 adsorption/desorption isotherms and pore size distributions of the different supports and Ni/supports calcined at 550 ^oC. Table 4.7 shows the textural parameters of the prepared samples.

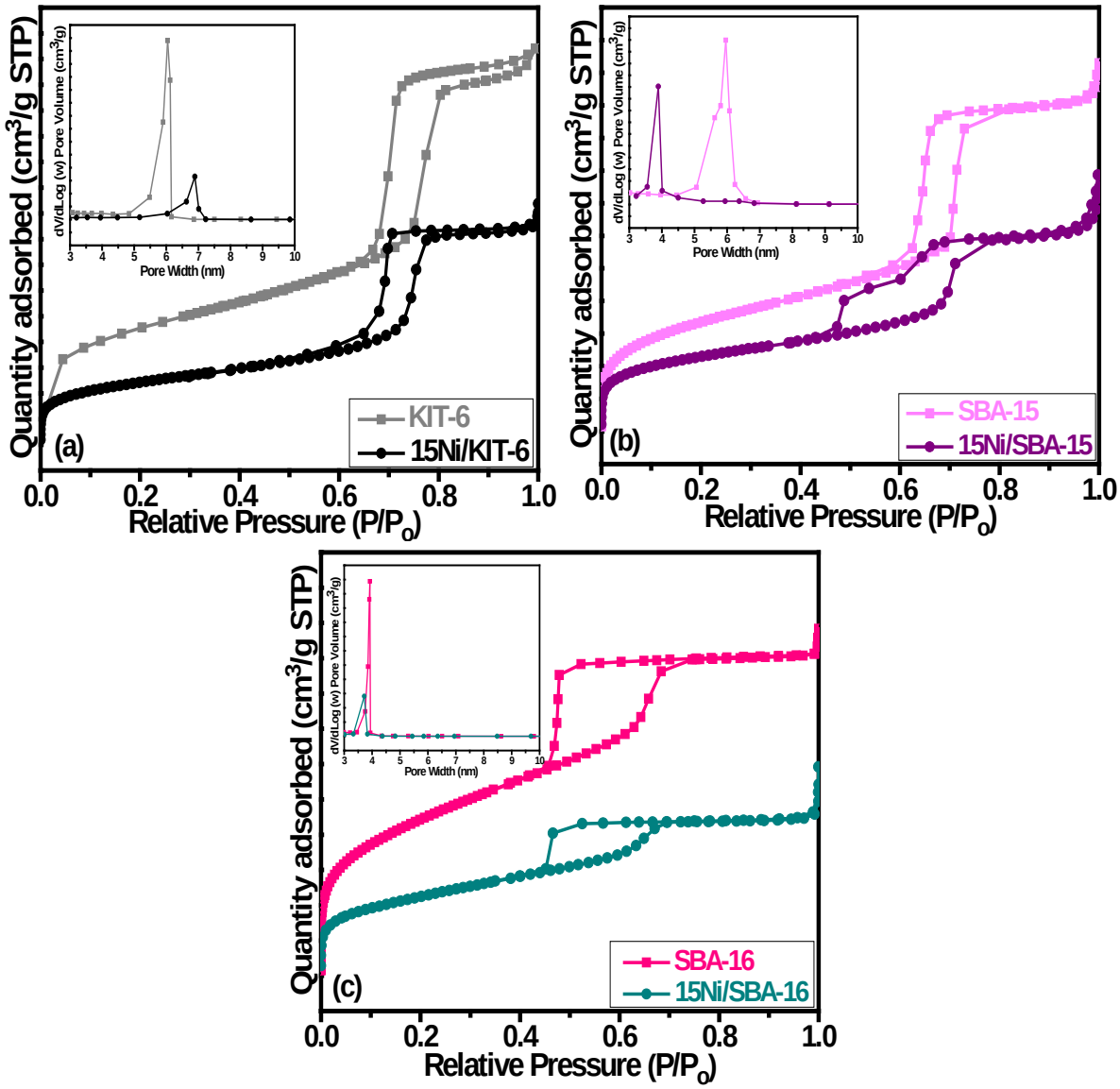

Figure 4.21: N_2 adsorption/desorption isotherms and pore size distributions of calcined (a) KIT-6 and 15Ni/KIT-6, (b) SBA-15 and 15Ni/SBA-15, and (c) SBA-16 and 15Ni/SBA-16

The N_2 adsorption/desorption isotherms of all supports and catalysts conform to type IVa isotherms which correspond to the typical features of mesoporous materials. Basically, for a mesoporous structure, the adsorption occurs on the outer surface when gas uptake is at a P/P_o range of 0.4–0.8; whereas, the adsorption of micropores occur at higher gas uptakes (P/P_o

between 0.8 and 1.0). Each isotherm obtained can be divided into three different regions: The first region is linear and corresponds to the monolayer adsorption that occurs at low relative pressure. The second region is steep, results from capillary condensation within the mesopores and occurs at an intermediate pressure. The third and last region at higher pressures can be attributed to multilayer adsorption of the N_2.

Although all supports and catalysts reveal a type IVa isotherm, a difference lies in the hysteresis loops obtained. Usually, an H1 hysteresis is associated with porous materials exhibiting a narrow distribution of relatively uniform cylindrical pores. On the other hand, materials that give rise to H2 hysteresis contain more complex pore networks consisting of pores with ill-defined shape and wide pore size distributions. From our results, the obtained isotherms of KIT-6 and SBA-15 reveal an H1 hysteresis and that of SBA-16 reveal an H2 hysteresis in accordance with the literature [167, 206]. After the Ni particles are loaded on the support, the mesoporous structure was quite maintained for 15Ni/KIT-6 and 15Ni/SBA-16 catalysts but the hysteresis loops were smaller than that of pure KIT-6 and SBA-16 due to NiO impregnation and the possibility of the partial occupancy of small Ni particles inside the support channel [84,209]. In contrast, the isotherm of 15Ni/SBA-15 catalyst shows a remarkable shift to lower P/P_0 position in the desorption branch as well as a change in the shape of the hysteresis. Among the three supports, SBA-16 demonstrated the highest surface area yet smallest volume of pores (table 4.7). Moreover, it is noticed from table 4.7 that the surface areas and pore volumes drastically decrease for all the catalysts after impregnation suggesting the possibility of some pore blockage. It is also noticed from figure 4.21 and table 4.7 that all supports and catalysts reveal a uniform narrow pore size distribution.

Table 4.7: Textural properties of the different supports and Ni/supports

Catalysts	Specific Surface area (m^2 /g)	Pore Volume (cm^3/g)	Pore Diameter (nm)
KIT-6	630	1	6
SBA-15	595	0.82	6
SBA-16	795	0.63	4
Ni/KIT-6	422	0.72	6.9
Ni/SBA-15	396	0.59	3.9
Ni/SBA-16	398	0.38	3.7

4.3.2.3. H_2-Temperature programmed reduction analyses (H_2-TPR)

Figure 4.22 shows the deconvoluted H_2-TPR profiles obtained for the 15Ni/KIT-6, 15Ni/SBA-15, and 15Ni/SBA-16 catalysts. Table 4.8 lists their experimental and theoretical H_2 consumption values which were used to calculate the Ni (wt %) and Type I and Type II NiO percentages.

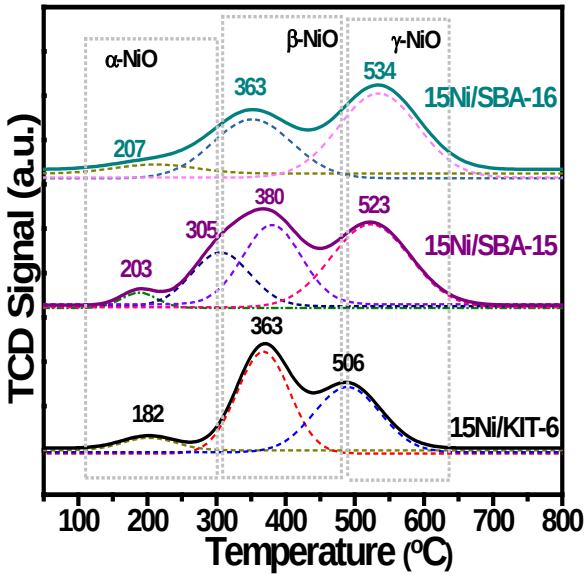

Figure 4.22: H_2-TPR profiles of the different Ni/supports

The H_2-TPR profiles of the supports alone (not shown) showed no reduction peaks in the considered temperature range. The TPR profiles of the Ni based catalysts marked the presence of different reduction zones attributed to different NiO species deposited on the support. The degrees of reduction were calculated based on the following equation: $NiO + H_2 \rightarrow Ni + H_2O$. Low reduction temperatures are required when the chemical interaction between Ni and SiO_2 support is weak (weak Ni-O-Si bond) and higher temperatures are

needed when the interaction is strong [120]. According to the literature [210,211], α-peaks around 250 °C – 300 °C with a very low intensity correspond to the reduction of free NiO, β-peaks around 450 °C – 500 °C are attributed to weak NiO-support interactions, and γ-peaks around 500 °C – 600 °C result from the reduction of nickel oxide species with medium interaction with support. Moreover, δ-peaks detected at temperatures higher than 600 °C correspond to strong NiO-support interaction. From our results, the TPR patterns of the 15Ni/KIT-6, 15Ni/SBA-15, and 15Ni/SBA-16 catalysts consist of three main reduction ranges.

For all the catalysts, the first low temperature, low intensity peak (α) highlights the presence of easily reducible free NiO species.

The β peaks centered at 363 ^{o}C for 15Ni/KIT-6 and 15Ni/SBA-16 and at 380 ^{o}C for 15Ni/BA-15 catalysts indicate the presence of NiO weakly bound to the mesoporous silica support. The peak centered at 305 ^{o}C for 15Ni/SBA-15 is assigned to a simultaneous reduction of NiO species that are free and/or in weak interaction with the support.

Finally, the γ peaks detected at 506 ^{o}C for 15Ni/KIT-6, 523 ^{o}C for 15Ni/BA-15, and 534 ^{o}C for 15Ni/SBA-16 are an indication of moderate NiO-support interactions.

The absence of reduction peaks at temperatures higher than 600 °C indicates the absence of strong metal-support interaction in all the catalysts.

Table 4.8: Redox properties of the different Ni/supports

Catalyst	Ni (wt%)	H_2 consumption [µmol H_2/g catalyst]							% NiO	
		Experimental					Theoretical			
		I	II	III	IV	Total	NiO/Ni	Total	Type I	Type II
15Ni/KIT-6	13.4	268	1309	1052	-	**2629**	2871	**2871**	**59%**	**41%**
15Ni/SBA-15	14.1	102	592	876	1234	**2804**	2871	**2871**	**56%**	**44%**
15Ni/SBA-16	13.8	161	1047	1530	-	**2738**	2871	**2871**	**44%**	**56%**

In addition, the Ni loadings of the different samples were estimated from the quantities of H_2 consumed in the NiO to Ni reduction. Table 4.8 shows that the estimated Ni loadings for all of the prepared catalysts are relatively close to that expected (15 wt%). Furthermore, the percentages of highly dispersed NiO that are either free or in weak contact with the support (type I) and complex NiO species that are in moderate contact or in the bulk of the support (type II) were calculated using the peak area concentrations for the catalysts and the values are shown in table 4.8. Peaks centered at temperatures lower than 400 ^{o}C ((α) and (β)) were considered of type I whereas peaks centered at temperatures higher than 400 ^{o}C (γ) were

considered of type II. It was found that the catalyst 15Ni/KIT-6 possesses the highest percentage of type I NiO (59 %) whereas the catalyst 15Ni/SBA-16 shows the highest percentage of type II NiO (56 %). From these results, the order of metal-support interaction is as follows: 15Ni/SBA-16 > 15Ni/SBA-15 > 15Ni/KIT-6. This difference indicates that the type of the support could influence the type of Ni species and that the 15Ni/SBA-16 catalyst gave a higher proportion of Ni strongly interacting with silica. This stronger interaction can possibly lead to a higher dispersion and inhibition of metal sintering.

4.3.2.4. CO_2-Temperature programmed desorption analyses (CO_2-TPD)

Figure 4.23 shows the CO_2-TPD profiles and table 4.9 represents the CO_2 consumption of the 15Ni/KIT-6, 15Ni/SBA-15, and 15Ni/SBA-16 catalysts.

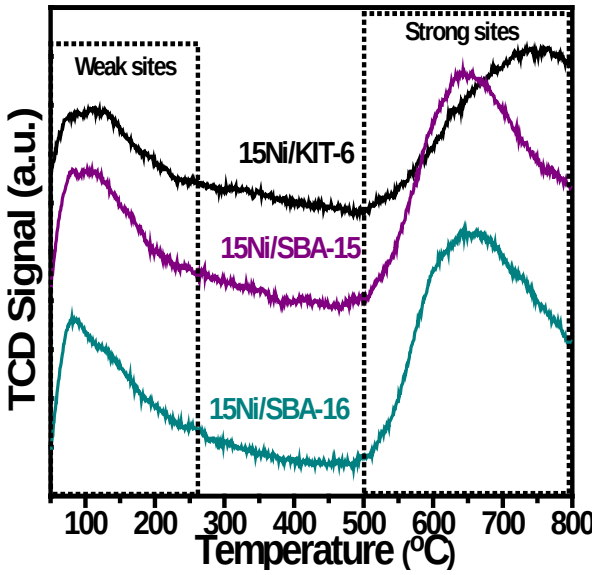

Figure 4.23: CO_2-TPD profiles of the different Ni/supports

All the catalysts show a first adsorption peak centered below 150 °C, which is the result of CO_2 being weakly chemisorbed on the support framework and the acidic CO_2 molecules physically adsorbed on SiO_2. A second larger peak centered at 752 °C for 15Ni/KIT-6, 632 °C for 15Ni/SBA-15, and 642 °C for 15Ni/SBA-16 is attributed to the CO_2 adsorbed on the strong basic sites of the catalysts [212]. SiO_2 based catalysts scarcely possess basic sites because the latter is a well-known weakly acidic molecule that has no basic properties. Hence, since silica alone does not adsorb significant amounts of CO_2 and it is reasonable to conclude that the adsorption occurs only over Ni species. For 15Ni/KIT-6, the second peak is completed outside of our studied temperature range indicating that not all strong basic sites

are quantified below 800 ^oC. From table 4.9, the CO_2 adsorption capacity of 15Ni/SBA-15 is the highest indicating that there are more basic sites on its surface. The total basicity increases as follows: 15Ni/KIT-6<15Ni/SBA-16<15Ni/SBA-15.

The contribution from weak basic sites is higher for the 15Ni/KIT-6 catalyst whereas the contribution from the strong basic sites was comparable between 15Ni/SBA-15 and 15Ni/SBA-16 (table 4.9).

Table 4.9: Basic site distribution of the different Ni/supports

Catalyst	CO_2 Quantity [µmol CO_2/g catalyst]			Distribution of basic sites (%)	
	Weak	Strong	Total	Weak	Strong
15Ni/KIT-6	56	37	**93**	60.2	39.8
15Ni/SBA-15	99	147	**246**	40.2	59.8
15Ni/SBA-16	88	134	**222**	39.6	60.4

4.3.2.5. Discussion

- Ni impregnation led to the shrinkage of the porous structure and filling of the pores of the mesoporous supports KIT-6, SBA-15 and SBA-16.
- The reducibility and basicity studies showed that the strongest Ni-support interaction and contribution from the strong basic sites were observed over the 15Ni/SBA-16 catalyst.

4.3.3. Catalytic Activity

In this part, the same DRM reaction conditions (P= 1atm, CH_4/CO_2= 1, temperature range: 500 ^oC – 800 °C, GHSV = 60,000 h^{-1}, and total flow = 100ml/min) were used.

4.3.3.1. Test results

Figures 4.24 (a), (b), (c), (d), and (e) show respectively the CH_4 conversion, CO_2 conversion, H_2/CO molar ratio, CO selectivity and the H_2 selectivity obtained in the presence of the 15Ni/KIT-6, 15Ni/SBA-15, and 15Ni/SBA-16 catalysts.

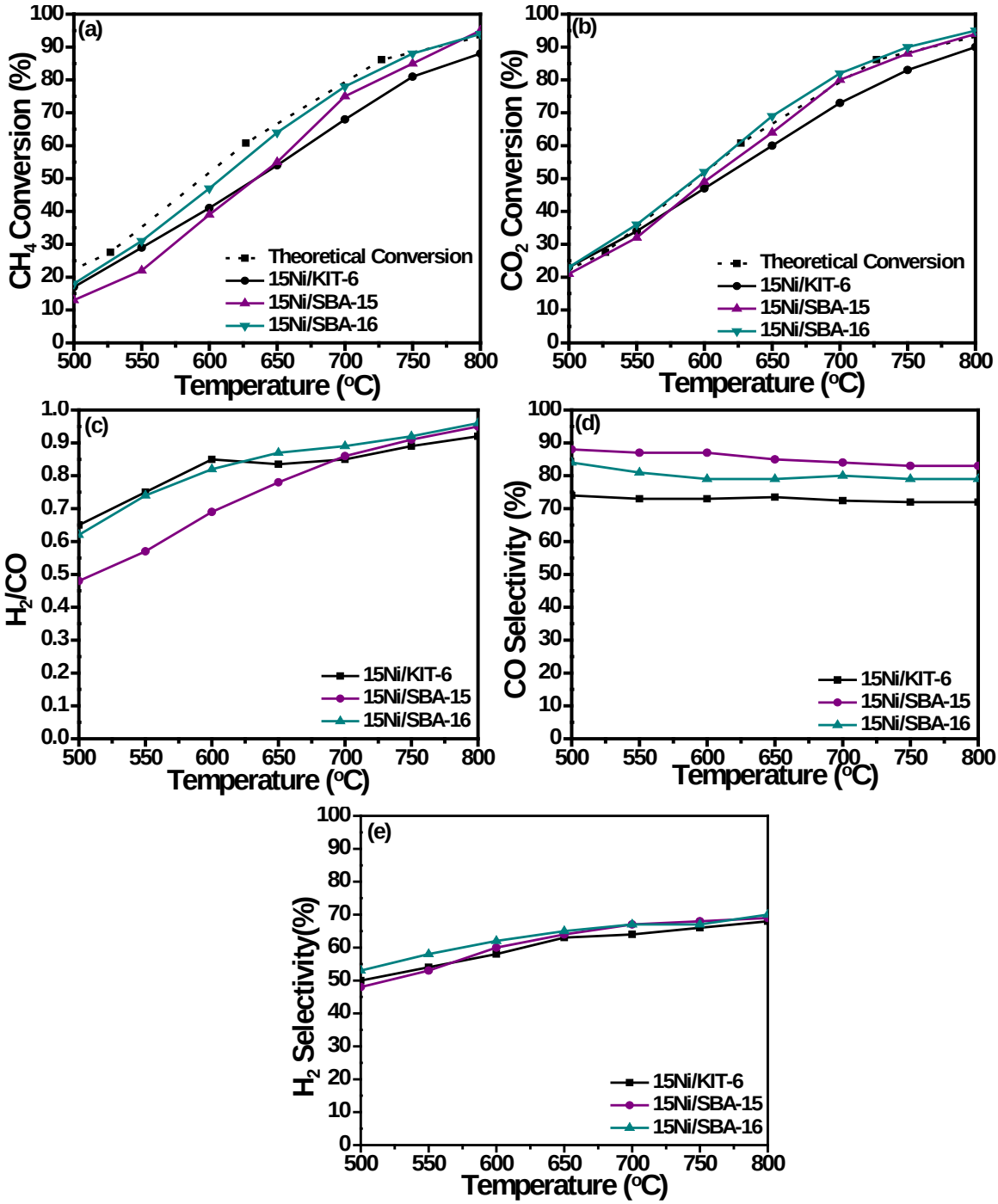

Figure 4.24: (a) CH_4 conversion, (b) CO_2 conversion, (c) H_2/CO molar ratios (d) CO selectivity and (e) H_2 selectivity in function of temperature of the different Ni/supports

In the 550 °C – 750 °C temperature range, the CH_4 and CO_2 conversions recorded over the 15Ni/SBA-16 catalyst were the highest compared to those recorded over the 15Ni/KIT-6 and 15Ni/SBA-16 catalysts. At 800 °C, the CH_4 and CO_2 conversions of both 15Ni/SBA-16 and 15Ni/SBA-15 became equal (94 % and 95 % respectively).

Among the studied catalysts, 15Ni/SBA-16 revealed the highest H_2/CO molar ratio at 800 °C as well as the highest H_2 selectivity. For every catalyst, the fact that the conversion of CO_2 was higher than the corresponding CH_4 conversion and the H_2/CO molar ratios were lower than unity is due to the influence from the RWGS reaction.

4.3.3.2. Characterization after test

Thermal analysis

Figures 4.25 (a), (b), and (c) show the thermal analyses of the different spent Ni/supports.

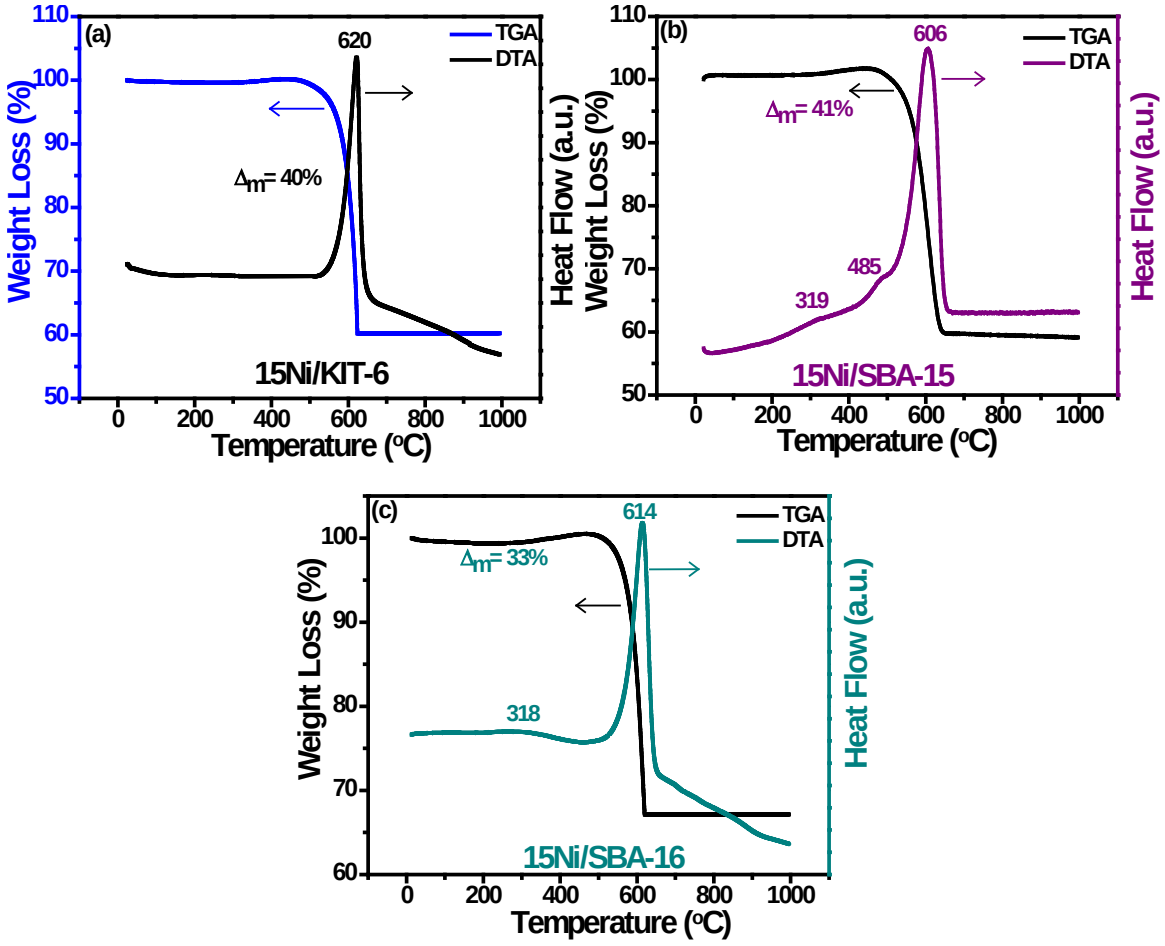

Figure 4.25: DTA/TGA curves of the spent (a) 15Ni/KIT-6, (b) 15Ni/SBA-15, and (c) 15Ni/SBA-16 catalysts

The DTA/TGA curves show the presence of weight losses accompanied with graphitic carbon combustion peaks centered at 620 ^oC, 606 ^oC, and 614 ^oC for 15Ni/KIT-6, 15Ni/SBA-15 and 15Ni/SBA-16 respectively. This indicates that all the catalysts were subject to carbon deposition during the DRM reaction. The DTA curves also show a small intensity exothermic peak centered at 319 ^oC and 318 ^oC for 15Ni/SBA-15 and 15Ni/SBA-16 respectively. These peaks are assigned to easily oxidized amorphous carbon species; whereas, the peak at 485 ^oC present on the DTA curve of 15Ni/SBA-15 is attributed to the oxidation of Ni particles.

X-ray diffraction

Figures 4.26 (a) and (b) show respectively the XRD patterns of the different Ni/supports after their reduction in a mixture of 5 % H_2/Ar at 800 ^oC for 2 h and after their usage in the DRM reaction. Table 4.10 lists the Ni crystallite sizes obtained after reduction and after test.

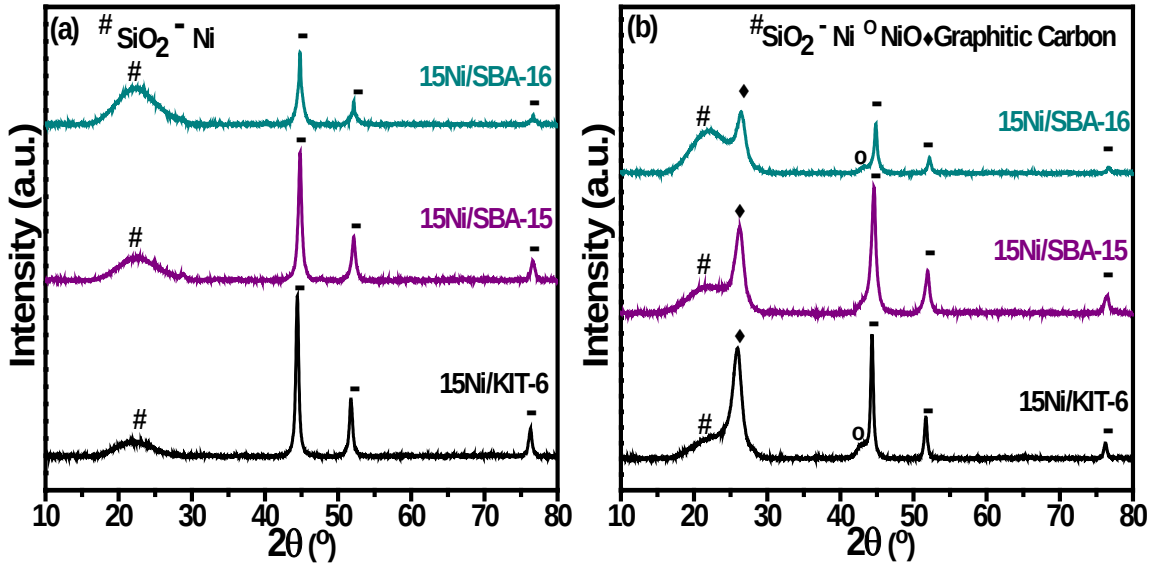

Figure 4.26: XRD patterns of the different (a) reduced and (b) spent Ni/supports

The XRD patterns of the reduced samples show reflections of SiO_2 and metallic Ni in all the catalysts. As expected, intense peaks were detected at $2\theta = 27^o$ indicating the presence of graphitic carbon along with metallic Ni reflections for all spent catalysts. NiO peaks are seen on the diffractograms of 15Ni/KIT-6 and 15Ni/SBA-16 catalysts. Table 4.10 shows that the crystallite sizes after test increase from 18.5 nm to 21.2 nm for 15Ni/KIT-6 and from 17.5 nm to 21.1 nm for 15Ni/SBA-16 as a result of active phase agglomeration.

Table 4.10: Crystallite sizes of the different reduced and spent Ni/supports

Catalyst	Ni Crystallite Size (nm)	
	Reduced	Spent
15Ni/KIT-6	18.5	21.2
15Ni/SBA-15	16.4	-
15Ni/SBA-16	17.5	21.1

*Ni crystallite size of spent 15Ni/SBA-15 could not be calculated because the Ni and NiO diffraction peaks overlapped and could not be properly identified

4.3.3.3. Discussion

- The catalytic performance of the mesoporous catalysts depended on the availability of the active metal for reaction: from the reducibility analysis (table 4.8), the 15Ni/SBA-16 catalyst possessed the highest percentage of type II NiO that are located in the bulk and are in contact with the support. This suggests that the stronger the interaction between the active phase and the support, the better the catalytic activity. In addition, 15Ni/SBA-16 showed a high amount of strong basic sites (table 4.9). The presence of strong basic sites is reported to enhance the catalytic performance in the DRM reaction [201,213].
- The obtained weight losses show that the 15Ni/SBA-16 catalyst had the lowest carbon deposition which is probably due to the higher metal support interactions and good basic properties of this catalyst.

4.3.4. Catalytic Stability

4.3.4.1. Stability test results

The long-term stability of 15Ni/KIT-6, 15 Ni/SBA-15, and 15Ni/SBA-16 is compared at 800 ^{o}C as shown on figure 4.27.

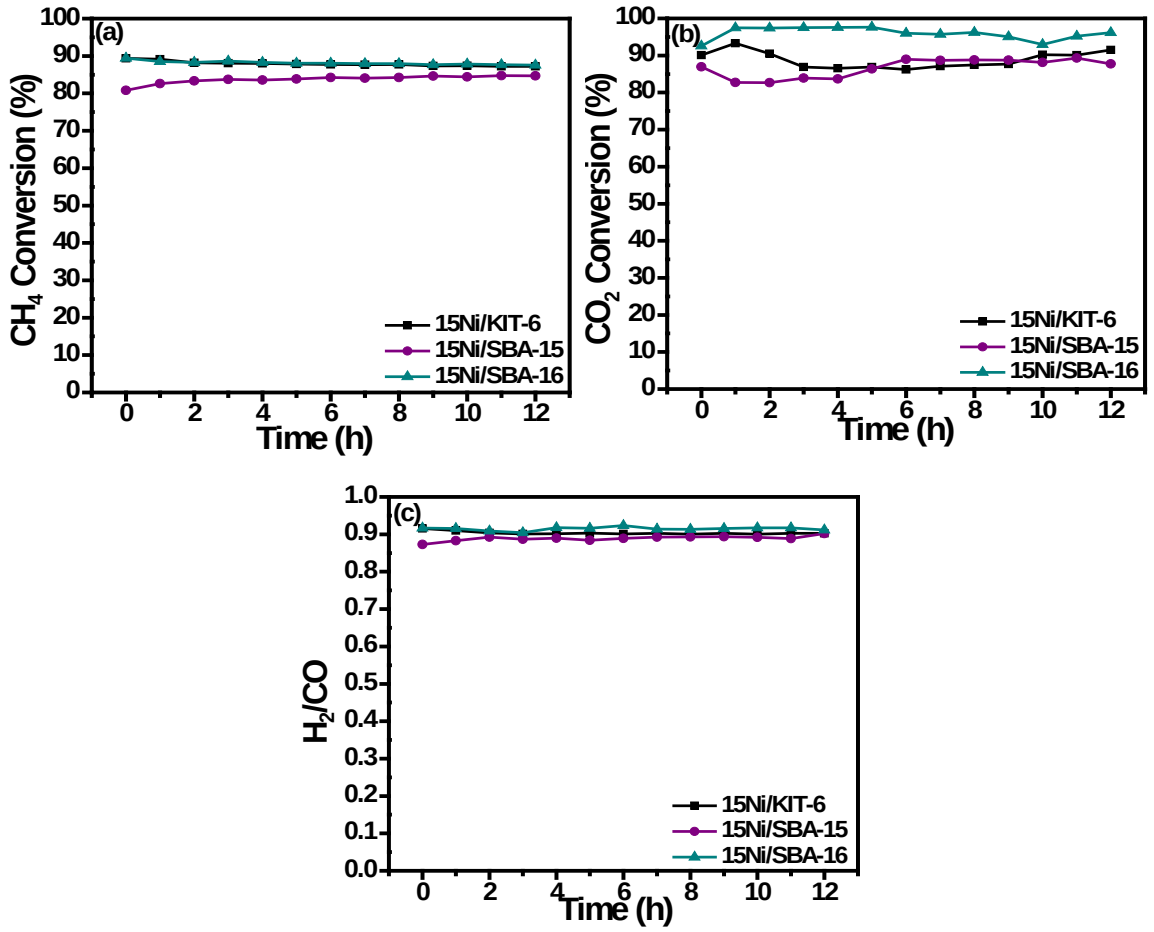

Figure 4.27: (a) CH_4 conversion, (b) CO_2 conversion, and (c) H_2/CO molar ratio versus time on stream at 800 ^{o}C in the presence of the different Ni/supports

At the beginning of the stability test, the CH_4 conversions over 15Ni/KIT-6 and 15Ni/SBA-16 were equal to 89.4 % and that of 15Ni/SBA-15 was 80.8 % respectively. After 12 h on stream, the CH_4 conversions for all the catalysts remained approximately constant. During the first hour on stream, the CO_2 conversion of 15Ni/SBA-15 decreased from 86.9 % to 82.7 % and at the 6th hour, it increased and was maintained at ~88 %. For 15Ni/KIT-6, the CO_2 conversions decreased by 6 % during the first 7 h but increased again to reach 91.5 % at the 12th hour. In agreement with the activity obtained in the dynamic tests, the CO_2 conversions of 15Ni/SBA-16 were also higher than those of 15Ni/SBA-15 and 15Ni/KIT-6 during the

whole time on stream. An increase from 92.5 % to 97.4 % during the first hour on stream was observed and the CO_2 conversions remained constant during the whole period on stream. The H_2/CO molar ratios were equal to ~0.9 for 15Ni/KIT-6 and 15Ni/SBA-16 and to ~0.88 for 15Ni/SBA-15.

4.3.4.2. Characterization after test

Figures 4.28 (a) and (b) show respectively the obtained TGA and DTA curves of the spent Ni/supports after stability. Figure 4.28 (c) shows the XRD patterns obtained.

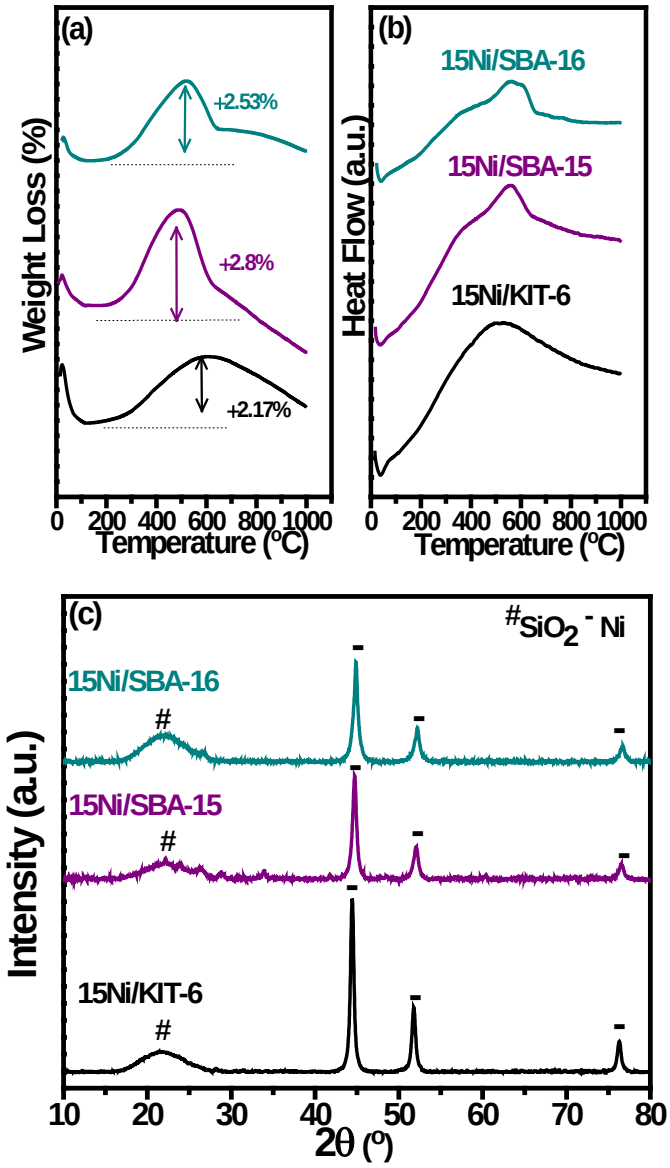

Figure 4.28: (a) TGA curves, (b) DTA curves, and (c) XRD patterns of the different Ni/supports after stability

The thermal analyses of the spent catalysts show a weight loss below 200 ^oC attributed to the loss of chemically adsorbed water and a second weight gain of less than 3 % in the 300 ^oC – 600 ^oC temperature range. This weight gain is accompanied with an exothermic peak attributed to the oxidation of Ni particles. XRD patterns of the spent catalysts are similar to the ones obtained after reduction (figure 4.26 (a)). The crystallite sizes of the catalysts after stability were 18.3 nm for 15Ni/KIT-6, 16.2 nm for 15Ni/SBA-15, and 15.1 nm for 15Ni/SBA-16. These values are very close to the ones obtained after reduction (table 4.10) which eliminates the possibility of Ni particle sintering after the reaction.

4.3.4.3. Effect of varying the GHSV

To verify if the above catalysts will maintain their superior catalytic activity and stability even under severe test conditions, a series of stability tests were performed over the 15Ni/KIT-6, 15Ni/SBA-15 and 15Ni/SBA-16 catalysts using higher gas hourly space velocities GHSVs. The stability tests done in part 4.3.4.1 were performed using a GHSV of 60,000 h^{-1}. The results obtained will be compared in this part to the results of stability tests performed using a GHSV of 80,000 h^{-1} and 120,000 h^{-1}. The change of the GHSV was made by varying the masses of the catalysts placed in the reactor. Table 4.9 evaluates the CO_2 and CH_4 deactivation rates obtained for every catalyst using different GHSVs.

Table 4.11: CO_2 and CH_4 deactivation rates of 15Ni/KIT-6, 15Ni/SBA-15, and 15Ni/BSA-16 using different GHSVs

Sample	GHSV	CO_2 conversion (%)			CH_4 conversion (%)		
		Initial t= 0 h	Final t= 12 h	Deactivation Rate	Initial t= 0 h	Final t= 12 h	Deactivation Rate
15Ni/KIT-6	**60,000 h^{-1}**	90.1%	91.5%	-	89.4%	87.2%	**2.5%**
	80,000 h^{-1}	87.7%	90.6%	-	81.7%	83.8%	-
	120,000 h^{-1}	86.9%	89%	-	81.6%	80.9%	**0.85%**
15Ni/SBA-15	**60,000 h^{-1}**	86.9%	87.8%	-	80.8%	84.7%	-
	80,000 h^{-1}	84.4%	79.9%	**5.3%**	79.4%	79.7%	-
	120,000 h^{-1}	80.2%	74.7%	**6.9%**	73%	72.8%	**0.3%**
15Ni/SBA-16	**60,000 h^{-1}**	92.5%	96%	-	89.4%	87.6%	**2%**
	80,000 h^{-1}	83.5%	77.9%	**6.7%**	75.4%	77.8%	-
	120,000 h^{-1}	78.7%	72.7%	**7.6%**	70%	72.5%	-

For all the catalysts, the recorded CO_2 and CH_4 conversions decrease when a higher GHSV is applied. Whatever the GHSV used, no CO_2 deactivation is observed for the 15Ni/KIT-6 catalyst. On the contrary, for 15Ni/SBA-15 and 15Ni/SBA-16, a deactivation of 5.3 % and

6.7 % is observed for a GHSV of 80,000 h^{-1} and of 6.7 % and 7.6 % is observed for a GHSV of 120,000 h^{-1}. It is clear from these results that these catalysts become less stable as the GHSV increases. For all the catalysts, no noticeable CH_4 deactivation pattern was observed. The CH_4 conversions were steady and fluctuated around close values during the whole time on stream.

4.3.4.4. Discussion

- When considering Ni based catalysts supported on mesoporous silica, one main reason to obtain a remarkable resistance to carbon formation is the confinement effect [204]. The confinement of well-dispersed small nickel particles in the mesopores of a support with high specific surface areas and finely controlled pore volumes is considered to be a good strategy to enhance the stability of Ni-based catalysts [214, 215]. Although the traditional impregnation technique does not always create stable and efficient catalysts for the DRM reaction, we have succeeded in creating stable Ni based catalysts that were confined in the pores of KIT-6, SBA-15, and SBA-16 and resisted sintering and carbon formation. From the evaluation of the porous structure of these catalysts (part 4.3.2.2.), it was clear that all supports and catalysts showed a mesoporous structure with high surface areas and large volume of pores. Moreover, the obtained Ni particles were in the range of 16 nm - 18.5 nm (table 4.10) which is relatively small for a 15 % Ni loading. Those particles were well-dispersed on the surface of the support and in moderate interactions with it (part 4.3.2.3.). All these factors were translated into a good catalytic activity and stability for all three Ni based mesoporous silica catalysts.

4.4. Comparison of Ni and/or Ru supported on KIT-6 and Ce-KIT-6

The support "KIT-6" (Korea Institute of Science and Technology) having an elevated surface area, a 3-D cubic *Ia3d* crystal structure, and a precise pore size distribution (5 nm -15 nm) has recently gained interest in different environmental reactions [102,216,217]. From the comparison of the different mesoporous silicas, it was noticed that the 15Ni/KIT-6 catalyst showed good activity and stability even at high GHSVs. It was noticed from previous parts that the catalytic performance is dependent on the active phase used and affected by the presence of a promoter. In this section, it seemed interesting to compare the catalytic performance of 15Ni/KIT-6 with the other active phases (Ru and Ni-Ru) with or without Ce promotion. It is important to mention that the Ce_{60}KIT-6 supported catalysts were chosen for comparison in this section. The characterization results of the promoted catalysts are found in chapter 3 (part 3.2.2.) The activity of Ni/KIT-6 catalysts in the DRM reaction has been previously reported in the literature [102, 199,218]. Nonetheless, testing a Ni loading of 15 wt% under our catalytic conditions (P = 1atm, CH_4/CO_2 = 1, temperature range: 500 ^oC – 800 °C, GHSV= 60,000 h^{-1}, and total flow = 100ml/min) have never been conducted. Up to our knowledge, the activity of Ru nanoparticles supported on KIT-6 mesoporous silica in DRM has never been reported before. The bi-metallic catalyst 15Ni1Ru/KIT-6 has been also studied in order to improve the activity and stability of the 15Ni/KIT-6 catalyst.

4.4.1. Catalytic Activity

Figures 4.29, 4.30, and 4.31 show the catalytic performances of Ni and/or Ru supported on KIT-6 and Ce-KIT-6 catalysts.

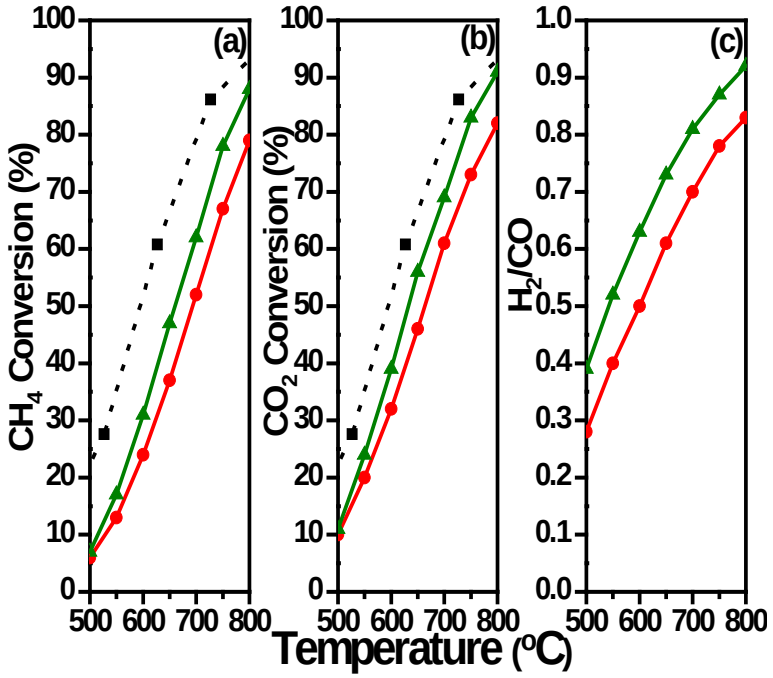

Figure 4.29: (a) CH_4 Conversion, (b) CO_2 conversion and (c) H_2/CO molar ratio of 1Ru/KIT-6 and 1Ru/Ce-KIT-6 catalysts (- ▪ - Theoretical Conversion, —●— 1Ru/KIT-6 —▲— 1Ru/Ce-KIT-6)

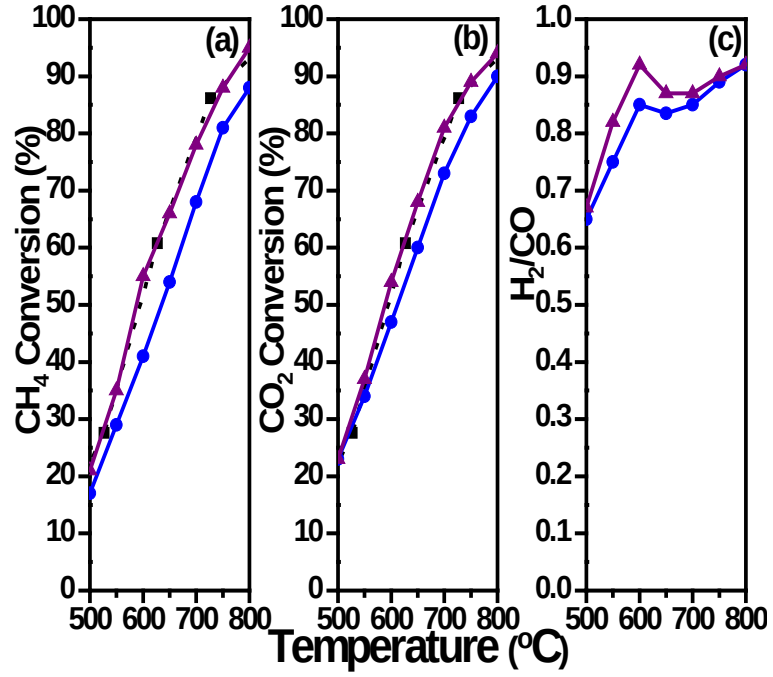

Figure 4.30: (a) CH_4 Conversion, (b) CO_2 conversion and (c) H_2/CO molar ratio of 15Ni/KIT-6 and 15Ni/Ce-KIT-6 catalysts (- ▪ - Theoretical Conversion, —●— 15Ni/KIT-6, —▲— 15Ni/Ce-KIT-6)

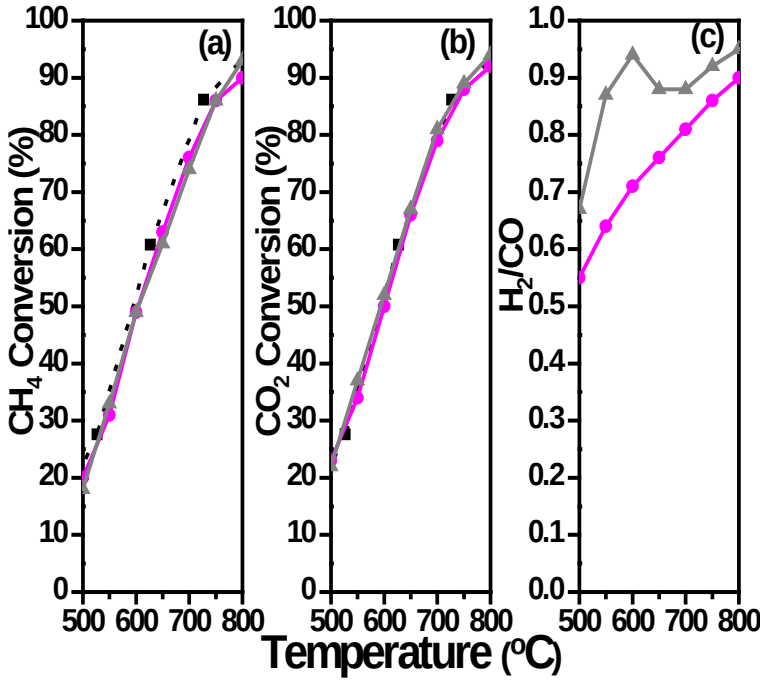

Figure 4.31: (a) CH_4 Conversion, (b) CO_2 conversion and (c) H_2/CO molar ratio of 15Ni1Ru/KIT-6 and 15Ni1Ru/Ce-KIT-6 catalysts (- ▪ - Theoretical Conversion, —●— 15Ni1Ru/KIT-6, —▲— 15Ni1Ru/Ce-KIT-6)

No reactants conversion was observed in the presence of the KIT-6 or the Ce-KIT-6 supports. It is observed that for KIT-6 supported catalysts, the 1Ru/KIT-6 catalyst was the least efficient while the highest conversions were obtained in the presence of the 15Ni1Ru/KIT-6 catalyst (90 % and 92 % conversions of CH_4 and CO_2 respectively at 800 °C). Promoting KIT-6 with Ce yielded more efficient catalysts in the DRM reaction over all the studied temperature range. For instance, at 800 ^oC, both CH_4 and CO_2 conversions, in the presence of 1Ru/Ce-KIT-6 catalyst were increased by 9 % compared to the 1Ru/KIT-6 catalyst (figure 4.29). This is due to the enhanced dispersion, reducibility, and basicity of the catalysts following the addition of Ce (chapter 3, part 3.2.2.). 15Ni/Ce-KIT-6 also showed superior catalytic performance compared to 15Ni/KIT-6 as CH_4 and CO_2 conversions increased from 88 % and 90 % (15Ni/KIT-6) to 94 % and 95 % (15Ni/Ce-KIT-6) respectively (figure 4.30). This is mainly due to the enhanced reducibility and basicity in the presence of cerium species. The effect of Ce addition was less expressed in the case of the bi-metallic active phase catalysts (figure 4.31) because conversions were already comparable to the maximum values dictated by the thermodynamics of the DRM reaction. Whatever the used catalyst, and at any temperature, the CO_2 conversions were always slightly higher than the CH_4 conversions. This indicates the operation of the reverse water gas shift. In addition, the H_2/CO molar were closer to 1 in the presence of Ce containing catalysts. This suggests that the addition of

cerium to the catalytic system resulted in an enhanced selectivity towards equimolar H_2/CO. For the 15Ni/KIT-6, 15Ni/Ce-KIT-6, and 15Ni1Ru/Ce-KIT-6 catalysts, the H_2/CO molar ratios increase in the 550 ^oC – 650 ^oC temperature range indicating a high H_2 yield compared to CO and thus a higher occurrence of the Boudouard or CH_4 cracking reaction in this temperature range.

4.4.2. Characterization after Test

Thermal analysis

Figures 4.32 (a) and (b) represent respectively the thermal analysis of the spent Ni and/or Ru supported on KIT-6 and Ce-KIT-6 catalysts.

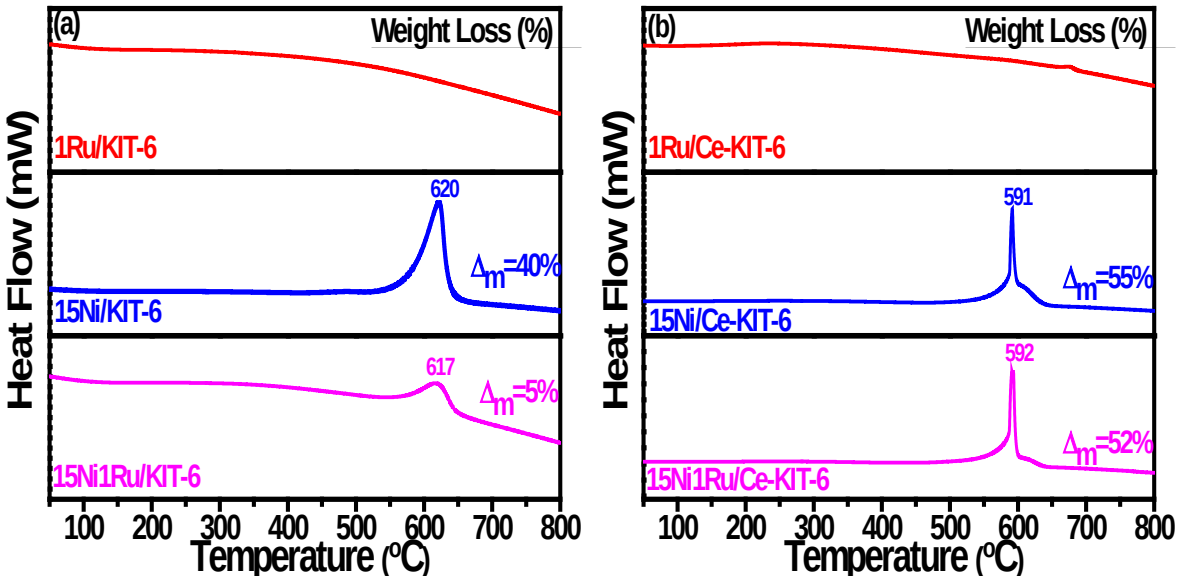

Figure 4.32: DTA curves and weight loss values obtained for (a) KIT-6 and (b) Ce-KIT-6 supported catalysts

For 1Ru/KIT-6 and 1Ru/Ce-KIT-6 catalysts, no exothermic phenomena were observed in the considered temperature range. This indicates the absence of deposited carbon on these catalysts which is due to the important role of ruthenium species in carbon gasification. This beneficial role of ruthenium is more clear when the amount of deposited carbon (40 %) on 15Ni/KIT-6 is compared to the amount deposited (5 %) on 15Ni1Ru/KIT-6. As for the 15Ni/Ce-KIT-6 and the 15Ni1Ru/Ce-KIT-6 catalysts, the amount of deposited carbon was 55 % and 52 % respectively. Ruthenium presence did slightly contribute to the decrease in the amount of deposited carbon in this case. These considerable amounts of deposited carbon

species are due to the superior catalytic activity of the Ce containing catalysts which at some point favors side reactions that led to carbon formation. All weight losses recorded over the catalysts were accompanied with an exothermic phenomenon in the 600 ^oC region corresponding to the oxidation of deposited carbon of the graphitic type. It is also observed that the rate at which the oxidation of deposited carbon is the highest occurs at T > 600 ^oC for 15Ni/KIT-6 and 15Ni1Ru/KIT-6 catalysts but at T < 600 ^oC for 15Ni/Ce-KIT-6 and 15Ni-1Ru/Ce-KIT-6 catalysts. This is mainly due to the excellent redox properties of systems combining Ru and Ce leading to facilitated carbon oxidation reactions [219].

X-ray diffraction

Figures 4.33 (a) and (b) show respectively the XRD patterns obtained for the spent Ni and/or Ru supported on KIT-6 and Ce-KIT-6 catalysts.

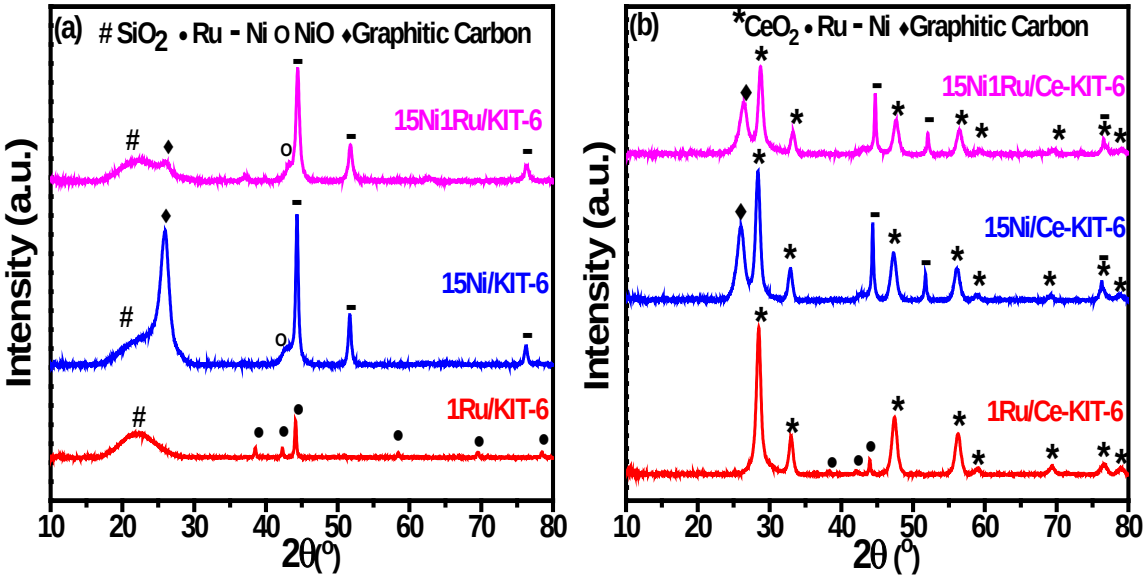

Figure 4.33: XRD patterns the spent (a) KIT-6 and (b) Ce-KIT-6 supported catalysts

Metallic Ru and Ni reflections are clearly present for all the catalysts. The appearance of Ru phase in the spent 1Ru/Ce-KIT-6 catalysts indicates the occurrence of active phase agglomeration after the DRM reaction. A diffraction line at $2\theta = 27^o$ is assigned to graphitic carbon and was observed for the 15Ni/KIT-6, 15Ni1Ru/KIT-6, 15Ni/Ce-KIT-6 and 15Ni1Ru/Ce-KIT-6 catalysts. These results are in accordance with the thermal analyses of the spent catalysts.

4.4.3. Effect of Ce Promotion on Catalytic Stability

As the bi-metallic 15Ni1Ru/KIT-6 catalyst showed the best catalytic performance in the non-promoted series, it was chosen along with 15Ni1Ru/Ce-KIT-6 to perform a stability study. Figures 4.34 (a) and (b) show the CH_4 and CO_2 conversions, the H_2 and CO selectivites, and the H_2/CO molar ratios obtained during a 12 hours on stream DRM reaction at 800 ^oC in the presence of 15Ni1Ru/KIT-6 and 15Ni1Ru/Ce-KIT-6 catalysts.

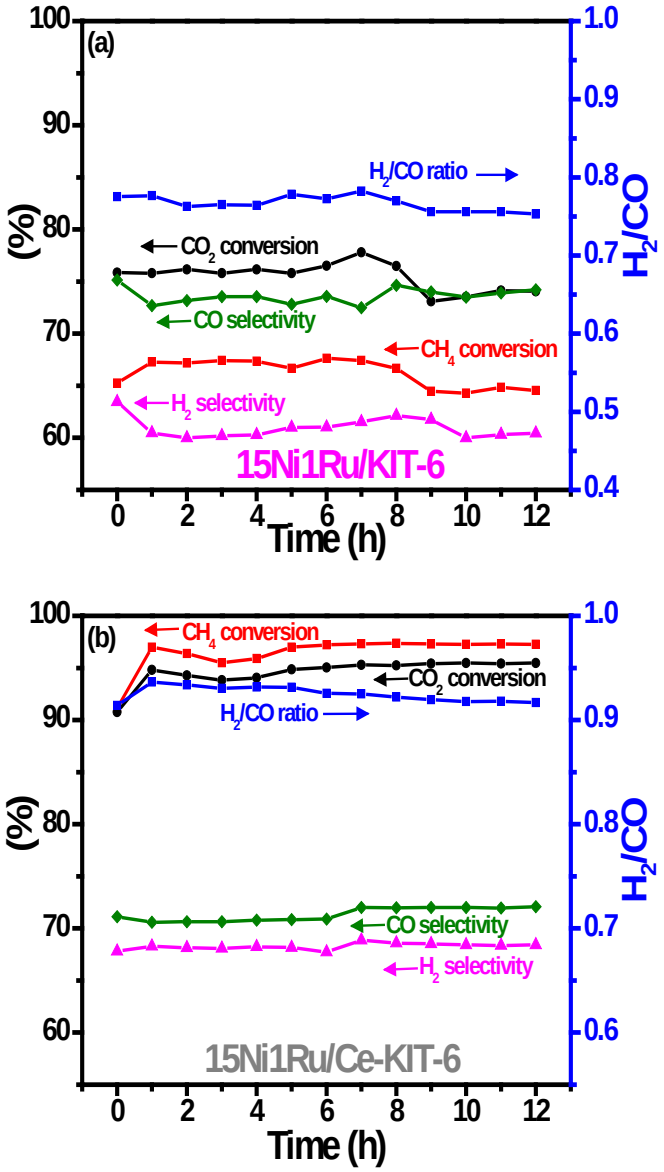

Figure 4.34: Stability tests at 800 ^oC for 12 h on stream in the presence of (a) 15Ni1Ru/KIT-6 and (b) 15Ni1Ru/Ce-KIT-6 catalysts

At the beginning of the test, the CH_4 and CO_2 conversions of the promoted catalyst were 91 % and 90 % respectively. However, in the absence of Ce, the 15Ni1Ru/KIT-6 catalyst revealed a CH_4 conversion that is lower by 26 % and a CO_2 conversion that is lower by 14.2 % than the 15Ni1Ru/Ce-KIT-6 catalyst. After 1 hour on stream, the CH_4 and CO_2 conversions of the 15Ni1Ru/Ce-KIT-6 catalyst increased to reach 97 % and 95 % respectively. These obtained conversion values remained stable during the whole time on stream. On the contrary, it is noticed from figure 4.34 (a) that after 7 hours on stream, a slight loss of activity was observed for the non-promoted catalyst. At the end of the run, the CH_4 and CO_2 deactivation rates of 15Ni1Ru/KIT-6 were 1 % and 2.4 % respectively.

Moreover, the H_2/CO molar ratio is higher and maintained at a value of ~ 0.93 for the 15Ni-1Ru/Ce-KIT-6 catalyst while at a value of ~0.76 for the non-promoted catalyst. H_2 selectivity is also higher (by approximately 8 %) in the 15Ni1Ru/Ce-KIT-6 catalyst. CO selectivity, on the other hand, is slightly higher in the absence of Ce. An average of 74 % and 71 % CO selectivity was witnessed over the 15Ni1Ru/KIT-6 and 15Ni1Ru/Ce-KIT-6 catalysts respectively during the whole time on stream. Thermal analyses after stability tests showed that the weight losses obtained over 15Ni1Ru/KIT-6 and 15Ni1Ru/Ce-KIT-6 are 1 % and 40 % respectively. This difference in carbon formation is again explained by the superior catalytic activity and the possible occurrence of secondary reactions in the presence of Ce. The higher H_2 selectivity (compared to the non-promoted catalyst) and the CH_4 conversions that were higher than CO_2 conversions during the whole time on stream suggest that DRM was accompanied by the occurrence of methane cracking which is also favored at 800 ^oC.

4.4.4. Discussion

- From the non-promoted series, the 15Ni1Ru/KIT-6 was the optimal catalyst. This latter presented enhanced redox properties (chapter 2, figure 2.11 and table 2.10), the smallest NiO crystallite sizes (chapter 2, table 2.8), as well as the highest basicity among the non-promoted catalysts (chapter 2, table 2.11), which explains its superior catalytic performance.
- In chapter 3, Ce_{60}KIT-6 supported catalysts revealed good dispersion, reducibility, and basicity as a result of the promotional effect of Ce. This was clear from the XRD (part 3.2.2.1.), TPR (part 3.2.2.3.), and TPD results (part 3.2.2.4.). All these factors translated into an ameliorated DRM catalytic activity for the promoted catalysts.

- Despite the greater carbon content, no deactivation was observed during 12 h on stream for the 15Ni1Ru/Ce-KIT-6 catalyst indicating that the deposited carbon did not completely encapsulate Ni sites that remained accessible to the reactants. A possible explanation is the regeneration of the active catalytic sites due to continuous coke removal via CO_2 gasification. Generally, during DRM, the oxygen vacancies provided by CeO_2 are said to prevent carbon deposition by enhancing the mobility of surface oxygen and adsorbing the CO_2 species on the catalyst surface [106,189]. In addition, as already established, ruthenium also played a vital role in catalyzing coke gasification. From our catalytic composition, it seems that the synergetic presence of both ruthenium and ceria led to an increased DRM intrinsic activity and stability.

Conclusion and Perspectives

The aim of this work was to compare different catalytic materials and evaluate the role of the support and the active phase in two reactions commonly adopted for CO_2 utilization and valorization. The work details the synthesis and characterization of Ni and/or Ru based catalysts supported on different mesoporous oxides and highlights the effect of promoting the supports with ceria.

The crystal and porous structures as well as the reducibility and basicity of all supports and catalysts were thoroughly investigated prior to catalytic testing. All supports and catalysts evaluated in this work revealed typical type IVa adsorption isotherms suggesting the meso-structure and occurrence of capillary condensation. For most of the catalysts, the mesoporous structure of the support was partially destroyed following promotion with Ce and/or active metal impregnation as was evidenced by the change in the shape of the isotherms and decreased surface areas and pore volumes. XRD and TPR results showed that in the monometallic Ru based catalysts (1Ru/CeO_2, 1Ru/Al_2O_3, and 1Ru/KIT-6, 1Ru/Ce_xKIT-6, 1Ru/Ce-Al_2O_3), the active phase dispersion and reducibility is enhanced when CeO_2 is used as the support and when KIT-6 and Al_2O_3 are promoted with Ce. The combination of Ni and Ru enhanced RuO_2 dispersion and NiO reducibility at lower temperatures whatever the support used.

In the CO_2 methanation reaction, the availability of the active sites was determined by the reduction treatment and affected the CO_2 methanation activity of the Ni based catalysts. For 15Ni/Al_2O_3 and 15Ni/KIT-6 catalysts, NiO species were not fully reduced at 350 ^oC in the absence of Ce promotion which resulted in a lower catalytic activity compared to the 15Ni/CeO_2 catalyst. 15Ni1Ru/Ce_{60}KIT-6 catalyst was chosen to study the effect of varying the GHSV on the catalytic activity. The optimal GHSV was found to be equal to 40,000 h^{-1}. Over long periods on stream, the 15Ni1Ru/CeO_2 catalyst showed the highest activity and stability. The deactivation of the catalysts containing less Ce was attributed to the Ni metal particle sintering.

In the CO_2 reforming of methane reaction, the support and the active phase determined the extent to which carbon was formed in the reaction. CeO_2 supported catalysts (1Ru/CeO_2, 15Ni/CeO_2, 15Ni1Ru/CeO_2) and Ru based catalysts (1Ru/Al_2O_3, 1Ru/Ce-Al_2O_3, 1Ru/KIT-6, 1Ru/Ce-KIT-6) were resistant to carbon formation. The amount of deposited carbon was lower in the bi-metallic 15Ni1Ru/Al_2O_3, 15Ni1Ru/KIT-6, and 15Ni1Ru/Ce-KIT-6 catalysts compared to the mono-metallic counter-parts. Despite the greater carbon content, no deactivation was observed for the Ce containing catalysts indicating that the active sites remained accessible to the reactants. A possible explanation is the regeneration of the active

catalytic sites due to continuous carbon removal via CO_2 gasification. Among all the tested catalysts in the CO_2 reforming of methane, the mesoporous silica supported catalysts 15Ni/KIT-6, 15Ni/SBA-15 and 15Ni/SBA-16 showed high activity and no deactivation in our adopted catalytic conditions.

Several additional studies that further validate the hypotheses used to explain and discuss the obtained results must be performed to complete the work done in this thesis. First and foremost, it is important to perform electron microscopy analysis (TEM) in order to verify the dispersion of the active phases on the mesoporous supports (surface or inside the pores) and evaluate clearly the incorporation of Ce. Microscopy techniques can be also helpful in evaluating the carbon deposition phenomena and confirming the hypotheses suggesting Ni sintering and agglomeration. Verification and measurement of the active phase loadings using quantitative techniques (ICP, XRF..) is also crucial in characterizing the catalysts. To understand more clearly the role played by the different active phases and the promoter in the mechanism of both studied reactions, it would be interesting to perform a mechanistic study and provide information on the nature of intermediate species and products in real time using In Situ Infrared Spectroscopy techniques.

In the CO_2 methanation, it is important to perform additional studies that can help in scaling up the processes for industrial application. A catalyst is not considered efficient unless it can be reused for several reaction cycles. Testing the optimal catalyst 15Ni1Ru/CeO_2 in a reusability study will make the usage of this catalyst more attractive for commercial use.

In the CO_2 reforming of methane, longer stability tests should be conducted on the promoted catalysts and the Ni based catalysts supported on mesoporous silica to verify if the regeneration of these catalysts will be effective after several carbon deposition-removal cycles.

Appendix A

This appendix contains a detailed explanation of the characterization techniques and the catalytic test set-up used for both reactions. All prepared samples were characterized using the following techniques: X-Ray Diffraction (XRD), Nitrogen adsorption/desorption, H_2-Temperature Programmed Reduction (H_2-TPR), CO_2-Temperature Programmed Desorption (CO_2-TPD), and Simultaneous Differential Thermal Analysis and Thermogravimetry Analysis (DTA/TGA). Two catalytic lab-scale set-ups were used: one for the CO_2 methanation tests and one for the CO_2 reforming of methane (DRM) tests. XRD, N_2 adsorption/desorption, DTA/TGA, and DRM tests were performed at the UCEIV (Unité de Chimie Environnementale et Interactions sur le Vivant) laboratories of the Université du Littoral Côte d'Opale in Dunkerque, France. H_2-TPR and CO_2-TPD experiments were performed at the Chemistry Lab in the University of Balamand (UOB), Lebanon. The CO_2 methanation tests were conducted in the Chemical Engineering Lab of UOB.

Characterization Techniques

A- X-ray diffraction

X-ray diffraction (XRD) is a worldwide qualitative analysis technique that can determine the nature and the structure of a crystal. The method involves sending an X-ray on a powdered sample deposited on a watch glass. As the beam reaches the sample, it will diffract by an angle θ that is detected by computer scintillation.

In order to determine the crystal structure of the calcined supports and catalysts and the spent catalysts, Powder X-Ray Diffraction (XRD) analyses were performed using a BRUKER Advance D8 powder apparatus (monochromatic Cu Kα radiation) at ambient temperature. The scattering intensities were measured over an angular range of $5° < 2\theta < 80°$ with a step-size of $2\theta = 0.02°$. The diffraction patterns have been indexed by comparison with standard XRD reference patterns from the JCPDS (Joint Committee on Powder Diffraction Standards) database established by the ICDD (International Center for Diffraction Data). This comparison is achieved using the EVA software. This technique also allows the determination of the size of the crystallites according to the Debye-Scherrer formula:

$$D = \frac{K\ x\ \lambda}{\beta X COS\theta}$$

Where:

D: mean crystallite size (nm)

K: Scherrer constant (0.9)

λ: wavelength of the incident radiation (1.5406^{o} A)

B: broadening at half maximum intensity (^{o})

θ: angle corresponding to the diffraction line (°)

The 2θ values of the most intense peaks used to calculate the crystallite sizes are shown in the table below:

Crystal Phase	CeO_2	RuO_2	NiO	Ru	Ni
2θ (^{o})	28^{o}	28^{o}	43.2^{o}	44^{o}	44^{o}

B- N_2 adsorption/desorption

To study the textural and porous properties of the calcined supports and catalysts, the surface areas, pore volumes and pore size distributions were recorded on a Sorptomatic 1990 Thermo Quest CE INSTRUMENTS. N_2 adsorption-desorption is a method that relies on the physical adsorption of nitrogen gas at liquid nitrogen temperature (-196^{o}C). The obtained adsorption isotherm is the result of the adsorbed amounts of nitrogen gas measured as a function of relative pressure. From these data, the surface area (*SA)* was calculated by the multipoint Brunauer–Emmet–Teller (BET) method (see equation below), the total pore volume (V_p) was estimated from the N_2 desorption amount at a relative pressure *(P/P_o)* of 0.99, and the pore size distribution was analyzed using the Barrett–Joyner–Halenda (BJH) method. Prior to any analysis, the adsorbents were degassed at 250 ^{o}C for 4 h to remove water and other atmospheric contaminants.

$$\frac{1}{V[(\frac{P_o}{P}-1)} = \frac{1}{V_m C} + \frac{C-1}{V_m C}\left(\frac{P}{P_0}\right)$$

Where:

P: partial pressure of nitrogen

P_0: saturation pressure at the experimental temperature

V: volume of N_2 adsorbed (cm^3/g)

V_m: volume of N_2 adsorbed at monolayer coverage (cm^3/g)

C: constant

The Surface Area (*SA)* is then calculated according to below:

$$S\ (m^2/g) = \frac{\alpha V_m\ N_A}{V}$$

Where:

$N_A = 6.023*10^{23}\ mol^{-1}$

$V_m = 22400\ cm^3/mol$

$\alpha = 16.2*10^{-20}$

The modern version of the IUPAC (International Union of Pure and Applied Chemistry) classification scheme has six types of isotherms for gas/solid equilibria as shown in figure A1 (a).

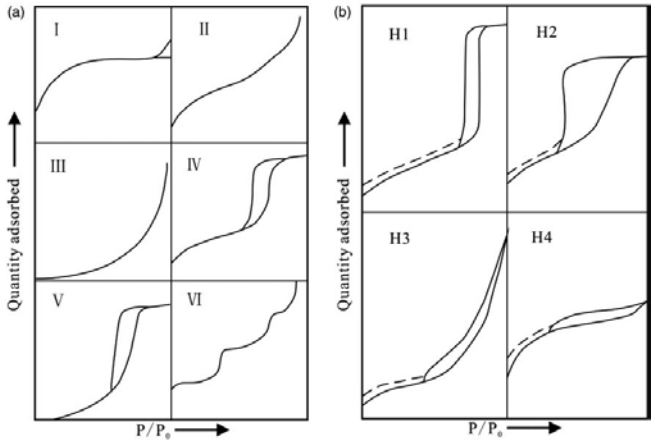

Figure A1: Types of isotherms (a) and Types of Hysteresis Loops (b)

Type I isotherms are given by microporous solids having relatively small external surfaces whereas types II and III are given by macroporous adsorbents with strong and weak affinities respectively. Adsorption on mesoporous solids occurs via multilayer adsorption followed by capillary condensation resulting in Type IVa and V isotherms. Type IVb is given when the capillary condensation is not accompanied with a hysteresis but with cylindrical mesopores that are closed at the tapered end. Type VI isotherms represent stepwise multilayer adsorption on a uniform non-porous surface. A classification of the shape of the hysteresis loops (figure A1 (b)) reflects the underlying pore condensation-evaporation mechanism. The steepness of the isotherm decreases from H1 to H4.

H_2- Temperature programmed reduction

Temperature Programmed Reduction (TPR) is an instrument that allows measuring the reduction extent of a given catalyst and estimating its reversible redox ability. In order to determine the reducibility of the supports and metal oxides that constitute the active phase of

the catalysts, H_2-Temperature-programmed reduction (H_2-TPR) experiments were carried out in a Micromeritics Autochem II chemisorption analyzer. 50 mg of the solid to be analyzed are homogeneously spread on the surface of a quartz cotton inside a U-shaped quartz tube. The latter is placed inside an oven where the thermocouple reads the catalyst temperature.

The mechanism of the analysis involves three steps:

1- Hydrogen consumption calibration.

2- Pretreatment of the sample in argon (50 mL/min) from room temperature till 150 °C for 30 min with a temperature increase of 5 °C/min. This step allows the activation of the catalyst by eliminating water and adsorbed surface impurities.

3- The temperature programmed reduction: samples are then heated from ambient temperature to 900 °C under an H_2 flow of 5 vol% in argon (50 mL/min) at a heating rate of 5 °C/min. The variation of the amount of H_2 consumed as a function of temperature is recorded by means of a thermal conductivity detector (TCD).

The obtained experimental hydrogen consumptions were compared with theoretical ones calculated as follows:

$aA + bH_2 \rightarrow cD + dH_2O$ (A: metal oxide, D: reduced metal)

a mol of A → b mol of H_2

$n_A = \frac{m_A}{MM_A}$ → x mol of H_2 (in µmol H_2/g)

The considered reduction reactions were:

$2CeO_2 + H_2 \rightarrow Ce_2O_3 + H_2O$

$Ni^{2+} + H_2 \rightarrow Ni^0 + 2H^+$

$Ru^{4+} + 2H_2 \rightarrow Ru^0 + 4H^+$.

C- CO_2- Temperature programmed desorption

The supports and catalysts basicity measurements were conducted on the same Micromeritics Autochem II chemisorption analyzer that was used to perform the H_2-TPR analyses. CO_2 was chosen as the probe gas because of its suitable acidity to evaluate all basic sites. The total basicity can be determined based on the amount of desorbed CO_2 molecules and the temperature of desorption. The strength of the basic sites is thus estimated. Around 50 mg of every sample were placed in a U-tube quartz reactor and first pretreated under helium flow (30 mL/min) at 500 °C for 1 h. Catalysts were then cooled to 50 °C and exposed to a flow of 10 % CO_2 in helium (10 % CO_2/He: 30 mL/min) for an hour for adsorption. The samples

were then purged with helium (30 mL/min) for half an hour and then heated to 600 °C at a rate of 10 °C/min to desorb the CO_2. TCD detector monitors the changes in the concentration of the desorbed gas.

D- Differential thermal analysis/thermogravimetry analysis

Differential thermal analysis (DTA) is a thermoanalytical technique in which the mass variations (heat transfer) of a sample are measured as function of temperature and time. Thermogravimetric analysis (TGA) measures the difference in temperature between the sample and a reference sample in function of temperature. As the latter increases, the sample will either undergo a release (exothermic reaction) or absorption (endothermic reaction) of heat, and a loss or a gain of mass. In order to evaluate the thermal stability of the spent catalysts as a function of temperature, thermal analysis was done using a Universal V4.7A TA Instruments apparatus capable of performing simultaneous DTA/TGA analyses. The samples were introduced in an alumina crucible and then heated from room temperature to 900 ^{o}C at 5 ^{o}C/min under an air flow equal to 50 ml/min. The TGA curve allows following the sample's weight (loss or gain) with respect to temperature while the DTA curve gives information on the endothermic and exothermic phenomena that take place during the heating of the sample.

Catalytic Tests

1- CO_2 Methanation

A- Test set-up

CO_2 methanation tests were conducted using a Microactivity-Efficient Catalytic Reactor from PID Eng & Tech Company. The catalytic tests were evaluated at atmospheric pressure in the 150 ^{o}C – 350 ^{o}C temperature range. The experimental set-up is shown on figure A2.

The set-up consists of a vertical stainless steel tube catalytic reactor with an internal diameter of 9 mm. The interior of the reactor is equipped with a porous plate. A thermocouple is inserted through the upper end of the reactor and is in contact with the catalytic bed. The whole system is placed in a hot box which keeps the system at a temperature of 110 °C in order to avoid any possible condensation in the lines.

The flow regulators maintain a constant flow of the introduced gases (CO_2, H_2 and Ar).

At the lower end of the reactor, the remaining reactants and the reaction products leave the hot box towards the liquid-gas separator where a cell Peltier permits the condensation of liquids at low temperatures. The upper portion of the separator provides the outlet for the

gases, which are reintroduced into the hot box, and directed to subsequent analysis by chromatography. An Agilent 490 brand gas micro-chromatography is used for the analysis of the reactants (CO_2 and H_2) and products (CH_4 and CO). Gas separation is carried out on a COX column using argon as the carrier gas. Outlet gases are analyzed by means of a thermal conductivity detector (TCD)

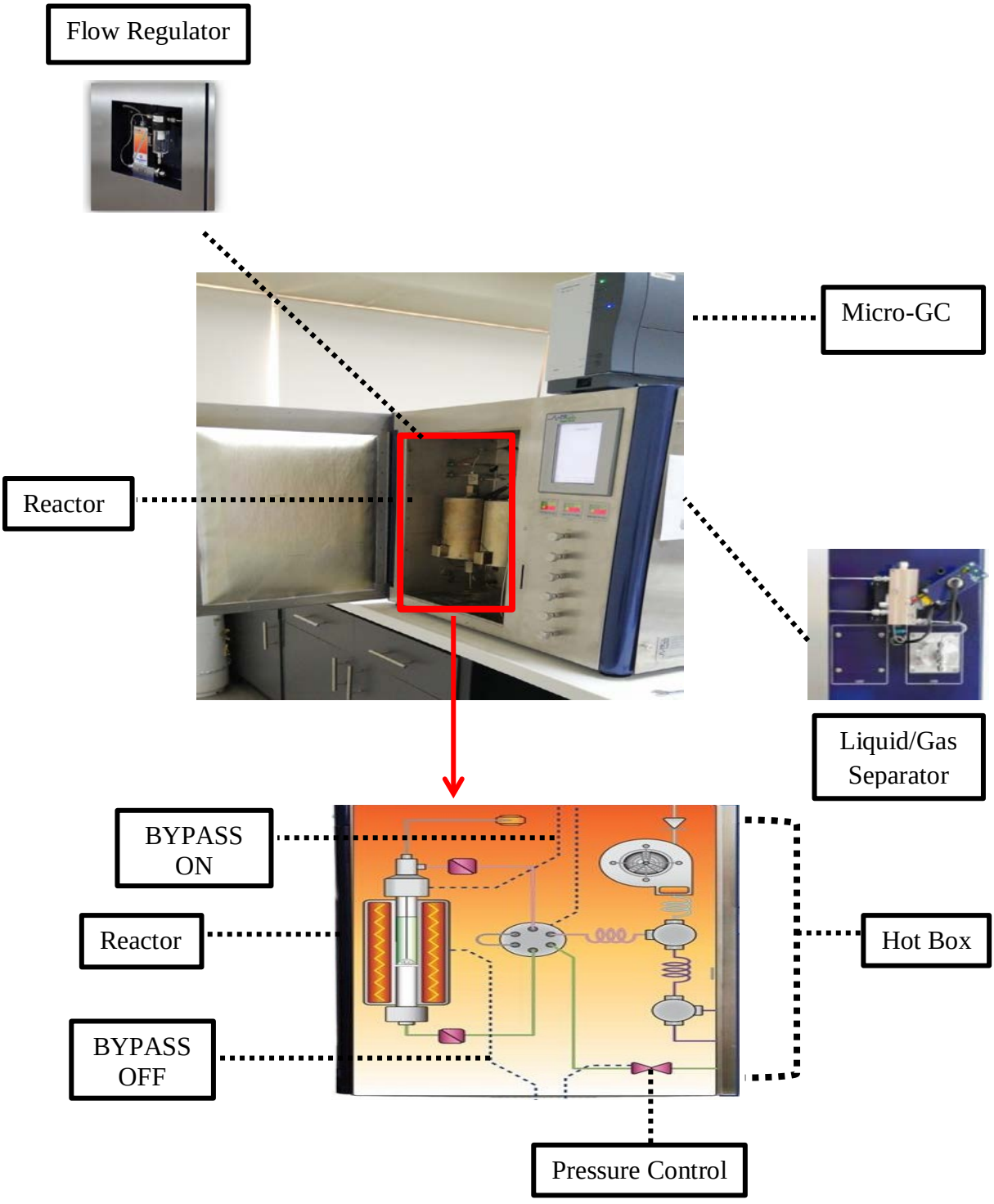

Figure A2: Experimental set-up of the CO_2 methanation reaction

B- Operation and calculation modes

The operating mode of the CO_2 methanation test is divided into four steps:

Step 1: Catalysts Preparation

First of all, 150 mg of the powdered catalysts were pelletized into a size fraction ranging between 350 μm and 800 μm in order to prevent mass and heat transfer limitations. Then, the catalysts were diluted with an inert SiC (ratio SiC/catalyst 2:1) so that the formation of hot spots and preferential gas flows are avoided. The catalyst is then deposited on a layer of quartz wool inside the tube reactor.

Step 2: Leak Test

A leak test is mandatory to check that the catalyst is well positioned and sealed in the reactor and that the flow of the inlet gases entering the reactor and placed in contact with the catalyst is exact. Once all gas bottles and valves are opened, the pressure control valve is closed in order to prevent any flow from passing and the pressure of the reactor is set to 5 bar. A flow of argon is then sent to the reactor. Normally, a pressure will be built up in the reactor as the flow reaches a dead end. Once the reactor pressure reaches 5 bar, the argon flow is cut. If then, the pressure remains constant, it is concluded that no leak is present. The pressure valve is reopened and step number 3 is initiated.

Step 3: Reduction

Before any catalytic test, the catalyst must undergo an activation step which consists of treating it with a reducing mixture (50 % H_2/Ar, 50 mL/min) after a rise in ambient temperature to 350 °C with a heating rate of 10 ^oC/min. The catalyst is maintained for 2 hours at 350 ^oC. The reactor is then kept under a stream of argon for half an hour.

Step 4: Dynamic Test

After the purge with argon, the blank injections are made: The reactor is set to BYPASS mode and fed with a gaseous mixture of CO_2/ H_2/ Ar (10 % /40 % / 50 %) to obtain a CO_2/H_2 molar ratio equal to 4 (stoichiometric conditions). The total flow was 100 mL/min and the GHSV= 40,000 h^{-1}. It is to note that a flow check is done prior to reduction and test using a Varian analytical instruments digital flow meter.

In BYPASS mode, the flow is directed towards the micro-GC and not the reactor (figure A2). Then, a sequence of 7 injections each requiring 3 minutes of analysis is manually submitted. After the blanks are made, the BYPASS mode is turned off, and a sequence of 7 injections is sent to the reactor at 350 ^oC. The reactor is then cooled to 300 ^oC and a second sequence is submitted. This step is repeated as the temperature is decreased to 250 ^oC, 200 ^oC and 150 ^oC.

CO_2, H_2, CO as well as CH_4 peak areas are obtained from the chromatograms and are inserted to an excel sheet and divided with molar coefficients obtained from the calibration curve of each gas. The excel sheet also calculates reagent conversions and selectivities according to the equations below:

CO_2 Conversion: X_{CO_2} (%) = $\frac{n_{CO_2 in} - n_{CO_2 out}}{n_{CO_2 in}}$ *x100*

CH_4 Selectivity: S_{CH_4} (%) = $\frac{n_{CH_4 formed}}{n_{CO_2 in} - n_{CO_2 out}}$ *x100*

CO Selectivity: S_{CO} (%) = $\frac{n_{CO\ formed}}{n_{CO_2 in} - n_{CO_2 out}}$ *x100*

2- CO_2 Reforming of Methane

A- Test set-up

The experimental set-up shown on figure A3 is developed in the lab. Catalytic tests were performed under atmospheric pressure in the 500 ^oC – 800 ^oC temperature range. Three main compartments are identified: a furnace equipped with a temperature control system where the catalytic bed is placed, a flow regulator (mixer) which maintains a predefined flow rate of the introduced gases and a micro-GC that analyzes the outlet gases. A detailed description of the set-up is presented below:

1- The furnace: a vertical compartment composed of ceramic fibers that holds the fixed bed U-shaped quartz micro-reactor coupled with a thermocouple connected to the mixer and placed at the level of the catalytic bed. The furnace is used to regulate the temperature. The thermocouple measures the exact temperature the catalyst is subject to. In order to limit the dissipation of heat and ensure better temperature control, high temperature quartz cotton wool are used to seal the upper and lower openings of the furnace.

2- The flow regulator: the gas introduction system that is connected to the reactor by a four-way valve. It reads the recipe “recette” that orders the flow of each gas (CO_2, CH_4, H_2 and Ar), as well as the reactor mode (BYPASS or REACTOR). In other words, it allows either to inject the gases into the reactor, or to short-circuit the reactor and to send the gases directly to the analyzers. The recipe also orders the injection sequence.

3- Micro-GC: a Varian CP micro-4900 gas phase micro-chromatography through which reagent gases (CH_4 and CO_2) and products (H_2 and CO) leaving the reactor are analyzed. Prior to analysis using a thermal conductivity detector (TCD), gas

separation occurs on a molecular sieve (H_2, CO and CH_4), and a Poraplot Q column (CO_2). The carrier gas used is high purity argon (P = 99.9999 %).

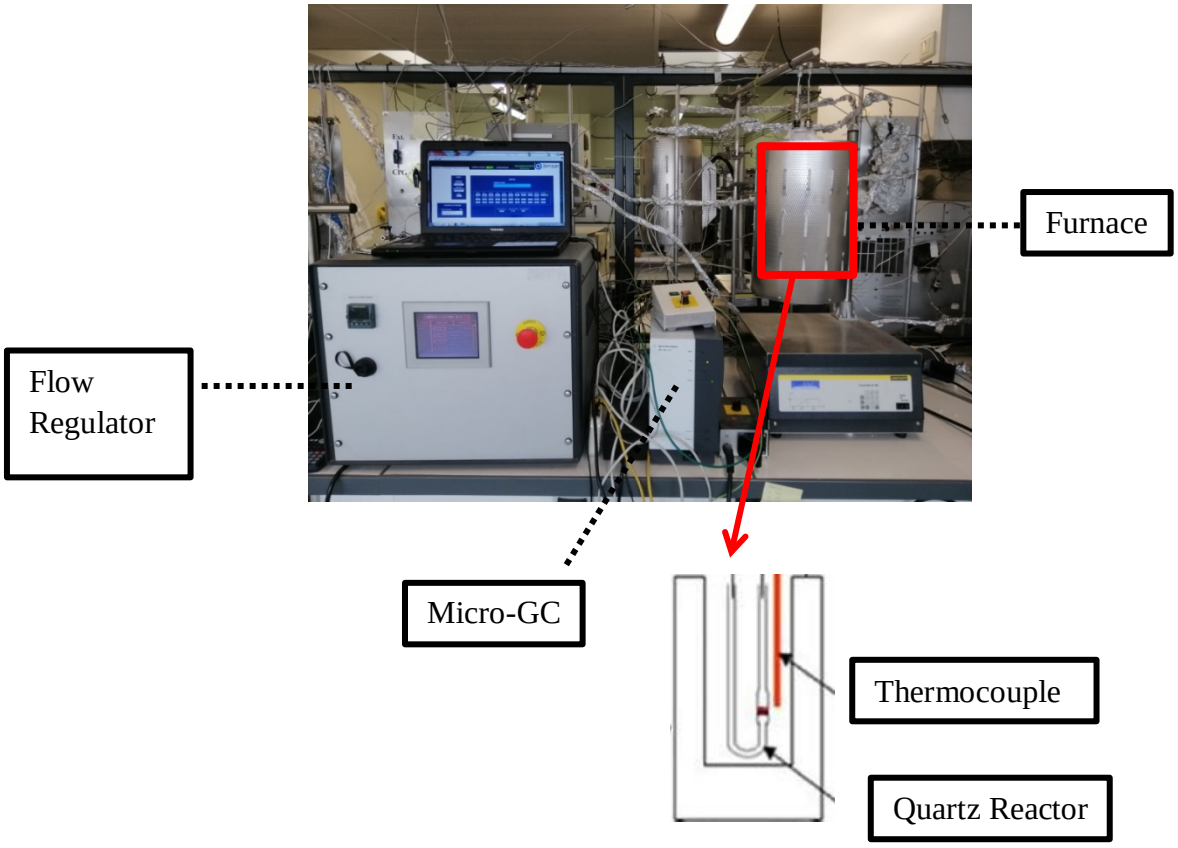

Figure A3: Experimental set-up of the CO_2 reforming of methane reaction

B- Operation and calculation modes

The operating mode of the CO_2 reforming of methane test is divided into three steps:

Step 1: Catalysts Preparation

100 mg of the catalysts (particle size between 350 µm and 800 µm) is placed on the frit which forms the catalytic bed in the quartz reactor.

Step 2: Reduction and Leak Test

Once all gas bottles and vans are opened, the pellets are reduced in situ at 800 ^{o}C with a heating rate of 10 ^{o}C/min for 2 h in a mixture of 5 vol% H_2/Ar. After the reducing gas flow is sent to the sealed reactor, a leak check is done using a hydrocarbon gas detector from Sensit technologies. After the reduction is complete, the reactor is then cooled to 500 ^{o}C under a flow of argon.

Step 3: Dynamic Test

Once the reactor temperature reaches 500 ^{o}C, the recipe is initiated; the reactor is switched to the BYPASS mode and fed with a gaseous mixture of CH_4/CO_2/Ar (20 % / 20 % /60 %) to obtain a CH_4/CO_2 molar ratio equal to 1 in agreement with the stoichiometry of the reaction. The total flow was 100 mL/min and the GHSV= 60,000 h^{-1}. Flow checks at the gas outlet are made using an Agilet ADM flowmeter.

The recipe automatically triggers microchromatography analyses in the form of 7 blank injections (5 min/injection). Next, as ordered by the recipe, the flow regulator is switched to REACTOR mode where a sequence of 7 injections is automatically made every 50 ^{o}C in the 500 ^{o}C – 800 ^{o}C temperature range. Once the test is complete, an acquisition with all needed values (furnace temperature, gas flows, and peak areas for every gas...) for each injection is obtained. CO_2, CH_4, H_2, and CO peak areas are obtained and are inserted to an excel sheet and divided with molar coefficients obtained from the calibration curve of each gas. Reagent conversions, as well as product ratios and selectivities are then calculated according to the equations below:

CO_2 Conversion: X_{CO_2} (%) = $\frac{n_{CO_2 in} - n_{CO_2 out}}{n_{CO_2 in}}$ *x100*

CH_4 Conversion: X_{CH4} (%) = $\frac{n_{CH_4 in} - n_{CH_4 out}}{n_{CH_4 in}}$ *x100*

$H_2/CO = \frac{moles\ of\ H_2\ produced}{moles\ of\ CO\ produced}$

H_2 Selectivity (%) = $\frac{n_{H_2 produced}}{2X(n_{CH_4 in} - n_{CH_4 out})}$ *x100*

CO Selectivity (%) = $\frac{n_{CO_{produced}}}{(n_{CH_4 in} + n_{CO_2 in}) - (n_{CH_4 out} + n_{CO_2 out})}$ *x100*

Appendix B

1- Thermodynamic Calculations

Thermodynamic calculation of the equilibrium constant *K* is carried out according to the following formula:

$$K = e^{\frac{-\Delta G_T}{RT}}$$

where: ΔG_T: Molar Gibbs energy of the reaction at a given temperature (J/mol)

R: Gas constant (8,314 J/mol.K)

T: Temperature (K)

ΔGT is calculated according to the following formula:

$$\Delta G_T = \Delta H_T - T\Delta S_T$$

where: ΔH_T: Molar enthalpy at a given temperature (J/mol)

ΔS_T: Molar entropy at a given temperature (J/mol.K)

ΔH_T and ΔS_T of the reactants or products at each temperature are taken from the "*CRC Handbook of Physics and Chemistry*

***A-Theoretical CO_2 conversion in the CO_2 methanation reaction is calculated according to the following steps*:**

$$CO_2 + 4\,H_2 \rightarrow CH_4 + 2\,H_2O$$

Initial	n_{oCO_2}	n_{oH_2}	0	0
Final	n_{oCO_2}-*x*	n_{oH_2}-*4x*	*x*	*2x*

Therefore, the total number of moles is:

$$n_f = n_{fCO_2} + 4n_{fH_2} + n_{f_{CH_4}} + 2n_{fH_2O} = \left(n_{oCO_2} - x\right) + \left(n_{oH_2} - 4x\right) + x + 2x$$

where n_o and n_f are the initial and total number of moles and $n_{fCO_2}, n_{fH_2}, n_{f_{CH_4}}$ and n_{fH_2O} the final number of moles of each reactant and product in the CO_2 methanation

The equilibrium constant of the CO_2 methanation reaction is:

$$K_{rxn} = \frac{X_{CH_4}\, x\, X_{H_2O}^2}{X_{CO_2}\, x\, X_{H_2}^4}$$

where X_{CH_4}, X_{H_2O}, X_{CO_2} and X_{H_2} are the molar fraction of each reactant and product in the CO_2 methanation reaction and can be written as follows:

$X_{CH_4} = \frac{n_{f_{CH4}}}{n_t}$; $X_{H_2O} = \frac{n_{f_{H_2O}}}{n_t}$; $X_{CO_2} = \frac{n_{f_{CO_2}}}{n_t}$; $X_{H_2} = \frac{n_{f_{H_2}}}{n_t}$

By replacing each component in the equilibrium constant K_{rxn} formula, a 5th degree equation is developed as a function of K_{rxn} and x.

Knowing the values of K_{rxn} as they were previously calculated at each temperature, and using a *MATLAB R2013b* software, *x* is found.

Therefore, $n_{f_{CO_2}}$ could be now calculated, and the theoretical conversion will be established according to the following formula:

CO_2 Conversion: X_{CO_2} (%) = $\frac{n_{i_{CO_2}} - n_{f_{CO_2}}}{n_{i_{CO_2}}}$ *x100*

The obtained theoretical conversions in the 300 K - 700 K (127 ^{o}C – 427 ^{o}C) temperature range are classified in the table below:

Temperature (^{o}C)	127	227	327	427
CO_2 Conversion (%)	99.9	97.2	89.4	72.6

X and Y values are plotted and the calculated theoretical thermodynamic curve is as follows:

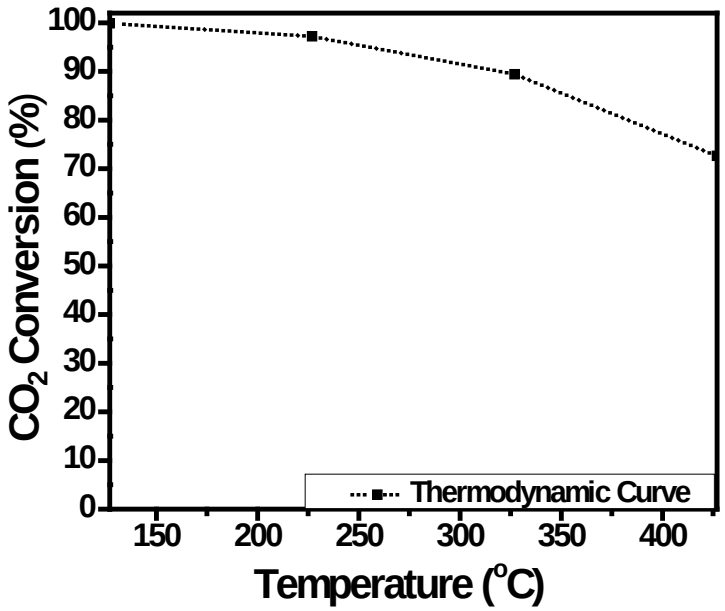

B-Theoretical CO_2 conversion in the DRM reaction is calculated according to the following steps:

	CO_2 +	CH_4 →	2 H_2 +	2 CO
Initial	n_{oCO_2}	n_{oCH_4}	0	0
Final	n_{oCO_2}-*x*	n_{oCH_4}-*4x*	*2x*	*2x*

The same steps as above were applied to obtain the theoretical conversion of CO_2 in the DRM reaction.

The obtained theoretical conversions in the 700 K - 1100 K (427 ^oC – 827 ^oC) temperature range are classified in the table below:

Temperature (^oC)	427	527	627	727	827
CO_2 Conversion (%)	7.85	27.6	60.8	86.15	95.8

X and Y values are plotted and the calculated theoretical thermodynamic curve is as follows:

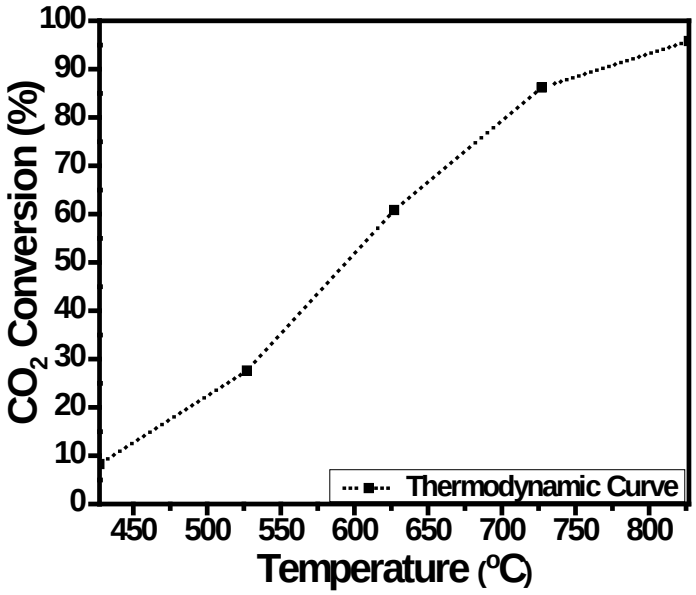

2- Active Phase Calculations

All the catalysts were synthesized via the wet impregnation technique. The formula adopted to calculate the mass of the precursors $Ni(NO_3)_2.6H_2O$ and/or $Ru(NO)(NO_3)_3$) (1.5 wt% Ru) to obtain an active phase (A.P.) of 1 % Ru, 15 % Ni, and 15 % Ni - 1 % Ru is:

$X = \frac{m_{A.P.}}{m_{support}+m_{A.P.}} X100$; X= Percentage of active phase

3- Ce Percentages Calculations

The formula adopted to calculate the mass of the precursor $Ce(NO_3)_3.6H_2O$ required to obtain Ce_xKIT-6 with x= 15, 30, or 60 wt% or Ce-Al_2O_3 with 60 wt% CeO_2 is the following:

$X = \frac{m_{Ce}}{m_{CeO_2}+m_{support}}$ x100

Where:

$m_{Ce} = n_{ce}\, x\, MM_{Ce}$ (n: number of moles; MM: molar mass)

$m_{CeO_2} = n_{ce}\, x\, MM_{Ce} + n_{ce}\, x\, MM_{O_2}$

For example, to obtain 30 wt% CeO_2 :

$0.3 = \frac{140.116\ x\ n_{Ce}}{(140.116\ x\ n_{Ce} + 32\ x\ n_{Ce}) + 0.5}$

$n_{Ce} = 1.69 \times 10^{-3}$ mol

1 mol Ce → 1 mol precursor

$m_{precursor} = 1.69 \times 10^{-3}$ mol x $MM_{precursor}$

References

[1] A. Quindimil *et al.*, "Effect of metal loading on the CO2 methanation: A comparison between alumina supported Ni and Ru catalysts," *Catalysis Today*, vol. 356, pp. 419-432, Jun. 2019.

[2] "Trends in Global CO2 and Total Greenhouse Gas emissions. Summary of the 2019 Report." [Online]. Available: https://www.pbl.nl/en/publications/trends-in-global-co2-and-totaal-greenhouse-gas-emissions-summary-of-the-2019-report (accessed Mar. 25, 2020).

[3] M. Crippa *et al.*, Fossil CO2 and GHG emissions of all world countries: 2019 report, EUR 29849 EN, Publications Office of the European Union, Luxembourg, 2019, ISBN 978-92-76-11100-9.

[4] "Global Energy & CO2 Status Report 2019 – Analysis,"[Online]. Available: https://www.iea.org/reports/global-energy-co2-status-report-2019 (accessed Mar. 25, 2020).

[5] H. Ritchie and M. Roser, "CO_2 and Greenhouse Gas Emissions," *Our World in Data*, May 2017, Accessed: Mar. 23, 2020. [Online]. Available: https://ourworldindata.org/co2-and-other-greenhouse-gas-emissions.

[6] "Global CO2 emissions in 2019 – Analysis." [Online]. Available: https://www.iea.org/articles/global-co2-emissions-in-2019 (accessed Mar. 25, 2020).

[7] "Each Country's Share of CO2 Emissions | Union of Concerned Scientists." [Online]. Available: https://www.ucsusa.org/resources/each-countrys-share-co2-emissions (accessed Mar. 24, 2020).

[8] "International Ambition on Targets for the Post-2020 Era | Climate Policy Info Hub."[Online]. Available: https://climatepolicyinfohub.eu/international-ambition-targets-post-2020-era (accessed Mar. 23, 2020).

[9] A. Mazza, E. Bompard, and G. Chicco, "Applications of power to gas technologies in emerging electrical systems," *Renewable and Sustainable Energy Reviews*, vol. 92, pp. 794–806, Sep. 2018.

[10] M. Nazari-Heris, M. A. Mirzaei, B. Mohammadi-Ivatloo, M. Marzband, and S. Asadi, "Economic-environmental effect of power to gas technology in coupled electricity and gas systems with price-responsive shiftable loads," *Journal of Cleaner Production*, vol. 244, p. 118769, Jan. 2020.

[11] A. Ricca, L. Truda, and V. Palma, "Study of the role of chemical support and structured carrier on the CO2 methanation reaction," *Chemical Engineering Journal*, vol. 377, p. 120461, Dec. 2019.

[12] M. Mihet, O. Grad, G. Blanita, T. Radu, and M. D. Lazar, "Effective encapsulation of Ni nanoparticles in metal-organic frameworks and their application for CO2 methanation," *International Journal of Hydrogen Energy*, vol. 44, no. 26, pp. 13383–13396, May 2019.

[13] M. Thema, F. Bauer, and M. Sterner, "Power-to-Gas: Electrolysis and methanation status review," *Renewable and Sustainable Energy Reviews*, vol. 112, pp. 775–787, Sep. 2019.

[14] K. Ghaib and F.-Z. Ben-Fares, "Power-to-Methane: A state-of-the-art review," *Renewable and Sustainable Energy Reviews*, vol. 81, pp. 433–446, Jan. 2018.

[15] M. A. Murcia Valderrama, R.-J. van Putten, and G.-J. M. Gruter, "The potential of oxalic – and glycolic acid based polyesters (review). Towards CO2 as a feedstock (Carbon Capture and Utilization – CCU)," *European Polymer Journal*, vol. 119, pp. 445–468, Oct. 2019.

[16] R. Muthuraj and T. Mekonnen, “Recent progress in carbon dioxide (CO2) as feedstock for sustainable materials development: Co-polymers and polymer blends,” *Polymer*, vol. 145, pp. 348–373, Jun. 2018.
[17] “Syngas Market | Growth, Trends, and Forecast (2020 - 2025).”[Online]. Available: https://www.mordorintelligence.com/industry-reports/syngas-market (accessed Mar. 26, 2020).
[18] B. Abdullah, N. A. Abd Ghani, and D.-V. N. Vo, “Recent advances in dry reforming of methane over Ni-based catalysts,” *Journal of Cleaner Production*, vol. 162, pp. 170–185, Sep. 2017.
[19] Q. Wei *et al.*, “Facile one-step synthesis of mesoporous Ni-Mg-Al catalyst for syngas production using coupled methane reforming process,” *Fuel*, vol. 211, pp. 1–10, Jan. 2018.
[20] S. S. Itkulova, Y. Y. Nurmakanov, S. K. Kussanova, and Y. A. Boleubayev, “Production of a hydrogen-enriched syngas by combined CO2-steam reforming of methane over Co-based catalysts supported on alumina modified with zirconia,” *Catalysis Today*, vol. 299, pp. 272–279, Jan. 2018.
[21] N. Kumar *et al.*, “Bi-reforming of methane on Ni-based pyrochlore catalyst,” *Applied Catalysis A: General*, vol. 517, pp. 211–216, May 2016.
[22] N. Kumar, M. Shojaee, and J. Spivey, “Catalytic bi-reforming of methane: from greenhouse gases to syngas,” *Current Opinion in Chemical Engineering*, vol. 9, pp. 8–15, Aug. 2015.
[23] L. Xu *et al.*, “CO2 methanation over CoNi bimetal-doped ordered mesoporous Al2O3 catalysts with enhanced low-temperature activities,” *International Journal of Hydrogen Energy*, vol. 43, no. 36, pp. 17172–17184, Sep. 2018.
[24] T. A. Le, M. S. Kim, S. H. Lee, T. W. Kim, and E. D. Park, “CO and CO2 methanation over supported Ni catalysts,” *Catalysis Today*, vol. 293–294, pp. 89–96, Sep. 2017.
[25] L. Falbo, C. G. Visconti, L. Lietti, and J. Szanyi, “The effect of CO on CO2 methanation over Ru/Al2O3 catalysts: a combined steady-state reactivity and transient DRIFT spectroscopy study,” *Applied Catalysis B: Environmental*, vol. 256, p. 117791, Nov. 2019.
[26] S. Rönsch *et al.*, “Review on methanation – From fundamentals to current projects,” *Fuel*, vol. 166, pp. 276–296, Feb. 2016.
[27] K. Hashimoto *et al.*, “Global CO2 recycling—novel materials and prospect for prevention of global warming and abundant energy supply,” *Materials Science and Engineering: A*, vol. 267, no. 2, pp. 200–206, Jul. 1999.
[28] W. Gac, W. Zawadzki, G. Słowik, A. Sienkiewicz, and A. Kierys, “Nickel catalysts supported on silica microspheres for CO2 methanation,” *Microporous and Mesoporous Materials*, vol. 272, pp. 79–91, Dec. 2018.
[29] T. Sakpal and L. Lefferts, “Structure-dependent activity of CeO2 supported Ru catalysts for CO2 methanation,” *Journal of Catalysis*, vol. 367, pp. 171–180, Nov. 2018.
[30] W. Jin Lee *et al.*, “Recent trend in thermal catalytic low temperature CO2 methanation: a Critical Review,” *Catalysis Today*, Feb. 2020. In press.
[31] L. Pastor-Pérez, V. Patel, E. Le Saché, and T. R. Reina, “CO2 methanation in the presence of methane: Catalysts design and effect of methane concentration in the reaction mixture,” *Journal of the Energy Institute*, vol. 93, pp. 415-424, Feb. 2019.
[32] K. Stangeland, D. Kalai, H. Li, and Z. Yu, “CO2 Methanation: The Effect of Catalysts and Reaction Conditions,” *Energy Procedia*, vol. 105, pp. 2022–2027, May 2017.

[33] J. Gao *et al.*, "A thermodynamic analysis of methanation reactions of carbon oxides for the production of synthetic natural gas," *RSC Advances*, vol. 2, no. 6, pp. 2358–2368, 2012.
[34] F. Massa, A. Coppola, and F. Scala, "A thermodynamic study of sorption-enhanced CO2 methanation at low pressure," *Journal of CO2 Utilization*, vol. 35, pp. 176-184, Jan. 2020.
[35] P. Frontera, A. Macario, M. Ferraro, and P. Antonucci, "Supported Catalysts for CO2 Methanation: A Review," *Catalysts*, vol. 7, no. 2, p. 59, Feb. 2017.
[36] X. Su, J. Xu, B. Liang, H. Duan, B. Hou, and Y. Huang, "Catalytic carbon dioxide hydrogenation to methane: A review of recent studies," *Journal of Energy Chemistry*, vol. 25, no. 4, pp. 553–565, Jul. 2016.
[37] M. Younas, L. Kong, M.J. K. Bashir, H. Nadeem, A. Shehzad, and S. Sethupathi, *Energy & Fuels* , vol. 30, no.11, pp. 8815-8831, Oct. 2016**.**
[38] M. Götz, A.M. Koch, and F. Graf,"State of the Art and Perspectives of CO2 Methanation Process Concepts for Power-to-Gas Applications," *International Gas Union Research Conference*, Copenhagen, 2014.
[39] D. Y. Shin, J. S. Won, J. A. Kwon, M.-S. Kim, and D.-H. Lim, "First-principles study of copper nanoclusters for enhanced electrochemical CO2 reduction to CH4," *Computational and Theoretical Chemistry*, vol. 1120, pp. 84–90, Nov. 2017.
[40] A. Kotsiras *et al.*, "Electrochemical promotion of nanodispersed Ru-Co catalysts for the hydrogenation of CO2," *Applied Catalysis B: Environmental*, vol. 232, pp. 60–68, Sep. 2018.
[41] M. Makri, A. Symillidis, D. Grigoriou, A. Katsaounis, and C. G. Vayenas, "Electrochemical Promotion of CO2 Reduction on a Dispersed Ru/YSZ Catalyst Supported on YSZ Solid Electrolyte," *Materials Today: Proceedings*, vol. 5, no. 14, Part 1, pp. 27617–27625, Jan. 2018.
[42] G. Zhou *et al.*, "Methanation of carbon dioxide over Ni/CeO2 catalysts: Effects of support CeO2 structure," *International Journal of Hydrogen Energy*, vol. 42, no. 25, pp. 16108–16117, Jun. 2017.
[43] K. Stangeland, D. Y. Kalai, H. Li, and Z. Yu, "Active and stable Ni based catalysts and processes for biogas upgrading: The effect of temperature and initial methane concentration on CO2 methanation," *Applied Energy*, vol. 227, pp. 206–212, Oct. 2018.
[44] R. Daroughegi, F. Meshkani, and M. Rezaei, "Characterization and evaluation of mesoporous high surface area promoted Ni- Al2O3 catalysts in CO2 methanation," *Journal of the Energy Institute*, Apr. 2020.
[45] C. Italiano, J. Llorca, L. Pino, M. Ferraro, V. Antonucci, and A. Vita, "CO and CO2 methanation over Ni catalysts supported on CeO2, Al2O3 and Y2O3 oxides," *Applied Catalysis B: Environmental*, vol. 264, p. 118494, May 2020.
[46] J. Lin *et al.*, "Enhanced low-temperature performance of CO2 methanation over mesoporous Ni/Al2O3-ZrO2 catalysts," *Applied Catalysis B: Environmental*, vol. 243, pp. 262–272, Apr. 2019.
[47] A. Aljishi, G. Veilleux, J. A. H. Lalinde, and J. Kopyscinski, "The effect of synthesis parameters on ordered mesoporous nickel alumina catalyst for CO2 methanation," *Applied Catalysis A: General*, vol. 549, pp. 263–272, Jan. 2018.
[48] X. Wang, L. Zhu, Y. Liu, and S. Wang, "CO2 methanation on the catalyst of Ni/MCM-41 promoted with CeO2," *Science of The Total Environment*, vol. 625, pp. 686–695, Jun. 2018

[49] R. Dębek, F. Azzolina-Jury, A. Travert, and F. Maugé, “A review on plasma-catalytic methanation of carbon dioxide – Looking for an efficient catalyst,” *Renewable and Sustainable Energy Reviews*, vol. 116, p. 109427, Dec. 2019.
[50] S. Tada *et al.*, “Sponge Ni catalyst with high activity in CO2 methanation,” *International Journal of Hydrogen Energy*, vol. 42, no. 51, pp. 30126–30134, Dec. 2017.
[51] B. Alrafei, I. Polaert, A. Ledoux, and F. Azzolina-Jury, “Remarkably stable and efficient Ni and Ni-Co catalysts for CO2 methanation,” *Catalysis Today*, vol. 346, pp. 23-33, Apr. 2020.
[52] C. Liang *et al.*, “Methanation of CO2 over Ni/Al2O3 modified with alkaline earth metals: Impacts of oxygen vacancies on catalytic activity,” *International Journal of Hydrogen Energy*, vol. 44, no. 16, pp. 8197–8213, Mar. 2019.
[53] S. Navarro-Jaén, J. C. Navarro, L. F. Bobadilla, M. A. Centeno, O. H. Laguna, and J. A. Odriozola, “Size-tailored Ru nanoparticles deposited over γ-Al2O3 for the CO2 methanation reaction,” *Applied Surface Science*, vol. 483, pp. 750–761, Jul. 2019.
[54] T. A. Le, J. Kim, J. K. Kang, and E. D. Park, “CO and CO2 methanation over Ni/Al@Al2O3 core–shell catalyst,” *Catalysis Today*, vol. 356, pp. 622-630, Oct. 2020.
[55] J. Gao, Q. Liu, F. Gu, B. Liu, Z. Zhong, and F. Su, “Recent advances in methanation catalysts for the production of synthetic natural gas", *RSC.Adv*, vol. 5, pp.22759–22776, Feb.2015.
[56] W. A. W. Abu Bakar, R. Ali, and S. Toemen, “Catalytic methanation reaction over supported nickel–ruthenium oxide base for purification of simulated natural gas,” *Scientia Iranica*, vol. 19, no. 3, pp. 525–534, Jun. 2012.
[57] R.-P. Ye *et al.*, “Enhanced stability of Ni/SiO2 catalyst for CO2 methanation: Derived from nickel phyllosilicate with strong metal-support interactions,” *Energy*, vol. 188, p. 116059, Dec. 2019.
[58] X. Wang, T. Zhen, and C. Yu, “Application of Ni–Al-hydrotalcite-derived catalyst modified with Fe or Mg in CO2 methanation,” *Applied Petrochemical Research*, vol. 6, no. 3, pp. 217–223, Sep. 2016.
[59] W. L. Vrijburg *et al.*, “Ni-Mn catalysts on silica-modified alumina for CO2 methanation,” *Journal of Catalysis*, vol. 382, pp. 358–371, Feb. 2020.
[60] A. Zhao, W. Ying, H. Zhang, M. Hongfang, and D. Fang, “Ni/Al2O3 catalysts for syngas methanation: Effect of Mn promoter,” *Journal of Natural Gas Chemistry*, vol. 21, no. 2, pp. 170–177, Mar. 2012.
[61] M. Guo and G. Lu, “The effect of impregnation strategy on structural characters and CO2 methanation properties over MgO modified Ni/SiO2 catalysts,” *Catalysis Communications*, vol. 54, pp. 55–60, Sep. 2014.
[62] S. Cimino, F. Boccia, and L. Lisi, “Effect of alkali promoters (Li, Na, K) on the performance of Ru/Al2O3 catalysts for CO2 capture and hydrogenation to methane,” *Journal of CO2 Utilization*, vol. 37, pp. 195–203, Apr. 2020.
[63] A. Rafiee, K. Rajab Khalilpour, D. Milani, and M. Panahi, “Trends in CO2 conversion and utilization: A review from process systems perspective,” *Journal of Environmental Chemical Engineering*, vol. 6, no. 5, pp. 5771–5794, Oct. 2018.
[64] W.-J. Jang, J.-O. Shim, H.-M. Kim, S.-Y. Yoo, and H.-S. Roh, “A review on dry reforming of methane in aspect of catalytic properties,” *Catalysis Today*, vol. 324, pp. 15-26, Mar. 2019.
[65] N. A. K. Aramouni, J. G. Touma, B. A. Tarboush, J. Zeaiter, and M. N. Ahmad, “Catalyst design for dry reforming of methane: Analysis review,” *Renewable and Sustainable Energy Reviews*, vol. 82, pp. 2570–2585, Feb. 2018.

[66] S. Aouad, M. Labaki, S. Ojala, P. Seelam, E. Turpeinen, C. Gennequin et al, "A Review on the Dry Reforming Processes for Hydrogen Production: Catalytic Materials and Technologies," In: *Frontiers in Ceramic Science*, 2018, pp. 60-128.

[67] R. K. Singha, A. Yadav, A. Shukla, M. Kumar, and R. Bal, "Low temperature dry reforming of methane over Pd-CeO2 nanocatalyst," *Catalysis Communications*, vol. 92, pp. 19–22, Mar. 2017.

[68] E. Dahdah *et al.*, "CO2 reforming of methane over NixMg6−xAl2 catalysts: Effect of lanthanum doping on catalytic activity and stability," *International Journal of Hydrogen Energy*, vol. 42, no. 17, pp. 12808–12817, Apr. 2017.

[69] D. Y. Kalai, K. Stangeland, H. Li, and Z. Yu, "The effect of La on the hydrotalcite derived Ni catalysts for dry reforming of methane," *Energy Procedia*, vol. 142, pp. 3721–3726, Dec. 2017.

[70] G. Moradi, F. Khezeli, and H. Hemmati, "Syngas production with dry reforming of methane over Ni/ZSM-5 catalysts," *Journal of Natural Gas Science and Engineering*, vol. 33, pp. 657–665, Jul. 2016.

[71] C. Tanios *et al.*, "Syngas production by the CO2 reforming of CH4 over Ni–Co–Mg–Al catalysts obtained from hydrotalcite precursors," *International Journal of Hydrogen Energy*, vol. 42, no. 17, pp. 12818–12828, Apr. 2017.

[72] Y. Kathiraser, U. Oemar, E. T. Saw, Z. Li, and S. Kawi, "Kinetic and mechanistic aspects for CO2 reforming of methane over Ni based catalysts," *Chemical Engineering Journal*, vol. 278, pp. 62–78, Oct. 2015.

[73] J. Zhang, H. Wang, and A. K. Dalai, "Development of stable bimetallic catalysts for carbon dioxide reforming of methane," *Journal of Catalysis*, vol. 249, no. 2, pp. 300–310, Jul. 2007.

[74] J. Niu, X. Du, J. Ran, and R. Wang, "Dry (CO2) reforming of methane over Pt catalysts studied by DFT and kinetic modeling," *Applied Surface Science*, vol. 376, pp. 79–90, Jul. 2016.

[75] A. Y. Khodakov, "Fischer-Tropsch synthesis: Relations between structure of cobalt catalysts and their catalytic performance," *Catalysis Today*, vol. 144, no. 3, pp. 251–257, Jun. 2009.

[76] C. G. Okoye-Chine, M. Moyo, X. Liu, and D. Hildebrandt, "A critical review of the impact of water on cobalt-based catalysts in Fischer-Tropsch synthesis," *Fuel Processing Technology*, vol. 192, pp. 105–129, Sep. 2019.

[77] A. K. Dalai and B. H. Davis, "Fischer–Tropsch synthesis: A review of water effects on the performances of unsupported and supported Co catalysts," *Applied Catalysis A: General*, vol. 348, no. 1, pp. 1–15, Sep. 2008.

[78] Y. Gao, J. Jiang, Y. Meng, F. Yan, and A. Aihemaiti, "A review of recent developments in hydrogen production via biogas dry reforming," *Energy Conversion and Management*, vol. 171, pp. 133–155, Sep. 2018.

[79] A. Abraham *et al.*, "Pretreatment strategies for enhanced biogas production from lignocellulosic biomass," *Bioresource Technology*, vol. 301, p. 122725, Apr. 2020.

[80] P. Peu *et al.*, "Prediction of hydrogen sulphide production during anaerobic digestion of organic substrates," *Bioresource Technology*, vol. 121, pp. 419–424, Oct. 2012.

[81] G. Zhang, J. Liu, Y. Xu, and Y. Sun, "A review of CH4CO2 reforming to synthesis gas over Ni-based catalysts in recent years (2010–2017)," *International Journal of Hydrogen Energy*, vol. 43, no. 32, pp. 15030–15054, Aug. 2018.

[82] A. Mourhly, M. Kacimi, M. Halim, and S. Arsalane, "New low cost mesoporous silica (MSN) as a promising support of Ni-catalysts for high-hydrogen generation via dry reforming of methane (DRM)," *International Journal of Hydrogen Energy*, vol. 45, pp. 11449-11459, Apr. 2020.

[83] Y. Wang, L. Yao, S. Wang, D. Mao, and C. Hu, “Low-temperature catalytic CO2 dry reforming of methane on Ni-based catalysts: A review,” *Fuel Processing Technology*, vol. 169, pp. 199–206, Jan. 2018.
[84] Q. Zhang *et al.*, “A sintering and carbon-resistant Ni-SBA-15 catalyst prepared by solid-state grinding method for dry reforming of methane,” *Journal of CO2 Utilization*, vol. 17, pp. 10–19, Jan. 2017.
[85] S. Zhang, S. Muratsugu, N. Ishiguro, and M. Tada, “Ceria-Doped Ni/SBA-16 Catalysts for Dry Reforming of Methane,” *ACS Catal.*, vol. 3, no. 8, pp. 1855–1864, Aug. 2013.
[86] G. Zhang, J. Liu, Y. Xu, and Y. Sun, “Ordered mesoporous Ni/Silica-carbon as an efficient and stable catalyst for CO2 reforming of methane,” *International Journal of Hydrogen Energy*, vol. 44, no. 10, pp. 4809–4820, Feb. 2019.
[87] L. Zhang, X. Wang, X. Shang, M. Tan, W. Ding, and X. Lu, “Carbon dioxide reforming of methane over mesoporous nickel aluminate/γ-alumina composites,” *Journal of Energy Chemistry*, vol. 26, no. 1, pp. 93–100, Jan. 2017.
[88] H. Mustu *et al.*, “Effect of synthesis route of mesoporous zirconia based Ni catalysts on coke minimization in conversion of biogas to synthesis gas,” *International Journal of Hydrogen Energy*, vol. 40, no. 8, pp. 3217–3228, Mar. 2015.
[89] X.-Y. Quek, D. Liu, W. N. E. Cheo, H. Wang, Y. Chen, and Y. Yang, “Nickel-grafted TUD-1 mesoporous catalysts for carbon dioxide reforming of methane,” *Applied Catalysis B: Environmental*, vol. 95, no. 3–4, pp. 374–382, Apr. 2010.
[90] K. Parkhomenko *et al.*, “Mesoporous amorphous silicate catalysts for biogas reforming,” *Catalysis Today*, vol. 189, no. 1, pp. 129–135, Jul. 2012.
[91] M. Wang *et al.*, “Facile one-pot synthesis of highly dispersed Ni nanoparticles embedded in HMS for dry reforming of methane,” *Chemical Engineering Journal*, vol. 313, pp. 1370–1381, Apr. 2017.
[92] B. Sarkar, R. Goyal, C. Pendem, T. Sasaki, and R. Bal, “Highly nanodispersed Gd-doped Ni/ZSM-5 catalyst for enhanced carbon-resistant dry reforming of methane,” *Journal of Molecular Catalysis A: Chemical*, vol. 424, pp. 17–26, Dec. 2016.
[93] B. Erdogan, H. Arbag, and N. Yasyerli, “SBA-15 supported mesoporous Ni and Co catalysts with high coke resistance for dry reforming of methane,” *International Journal of Hydrogen Energy*, vol. 43, no. 3, pp. 1396–1405, Jan. 2018.
[94] K. Rouibah *et al.*, “Dry reforming of methane on nickel-chrome, nickel-cobalt and nickel-manganese catalysts,” *International Journal of Hydrogen Energy*, vol. 42, no. 50, pp. 29725–29734, Dec. 2017.
[95] X. Zhang, C. Yang, Y. Zhang, Y. Xu, S. Shang, and Y. Yin, “Ni–Co catalyst derived from layered double hydroxides for dry reforming of methane,” *International Journal of Hydrogen Energy*, vol. 40, no. 46, pp. 16115–16126, Dec. 2015.
[96] C. Anil, J. M. Modak, and G. Madras, “Syngas production via CO2 reforming of methane over noble metal (Ru, Pt, and Pd) doped LaAlO3 perovskite catalyst,” *Molecular Catalysis*, vol. 484, p. 110805, Mar. 2020.
[97] H. S. Whang *et al.*, “Enhanced activity and durability of Ru catalyst dispersed on zirconia for dry reforming of methane,” *Catalysis Today*, vol. 293–294, pp. 122–128, Sep. 2017.
[98] R. Debek and R. Dębek, “Novel catalysts for chemical CO2 utilization,” phdthesis, Université Pierre et Marie Curie - Paris VI, July 2016.
[99] Y. Turap, I. Wang, T. Fu, Y. Wu, Y. Wang, and W. Wang, “Co–Ni alloy supported on CeO2 as a bimetallic catalyst for dry reforming of methane,” *International Journal of Hydrogen Energy*, vol. 45, no. 11, pp. 6538–6548, Feb. 2020.

[100] T. Zhang *et al.*, “Dry reforming of methane on Ni-Fe-MgO catalysts: Influence of Fe on carbon-resistant property and kinetics,” *Applied Catalysis B: Environmental*, vol. 264, p. 118497, May 2020.
[101] S. Wang and G. Q. (Max) Lu, “Role of CeO2 in Ni/CeO2–Al2O3 catalysts for carbon dioxide reforming of methane,” *Applied Catalysis B: Environmental*, vol. 19, no. 3, pp. 267–277, Dec. 1998.
[102] K. Świrk, M. E. Gálvez, M. Motak, T. Grzybek, M. Rønning, and P. Da Costa, “Syngas production from dry methane reforming over yttrium-promoted nickel-KIT-6 catalysts,” *International Journal of Hydrogen Energy*, vol. 44, pp. 274-286, Jan. 2019.
[103] Z. Taherian, M. Yousefpour, M. Tajally, and B. Khoshandam, “Promotional effect of samarium on the activity and stability of Ni-SBA-15 catalysts in dry reforming of methane,” *Microporous and Mesoporous Materials*, vol. 251, pp. 9–18, Oct. 2017.
[104] Z. Alipour, M. Rezaei, and F. Meshkani, “Effect of alkaline earth promoters (MgO, CaO, and BaO) on the activity and coke formation of Ni catalysts supported on nanocrystalline Al2O3 in dry reforming of methane,” *Journal of Industrial and Engineering Chemistry*, vol. 20, no. 5, pp. 2858–2863, Sep. 2014.
[105] L. Yao, J. Shi, H. Xu, W. Shen, and C. Hu, “Low-temperature CO2 reforming of methane on Zr-promoted Ni/SiO2 catalyst,” *Fuel Processing Technology*, vol. 144, pp. 1–7, Apr. 2016.
[106] H. D. Setiabudi, C. C. Chong, S. M. Abed, L. P. Teh, and S. Y. Chin, “Comparative study of Ni-Ce loading method: Beneficial effect of ultrasonic-assisted impregnation method in CO2 reforming of CH4 over Ni-Ce/SBA-15,” *Journal of Environmental Chemical Engineering*, vol. 6, no. 1, pp. 745–753, Feb. 2018.
[107] J. Juan-Juan, M. C. Román-Martínez, and M. J. Illán-Gómez, “Effect of potassium content in the activity of K-promoted Ni/Al2O3 catalysts for the dry reforming of methane,” *Applied Catalysis A: General*, vol. 301, no. 1, pp. 9–15, Feb. 2006.
[108] A. Kambolis, H. Matralis, A. Trovarelli, and Ch. Papadopoulou, “Ni/CeO2-ZrO2 catalysts for the dry reforming of methane,” *Applied Catalysis A: General*, vol. 377, no. 1, pp. 16–26, Apr. 2010.
[109] M. A. A. Aziz, H. D. Setiabudi, L. P. Teh, N. H. R. Annuar, and A. A. Jalil, “A review of heterogeneous catalysts for syngas production via dry reforming,” *Journal of the Taiwan Institute of Chemical Engineers*, vol. 101, pp. 139–158, Aug. 2019.
[110] A. Abdulrasheed, A. A. Jalil, Y. Gambo, M. Ibrahim, H. U. Hambali, and M. Y. Shahul Hamid, “A review on catalyst development for dry reforming of methane to syngas: Recent advances,” *Renewable and Sustainable Energy Reviews*, vol. 108, pp. 175–193, Jul. 2019.
[111] R. Y. Chein, W. H. Hsu, and C. T. Yu, “Parametric study of catalytic dry reforming of methane for syngas production at elevated pressures,” *International Journal of Hydrogen Energy*, vol. 42, no. 21, pp. 14485–14500, May 2017.
[112] K. Ghaib, K. Nitz, and F.-Z. Ben-Fares, “Chemical Methanation of CO2: A Review,” *ChemBioEng Reviews*, vol. 3, no. 6, pp. 266–275, Nov. 2016.
[113] M. D. Argyle and C. H. Bartholomew, “Heterogeneous Catalyst Deactivation and Regeneration: A Review,” *Catalysts*, vol. 5, no. 1, pp. 145–269, Mar. 2015.
[114] P. Unnikrishnan and D. Srinivas, “Chapter 3 - Heterogeneous Catalysis,” In: *Industrial Catalytic Processes for Fine and Specialty Chemicals*, 2016, pp. 41–111.
[115] L. Dehimi, Y. Benguerba, M. Virginie, and H. Hijazi, “Microkinetic modelling of methane dry reforming over Ni/Al2O3 catalyst,” *International Journal of Hydrogen Energy*, vol. 42, no. 30, pp. 18930–18940, Jul. 2017.

[116] C. Tanios, “Caractérisation, évaluation de la toxicité du biogaz issu de déchets ménagers et valorisation par reformage catalytique,” phdthesis, Université du Littoral Côte d’Opale, 2017.
[117] Y. Yan, Y. Dai, Y. Yang, and A. A. Lapkin, “Improved stability of Y2O3 supported Ni catalysts for CO2 methanation by precursor-determined metal-support interaction,” *Applied Catalysis B: Environmental*, vol. 237, pp. 504–512, Dec. 2018.
[118] H. Liu, S. Xu, G. Zhou, K. Xiong, Z. Jiao, and S. Wang, “CO2 hydrogenation to methane over Co/KIT-6 catalysts: Effect of Co content,” *Fuel*, vol. 217, pp. 570–576, Apr. 2018.
[119] J. Guo, H. Lou, H. Zhao, D. Chai, and X. Zheng, “Dry reforming of methane over nickel catalysts supported on magnesium aluminate spinels,” *Applied Catalysis A: General*, vol. 273, no. 1, pp. 75–82, Oct. 2004.
[120] Y. Xu *et al.*, “A comparison of Al2O3 and SiO2 supported Ni-based catalysts in their performance for the dry reforming of methane,” *Journal of Fuel Chemistry and Technology*, vol. 47, no. 2, pp. 199–208, Feb. 2019.
[121] M. Guo and G. Lu, “The difference of roles of alkaline-earth metal oxides on silica-supported nickel catalysts for CO2 methanation,” *RSC Adv.*, vol. 4, no. 102, pp. 58171–58177, Nov. 2014.
[122] H. Arbag, S. Yasyerli, N. Yasyerli, G. Dogu, and T. Dogu, “Enhancement of catalytic performance of Ni based mesoporous alumina by Co incorporation in conversion of biogas to synthesis gas,” *Applied Catalysis B: Environmental*, vol. 198, pp. 254–265, Dec. 2016.
[123] R. O. da Fonseca, R. C. Rabelo-Neto, R. C. C. Simões, L. V. Mattos, and F. B. Noronha, “Pt supported on doped CeO2/Al2O3 as catalyst for dry reforming of methane,” *International Journal of Hydrogen Energy*, vol. 45, no. 8, pp. 5182–5191, Feb. 2020.
[124] I. Iglesias, A. Quindimil, F. Mariño, U. De-La-Torre, and J. R. González-Velasco, “Zr promotion effect in CO2 methanation over ceria supported nickel catalysts,” *International Journal of Hydrogen Energy*, vol. 44, no. 3, pp. 1710–1719.
[125] S. Toemen, W. A. W. Abu Bakar, and R. Ali, “Effect of ceria and strontia over Ru/Mn/Al2O3 catalyst: Catalytic methanation, physicochemical and mechanistic studies,” *Journal of CO2 Utilization*, vol. 13, pp. 38–49, Mar. 2016.
[126] Q. Pan, J. Peng, T. Sun, S. Wang, and S. Wang, “Insight into the reaction route of CO2 methanation: Promotion effect of medium basic sites,” *Catalysis Communications*, vol. 45, pp. 74–78, Feb. 2014.
[127] N. D. Charisiou *et al.*, “An in depth investigation of deactivation through carbon formation during the biogas dry reforming reaction for Ni supported on modified with CeO2 and La2O3 zirconia catalysts,” *International Journal of Hydrogen Energy*, vol. 43, no. 41, pp. 18955–18976, Oct. 2018.
[128] N. A. Abd Ghani, A. Azapour, A. F. Syed Muhammad, and B. Abdullah, “Dry reforming of methane for hydrogen production over NiCo catalysts: Effect of NbZr promoters,” *International Journal of Hydrogen Energy*, vol. 44, pp.20881-20888, Aug. 2019.
[129] A. F. Lucrédio, J. M. Assaf, and E. M. Assaf, “Reforming of a model sulfur-free biogas on Ni catalysts supported on Mg(Al)O derived from hydrotalcite precursors: Effect of La and Rh addition,” *Biomass and Bioenergy*, vol. 60, pp. 8–17, Jan. 2014.
[130] H. Liu *et al.*, “La-promoted Ni-hydrotalcite-derived catalysts for dry reforming of methane at low temperatures,” *Fuel*, vol. 182, pp. 8–16, Oct. 2016.

[131] X. Yu, N. Wang, W. Chu, and M. Liu, “Carbon dioxide reforming of methane for syngas production over La-promoted NiMgAl catalysts derived from hydrotalcites,” *Chemical Engineering Journal*, vol. 209, pp. 623–632, Oct. 2012.
[132] C. C. Chong, Y. W. Cheng, H. D. Setiabudi, N. Ainirazali, D.-V. N. Vo, and B. Abdullah, “Dry reforming of methane over Ni/dendritic fibrous SBA-15 (Ni/DFSBA-15): Optimization, mechanism, and regeneration studies,” *International Journal of Hydrogen Energy*, vol. 45, no. 15, pp. 8507–8525, Mar. 2020.
[133] F. Kosaka *et al.*, “Effect of Ni content on CO2 methanation performance with tubular-structured Ni-YSZ catalysts and optimization of catalytic activity for temperature management in the reactor,” *International Journal of Hydrogen Energy*, vol. 45, no. 23, pp. 12911–12920, Apr. 2020.
[134] R.-P. Ye *et al.*, “High-performance of nanostructured Ni/CeO2 catalyst on CO2 methanation,” *Applied Catalysis B: Environmental*, vol. 268, p. 118474, Jul. 2020.
[135] G. P. Figueredo *et al.*, “A comparative study of dry reforming of methane over nickel catalysts supported on perovskite-type LaAlO3 and commercial α-Al2O3,” *International Journal of Hydrogen Energy*, vol. 43, no. 24, pp. 11022–11037, Jun. 2018.
[136] S. Chai *et al.*, “Boosting CO2 methanation activity on Ru/TiO2 catalysts by exposing (001) facets of anatase TiO2,” *Journal of CO2 Utilization*, vol. 33, pp. 242–252, Oct. 2019.
[137] H. T. T. Nguyen, Y. Kumabe, S. Ueda, K. Kan, M. Ohtani, and K. Kobiro, “Highly durable Ru catalysts supported on CeO2 nanocomposites for CO2 methanation,” *Applied Catalysis A: General*, vol. 577, pp. 35–43, May 2019.
[138] P. A. U. Aldana *et al.*, “Catalytic CO2 valorization into CH4 on Ni-based ceria-zirconia. Reaction mechanism by operando IR spectroscopy,” *Catalysis Today*, vol. 215, pp. 201–207, Oct. 2013.
[139] M. A. A. Aziz, A. A. Jalil, S. Triwahyono, and S. M. Sidik, “Methanation of carbon dioxide on metal-promoted mesostructured silica nanoparticles,” *Applied Catalysis A: General*, vol. 486, pp. 115–122, Sep. 2014.
[140] J. Y. Ahn *et al.*, “Developing Ni-based honeycomb-type catalysts using different binary oxide-supported species for synergistically enhanced CO2 methanation activity,” *Fuel*, vol. 250, pp. 277–284, Aug. 2019.
[141] W. Zhen, B. Li, G. Lu, and J. Ma, “Enhancing catalytic activity and stability for CO2 methanation on Ni–Ru/γ-Al2O3via modulating impregnation sequence and controlling surface active species,” *RSC Advances*, vol. 4, p. 16472, Apr. 2014.
[142] J. Estephane *et al.*, “CO2 reforming of methane over Ni–Co/ZSM5 catalysts. Aging and carbon deposition study,” *International Journal of Hydrogen Energy*, vol. 40, no. 30, pp. 9201–9208, Aug. 2015.
[143] I. Luisetto *et al.*, “Ni supported on γ-Al2O3 promoted by Ru for the dry reforming of methane in packed and monolithic reactors,” *Fuel Processing Technology*, vol. 158, pp. 130–140, Apr. 2017.
[144] Q. Ma *et al.*, “Stabilizing Ni on bimodal mesoporous-macroporous alumina with enhanced coke tolerance in dry reforming of methane to syngas,” *Journal of CO2 Utilization*, vol. 35, pp. 288–297, Jan. 2020.
[145] I. Luisetto *et al.*, “Dry reforming of methane over Ni supported on doped CeO2: New insight on the role of dopants for CO2 activation,” *Journal of CO2 Utilization*, vol. 30, pp. 63–78, Mar. 2019.
[146] A. I. Tsyganok, M. Inaba, T. Tsunoda, S. Hamakawa, K. Suzuki, and T. Hayakawa, “Dry reforming of methane over supported noble metals: a novel approach to preparing catalysts,” *Catalysis Communications*, vol. 4, no. 9, pp. 493–498, Sep. 2003.

[147] H. Zhou *et al.*, "A single source method to generate Ru-Ni-MgO catalysts for methane dry reforming and the kinetic effect of Ru on carbon deposition and gasification," *Applied Catalysis B: Environmental*, vol. 233, pp. 143–159, Oct. 2018.
[148] S. Aouad, E. Abi-Aad, and A. Aboukaïs, "Simultaneous oxidation of carbon black and volatile organic compounds over Ru/CeO2 catalysts," *Applied Catalysis B: Environmental*, vol. 88, no. 3, pp. 249–256, May 2009.
[149] J. M. López *et al.*, "Au deposited on CeO2 prepared by a nanocasting route: A high activity catalyst for CO oxidation," *Journal of Catalysis*, vol. 317, pp. 167–175, Aug. 2014.
[150] B. Puertolas *et al.*, "The catalytic performance of mesoporous cerium oxides prepared through a nanocasting route for the total oxidation of naphthalene," *Applied Catalysis B: Environmental*, vol. 93, no. 3, pp. 395–405, Jan. 2010.
[151] V. Alcalde-Santiago, A. Davó-Quiñonero, D. Lozano-Castelló, and A. Bueno-López, "On the soot combustion mechanism using 3DOM ceria catalysts," *Applied Catalysis B: Environmental*, vol. 234, pp. 187–197, Oct. 2018.
[152] S. Tada, O. J. Ochieng, R. Kikuchi, T. Haneda, and H. Kameyama, "Promotion of CO2 methanation activity and CH4 selectivity at low temperatures over Ru/CeO2/Al2O3 catalysts," *International Journal of Hydrogen Energy*, vol. 39, no. 19, pp. 10090–10100, Jun. 2014.
[153] R. K. Singha, A. Shukla, A. Yadav, L. N. Sivakumar Konathala, and R. Bal, "Effect of metal-support interaction on activity and stability of Ni-CeO2 catalyst for partial oxidation of methane," *Applied Catalysis B: Environmental*, vol. 202, pp. 473–488, Mar. 2017.
[154] L. Jalowiecki-Duhamel, H. Zarrou, and A. D'Huysser, "Hydrogen production at low temperature from methane on cerium and nickel based mixed oxides," *International Journal of Hydrogen Energy*, vol. 33, no. 20, pp. 5527–5534, Oct. 2008.
[155] A. Löfberg, J. Guerrero-Caballero, T. Kane, A. Rubbens, and L. Jalowiecki-Duhamel, "Ni/CeO2 based catalysts as oxygen vectors for the chemical looping dry reforming of methane for syngas production," *Applied Catalysis B: Environmental*, vol. 212, pp. 159–174, Sep. 2017.
[156] S. Tada, T. Shimizu, H. Kameyama, T. Haneda, and R. Kikuchi, "Ni/CeO2 catalysts with high CO2 methanation activity and high CH4 selectivity at low temperatures," *International Journal of Hydrogen Energy*, vol. 37, no. 7, pp. 5527–5531, Apr. 2012.
[157] H. Yu *et al.*, "Bimetallic Ru-Ni/TiO2 catalysts for hydrogenation of N-ethylcarbazole: Role of TiO2 crystal structure," *Journal of Energy Chemistry*, vol. 40, pp. 188–195, Jan. 2020.
[158] L. S. Ribeiro, J. J. Delgado, J. J. M. Órfão, and M. F. R. Pereira, "Carbon supported Ru-Ni bimetallic catalysts for the enhanced one-pot conversion of cellulose to sorbitol," *Applied Catalysis B: Environmental*, vol. 217, pp. 265–274, Nov. 2017.
[159] A. Á. M., L. F. Bobadilla, V. Garcilaso, M. A. Centeno, and J. A. Odriozola, "CO2 reforming of methane over Ni-Ru supported catalysts: On the nature of active sites by operando DRIFTS study," *Journal of CO2 Utilization*, vol. 24, pp. 509–515, Mar. 2018.
[160] J. Zhang, A. Dasgupta, Z. Chen, D. Xu, P. E. Savage, and Y. Guo, "Supercritical water gasification of phenol over Ni-Ru bimetallic catalysts," *Water Research*, vol. 152, pp. 12–20, Apr. 2019.
[161] L. Bian, L. Zhang, R. Xia, and Z. Li, "Enhanced low-temperature CO2 methanation activity on plasma-prepared Ni-based catalyst," *Journal of Natural Gas Science and Engineering*, vol. 27, pp. 1189–1194, Nov. 2015.

[162] V. Vosoughi, S. Badoga, A. K. Dalai, and N. Abatzoglou, “Modification of mesoporous alumina as a support for cobalt-based catalyst in Fischer-Tropsch synthesis,” *Fuel Processing Technology*, vol. 162, pp. 55–65, Jul. 2017.
[163] B. Huang, C. H. Bartholomew, S. J. Smith, and B. F. Woodfield, “Facile solvent-deficient synthesis of mesoporous γ-alumina with controlled pore structures,” *Microporous and Mesoporous Materials*, vol. 165, pp. 70–78, Jan. 2013.
[164] P. Betancourt, A. Rives, R. Hubaut, C. E. Scott, and J. Goldwasser, “A study of the ruthenium–alumina system,” *Applied Catalysis A: General*, vol. 170, no. 2, pp. 307–314, Jun. 1998.
[165] M. Ameen, M. T. Azizan, A. Ramli, S. Yusup, and B. Abdullah, “The effect of metal loading over Ni/γ-Al2O3 and Mo/γ-Al2O3 catalysts on reaction routes of hydrodeoxygenation of rubber seed oil for green diesel production,” *Catalysis Today*, vol. 355, pp. 51-64, Sep. 2020.
[166] A. Alihosseinzadeh, B. Nematollahi, M. Rezaei, and E. N. Lay, “CO methanation over Ni catalysts supported on high surface area mesoporous nanocrystalline γ-Al2O3 for CO removal in H2-rich stream,” *International Journal of Hydrogen Energy*, vol. 40, no. 4, pp. 1809–1819, Jan. 2015.
[167] S. Liu *et al.*, “Studies on toluene adsorption performance and hydrophobic property in phenyl functionalized KIT-6,” *Chemical Engineering Journal*, vol. 334, pp. 191–197, Feb. 2018.
[168] Y. Lv, Z. Xin, X. Meng, M. Tao, and Z. Bian, “Ni based catalyst supported on KIT-6 silica for CO methanation: Confinement effect of three dimensional channel on NiO and Ni particles,” *Microporous and Mesoporous Materials*, vol. 262, pp. 89–97, May 2018.
[169] G. Kamath, S. Badoga, M. Shakouri, Y. Hu, and A. K. Dalai, “Influence of calcination on physico-chemical properties and Ficher–Tropsch activity of titanosilicate supported cobalt catalysts with different pore sizes,” *Applied Catalysis A: General*, vol. 598, p. 117563, May 2020.
[170] L. Wang, J. Chen, A. Patel, V. Rudolph, and Z. Zhu, “Catalytic performance of Ru nanoparticles supported on different mesoporous silicas for preferential oxidation of CO in H2-rich atmosphere,” *Applied Catalysis A: General*, vol. 447–448, pp. 200–209, Dec. 2012.
[171] H.-X. Cao, J. Zhang, C.-L. Guo, J. G. Chen, and X.-K. Ren, “Highly dispersed Ni nanoparticles on 3D-mesoporous KIT-6 for CO methanation: Effect of promoter species on catalytic performance,” *Chinese Journal of Catalysis*, vol. 38, no. 7, pp. 1127–1137, Jul. 2017.
[172] A. Cárdenas-Arenas *et al.*, “Isotopic and in situ DRIFTS study of the CO2 methanation mechanism using Ni/CeO2 and Ni/Al2O3 catalysts,” *Applied Catalysis B: Environmental*, vol. 265, p. 118538, May 2020.
[173] X. Shang *et al.*, “Enhanced low-temperature activity for CO2 methanation over Ru doped the Ni/CexZr(1−x)O2 catalysts prepared by one-pot hydrolysis method,” *International Journal of Hydrogen Energy*, vol. 43, no. 14, pp. 7179–7189, Apr. 2018.
[174] F. Wang *et al.*, “Active Site Dependent Reaction Mechanism over Ru/CeO2 Catalyst toward CO2 Methanation,” *J. Am. Chem. Soc.*, vol. 138, no. 19, pp. 6298–6305, May 2016.
[175] H. Liu, S. Xu, G. Zhou, G. Huang, S. Huang, and K. Xiong, “CO2 hydrogenation to methane over Co/KIT-6 catalyst: Effect of reduction temperature,” *Chemical Engineering Journal*, vol. 351, pp. 65–73, Nov. 2018.
[176] R. Merkache *et al.*, “3D ordered mesoporous Fe-KIT-6 catalysts for methylcyclopentane (MCP) conversion and carbon dioxide (CO2) hydrogenation for

energy and environmental applications," *Applied Catalysis A: General*, vol. 504, pp. 672–681, Sep. 2015.
[177] G. Zhou, T. Wu, H. Xie, and X. Zheng, "Effects of structure on the carbon dioxide methanation performance of Co-based catalysts," *International Journal of Hydrogen Energy*, vol. 38, no. 24, pp. 10012–10018, Aug. 2013.
[178] M.C. Bacariza, I.Graça, A. Westermann, M.F. Ribeiro, J.M. Lopes, and C. Henriques," CO_2 Hydrogenation Over Ni-Based Zeolites: Effect of Catalysts Preparation and Pre-reduction Conditions on Methanation Performance," *Top Catal*, vol. 59, pp. 314–325, Feb. 2016.
[179] Y. Xu *et al.*, "A comparison of Al2O3 and SiO2 supported Ni-based catalysts in their performance for the dry reforming of methane," *Journal of Fuel Chemistry and Technology*, vol. 47, no. 2, pp. 199–208, Feb. 2019.
[180] V. Palma, C. Ruocco, and A. Ricca, "Oxidative steam reforming of ethanol in a fluidized bed over CeO2-SiO2 supported catalysts: effect of catalytic formulation," *Renewable Energy*, vol. 125, pp. 356–364, Sep. 2018.
[181] J. Hu, C. Yu, Y. Bi, L. Wei, J. Chen, and X. Chen, "Preparation and characterization of Ni/CeO2-SiO2 catalysts and their performance in catalytic partial oxidation of methane to syngas," *Chinese Journal of Catalysis*, vol. 35, no. 1, pp. 8–20, Jan. 2014.
[182] A. Prabhu, L. Kumaresan, M. Palanichamy, and V. Murugesan, "Cerium-incorporated cage-type mesoporous KIT-6 materials: Synthesis, characterization and catalytic applications," *Applied Catalysis A: General*, vol. 374, no. 1, pp. 11–17, Feb. 2010.
[183] V. Palma, C. Ruocco, E. Meloni, and A. Ricca, "Highly active and stable Pt-Ni/CeO2-SiO2 catalysts for ethanol reforming," *Journal of Cleaner Production*, vol. 166, pp. 263–272, Nov. 2017.
[184] F. Hu *et al.*, "Reduced graphene oxide supported Ni-Ce catalysts for CO2 methanation: The support and ceria promotion effects," *Journal of CO2 Utilization*, vol. 34, pp. 676–687, Dec. 2019, doi: 10.1016/j.jcou.2019.08.020.
[185] M. Piumetti, S. Bensaid, N. Russo, and D. Fino, "Nanostructured ceria-based catalysts for soot combustion: Investigations on the surface sensitivity," *Applied Catalysis B: Environmental*, vol. 165, pp. 742–751, Apr. 2015.
[186] S. Aouad *et al.*, "Carbon black and propylene oxidation over Ru/CoxMgyAl2Oz catalysts," *Comptes Rendus Chimie*, vol. 16, no. 10, pp. 868–871, Oct. 2013.
[187] F. Ocampo, B. Louis, L. Kiwi-Minsker, and A.-C. Roger, "Effect of Ce/Zr composition and noble metal promotion on nickel based CexZr1−xO2 catalysts for carbon dioxide methanation," *Applied Catalysis A: General*, vol. 392, no. 1, pp. 36–44, Jan. 2011.
[188] S. N. Bukhari, C. C. Chong, H. D. Setiabudi, Y. W. Cheng, L. P. Teh, and A. A. Jalil, "Ni/Fibrous type SBA-15: Highly active and coke resistant catalyst for CO2 methanation," *Chemical Engineering Science*, vol. 229, p. 116141, Jan. 2021.
[189] I. Luisetto, S. Tuti, C. Battocchio, S. Lo Mastro, and A. Sodo, "Ni/CeO2–Al2O3 catalysts for the dry reforming of methane: The effect of CeAlO3 content and nickel crystallite size on catalytic activity and coke resistance," *Applied Catalysis A: General*, vol. 500, pp. 12–22, Jul. 2015.
[190] C. Gennequin *et al.*, "Influence of the presence of ruthenium on the activity and stability of Co-Mg-Al-based catalysts in CO2 reforming of methane for syngas production," *Environ Sci Pollut Res Int*, vol. 23, no. 22, pp. 22744–22760, Nov. 2016.
[191] M. Safariamin, L. H. Tidahy, E. Abi-Aad, S. Siffert, and A. Aboukaïs, "Dry reforming of methane in the presence of ruthenium-based catalysts," *Comptes Rendus Chimie*, vol. 12, no. 6, pp. 748–753, Jun. 2009.

[192] S. Singh *et al.*, "Boron-doped Ni/SBA-15 catalysts with enhanced coke resistance and catalytic performance for dry reforming of methane," *Journal of the Energy Institute*, vol. 93, no. 1, pp. 31–42, Feb. 2020.
[193] A. D. D. Kaynar, D. Dogu, and N. Yasyerli, "Hydrogen production and coke minimization through reforming of kerosene over bi-metallic ceria–alumina supported Ru–Ni catalysts," *Fuel Processing Technology*, vol. 140, pp. 96–103, Dec. 2015.
[194] K. M. S. Khalil, "Synthesis and characterization of mesoporous ceria/alumina nanocomposite materials via mixing of the corresponding ceria and alumina gel precursors," *Journal of Colloid and Interface Science*, vol. 307, no. 1, pp. 172–180, Mar. 2007.
[195] S. Damyanova *et al.*, "Structure and surface properties of ceria-modified Ni-based catalysts for hydrogen production," *Applied Catalysis B: Environmental*, vol. 225, pp. 340–353, Jun. 2018.
[196] J. Pu, F. Ikegami, K. Nishikado, and E. W. Qian, "Effect of ceria addition on NiRu/CeO2Al2O3 catalysts in steam reforming of acetic acid," *International Journal of Hydrogen Energy*, vol. 42, no. 31, pp. 19733–19743, Aug. 2017.
[197] S. Aouad, E. Saab, E. Abi Aad, and A. Aboukaïs, "Reactivity of Ru-based catalysts in the oxidation of propene and carbon black," *Catalysis Today*, vol. 119, no. 1, pp. 273–277, Jan. 2007.
[198] A. Iriondo *et al.*, "Glycerol steam reforming over Ni catalysts supported on ceria and ceria-promoted alumina," *International Journal of Hydrogen Energy*, vol. 35, no. 20, pp. 11622–11633, Oct. 2010.
[199] D. Xia, Y. Chen, C. Li, C. Liu, and G. Zhou, "Carbon dioxide reforming of methane to syngas over ordered mesoporous Ni/KIT-6 catalysts," *International Journal of Hydrogen Energy*, vol. 43, no. 45, pp. 20488–20499, Nov. 2018.
[200] N. D. Charisiou *et al.*, "Syngas production via the biogas dry reforming reaction over nickel supported on modified with CeO2 and/or La2O3 alumina catalysts," *Journal of Natural Gas Science and Engineering*, vol. 31, pp. 164–183, Apr. 2016.
[201] R. Dębek *et al.*, "Ni-containing Ce-promoted hydrotalcite derived materials as catalysts for methane reforming with carbon dioxide at low temperature – On the effect of basicity," *Catalysis Today*, vol. 257, pp. 59–65, Nov. 2015.
[202] "Synthesis of Ni-based catalysts supported on nitrogen-incorporated SBA-16 and their catalytic performance in the reforming of methane with carbon dioxide," *Journal of Fuel Chemistry and Technology*, vol. 45, no. 2, pp. 172–181, Feb. 2017.
[203] "Temperature-dependent anti-coking behaviors of highly stable Ni-CaO-ZrO2 nanocomposite catalysts for CO2 reforming of methane," *Chemical Engineering Journal*, vol. 320, pp. 63–73, Jul. 2017.
[204] Q. Zhang *et al.*, "A sintering and carbon-resistant Ni-SBA-15 catalyst prepared by solid-state grinding method for dry reforming of methane," *Journal of CO2 Utilization*, vol. 17, pp. 10–19, Jan. 2017.
[205] S. N. Bukhari, C. Y. Chin, H. D. Setiabudi, and D.-V. N. Vo, "Tailoring the properties and catalytic activities of Ni/SBA-15 via different TEOS/P123 mass ratios for CO2 reforming of CH4," *Journal of Environmental Chemical Engineering*, vol. 5, no. 4, pp. 3122–3128, Aug. 2017.
[206] N. Zucchetto, M. J. Reber, L. Pestalozzi, R. Schmid, A. Neels, and D. Brühwiler, "The structure of mesoporous silica obtained by pseudomorphic transformation of SBA-15 and SBA-16," *Microporous and Mesoporous Materials*, vol. 257, pp. 232–240, Feb. 2018.

[207] L. Karam and N. El Hassan, “Advantages of mesoporous silica based catalysts in methane reforming by CO2 from kinetic perspective,” *Journal of Environmental Chemical Engineering*, vol. 6, no. 4, pp. 4289–4297, Aug. 2018.
[208] K. Sayadi, A. Rahdar, M. R. Hajinezhad, S. Nikazar, and M. A. B. H. Susan, “Atorvastatin-loaded SBA-16 nanostructures: Synthesis, physical characterization, and biochemical alterations in hyperlipidemic rats,” *Journal of Molecular Structure*, vol. 1202, p. 127296, Feb. 2020.
[209] N. Abdullah, N. Ainirazali, and H. Ellapan, “Structural effect of Ni/SBA-15 by Zr promoter for H2 production via methane dry reforming,” *International Journal of Hydrogen Energy*, Jul. 2020. In press.
[210] C. C. Chong, L. P. Teh, and H. D. Setiabudi, “Syngas production via CO2 reforming of CH4 over Ni-based SBA-15: Promotional effect of promoters (Ce, Mg, and Zr),” *Materials Today Energy*, vol. 12, pp. 408–417, Jun. 2019.
[211] E. Akiki *et al.*, “Production of hydrogen by methane dry reforming: A study on the effect of cerium and lanthanum on Ni/MgAl2O4 catalyst performance,” *International Journal of Hydrogen Energy*, vol. 45, pp. 21392-21408, Jul. 2020.
[212] Y. Ruan *et al.*, “Mesoporous LaAl0.25Ni0.75O3 perovskite catalyst using SBA-15 as templating agent for methane dry reforming,” *Microporous and Mesoporous Materials*, vol. 303, p. 110278, Aug. 2020.
[213] M. Yusuf, A. S. Farooqi, L. K. Keong, K. Hellgardt, and B. Abdullah, “Contemporary trends in composite Ni-based catalysts for CO2 reforming of methane,” *Chemical Engineering Science*, vol. 229, p. 116072, Jan. 2021.
[214] O. Daoura *et al.*, “One-pot prepared mesoporous silica SBA-15-like monoliths with embedded Ni particles as selective and stable catalysts for methane dry reforming,” *Applied Catalysis B: Environmental*, vol. 280, p. 119417, Jan. 2021.
[215] O. Daoura *et al.*, “Aqueous nickel(II) hydroxycarbonate instead of nickel(0) colloids as precursors of stable Ni-silica based catalysts for the dry reforming of methane,” *Catalysis Communications*, vol. 138, p. 105953, Apr. 2020.
[216] M. Taghizadeh, H. Akhoundzadeh, A. Rezayan, and M. Sadeghian, “Excellent catalytic performance of 3D-mesoporous KIT-6 supported Cu and Ce nanoparticles in methanol steam reforming,” *International Journal of Hydrogen Energy*, vol. 43, no. 24, pp. 10926–10937, Jun. 2018.
[217] H.-X. Cao, J. Zhang, C.-L. Guo, J. G. Chen, and X.-K. Ren, “Highly dispersed Ni nanoparticles on 3D-mesoporous KIT-6 for CO methanation: Effect of promoter species on catalytic performance,” *Chinese Journal of Catalysis*, vol. 38, no. 7, pp. 1127–1137, Jul. 2017.
[218] L. Qian *et al.*, “Evaluation of the catalytic surface of Ni impregnated meso-microporous silica KIT-6 in CH4 dry reforming by inverse gas chromatography,” *Microporous and Mesoporous Materials*, vol. 243, pp. 301–310, May 2017.
[219] S. Aouad, E. Saab, E. Abi-Aad, and A. Aboukaïs, “Study of the Ru/Ce system in the oxidation of carbon black and volatile organic compounds,” *Kinetics and Catalysis*, vol. 48, no. 6, pp. 835–840, Nov. 2007.

Dissemination of Research Results

Some of the results of this thesis have already been published, and were also presented as oral communications. Additional papers are accepted, submitted or in preparation.

Conference Proceedings and Oral Presentations:

- **Ni/Ce_xKIT-6, Ru/Ce_xKIT-6 and Ni-Ru/Ce_xKIT-6 catalysts for the dry reforming of methane: a comparative study**
  R. Mahfouz et al, "Ni/CexKIT-6, Ru/CexKIT-6 and Ni-Ru/CexKIT-6 catalysts for the dry reforming of methane: a comparative study," *4th Renewable Energy Sources - Research and Business RESRB 2019 conference*, July 2019.
- **CO_2 Methanation over Ru and/or Ni based catalysts supported on KIT-6, Al_2O_3 and CeO_2** *(IREC 2020 Online Research Exhibit)*

Publications:

- **CO_2 reforming of methane over Ni and/or Ru catalysts supported on mesoporous KIT-6: Effect of promotion with Ce**
  R. Mahfouz, J. Estephane, C. Gennequin, L. Tidahy, S. Aouad, and E. Abi-Aad, "CO2 reforming of methane over Ni and/or Ru catalysts supported on mesoporous KIT-6: Effect of promotion with Ce," *J. Environ. Chem. Eng*, vol. 9, pp. 104662, Feb. 2021. https://doi.org/10.1016/j.jece.2020.104662.
- **Ni based catalysts supported on mesoporous Ce_xKIT-6 for CO_2 methanation: Role of Ru promotion in the catalytic activity** *(In preparation)*